2017

Intelligent Nanocoatings for Corrosion Protection of Steels

Feng, Yuanchao

UNIVERSITY OF CALGARY

Intelligent Nanocoatings for Corrosion Protection of Steels

by

Yuanchao Feng

A THESIS

SUBMITTED TO THE FACULTY OF GRADUATE STUDIES

IN PARTIAL FULFILMENT OF THE REQUIREMENTS FOR THE

DEGREE OF DOCTOR OF PHILOSOPHY

GRADUATE PROGRAM IN MECHANICAL AND MANUFACTURING

ENGINEERING

CALGARY, ALBERTA

JUNE, 2017

Abstract

Intelligent coatings, also called smart coatings, refer to coating systems capable of sensing the generation of corrosive environments, and self-responding to corrosion occurrence in demand. In this research, an intelligent coating technology based on doping of home-prepared nanocontainers pre-loaded with inhibitors- in an epoxy host coating was developed for effective corrosion protection of pipeline steel.

The performance of benzotriazole (BTA) inhibitors on preventing corrosion of an X65 pipeline steel was investigated in a bicarbonate solution. A layer of protective inhibitor film with a roughness of nano-meter scale was formed on the steel surface, inhibiting corrosion of the steel.

To determine the compatibility of nanocontainers with the host coating, multi-layered Halloysite polyelectrolyte nanocontainers were fabricated and doped in an epoxy coating. The coating containing Halloysite nanocontainers possessed enhanced corrosion resistance. The corrosion resistance of the coating was improved with the increasing content of the Halloysite nanocontainers in the coating.

To improve the ability of nanocontainers to encapsulate inhibitors BTA, a SiO_2 nanoparticle based polyelectrolyte assembly was prepared as the BTA-encapsulating nanocontainers. At either low or high pH value (e.g., pH 2 or 11), the BTA was released to prevent steel from corrosion in chloride solutions. The Korsemeyer-Peppas model provided an estimation of the inhibitor-releasing rate, which served as the base for prediction of the service life of the intelligent coatings.

An intelligent coating was developed by doping the BTA-encapsulated, SiO_2 nano-particle-based polyelectrolyte nanocontainers in the epoxy coating. For the pipeline steel

coated with the intelligent coatings, the corrosion inhibition was time dependent upon self-releasing of the encapsulated inhibitors from the nanocontainers. With the increasing content of the BTA-encapsulated nanocontainers in the coating, both the coating resistance and corrosion resistance of the steel increase, resulting in a reduced corrosion of the steel.

Furthermore, superhydrophobic zinc nano-films were fabricated on X65 pipeline steel. The optimal condition for electrodeposition was under the current density of 100 mA/cm^2 for 20 mins. The fabricated superhydrophobic, which had a water contact angle up to 158.4° ± 1.5°, possessed a satisfactory antifouling and self-cleaning ability, and provided an effective corrosion protection to the steel in a chloride solution.

Acknowledgements

The research work reported in this thesis was carried out in the Department of Mechanical and Manufacturing Engineering at the University of Calgary under the supervision of Dr. Frank Cheng.

Firstly, I would like to express my sincere gratitude to my supervisor, Dr. Cheng for his excellent supervision, invaluable guidance, constant encouragement, careful and patient assistance and friendly help throughout my whole Ph.D. program. His deep love and perception of science, his persistent endeavour for pursuing the truth, and his consistent efforts at achieving perfection have always inspired and helped me carry out this research project.

Thanks are also given to the members in my group for their companion, helps and valuable discussions in this work. Sincere acknowledgment is also made to the students in Dr. Hua Song's group in the Department of Chemical and Petroleum Engineering for their useful assistance. I wish to express my deep gratitude to Dr. Michael Schoel for his sincere help in technical guidance.

This research was supported by the University of Calgary through the Seed Grant Program, CH2M Hill, and Natural Science and Engineering Research Council of Canada (NSERC).

Dedication

For

my parents and other family relatives,

and for others who have taught, encouraged and supported me over the past years.

Table of Contents

List of Tables

List of Figures and Illustrations

List of Symbols, Abbreviations and Nomenclature

Symbol	Definition
BTA	Benzotriazole
GDP	Gross Domestic Product
HIC	Hydrogen-induced corrosion
MIC	Microbiologically influenced corrosion
SCC	Stress-corrosion cracking
CP	Cathodic protection
NACE	National Association of Corrosion Engineers
FBE	Fusion-bonded epoxy
PE	Polyethylene
LDPE	Low density polyethylene
HDPE	High density polyethylene
3LPE	Three-layer polyethylene
nm	Nanometer
mm	Millimeter
TEOS	Tetraethyl orthosilicate
MMA	Methyl methacrylate monomers
EIS	Electrochemical impedance spectroscopy
PS	Polystyrene
PEI	Polyethylenimine
PU	Polyurethane
PUA	Polyurea
PA	Polyamide
LbL	Layer-by-layer
SVET	Scanning vibrating electrode technique
MBT	2-mercaptobenzothiazole
wt.%	percentage by weight
h	Hour
min	Minute
μA	Microampere
DC	Direct current
PVB	Polyvinylbutyral
CA	Contact angles
γ_{sv}	Solid-vapor surface tensions
γ_{sl}	Solid-liquid surface tensions
γ_{lv}	Liquid-vapor surface tensions
pDop	Polydopamine
NDM	n-dodecyl mercaptan
PDDA, PDDAC	Poly-(diallyldimethylammonium chloride)
PSS, SPSS	Sodium poly-(styrene sulfonate)
DGEBA	Diglycidyl ether of bisphenol A
NAEP	N-Aminoethylpiperazine

WE	Working electrode
SCE	Saturated calomel electrode
RE	Reference electrode
CE	Counter electrode
AC	Alternating current
BADE	Bisphenol a diglycidyl ether resin
CPE	Constant phase element
Rs	Solution resistance
Rct	Charge-transfer resistance
Rc	Coating resistance
R_{prod}	Resistance of the corrosion product layer
CPE_{dl}	CPE of double-charge layer
CPE_c	CPE of the coating
CPE_{prod}	CPE of the corrosion product layer
AFM	Atomic Force Microscope
M	Mole
OCP	Open-circuit potential
E_{corr}	Corrosion potential
i_{corr}	Corrosion current density
β_c	Cathodic Tafel slope
β_a	Anodic Tafel slope
IE	Inhibiting efficiency
BTA^-	Negatively charged BTA
$BTAH^+$	Protonated cations formed BTA
kDa	Atomic mass unit, dalton
FTIR	Fourier transform infrared spectroscopy
TGA	Thermal gravity analysis
Min	Minute
Ref.	Reference
C_{dl}	Double-layer capacitance
ε^0	Vacuum permittivity
ε	Local dielectric constant
d	Thickness of the film
A	Electrode area
Eq.	Equation
η	Inhibition efficiency
θ	Proportional to the surface coverage
t	Time
η_t	Inhibition efficiency after t h
θ_t	Instant surface coverage
C_t	Concentration of the released inhibitors in the solution
K_a	Adsorptive equilibrium constant
K_r	Releasing rate constant
n	Diffusion exponent

R^2	Reliability of data fitting
SEM	Scanning electron microscopy
EDS	Energy-dispersive X-ray spectrum
DTG	Differential thermal gravity
DSC	Differential scanning calorimetry
M_w	Molecular Weight
T_g	Glass-transition temperatures
C_x	Capacitance
Q_x	Constant-phase element
R_x	Resistance (either R_{ct} or R_c)
XRD	X-ray diffraction
DC	Direct current
f_1	Fractional areas estimated for the solid contact with the surface
f_2	Fractional areas estimated for the air contact with the surface
Fig.	Figure

Chapter One: Introduction

1.1 Research background

Industrial infrastructure, such as oil and gas pipelines, are mostly made of metals, especially steels. Corrosion is one of the primary mechanisms that lead to failure of metallic facilities. For pipelines, corrosion can cause leaks, fire and explosion, resulting in serious environmental and economic consequences [1, 2]. In the oil and gas industry, it was estimated that the total annual cost of corrosion is US $ 1.37 billion, with the associated losses due to lost income and remediation measures running into tens of billions of dollars every year [3, 4]. Therefore, corrosion protection has been of great importance for structural integrity management and production assurance.

Two main approaches, an active one and a passive one, are mainly used for corrosion protection. The passive corrosion protection is achieved by application of a barrier layer preventing contact of the structural material with corrosive environments. The active corrosion protection aims at a decrease of the corrosion rate when the main barrier, such as a coating, is damaged and corrosive species come in contact with the substrate material [5]. One of the active protection techniques is the introduction of corrosion inhibitors in the corrosive environment [6]. Application of protective coatings is the most common passive corrosion protection strategy to protect metals from corrosion. There is a great variety of coatings, which can be broadly divided into metallic, inorganic, and organic coatings.

Nowadays, organic coatings have been widely used in various industry sectors, especially oil and gas industry [7]. Generally, coatings selected for corrosion protection

must offer an effective physical barrier, separating the access of water and aggressive species to the metal surface. In addition to the barrier effect, the coating is preferred to have the ability to inhibit the corrosion process if the protective barrier is degraded and failed. Moreover, organic coatings usually contain pinholes and micro-cracking, which can be generated during manufacturing, transportation, construction and service. The presence of the pinholes and cracks exposes the substrate metal to corrosive environments, leading to further failure of the coatings and corrosion of the metals. The timely detection of initial micro-cracks and pinholes is usually difficult due to their small size. This challenge is especially important for pipeline coatings which are buried in soils, and have a design service life of several decades.

One of the solutions to overcome this shortcoming is to combine both passive and active corrosion protection approaches by introducing corrosion inhibitors into the coatings, and the inhibitors can release "smartly" in response to the coating damage. A protective environment is thus generated at the damage area, mitigating or eliminating corrosion of the substrate metal. However, a direct addition of corrosion inhibitors in coatings can cause some detrimental interactions among components, forming electrolyte pathways and compromising the barrier properties of the coatings. In order to possess the corrosion inhibition ability for organic coatings, to the inhibitors can be pre-stored inside nano- or micro-capsules which are compatible with the coating matrix and are able to sense the changes associated with the generation of corrosive environments. As a result, the loaded inhibitors can self-release from the capsules for corrosion inhibition to the metal [8].

Intelligent coatings refer to the ones doped with inhibitor-encapsulated micro- or nano-containers which can sense the generation of corrosive environments due to coating failure and self-release the inhibitors in response to environmental stimuli such as heat, light irradiation, mechanical induction, pH, temperature, aggressive corrosive ions, etc., preventing metallic corrosion without any external intervention [9-11]. Thus, intelligent coatings provide a novel alternative for corrosion protection of engineering infrastructure [12].

Based on functional ingredients of the coating, application, fabrication methods, etc. intelligent coating can be categorized in many different ways. Stimuli/response materials include coatings acting as sensors; coatings that respond to changes in light, heat, or pressure, corrosion control coatings, and color shifting coatings. Other intelligent coatings that are more difficult to classify include self-assembling polymers/coatings, electrically conducting coatings, self-repair and self-healing coatings, superhydrophobic coatings, and optically active coatings [13]. The potential applications for these numerous types of intelligent coatings are broad. The industry is interested in many types of intelligent coatings for corrosion control, environmental protection, and other safety applications [14]. The need for functional surfaces also exists in the marine, automotive, construction, communication, energy, and many other industries. While the intelligent coatings have been proposed and tested as a promising coating alternative for corrosion prevention, none of them were developed at an industrial scale, especially for heavily corrosive environments such as those encountered in oil/gas and pipeline industries. Moreover, most of the intelligent coating research were focus on the lab study. Most importantly, some of the smart coating technologies are very complicated, such as using

vacuum method to encapsulate the inhibitor in hollow mesoporous silica spheres, and also, those should control the experimental parameters, such as fabrication time and temperature. Those methods increased the cost of the intelligent coating and lead to the intelligent coating technology too complex to use in large-scale industrial application.

To date, there has been no intelligent coating technology available for corrosion protection of oil and gas pipelines. Development of high-performance intelligent coatings which are capable of sensing the corrosion occurrence and smartly releasing pre-loaded corrosion inhibitors for effective protection for pipelines is expected to revolutionize the pipeline coating uses and cause a significant technology innovation and breakthrough. It will further improve the pipeline integrity, prolong the service life of pipelines, and reduce the maintenance cost.

1.2 Research objectives

The overall objective of this research is to develop a high-performance intelligent coating technology for effective pipeline corrosion sensing and protection. Progress will be made in the following areas:

1) To investigate the inhibiting mechanism and performance of inhibitors BTA for corrosion of an X65 pipeline steel in bicarbonate solution.

2) To fabricate multi-layered Halloysite polyelectrolyte nanocontainers and investigate their compatibility with an epoxy coating.

3) To fabricate SiO_2 nanoparticle based polyelectrolyte nanocontainers to encapsulate BTA, and to determine the appropriate mechanism to trigger self-releasing of the inhibitors from the nanocontainers.

4) To derive the releasing mechanism and kinetics of BTA inhibitors from the nanocontainers.

5) To develop an intelligent coating by doping uniformly the prepared BTA-encapsulated nanocontainers in an epoxy coating, and to characterize the corrosion protection of the coated pipeline steel in corrosive environments.

6) To prepare superhydrophobic zinc nano-coatings on X65 pipeline steel by electrodeposition technique and stearic acid modification, and to investigate the corrosion resistance, self-cleaning and antifouling of the coatings by optimizing the preparation conditions.

1.3 Content of thesis

The thesis contains eight chapters, with Chapter One giving an overall introduction of the research background and objectives of the work.

Chapter Two presents a comprehensive literature review on development of intelligent coatings and superhydrophobic coatings for corrosion protection, including fabrication of micro- and nano-containers for inhibitor encapsulation, mechanisms for self-releasing of pre-loaded inhibitors from the containers, performance of intelligent coatings for corrosion protection, and preparation of superhydrophobic coatings.

Chapter Three studied the mechanism and inhibiting effect of inhibitors BTA on corrosion of X65 pipeline steel in bicarbonate solution.

Chapter Four investigated the compatibility of the prepared multi-layered Halloysite polyelectrolyte nanocontainers with an epoxy coating and the potential effect of the nanocontainer doping on the coating properties.

In Chapter Five, SiO_2 nanoparticle based polyelectrolyte nanocontainers were fabricated to encapsulate inhibitors BTA. The trigger mechanism for self-releasing of BTA was determined, and releasing kinetics of the inhibitor molecules from the nanocontainers was derived.

Chapter Six developed an intelligent coating by doping uniformly with the prepared SiO_2 nanoparticle based polyelectrolyte nanocontainers in the epoxy coating. The morphology and structure of the intelligent coating were characterized, and its corrosion inhibition performance was determined.

Chapter Seven developed a convenient method to fabricate superhydrophobic zinc nano-films on X65 pipeline steel by electrodeposition and stearic acid modification. The films were characterized, and the self-cleaning, antifouling and anticorrosion performance of the film were investigated.

Chapter Eight summarized the main conclusions of this research, and recommendations for the further work were suggested.

Chapter Two: Literature Review

2.1 Corrosion as a primary mechanism resulting in failure of engineering structures

Based on data published by NACE International in 2013, the global cost of corrosion is estimated to be US$ 2.5 trillion, which is equivalent to 3.4% of the global Gross Domestic Product (GDP) (2013) [15]. By using available corrosion control practices, it is estimated that saving of between 15 and 35% of the cost of corrosion could be realized, i.e. between US$375 and $875 billion annually on a global basis. These costs typically do not include individual safety or environmental consequences. Through near misses, incidents, forced shutdowns, accidents, etc., several industries have come to realize that lack of corrosion control can be very costly and that, through proper corrosion control, significant cost savings can be achieved over the lifetime of an asset.

The essential condition for corrosion to happen is the formation of a corrosion cell on material surface with corrosive media [16]. A basic corrosion cell is comprised of an anode (where an oxidation reaction occurs), a cathode (where the reduction reaction occurs), and a conducting electrolyte. The only difference is that the anodic area corrodes while the cathodic area does not. Instead, the cathodic area becomes the place for cathodic reactions, such as the reduction of H^+ and O_2, to happen. The conducting electrolyte is usually a salt solution. The salinity or resistivity of the solution also affects the corrosion rate.

Almost all industrial facilities and equipment are made of steels, especially carbon steels [2], various corrosive environments and operating conditions in different production sectors have been found to result in a wide variety of corrosion types,

including general corrosion, localized corrosion, stress corrosion cracking (SCC), erosion, hydrogen-induced corrosion (HIC), microbial influenced corrosion (MIC), etc. [17].

The fact that corrosion control can be profitable has been realized over and over again by industry, often following costly business interruptions due to failures of equipment and assets to perform as intended. Cost savings from corrosion control are often not obvious for some period of time; i.e. [15], (i) maintenance costs slowly decrease; (ii) monitoring or inspection costs decrease or inspection intervals increase; (iii) fewer failures save lost production time and/or lost product, decreases injuries, decrease property damage, decrease environmental releases, and improve public relations; and (iv) life extension of the asset. All of these can be included in the business case for enhanced corrosion control. Achieving the most benefit form corrosion control practices is dependent on good business decisions.

2.2 Corrosion protection by the combination of coatings and cathodic protection

Two common methods used to control corrosion, especially external corrosion, of industry infrastructure (e.g., pipelines) are protective coatings and cathodic protection [18]. This design is actually based on the principle that the coating, if intact, provides full protection to the underlying steel. When the coating fails, CP works as a backup to provide continued protection. Thus, the coating used should be compatible with CP, as standards. In other words, the coating used for pipelines should not be cathodic shielding [19].

According to NACE Standard RP0169-2013 [20], a desirable coating should possess the following properties.

1. Effective electrical insulation. As corrosion is an electrochemical process, a good coating must break the current circuit by isolating the metal from its environment (electrolyte). To assure a high electrical resistance, the coating should have a high dielectric strength.

2. High moisture (water) resistance. Water transfer through the coating film may cause blistering, and contribute to corrosion of the metal.

3. Easy applicability. Application of the coating to structures must be possible by a method that will not adversely affect the properties of the structure and with a minimum of defects.

4. Ability to resist development of holidays with time. The coating's resistance to chemicals, hydrocarbons, and acidic or alkaline conditions should be sufficient to ensure their performance in contaminated environments.

5. Good adhesion to metal surface. The coating requires a sufficient adhesion to prevent water ingress or migration between the coating and the metal structure.

6. Ease of repair. As coatings would degrade gradually in service, repairs and recoating in the field are expected.

Pipeline coatings have experienced innovative developments in the past six decades. The product evolution for protection of steel pipes has migrated from field-applied asphalt and coal tar-based materials to the currently used high-performance, field-applied and plant-applied coatings, such as fusion-bonded epoxy (FBE), spray-applied liquid coatings, and two- and three-layer polyolefin coatings, as shown in Fig. 2.1 [21].

Coal tar acted as a filler within the crosslinked epoxy matrix, and the resulting film possesses a proper toughness, adhesion, UV resistance and thermal stability. It was often

used as coating to the offshore pipelines operating at ambient temperatures. However, it was reported that coal tar had some adverse effects on health. Asphalt was then used as a substitute for coal tar because the former contained lower levels of carcinogen. Asphalt coatings had some limitations in terms of flexibility at very low temperatures. Moreover, health and safety restrictions resulted in the continuing decline in the use of the asphalt coatings [22].

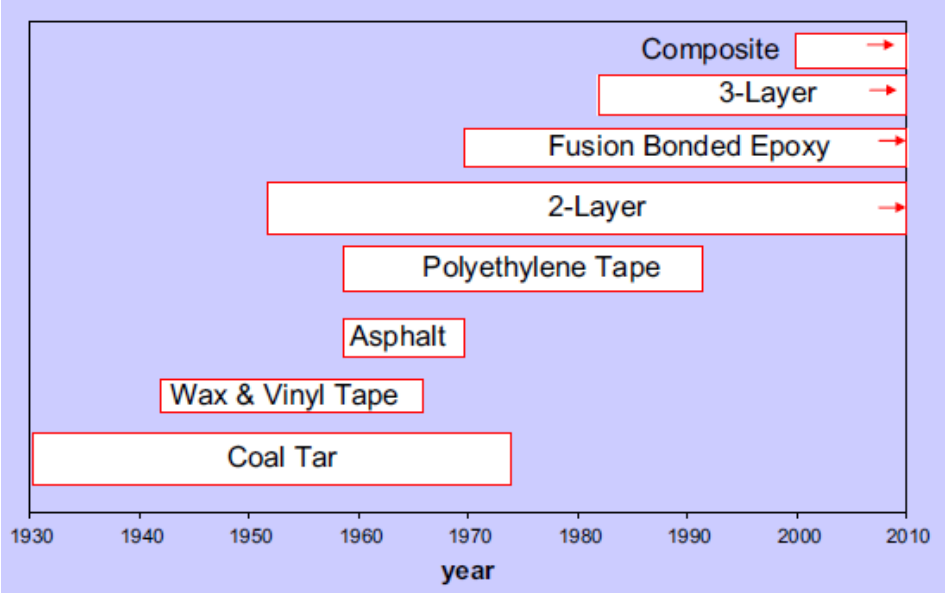

Fig. 2.1 Development of coating technology in oil/gas pipeline systems [21].

Polyethylene (PE) tapes have commonly been used as pipeline coatings. PE is a linear polymer with a crystalline structure. Based on its densities that decided by its molecular weight, there are low density polyethylene (LDPE, with a density of 0.91-0.94 g/cm^3) and high density polyethylene (HDPE, with a density of 0.94-0.97 g/cm^3). When compared to LDPE, the HDPE has a larger crystalline structure, higher yield strength,

and is less permeable to aqueous phase, but it has lower resistance to elongation. So, LDPE, or a blend of LDPE and HDPE is mainly used as PE tape coatings. One typical PE tape consists of three layers: adhesive, inner anti-corrosion tape, and outer mechanical protection tape. The adhesive is a mixture of rubber and synthetic compounds in a suitable solvent, providing a bond between the surface and the inner tape layer. PE backing layer and a laminated butyl-adhesive layer are the main parts for the inner tape layer. The outer layer is also a two-layer tape consisting of a polyolefin backing layer and a laminated butyl-adhesive layer. Disbondment is one common failure style of PE type, usually caused by soil stress. The disbonded PE tape coating normally shields the cathodic protection current, and if water enters the area beneath the disbonded PE tape, corrosion occurs.

Fusion bonded epoxy (FBE) coatings, sometimes called thin-film epoxy, are epoxy-based powder coatings that are widely used to protect pipelines. As a thermoset polymer coating, FBE is made from dry powders. The resin and hardener parts of the dry powders remain unreacted at ambient conditions. At typical coating application temperatures, which are usually in the range of 180 °C to 250 °C, the solid powder melts and transforms into a liquid. The liquid FBE film flows onto and wets the steel surface, and, assisted by heating, becomes a solid coating by chemical cross-linking. This process is known as “fusion bonding”. The chemical cross-linking reaction that takes place in this case is irreversible, which means that, once the curing takes place, the coating cannot be converted back to its original form by any means. A primary disadvantage of the FBE coatings is that they cannot hide apparent surface defects. Therefore, the steel surface has to be inspected after it is coated. The number of holidays contained in the coating is a

function of the surface condition of the steel and the thickness of the coating applied. Increasing the coating thickness could minimize this problem, but the internal stress may be increased up. The FBE usually possesses a superior adhesion to the pipe steel if the steel surface is properly treated.

Three-layer polyolefin pipeline coatings were developed in the 1990s as a way to combine the excellent adhesion of FBE with the strong mechanical strength of extruded PE. These systems consist of an FBE primer, an intermediate copolymer layer, and a topcoat consisting of PE. The function of the intermediate copolymer is to bond the FBE primer with the polyolefin topcoat. Early generations of this coating utilized a 50-75 μm primer which often proved to be inadequate to achieve the desired performance. More recent three-layer systems utilize a 200-300 μm primer as a standard thickness is shown in Fig. 2.2 [23].

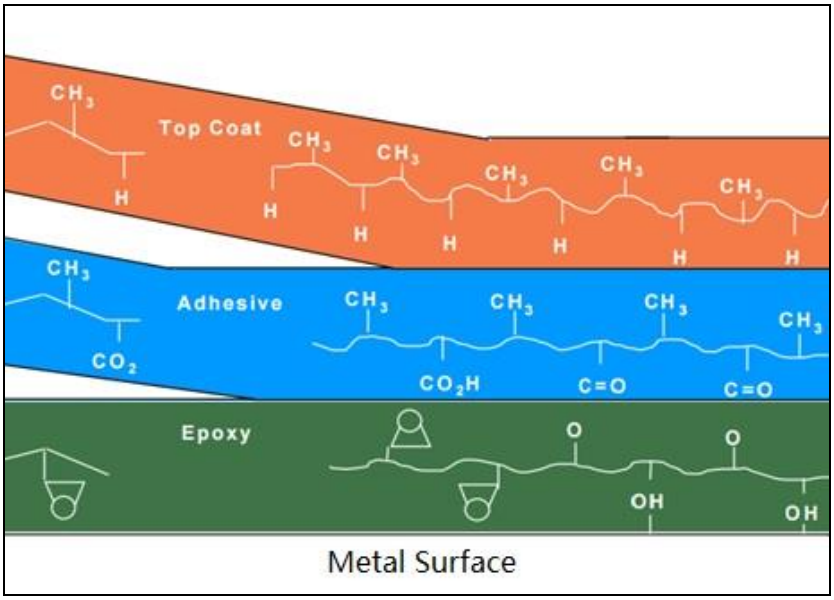

Fig. 2.2 Schematic diagram of three-layer polyolefin coating systems [23].

2.3 Technical challenges in conventional coatings for corrosion protection

Maintenance of structural integrity in increasingly corrosive environments provides great challenges and opportunities for development of new and innovative coating technologies. Generally, organic coatings can effectively withstand the corrosion attack during earlier stages of their service life. At the later stage the barrier performance of the coatings will be adversely affected due to degradation of the coating in exposure to the corrosive electrolyte. Furthermore, when the electrolyte reaches to the adhesive bonds at coating/metal interface, the coating would further disbond and corrosion occurs on the steel under the disbonded coating [24].

Moreover, the polymeric coatings such as epoxy coatings usually contain defects and cracks, which can act as pathways for the ingress of water, oxygen, carbon dioxide, and aggressive species towards the metallic substrate, resulting in corrosion occurrence. Moreover, being hydrophilic in nature, epoxy coatings experience large volume shrinkage upon curing and can absorb water from surroundings [25]. The pores in the cured epoxy coating can assist in the migration of absorbed water and other species to the coating/steel interface, leading to corrosion [26]. Field experiences in pipelines [27] have found a great number of corrosion pits and cracks on the external surface of the pipelines under failed coatings after several years of service [28, 29].

Furthermore, coating disbondment is another common mode encountered on infrastructure including pipelines. The disbonding of coatings can be resulted from either a poor surface preparation condition of the pipeline steel or the stretching of the coating during alternating dry-wet cycling and/or significant ground movement. The disbonded coating usually shields the cathodic protection current from reaching the pipe steel

surface for corrosion protection, as shown in Fig. 2.3 [30]. Water, carbon dioxide and chemicals could enter the disbonded area under the coating, generating a corrosive environment. However, the applied CP has access to the open defect only, and is shielded, at least partially, from reaching the depth of the disbondment. The CP shielding occurs due to the geometrical limitation of the disbonding crevice for mass transport of conductive chemical ions in the trapped electrolyte. Accumulation of corrosion products can also block the diffusion of ions in the crevice. Thus, the cathodic current cannot fully flow into the disbondment, especially its bottom, for corrosion protection. It has been demonstrated that CP shielding by disbonded coatings has been the primary mechanism to cause external corrosion of pipelines in practice [28].

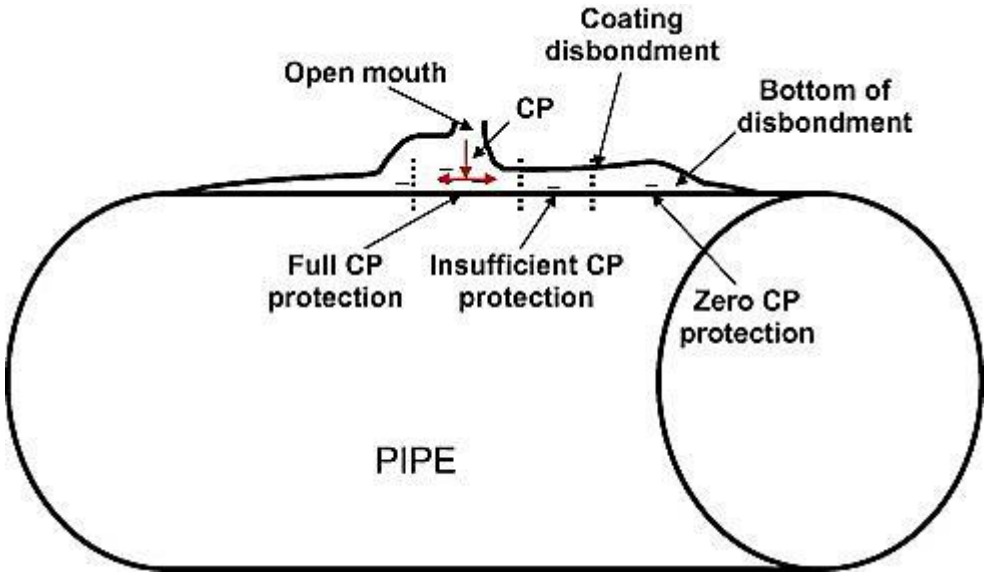

Fig. 2.3 CP shielding under disbonded coating [30].

Although both coatings and CP are applied on the metallic structures such as pipelines, corrosion still occurs and potentially causes the facility failures. Thus, development of high performance functional intelligent coatings, such as intelligent coatings and superhydrophobic coatings, provides an effective way to obtain reliable corrosion protective performance.

2.4 Intelligent coating technology

2.4.1 Recognition of intelligent coatings

Almost all of the organic coatings are susceptible to cracks formed deep within the structure because of changes in the mechanical properties of the coatings during their service life. The cracks propagate and expose the substrate to corrosive environments, finally leading to the failure of the coatings. The detection of initial micron cracks is difficult and their reparation is almost impossible. This challenge is especially important for pipeline coatings which has been designed in service for several decades and are buried in soil. Therefore, efforts have been made to find proper methods to improve the anticorrosion properties of the organic coatings [31-34]. Intelligent coatings technology have evolved from a coating with a specialized resin, pigment, or other material that can respond to an environmental stimulus and react to it. This response can be used in various ways to protect materials from corrosion and other types of damage. There are two basic mechanisms by which intelligent coatings provide corrosion protection: i.e., blocking barrier and chemical inhibition. As mentioned above, organic coatings can retard corrosion through a barrier mechanism, which is achieved via a coating that effectively isolates the substrate from corrosive elements such as moisture, oxygen and ionic species

that can react with the substrate [35]. Organic coating with intelligent properties means that this coating can allows release of the inhibiting species into the aqueous environment present on the metal substrate to retard corrosion via barrier, chemical inhibition or sacrificial mechanism [36]. Barrier protection is achievable only when the coating completely isolates the metal substrate from the corrosive environment. Chemical inhibition refers to the ability of a coating system to release inhibitors to retard corrosion. Sacrificial corrosion protection refers to an active metal coated on a substrate that corrodes at a faster rate due to its more negative electrochemical equilibrium potential of the active metal than the substrate itself. The coating therefore acts as a sacrificial anode, and the substrate is cathodic in the corrosion cell.

The inhibitors that are used in intelligent coating system can be organic or inorganic ones depending on operating conditions and corrosion-inhibiting properties. The most effective inorganic inhibitors are chromates, nitrates, carbonates and phosphates. The most effective organic corrosion inhibitors are amines, heterocyclic nitrogen compounds, and natural compounds such as glue and proteins. These inhibitors act through absorbed films, formation of compact precipitates and/or passivation mechanisms. Two strategies have been reported for designing intelligent coatings, i.e., direct doping of coatings with inhibitors, and encapsulation of inhibitors in prepared micro/nanocontainers or reservoirs that are distributed uniformly in the host coating [37]. For the direct doping technique, there are problems of early leakage of the inhibitors and undesirable interactions between the matrix and the inhibitors, which disrupt the barrier properties of the coatings. Moreover, direct addition of corrosion inhibitors to coatings can cause some detrimental interactions between components, as well as formation of preferential electrolyte

pathways, compromising the barrier properties. In contrast, encapsulation of active materials inside micro/ nanocontainers which are compatible with the coating matrix and are able to sense the local changes induced by the corrosion process can overcome the aforementioned limitations of direct doping. Moreover, the incorporation of nanoparticles into polymers offers an environmentally benign solution to enhance the durability of the coatings. The fine particles dispersed in the coating can fill cavities and cause crack bridging, crack deflection and crack bowing [38, 39]. Nanoparticles tend to occupy small defects formed from local shrinkage during curing of the polymer, and act as a bridge interconnecting more molecules. This results in a reduced total free volume as well as an increase in the cross-linking density [40]. In addition, polymer coatings containing nanoparticles offer significant barrier properties for corrosion protection, and reduce the trend for the coating to blister or delaminate [41].

The intelligent coatings can sense the environment and provide an appropriate response. It can control at an early stage to prevent further corrosion and provide coatings with reliable corrosion protection properties during long service life. Using such capsules, the corrosion protection properties of the organic coatings can be improved significantly. This can be attributed to the slight releasing of small amount of inhibitive species triggered by the external environment, such as variation in pH, increased chloride ion concentration or mechanical damage. Then, the inhibitive species reach the active sites present on the steel surface. In this way, they can restrict the access of the aggressive ions to the active sites of the metal surface. This strategy has led to the development of a new generation of intelligent coatings for anti-corrosion purpose. The mechanism of an intelligent anticorrosion coating is shown schematically in Fig. 2.4 [42]. It is seen that

micro/nanocontainers are doped in the coating to protect the substrate material from corrosion. However, if the coating is damaged by mechanical impact or chemical attack, it can release pro-loaded chemical to repair the coating itself or form protection film underneath the coating on substrate metals. As a result, the ongoing corrosion that caused by the failure of applied coating can be retard without any human interference.

Generally, micro/nanocapsules are particles (ranging from several nm to a few mm in diameter) containing a core (solids, droplets of liquids, or gases) surrounded by a shell (micro/nanocontainers) [43]. The ideal micro/nanocontainers are proposed to be featured with (1) chemical and mechanical stability, (2) compatibility with the coating matrix, (3) sufficient loading capacity, (4) an impermeable shell wall to prevent leakage of the active substance, (5) the ability to sense corrosion onset, and (6) release of the active substance on demand. Some commonly used methods to fabricate the micro/nanocapsules are briefed as follows. The contents from chapter 3 to chapter 6 are aimed to use an easy and economic method to fabricate the smart capsules and intelligent coating.

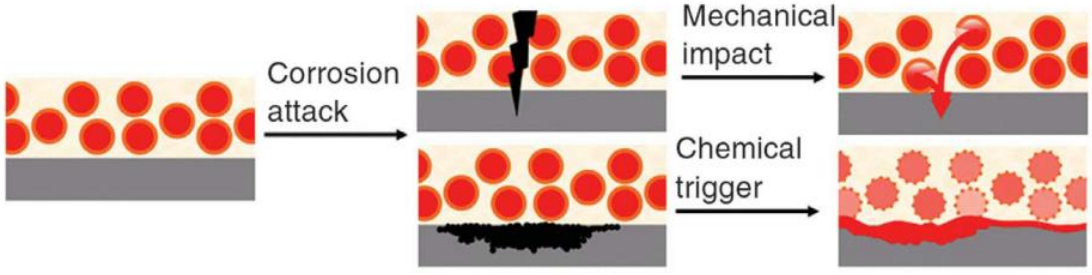

Fig. 2.4 The mechanism of self-healing action of an intelligent anticorrosion coating[42].

2.4.2 Fabrication of micro/nanocontainers

Carriers that can be loaded with functional species, such as corrosion inhibitors, are added to the coating formulation and to become dispersed in the coating matrix. These carriers work as reservoirs, in which the functional species are stored, until they are needed. Suitable carriers include polymeric capsules, porous and hollow particles, nanotubes, clays and a wide array of mesoporous inorganic particles. When added to coatings it is essential to ensure a good compatibility between the guest carriers and the host coating matrix. This is mandatory to maintain the expected barrier performance of the protective coating. Moreover, the guest carriers must be stable and able to store the functional agent for long periods, releasing it only if required. Several functionalities can be inserted in protective coatings using this approach to fabricate intelligent coating, as shown below.

Interfacial self-assembly method

He *et al*. [44] studied the interfacial self-assembly process to make cagelike intelligent porous microcapsules. The overall preparation procedure of the cagelike particle composites is illustrated in Fig. 2.5. The first step was to self-assemble surface sulfonated polystyrene particles, consisting of tetraethyl orthosilicate (TEOS) and methyl methacrylate monomers (MMA), at the water-oil droplet interface. Then 1 g of oil phase (MMA/TEOS = 17/3, mol/mol) was introduced and stirred in the system. In this reserving period, TEOS diffused into the interface of oil phase and water, leading to hydrolysis and condensation reactions of alkoxysilane precursors that were catalyzed by surface sulfogroup of the sulfonated polystyrene particles to form cagelike microspheres.

The cagelike particles were used as reservoirs for encapsulating repairing agents and chemical initiators, which provide self-repairing ability to the protective system after self-assembling into ordered sol-gel coatings. The electrochemical impedance spectroscopy (EIS) measurements for sol-gel film containing this kind of cagelike capsules demonstrated the self-repairing effect after 2 h of immersion in 3 wt.% NaCl solution.

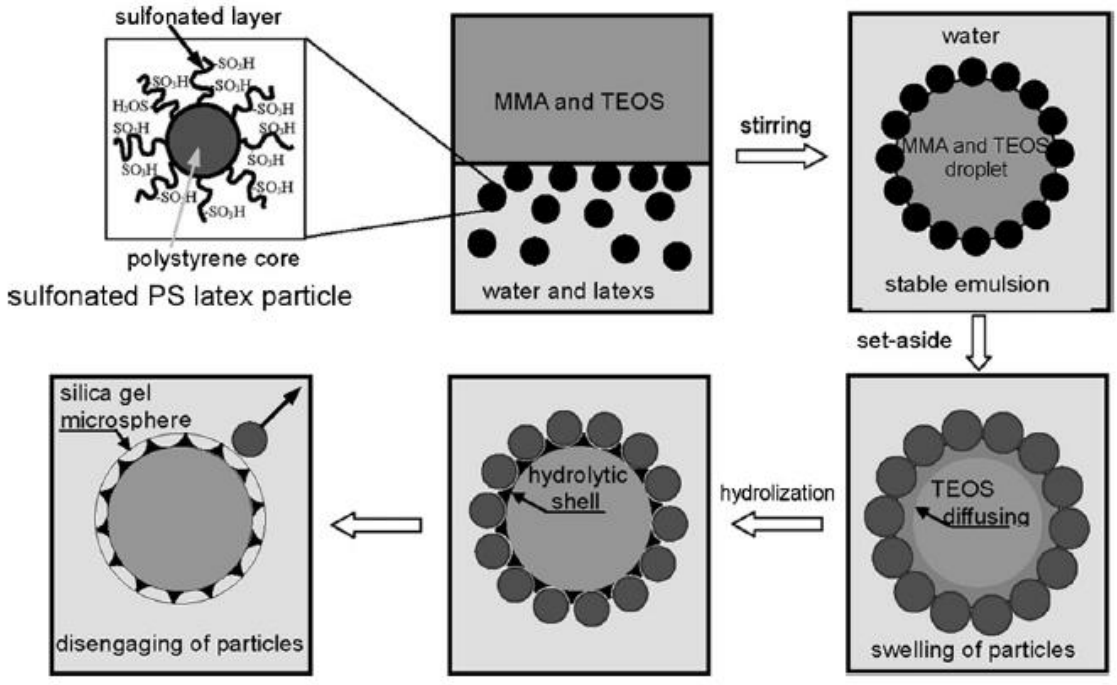

Fig. 2.5 Illustration of the preparation procedure of cagelike silica gel microspheres [44].

Polymeric nanocontainers method

Li *et al.* [45] studied the pH-responsive polystyrene (PS) as polymeric nanocontainers loaded with corrosion inhibitors for anticorrosion coatings. Corrosion

inhibitors (benzotriazole, BTA) are encapsulated in the PS matrix during the polymerization process, which was followed by adsorption of a highly branched polyethylenimine (PEI) as a regulated release of BTA in the response to external pH, as shown in Fig. 2.6. It was proved that the inhibitor-loaded nanocontainers can quickly respond to environmental changes caused by the electrochemical corrosion process, releasing the inhibitors quickly to corrosion areas in response to the pH changes, and forming an organic barrier to block diffusion of corrosive species and terminating further corrosion growth. The shortcoming of this method is its complicated fabricating method, which restricts its application mostly in lab research. Moreover, Latnikova *et al.* [46] developed a method to encapsulate inhibitors by interfacial polymerization with three types of high cross-link density polymers, i.e., polyurethane (PU), polyurea (PUA), and polyamide (PA). It was found that the type of polymer has a great impact on the structure of the resulting capsules. For PU and PUA compact particles loaded with the inhibitors are homogeneously distributed in the polymer matrix when compared with PA capsules, as shown in Fig. 2.7 [47]. However, the release of inhibitors has not been studied well in this work.

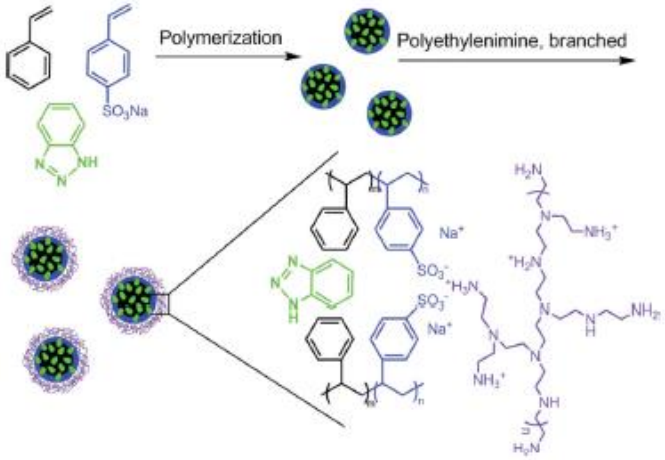

Fig. 2.6 Illustration of the synthesis of corrosion inhibitor-loaded PS-BTA/PEI core-shell polymeric nanocontainers [45].

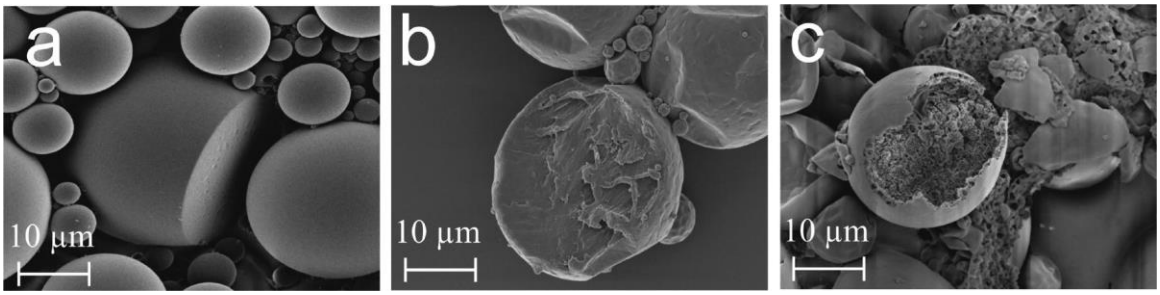

Fig. 2.7 SEM images of crushed PU (a), PUA (b), and PA (c) capsules [47].

Halloysite inorganic clays as container method

Natural halloysite ($Al_2Si_2O_5(OH)_4 \cdot nH_2O$) inorganic clays have attracted significant interest to develop intelligent coatings [48]. One predominant form is the hollow tubular structure with a very small inner diameter in the sub-micron range. A strong surface charge of the Halloysite tubules enables a multilayer assembly at nanoscale using layer-by-layer (LbL) adsorptions [49]. By covering with polyelectrolyte to form nano-shells

over the nanotubes and blocking the tube ends, it is possible to develop further means of controlling the rate of release, as shown in Fig. 2.8 [50]. The results showed that the release of the encapsulated inhibitors was regulated by pH changes in local corrosion areas because of the sensitivity of polyelectrolyte multilayers to changes in the surrounding environment. The scanning vibrating electrode technique (SVET) measurements of alumina coated with sol-gel containing halloysite tubes filled with BTA inhibitors indicated that the corrosion rate at the defect points was remarkably slowed down (3 $\mu A/cm^2$ compared with the corrosion rate of 18 $\mu A/cm^2$ for a pure sol-gel coating). Borisova *et al.* studied the concentration and position of the mesoporous halloysite silica nanocontainers loaded with 2-mercaptobenzothiazole as inhibitors (MBT@NCs) in a hybrid sol-gel (SiO*x*/ ZrO*x*) layer coated on an aluminum alloy AA2024-T3 [51, 52]. The results showed that a very low concentration (0.04 wt.%) of the nanocontainers led to good coating barrier properties, but unsatisfactory corrosion inhibition because of an insufficient amount of available inhibitors. In contrast, a high concentration (0.8-1.7 wt.%) of the nanocontainers deteriorated the coating integrity by introducing diffusion paths for aggressive electrolyte species, resulting in a loss of anticorrosion efficiency. It was also found that the inhibitors can quickly release from the nanocontainers as the corrosion proceeded and improved the corrosion resistance and self-healing ability. The drawback with the inorganic clay based halloysite particles is their lower loading efficiency. Moreover, some kinds of inorganic clay have too long length that they usually form defects such as tunnels from the metal surface to outside environments. This can degrade the anti-corrosion performance of the coating matrix.

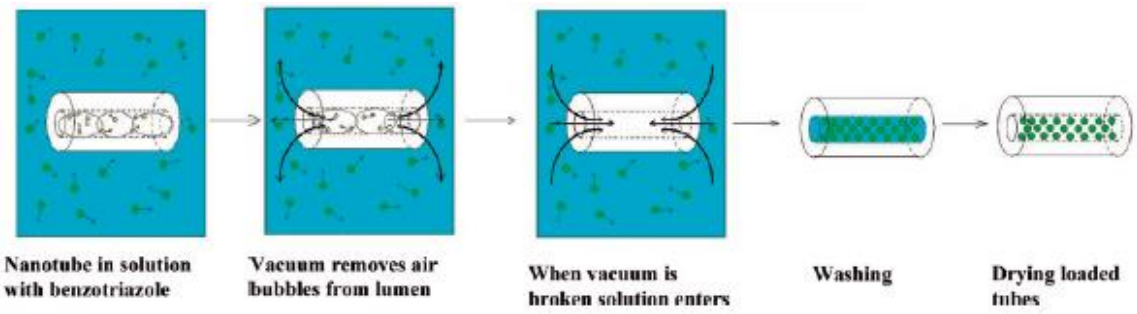

Fig. 2.8 Loading procedure of halloysite nanotubes with benzotriazole [50].

Nanoparticle based polyelectrolyte multilayer method

In addition to the above mentioned fabrication methods, polyelectrolyte multilayers develop new opportunities for anticorrosion protection of intelligent coatings [53]. The sensitivity of the polyelectrolyte film to a variety of physical and chemical conditions such as pH-shift or mechanical impact of the surrounding media provides the ability of a controlled release of the inhibitors entrapped into multilayers. Polyelectrolytes are usually assembled on the surface of nanoparticles via a layer-by-layer (LBL) approach to form inhibitor-loaded nanocontainers. The LBL deposition procedure involves the stepwise electro-static assembly of oppositely charged species on the substrate surface with a nanometer scale precision, and allows the formation of a coating with multiple functionalities. The coating properties can be controlled by the number of deposition cycles and the types of polyelectrolytes used. The conformation of polyelectrolytes is mostly dependent on their nature and adsorption conditions, and much less dependent on the substrate and charge density of the substrate surface. The inhibitors will be released in a controllable way from the host structure when the conformation of the polyelectrolyte molecules changes due to changes in pH, as shown in Fig. 2.9 [54]. The intelligent

release properties of the polyelectrolyte multilayers system are based on following two steps: (i) the polyelectrolytes have pH-buffering activity and can stabilize the pH change on the metal surface in corrosive media; (ii) the inhibitors are released from polyelectrolyte multilayers shell only after start of the corrosion process, directly preventing the corrosion propagation in the rusted area [55].

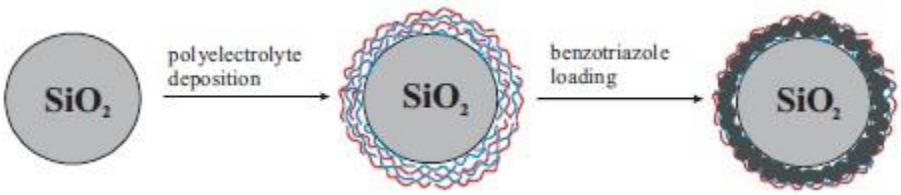

Fig. 2.9 Schematic illustration of the procedure for benzotriazole loading for SiO_2 nanoparticle containers [54].

2.4.3 Releasing mechanisms of encapsulated inhibitors from the micro-/nanocontainers

Encapsulation or intercalation of corrosion inhibitors in micro/nanostructured hosting systems have been developed for fabricating intelligent coating, and various nanocontainers serving as inhibitor-carriers with specific triggering mechanisms for inhibitor-releasing. In this part, some typical triggering mechanisms that are proper to development of intelligent coatings are reviewed.

Desorption controlled releasing

The hybrid sol-gel film on different metals can work by desorption controlled releasing of encapsulated inhibitors [56]. Zheludkevich *et al.* [57] reported an inhibitor

immobilization strategy by incorporation of inhibiting cations such as Ce^{3+} in amorphous ZrO_2 nanoparticles. It was found that sol-gel films with Ce-doped ZrO_2 followed a slow releasing of inhibitors Ce^{3+} by the interaction between cerium cations and ZrO_2 nanoparticles. The releasing of cerium cations resulted in a decease of electron binding energy of Zr in ZrO_2 nanoparticles, indicating that cerium inhibitor interacted directly with the nanostructured particles by adsorption and absorption mechanism.

pH- controlled releasing

A different strategy was used to provide coatings intelligent ability, based on the release of inhibitor on demand by using local changes of pH during corrosion processes as the trigger [58, 59]. In corrosion processes, perhaps the most relevant trigger is pH, as the initiation of corrosion activity is accompanied by local changes of pH in anodic and cathodic sites. The corrosion inhibitors, such as BTA, are incorporated between oppositely charged polyelectrolyte layers on inorganic nanocarriers. The mechanism of this method is to use the permeability dependence of polyelectrolyte shells on pH, providing release of corrosion inhibitors. It can release the inhibitors only when corrosion processes are about to start or have already started, and the surrounding pH changes at the same time to trigger the releasing of the pro-loaded inhibitors [60, 61]. In this method, the negative charged particles are firstly coated with a layer of positively charged polyelectrolyte, followed by adsorption of negatively charged polyelectrolyte and then positively charged BTA as corrosion inhibitors. Shi *et al.* [62] found that polyelectrolytes were sensitive to the pH change, with “open” or “close” state by swelling to thicker layer or shrinking to thinner original state, as shown in Fig. 2.10. It was reported that

polyelectrolytes had a pH-buffering activity and could stabilize pH values between 5 and 7.5 on the metal surface in corrosive media. If polyelectrolytes are used as carriers, inhibitors are able to be released out from the “open” polyelectrolyte multilayers and inhibit corrosion, triggered by the pH changes to more acid or alkaline range due to the corrosion attack on substrate. When pH returns to neutral values, polyelectrolytes recover to “close” state and the inhibitors are sealed again.

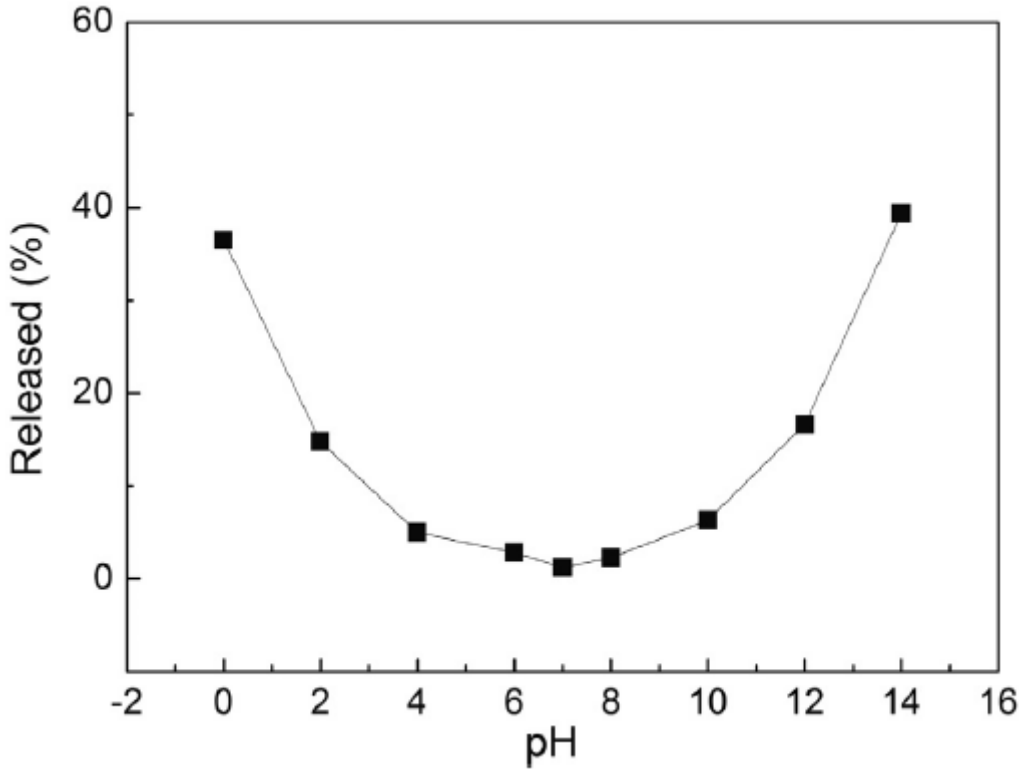

Fig. 2.10 Release of benzotriazole from microcapsules/PEI/PSS/Benzotriazole/PSS/PEI in water solutions with different pH values [62].

Ion-exchange control of inhibitor releasing

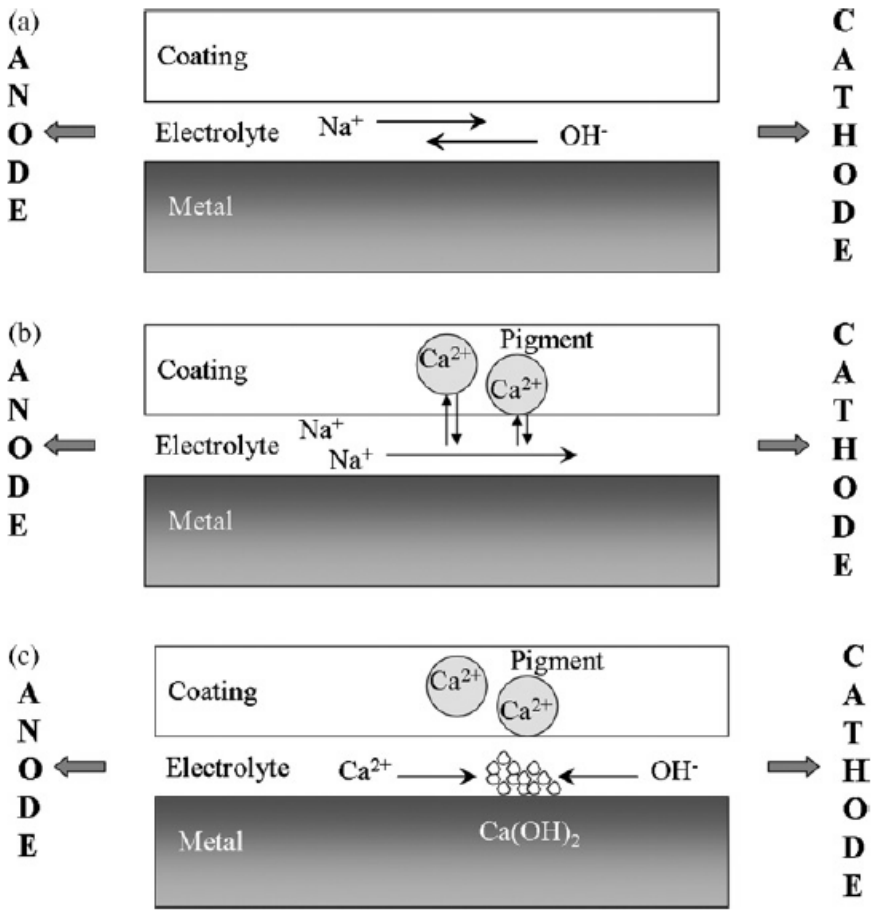

Fig. 2.11 Schematic representation of underfilm inhibition of corrosion-driven delamination occurring in the presence of in-coating Bentonite-Ca^{2+} pigment showing (a) underfilm ion transport in the absence of pigment, (b) cation exchange and (c) cation hydrolysis at elevated pH [63].

In addition to the mechanism for inhibitor releasing from simple desorption to pH-triggered release of inhibitors, another type of intelligent nanoreservoirs for corrosion inhibitors releasing on demand is by ion-exchange. Bentonite is a cation-exchanger,

consisting of stacks of negatively charged aluminosilicate sheets, between which inhibiting cations can be intercalated [64].

Williams *et al.*[63] reported that bentonite pigments exchanged with zinc could act as inhibitors of corrosion-driven cathodic disbondment of polyvinylbutyral (PVB) coatings adherent to the intact zinc surface of hot dip galvanised steel. It was proposed that the decrease in cathodic delamination rates resulted principally from the underfilm Ca^{2+} cation hydrolysis, giving rise to ohmic inhibition through a reduction in mass transport rates, as shown in Fig. 2.11. Incomplete exchange of underfilm Na^{+} by the in-coating bentonite pigments was thought to account for the observation that delamination rates could be slowed down by Ca^{2+} cations, but not completely halted.

Mechanical rapture control of inhibitor releasing

The mechanical rapture trigger mechanism is not corrosion-related but can cause coating degradation and ultimately uncover the metallic substrate, making it accessible to corrosion attack. Kumar *et al.* [65] proposed the feasibility of developing intelligent coatings based on mechanical rapture releasing of corrosion inhibitors by using formulations and embedding microcapsules in commercially available coating systems, as shown in Fig. 2.12. Laboratory tests showed that, when the coating system was damaged by abrasion, the microcapsules released the corrosion inhibiting compounds. Growth of coating damage at the scribe was arrested in self-healing coatings with all microcapsule formulations compared to control samples.

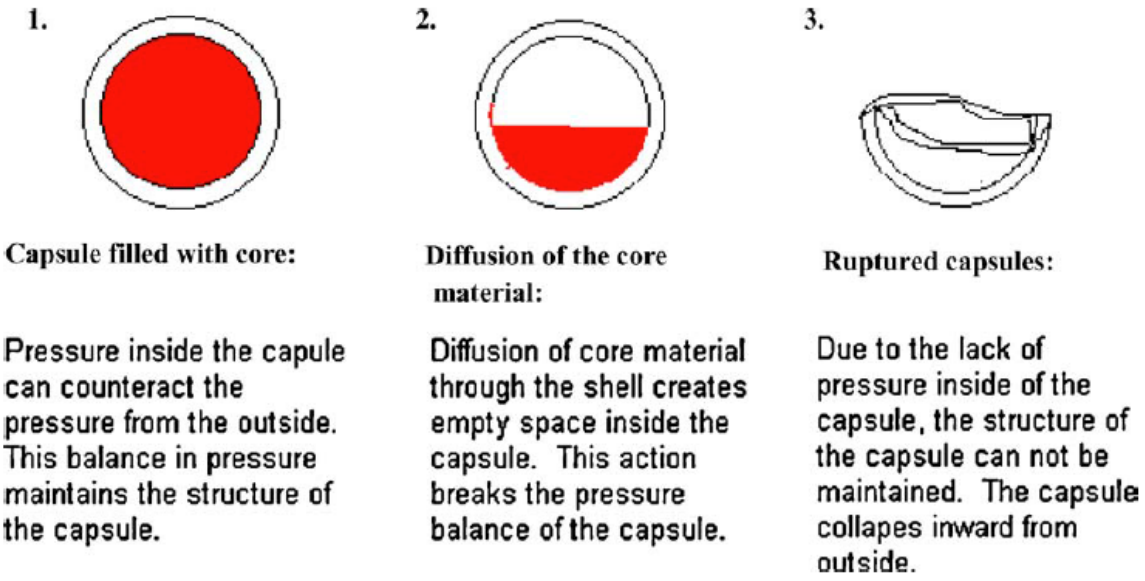

Fig. 2.12 Mechanism for collapse of microcapsules due to attack by solvents in paint [65].

2.5 Superhydrophobic coatings

2.5.1 Recognition of superhydrophobic coatings

Superhydrophobicity is a key surface property enabling corrosion protection because the metal surface results in water and aqueous electrolyte repellence. Superhydrophobic surfaces are characterized by a static contact angles (CA) with water above 150° [66]. The surface hydrophobicity can be achieved by changing the composition, structure or morphology of the outermost surface layer of the coating system. The lotus leaf effect is one of the most effective routes to create superhydrophobic surfaces. Such surface properties attract researchers interested in fabricating such surfaces for self-cleaning and anti-corrosion performance [67]. One important parameter is required to produce superhydrophobic properties, i.e., a surface micro- and/or nano- scale roughness.

Many processes have been employed to control the surface roughness. Particularly, electrochemical methods combine both ease of implementation, even on very large area surfaces, and the possibility to obtain various surface morphologies [68-70]. The electrochemical processes are easy to work out, relatively fast, and very reproducible. Contrary to most of the other techniques, the electrochemical methods are able to create a very large variety of surface morphologies including needles, rods, sheets, and flower-like structures conveniently [66]. Chapter 7 provides the electrodeposition with stearic acid modification method to fabricate the superhydrophobic coating on pipeline steel surface.

2.5.2 Fundamentals of surface superhydrophobicity

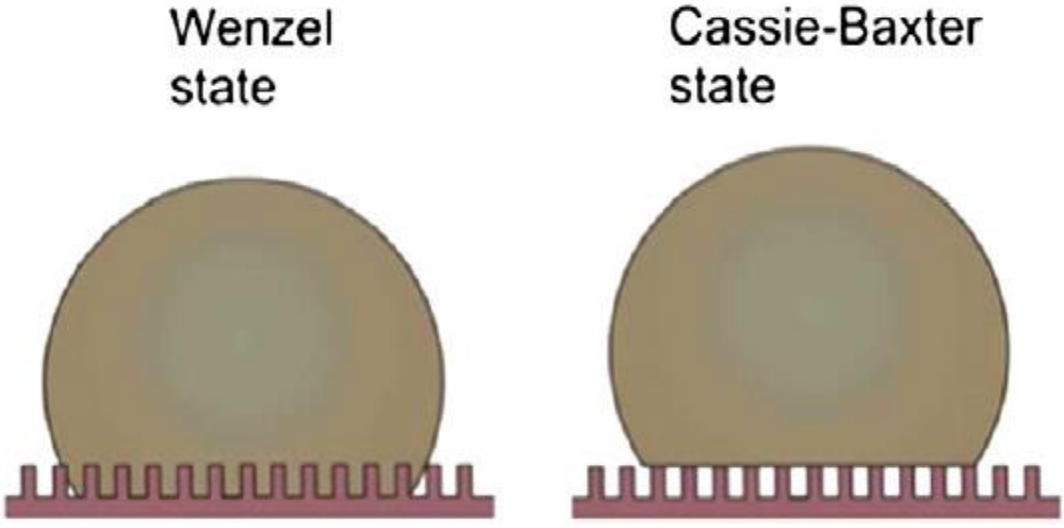

Fig. 2.13 Schematic illustration of a water droplet in the Wenzel and Cassie–Baxter state [71].

The contact angle of a liquid droplet on an ideally flat and chemically homogeneous surface is given by the Young's relation: $\cos\theta = \gamma_{sv} - \gamma_{sl}/ \gamma_{lv}$ with γ_{sv}, γ_{sl} and γ_{lv} are the solid-vapor, solid-liquid, and liquid-vapor surface tensions, respectively [72]. The water contact angle is dominated by the interactions along the three interfaces on the flat surface. Using water as the liquid target, the contact angle of smooth surfaces does not exceed about 125-130° whatever the nature of the material. If the contact angle is above 90°, the surface is intrinsically hydrophobic, and reversely. To obtain superhydrophobic surfaces with contact angles above 150°, a necessary condition is related to the surface roughness, as described by the Cassie-Baxter state and Wenzel state [73, 74], in which the water either sits upon the surface protrusions or penetrates into the surface porosity, respectively, as shown in Fig. 2.13 [71].

In Wenzel model, the interface between the water droplet and the surface is a solid-liquid interface. Such surfaces are often known as a stickiness surface. The Cassie-Baxter model can be used to explain the superhydrophobicity. In this model, the water droplet is suspended on the top of the asperities, and the air fraction present between the surface and the water droplet makes its suspension much easier. A large amount of air is trapped in the microgrooves of a rough surface, and water droplets rest on a composite surface comprising air and the top micro-protrusions.

2.5.3 Typical functions of a superhydrophobic surface

Owing to the unique liquid-repellence, low adhesion and other promising properties, coatings with a superhydrophobicity have been explored their utilities in many different fields during the past decades. Nowadays, a great variety of superhydrophobic surfaces

have shown their commercial potentials. In this work, discussions will be focused on the applications such as self-cleaning and corrosion resistance.

Self-cleaning properties

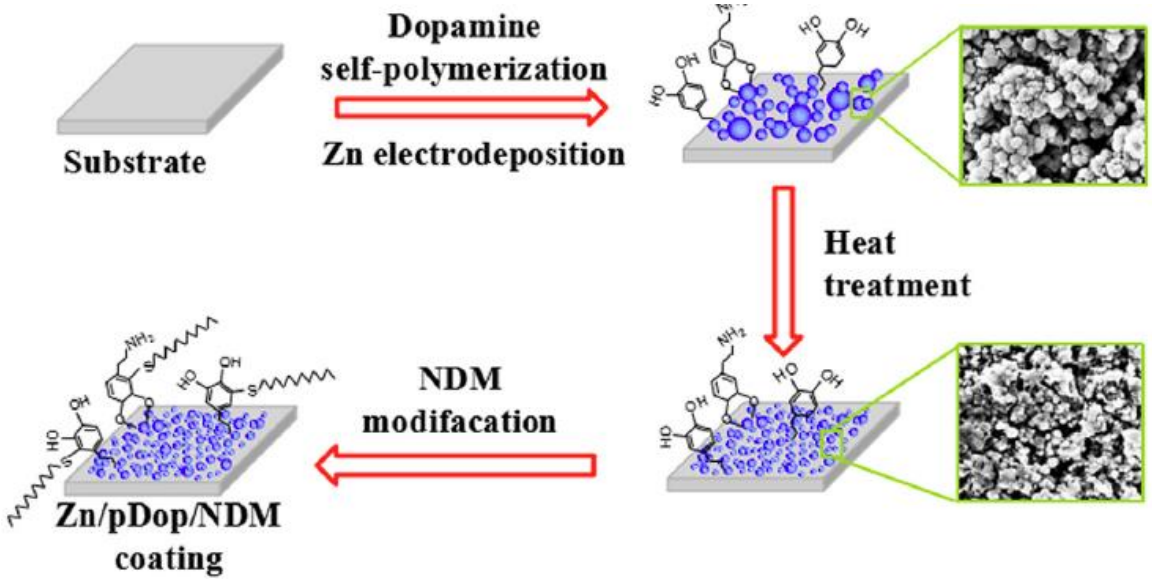

Fig. 2.14 Scheme of the preparation process of Zn electrodeposition self-cleaning coating [75].

Self-cleaning technology indicates the ability to self-repel contamination. It is essential for improved corrosion protection. Self-cleaning coatings can be applied in diverse domains in industry, agriculture, daily life, and military. The concept of self-cleaning surfaces is inspired by the natural lotus because of water droplets are repelled by the lotus leaves, allowing them roll freely towards all directions and then collect dirt particles [76]. The cooperation between a low surface energy and micro/nanoscale structures contributes to a high static water contact angle, which is essential for the

formation of superhydrophobicity induced self-cleaning surfaces. Lots of experimental attempts have been done to generate superhydrophobic self-cleaning products. In particular, ZnO and similar metallic oxides are the most promising superhydrophobic materials [77-79]. Wang et al. [75] reported an electrodeposition method to fabricate superhydrophobic surfaces with excellent self-cleaning properties by using multifunctional Zn/polydopamine(pDop)/n-dodecyl mercaptan(NDM) composite coatings, as shown in Fig. 2.14.

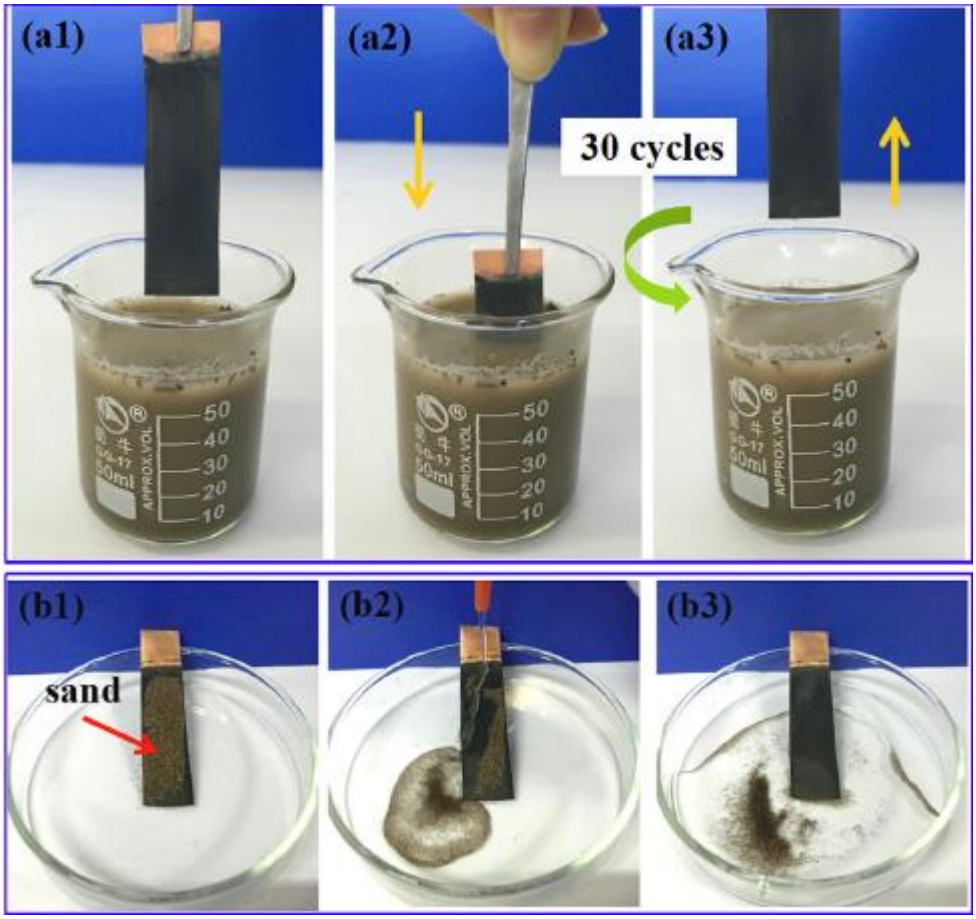

Fig. 2.15 Self-cleaning effect experiments: (a) coating immersed into the muddy water; (b) sand contaminated coating cleaned with distilled water[75].

They obtained a hierarchical cauliflower-like structure on electrodeposited Zn/pDop coatings. After modification with NDM, the prepared Zn/pDop/NDM coatings on different substrate possessed excellent superhydrophobicity, exhibiting a maximum water contact angle of 167.6°. The coated surface could maintain its clean surface without any contaminants after 30 testing cycles when immersed into muddy water. After dropping sands on the coating surface, all sand particles could be easily washed away by water, as shown in Fig. 2.15. The outstanding self-cleaning property can be explained by the joint action of the hierarchical rough structure and the low-surface-energy materials. On the one hand, the hierarchical rough structures trapped air, efficiently restraining the contact of dirt with the surface. On the other hand, the introduction of NDM decreased the surface energy of the as-prepared coatings, which further prevented the infiltrating of liquid into the coating.

Corrosion resistance properties

Superhydrophobic coatings can be developed and employed on various engineering metallic materials to prevent them from corrosion. Direct fabrication of superhydrophobic coatings on metals provide a promising solution for improved anti-corrosion performance due to its low cost, convenient controlling of operating conditions, and high effectiveness. The corrosion resistance mechanism of superhydrophobic surfaces is attributed by the existence of air pockets between the substrate and the corrosive solution, providing an effective blocking to the migration of corrosive ions, as shown in Fig. 2.16 [80].

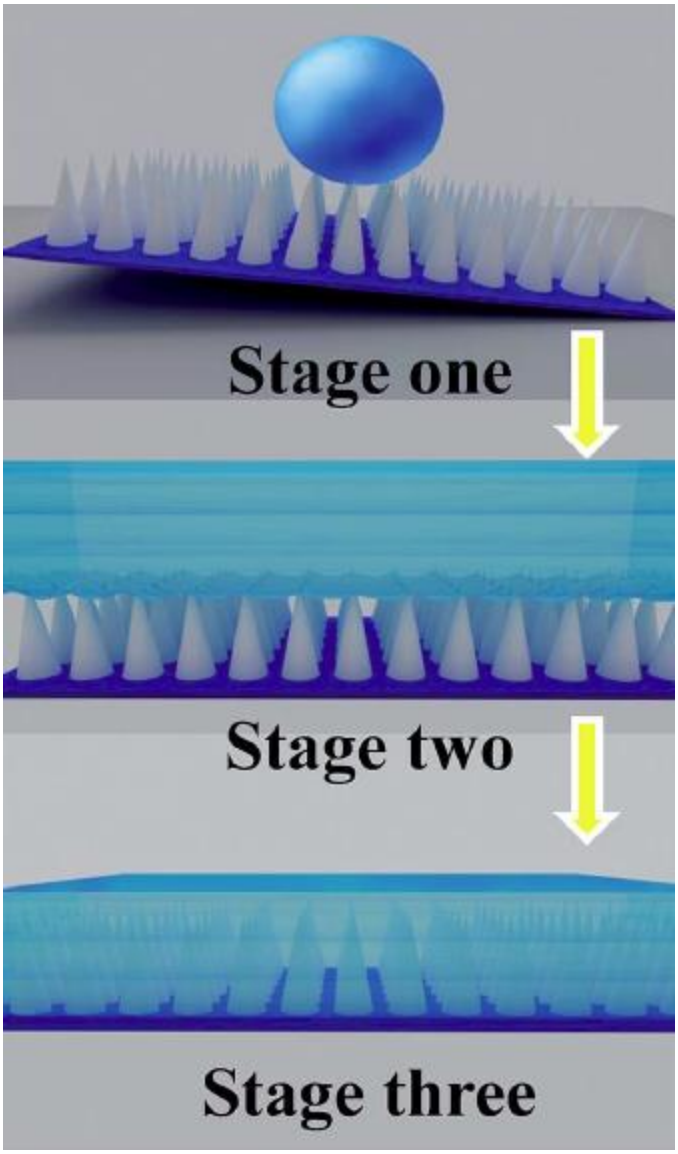

Fig. 2.16 A sketch of the three stages in the anticorrosion process of the superhydrophobic surface [80].

A superhydrophobic carbon steel surface can be fabricated with enhanced corrosion resistance by a convenient electrochemical method and post-modification with low

surface energy materials. For example, Zhang *et al.* [81] reported a method to fabricate a superhydrophobic surface by a two-step method on carbon steels. Highly porous and hierarchically nano/micro-structure silica films were prepared by electrodeposition first. A long alkyl-chained dodecyltrimethoxysilane was then used to further modify the prepared surface to have superhydrophobicity properties. The results showed that this superhydrophobic surface provided an effective corrosion protection for the carbon steel when immersed in aggressive chloride solutions by monitoring the water contact angel and electrochemical measurements, as shown in Fig. 2.17. Nyquist diagrams (Fig. 2.17a) clearly showed much higher impedance values of the superhydrophobic sample (curve 4), in comparison with other specimens (curves 1-3). Warburg impedance characteristic appeared in the superhydrophobic surface in the low frequency domain (curve 4), indicating the restriction of diffusion of corrosion products from the steel surface to bulk solution or that of the reactants (e.g. dissolved oxygen) from the opposite direction. This phenomenon was a result of the promising barrier property of superhydrophobic films. Evolution of the low-frequency impedance module with the immersion time showed the good corrosion performance of the superhydrophobic films (Fig. 2.17c). The impedance values of the superhydrophobic sample decreased with the increasing time, suggesting a degradation process of the superhydrophobic films due to the escaping of the entrapped air layer from the porous structure induced by the continuous attack of water and other aggressive ions. It was noted that, even though immersed in 3.5 wt.% NaCl solution for 120 h, the superhydrophobic sample still had a relatively higher impedance when compare with other samples (Fig. 2.17d).

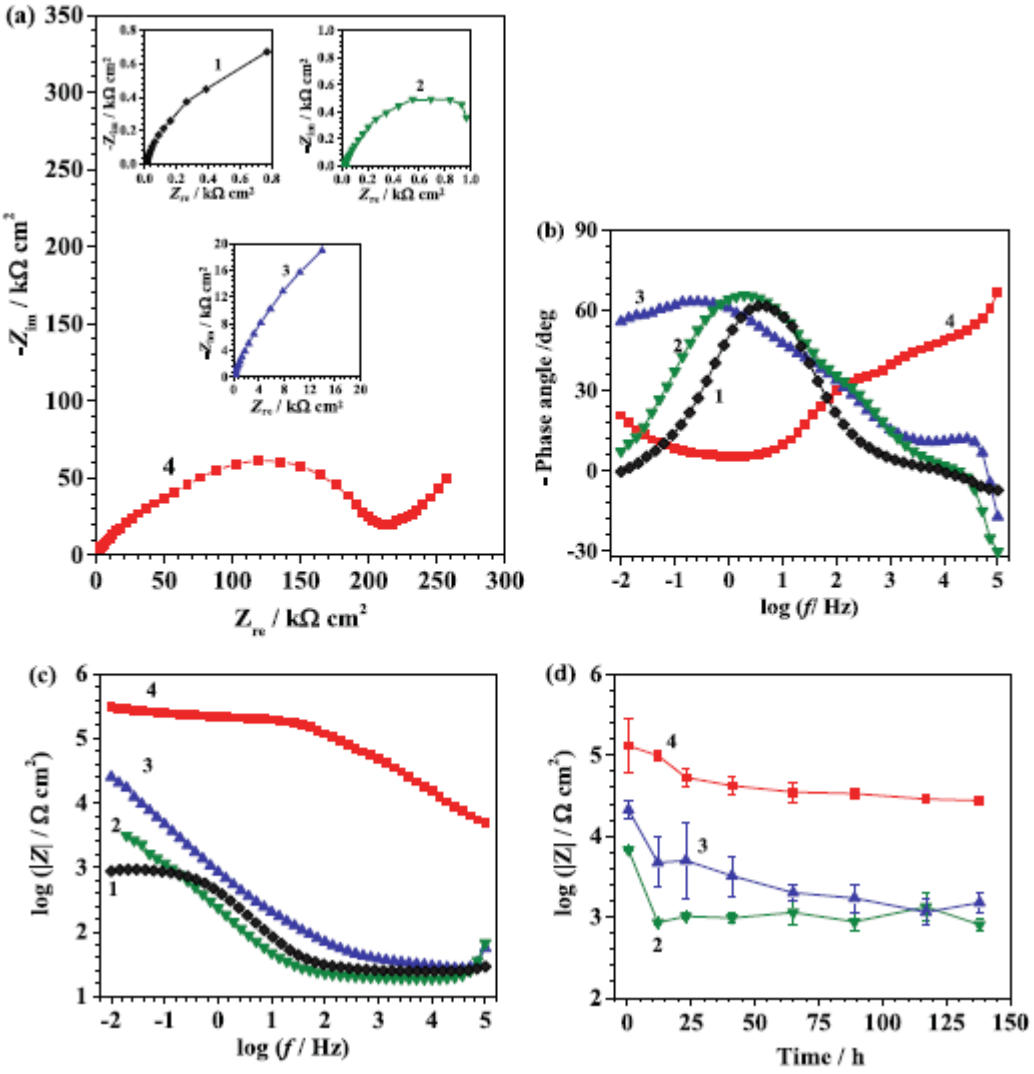

Fig. 2.17 Nyquist diagrams (a), Bode phase angle plots (b), Bode log (|Z|) vs. log (f) plots (c) after immersion for 0.5 h and (d) evolution of low-frequency impedance with immersion time (at 0.01 Hz) in 3.5 wt.% NaCl solution of bare steel (1), DTMD-only treated (2), SiO_2 film-only coated (3) and superhydrophobic coated steel (4) [81].

Superhydrophobic coatings were also prepared on pipeline steels. Li *et al.* [82] demonstrated the corrosion resistance of a superhydrophobic coating on X90 pipeline steel by electrodeposition and solution immersion process, as shown in Fig. 2.18. The CuO flower-like structures in situ grew on the surface of steel via chemical reactions, which was similar to the surface morphology of the lotus leaf. After fluorinated modification, the CuO film on X90 pipeline steel exhibited a fine superhydrophobic, and an excellent anticorrosion performance. Potentiodynamic polarization measurements indicated that the superhydrophobic CuO film on steel surface obviously improved the corrosion resistance of the steel.

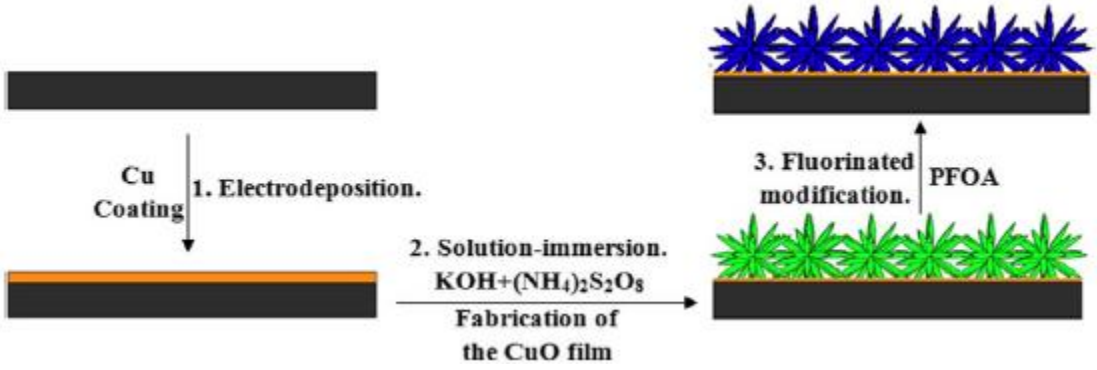

Fig. 2.18 Scheme of the preparation of superhydrophobic CuO film on X90 pipeline steel surface [82].

Chapter Three: Inhibitive Performance of Benzotriazole for Steel Corrosion Studied by Electrochemical and AFM Characterization*

3.1 Introduction

Inhibitor technology provides an effective method to control steel corrosion even at a very small concentration [83]. Nitrogen-based organic molecules, such as benzotriazole (BTA), have been widely used as corrosion inhibitors to prevent steels from corrosion attack [84, 85]. The nitrogen-based corrosion inhibitors are able to adsorb on the steel surface to form a protective layer due to the fact that the inhibitor molecules contain electronegative atoms such as nitrogen (N), unsaturated bonds (e.g., double bonds or triple bonds), and planar conjugated systems including aromatic ring [86]. Moreover, the mechanistic study can be useful for optimization of the concentration of inhibitors in order to maximize the corrosion control.

This work is attempted to investigate the inhibiting mechanism and performance of inhibitors BTA for corrosion of an X65 pipeline steel in a diluted bicarbonate solution (0.01M $NaHCO_3$), a typical electrolyte generated under disbonded coating in the field [28]. Moreover, the effect of the inhibitor concentration on the corrosion inhibition was determined in order to optimize inhibitor uses and maximize the inhibiting performance. A conceptual model was developed to illustrate the inhibiting mechanism.

---

* This work has been published as: Yuanchao Feng, Y. Frank Cheng, Inhibitive performance of benzotriazole for steel corrosion studied by electrochemical and AFM characterization, *Journal of Materials Engineering and Performance* 24 (2015) 4997-5001.

3.2 Experimental

3.2.1 Specimens, solution and inhibitor

Specimens used in this work were cut from a X65 pipeline steel plate, with a chemical composition (wt.%): C 0.04%, Si 0.2%, Mn 1.5%, P 0.011%, S 0.003%, Mo 0.02% and Fe balance. The X65 pipeline steel is a commonly used steel in pipeline industry. The specimen used for electrochemical testing was cut into 1 cm × 1 cm and sealed by epoxy. The work face was subsequently ground up to 1200 grits SiC emery paper. It was then washed with deionized water and degreased with ethanol and acetone, and dried in air before testing. The specimen used for atomic force microscopy (AFM) characterization was ground sequentially to 1500 grit SiC emery paper, polished with 1 μm diamond pastes, washed with deionized water, degreased with ethanol and acetone, and dried in air.

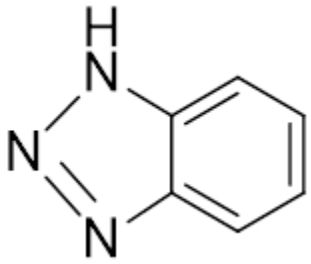

Fig. 3.1 Molecular structure of corrosion inhibitor benzotriazole (BTA).

The testing solution was 0.01 M sodium bicarbonate ($NaHCO_3$) solution, with BTA added at various concentrations (0, 0.005, 0.01, 0.03 and 0.05 M). All solutions were prepared using analytical grade chemicals and deionized water.

The molecular structure of the inhibitor BTA is shown in Fig. 3.1. As an anodic inhibitor, the BTA can adsorb on metal surface, improving the corrosion resistant of the metal [87].

3.2.2 Electrochemical testing

Electrochemical measurements were conducted on a three-electrode cell using a Solartron 1280C electrochemical workstation. The steel specimen was used as the working electrode, and a saturated calomel electrode (SCE) and a platinum plate used as reference and counter electrodes, respectively.

Prior to testing, the working electrode was immersed in the solution for 1 h to reach a steady state, as indicated by the unchanged open-circuit potential (OCP). EIS measurements were carried out on the steel electrode at its corrosion potential over a frequency range from 10 kHz to 0.01 Hz and an AC amplitude voltage of 10 mV. Potentiodynamic polarization curves were measured at a potential scan rate of 0.167 mV/s. The electrochemical corrosion parameters, including corrosion potential (E_{corr}), corrosion current density (i_{corr}), cathodic Tafel slope (β_c), the anodic Tafel slope (β_a) were derived from the polarization curves. The data in the ranges of +70 to +170 mV (versus corrosion potential) and -170 to -70 mV (versus corrosion potential) were used to calculate the anodic and cathodic Tafel slopes, respectively. The total testing duration for the measurements of OCP, EIS and polarization curves was about 4 h.

The inhibiting efficiency, IE, was calculated by:

$$IE\% = \frac{i_{corr}^{0} - i_{corr}}{i_{corr}^{o}} \times 100\% \quad (3\text{-}1)$$

where i_{corr}^{0} (μA/cm^2) and i_{corr}(μA/cm^2) are corrosion current density in the absence and presence of inhibitor in the solution, respectively.

3.2.3 Surface characterization

AFM characterization was conducted on the steel electrode after 2 h of immersion in the solution containing various concentrations of BTA using a Keysight 5500 AFM system. The AFM tip was made of Si, and mounted on triangular cantilevers (450 μm × 50 μm × 2 μm) with an average spring constant of 0.02~0.77 N/m. The scanning process was configured as contact model, with a scanning rate of 1 Hz, scanning rang of 10 μm × 10 μm, and a resolution of 256 × 256 pixel.

3.3 Results and discussion

3.3.1 OCP measurements

Fig. 3.2 shows the time dependence of OCP of the steel electrode in the test solution containing various concentrations of BTA. It is seen that, generally, the addition of BTA shifts the OCP less negatively. Moreover, with the increasing BTA concentration, the OCP is less negative. Particularly, in the blank solution, the OCP reaches a steady value of about -0.70 V(SCE) after 1 h of immersion. When the concentration of BTA is small, i.e., 0.005 and 0.01 M/, the OCP decreases sharply at first and then gradually recovers to

reach a relatively constant value. This indicates that the inhibiting effect of BTA on steel corrosion is dependent on its concentration. At small concentrations, the BTA does not adsorb on the steel surface for corrosion inhibition in the beginning. The corrosion control is time dependent. Along with the increase in the concentration of BTA, the OCP is shifted to less negative value rapidly, indicating that the inhibitor is able to control corrosion upon immersion in the solution.

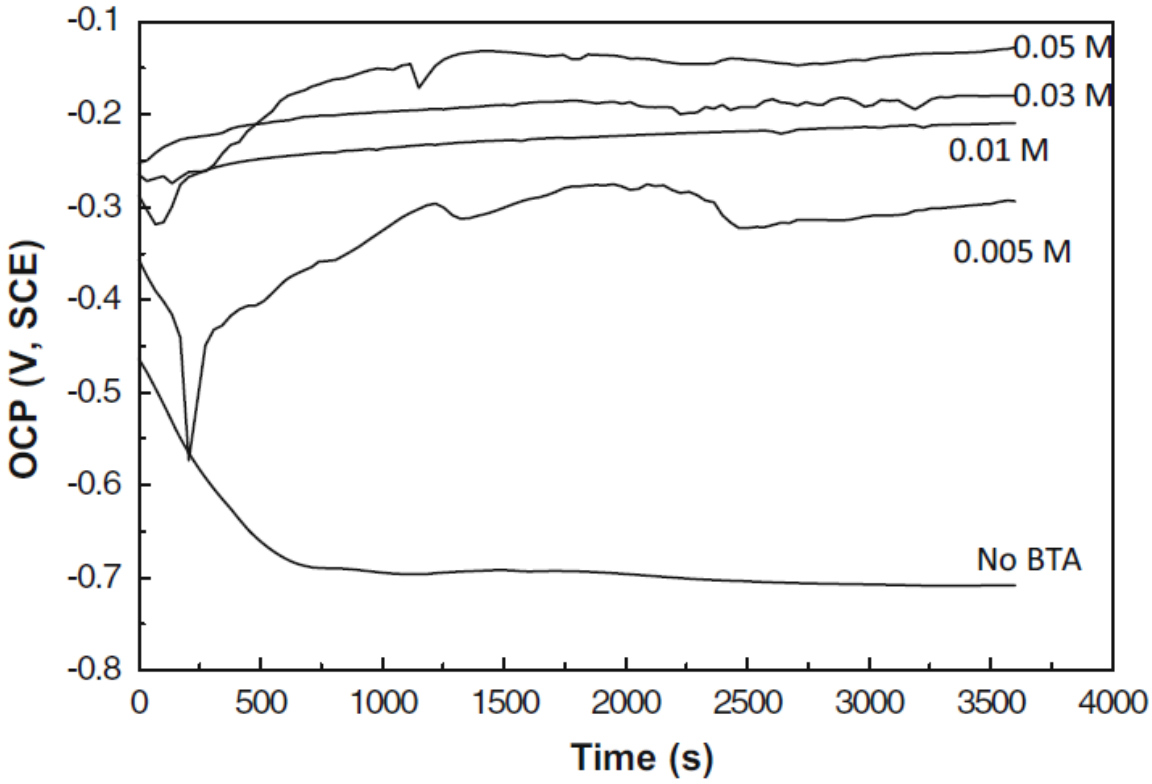

Fig. 3.2 Open-circuit potential of X65 steel in 0.01 M $NaHCO_3$ solution containing various concentrations of BTA.

3.3.2 Polarization curve measurements

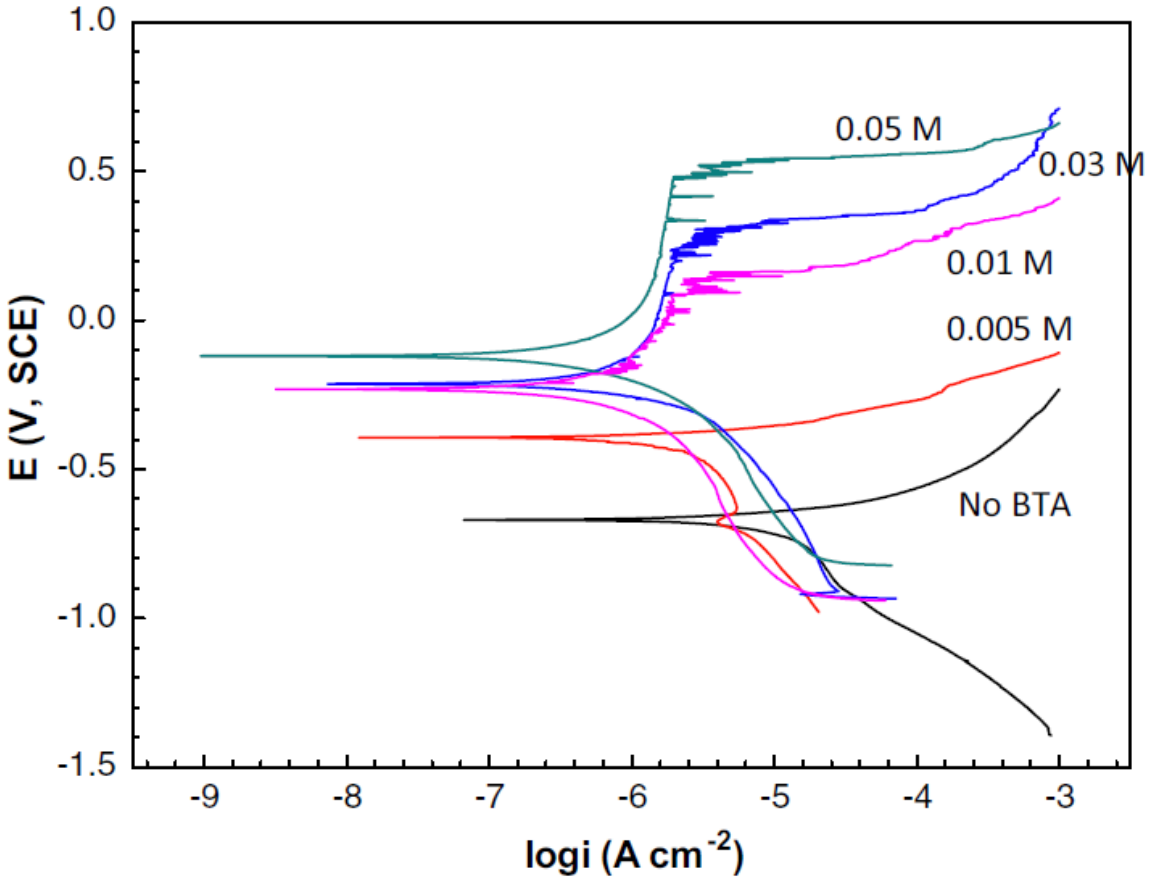

Fig. 3.3 Potentiodynamic polarization curves measured on X65 steel in 0.01 M $NaHCO_3$ solution containing various concentrations of BTA.

Fig. 3.3 shows the potentiodynamic polarization curves of X65 steel in 0.01 M $NaHCO_3$ solution containing various concentrations of BTA. It is seen that the addition of BTA in the solution elevates the corrosion potential. Moreover, the anodic curves are shifted to lower current densities. At individual potential, the anodic current density decreases with the increasing BTA concentration, while the effect of BTA on cathodic

branches is not apparent. Moreover, when the BTA concentration is up to 0.01 M, the steel becomes passivated, as indicated by the presence of passive curves in the anodic polarization branches. Obviously, as an anodic inhibitor, the BTA is effective to inhibit corrosion of the steel in the testing solution.

Table 3.1 Electrochemical corrosion parameters fitted from the polarization curves measured on X65 steel in 0.01 M $NaHCO_3$ solution containing different concentrations of BTA.

Conc., M	E_{corr}, V/SCE	i_{corr}, μA/cm^2	β_a, mV/dec	β_c, mV/dec	IE (%)
Blank	-0.670±0.028	3.295±2.262	62.66±16.54	105.48±21.43	…
0.005	-0.394±0.210	1.241±0.311	35.22±5.08	48.00±10.61	62.3
0.01	-0.214±0.352	0.706±0.244	65.76±17.84	111.18±2.60	78.6
0.03	-0.232±0.016	0.344±0.021	108.42±17.23	101.36±29.91	89.5
0.05	-0.120±0.106	0.164±0.335	73.27±16.75	78.79±22.05	95.0

Table 3.1 shows the fitted values of various electrochemical corrosion parameters, including i_{corr}, E_{corr}, β_c, β_a, and the inhibition efficiency, IE, as a function of the BTA concentration, where the mean value and the range are present. It is noted that the reproducibility of the electrochemical results is quite high, with the fact that the electrode preparation and testing procedure are under a careful control. It is seen that the corrosion current density decreases and corrosion potentials increases with the increasing concentration of BTA in the base solution. The inhibiting efficiency increases continuously with the BTA content. When the BTA concentration is 0.05 M, the

inhibiting efficiency is up to 95%. Thus, the BTA is effective to inhibit corrosion of steel. Moreover, the increase in corrosion potential with the BTA concentration and the presence of anodic passive curves mean that a layer of protective film can be formed on the steel surface for corrosion protection.

3.3.3 EIS measurements

Fig. 3.4 shows the Nyquist diagrams measured on X65 steel in 0.01 M $NaHCO_3$ solution containing various concentrations of BTA. It is seen that the Nyquist diagram obtained in the blank solution exhibits a depressed semicircle in the high frequency range and a straight line in the low-frequency range. While the high-frequency semicircle is associated with the interfacial charge-transfer reaction during corrosion, the low frequency straight line is due to the diffusion of dissolved oxygen towards the steel surface for corrosion reaction. Thus, corrosion of X65 steel in the bicarbonate solution is mixed controlled by both activation and diffusion steps.

Upon addition of BTA in the solution, the impedance plots are re-shaped. At the small concentration of BTA, such as 0.005 M, two overlapped semicircles are observed in the high and low-frequency ranges. Moreover, the high-frequency semicircle becomes bigger compared to that recorded in the blank solution. With the further increase in BTA concentration, in addition to the high-frequency semicircle, a new depressed semicircle is observed in the low-frequency range. This is attributed to the formation of a protective inhibitor film on the steel surface. Moreover, the size of the low-frequency semicircle increases with the increasing BTA concentration. Since the diameter of the semicircle is proportional to the resistance of charge-transfer reaction or the surface film, the enlarged

semicircle indicates the improving structure, coverage or thickness of the film for enhanced corrosion inhibition.

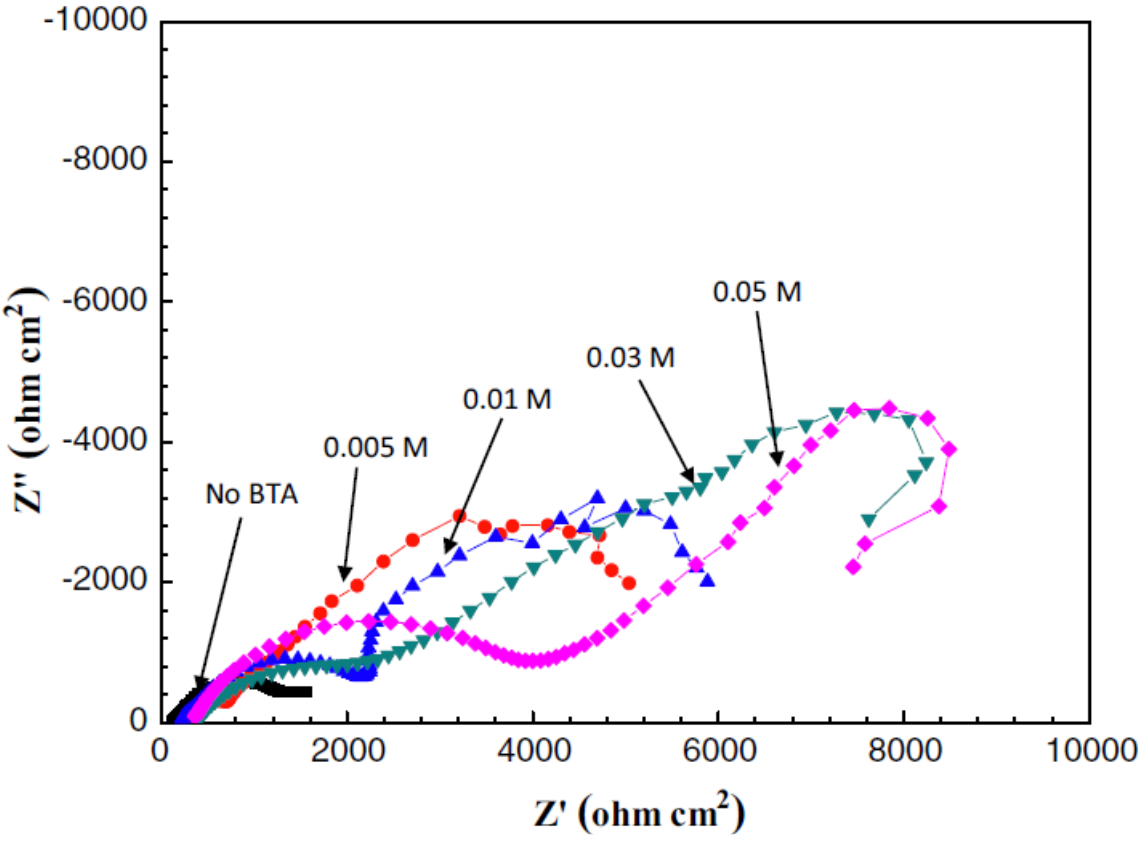

Fig. 3.4 Nyquist diagrams measured on X65 steel in 0.01 M $NaHCO_3$ solution containing various concentrations of BTA.

3.3.4 AFM characterization

Fig. 3.5 shows the AFM surface topography of X65 steel after 2 h of immersion in 0.01 M $NaHCO_3$ solution in the absence and presence of BTA at varied concentrations. In the absence of BTA, the steel suffers from obvious corrosion, and its surface is quite rough and uneven, as shown in Fig. 3.5(a). When the BTA is added in the solution at low

concentrations such as 0.005 M and 0.01 M, the surface of steel specimen becomes smoother compared to that obtained in the blank solution, with tiny spikes only along the mechanical scratches generated during the specimen preparation, as seen in Figs. 3.5(b) and 3.5(c). As the BTA concentration increases, the scratches become almost non-visible, especially for that 0.05 M BTA is contained, and the steel surface is covered with a layer of film, which is due to the adsorption of BTA on the steel, as shown in Figs. 3.5(d) and 3.5(e). The homogeneous film is able to protect effectively the steel from corrosion attack.

3.3.5 Analysis of inhibiting mechanism of BTA

The present work shows that BTA is able to inhibit the corrosion of X65 steel in bicarbonate solution, and the inhibiting efficiency is increased by the increasing inhibitor concentration. Moreover, a layer of film is identified to form on the steel surface in BTA-containing solutions. Generally, organic inhibitors establish their corrosion inhibition action through adsorption of the inhibitor molecules on the metal surface [88]. The adsorption is affected by the structure of the inhibitor, the charged surface of the metal, and the distribution of charges over the whole inhibitor molecule. The BTA molecule can become charged in aqueous solutions, and the charging type depends on the solution pH. In weakly alkaline sodium bicarbonate solution, the BTA is negatively charged (BTA^-), which can react with the positively charged corrosion product such as ferrous ions to form un-dissolved deposit on the steel surface through electrostatic interaction. The BTA molecule contains two –C-N groups and one secondary amino group. When negatively charged BTA^- is adsorbed on steel, coordinate bonds may be formed by transferring

electrons form polar N atoms to the steel surface [89]. BTA thus combines with the generated Fe^{2+} ions to form metal-inhibitor complexes by:

$$nBTA^- + nFe^{2+} \rightarrow [Fe(BTA)_2]_n \quad (3\text{-}2)$$

It is obvious from AFM images that a layer of film is formed on the steel surface in the presence of BTA in the solution, which might be ascribed to the generated $[Fe(BTA)_2]_n$ aggregate. At lower BTA concentrations, there is not sufficient BTA^- reacting with the corrosion-generated Fe^{2+} to form the aggregate. With a higher BTA concentration in the solution, the abundant BTA^- is reacted with Fe^{2+} to form metal-inhibitor complexes. These complexes might adsorb on the steel surface to form a protective film. Moreover, the AFM images show that the film is quite smooth, with a roughness at nano-meter scale, especially at high BTA concentrations.

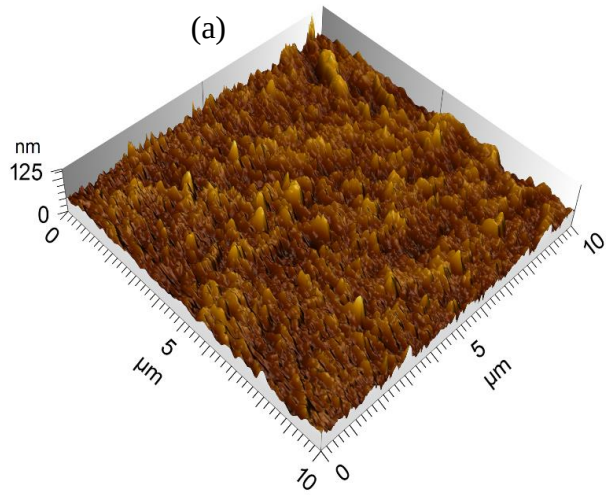

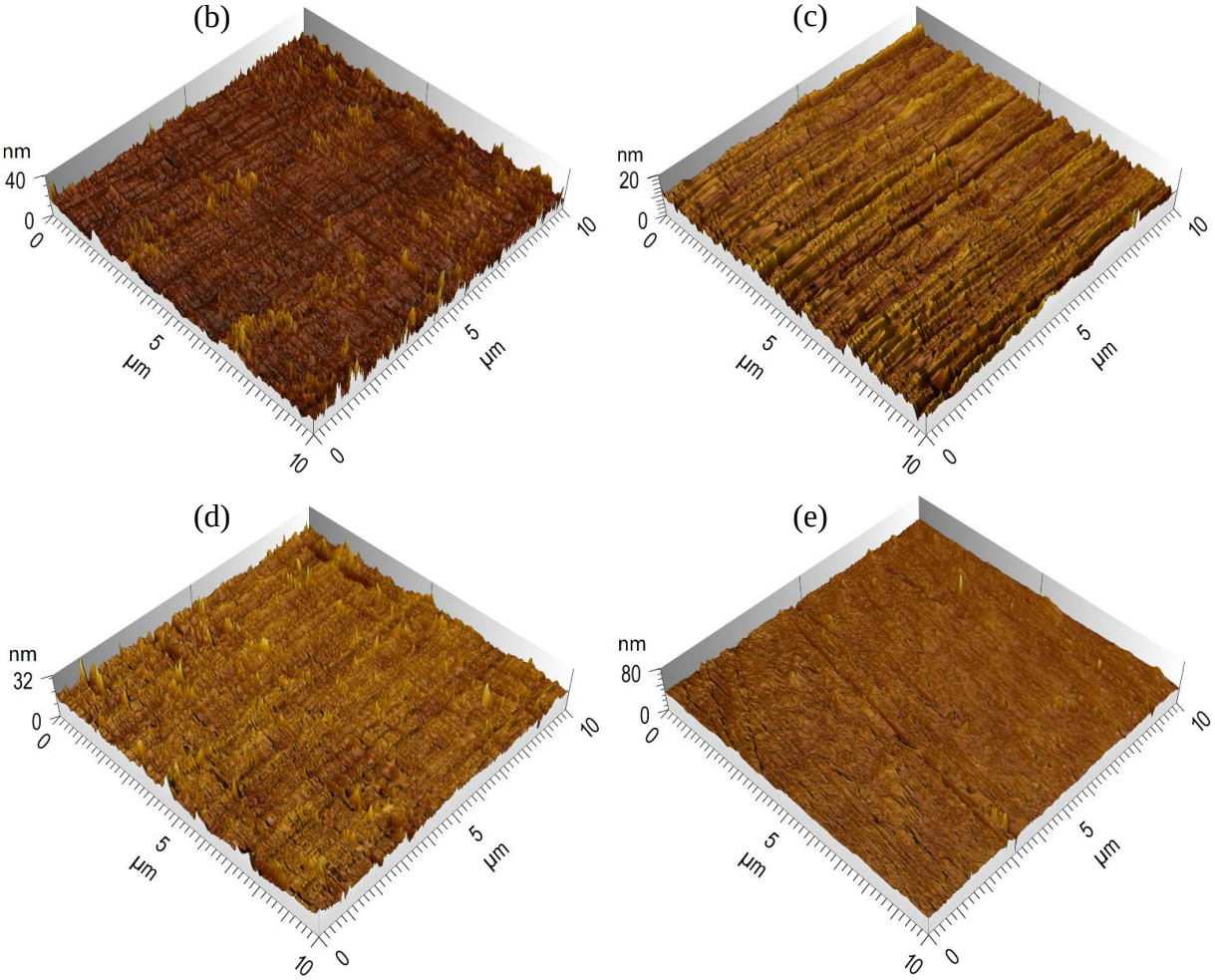

Fig. 3.5 AFM images of X65 steel after 2 h of immersion in 0.01 M $NaHCO_3$ solution containing various concentrations of BTA (a) blank, (b) 0.005 M, (c) 0.01 M, (d) 0.03 M, (e) 0.05 M.

3.4 Summary

BTA is able to inhibit the corrosion of X65 steel in bicarbonate solution, and the inhibiting efficiency is increased by the increasing inhibitor concentration. The BTA is an anodic inhibitor, which shifts the corrosion potential of the steel less negatively and decreases the anodic current density at individual potential.

A layer of film, which is probably the metal-inhibitor complex aggregate, is formed on the steel surface to inhibit corrosion reaction. The presence of the film is demonstrated by the AFM imaging, and changes the corrosion process, as indicated by the different impedance feature from that obtained in the absence of BTA in the solution.

Moreover, the formed film on the steel surface is quite smooth, with a roughness at the nano-meter scale. This ensures an effective protection of the steel from corrosion and localized corrosion attack.

Chapter Four: Fabrication of Halloysite Nanocontainers and Their Compatibility with Epoxy Coating for Anticorrosion Performance*

4.1 Introduction

In the former chapter, the inhibitive performance of BTA for X65 pipeline steel was discussed. It is confirmed that BTA is an effective inhibitor for protection steel from corrosion. The combination of inhibitor BTA with epoxy coating to fabricate the intelligent coating will be discussed in the following parts.

Generally, organic coatings can experience degradation in service, and are not able to maintain long-term corrosion-protective properties due to water permeation, disbondment, mechanical damage, etc. [90-92]. Efforts have been made to develop proper methods to improve the anticorrosion properties of the coatings [93-96]. For example, the addition of various pigments, e.g., barrier, sacrificial and inhibitive pigments, to the coating is effective to enhance its performance for corrosion resistance [97]. This is attributed to the slight solubility of these pigments in water, releasing small amount of inhibitive species, which then reach the active sites on the steel surface to restrict the access of aggressive ions [98]. However, a direct addition of corrosion inhibitors and/or inhibitive pigments, especially some organic inhibitors, to coatings can cause detrimental interactions among components, as well as formation of preferential electrolyte pathways, compromising the barrier properties of the coating. In order to overcome these shortcomings, one possible solution is to store the inhibitor in certain containers that is

* This work has been published as: Yuanchao Feng, Y. Frank Cheng, Fabrication of Halloysite nanoparticles and their compatibility with epoxy coating for anticorrosion performance, *Corrosion Engineering Science and Technology* 51 (2016) 489-497.

compatible with the coating matrix and able to sense the local changes induced by corrosion process [8]. This strategy has led to the development of a new generation of intelligent coatings for anticorrosion purpose [99].

Halloysite ($Al_2Si_2O_5(OH)_4 \cdot nH_2O$), an economic clay material that can be mined as a raw mineral, is a two-layered 1:1 aluminosilicate, which exhibits a range of morphologies. One predominant form is a hollow tubular structure with a very small inner diameter in the sub-micron range. A strong surface charge on the Halloysite tubules enables a multilayer assembly at nanoscale using layer-by-layer (LbL) adsorptions [100]. The shell of the resulting polyelectrolyte capsules is sensitive to a variety of physical and chemical conditions of the environment. The Halloysite polyelectrolyte capsules can thus be used to store corrosion inhibitors in coatings, and to release the inhibitor upon appropriate triggering mechanisms to sense the environment, and generate an appropriate response to corrosion occurrence [101].

In this work, multi-layered Halloysite polyelectrolyte nanocontainers, which would be used for storage of corrosion inhibitors, were fabricated by the LbL method, and were doped in an epoxy coating. The coating was then painted on a X65 pipeline steel, which was exposed to a chloride solution. The effect of the nanocontainer loading on corrosion protection of the coating was investigated. The corrosion morphology was observed.

4.2 Experimental

4.2.1 Preparation of Halloysite polyelectrolyte nanocontainers

Halloysite clay (Aldrich) as-received contained over 70% of tubulars with an outer diameter of 50 ± 5 nm, inner diameter of 15 - 20 nm, and a length less than 1 μm. A 15

wt.% water suspension was prepared by adding water to dry Halloysite powder under continuous stirring in a lab-used blender to avoid clay aggregation. The dispersion of the Halloysite particles was further improved by heating at 60°C on a stirring hotplate for 12 h. The resulting Halloysite nanotubes were separated by centrifugation, then washed three times with distilled water, and dried at 60°C in air for 12 h. The dry Halloysite nanotubes were stored in a desiccator with the protection of nitrogen for further use [102].

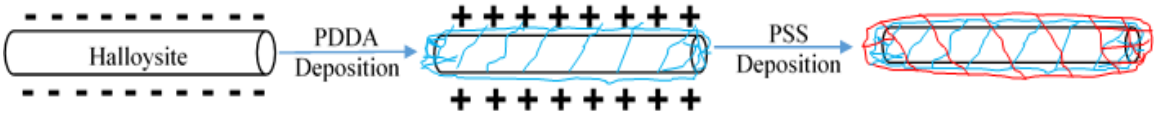

Fig. 4.1 Schematic illustration of the procedure for preparation of 4-layer Halloysite nanocontainers, where PDDA and PSS are poly- (diallyldimethylammonium chloride) and poly-(styrene sulfonate), respectively.

To maintain controlled release of corrosion inhibitors pre-loaded in the Halloysite nanotubes, their surface was modified by LbL deposition of four layers of polyelectrolyte in 2 mg/mL polyelectrolyte + 0.5 M NaCl solution, as shown in Fig. 4.1. A layer of positively charged poly-(diallyldimethylammonium chloride) (PDDA) was formed for 15 min. The resulting materials were washed by centrifugation to remove adsorbed polyelectrolyte molecules, and another layer was then deposited in sodium poly-(styrene sulfonate) (PSS). Alternating adsorption was repeated until the final

PSS/PDDA/Halloysite four-layer structure was assembled on the surface of the Halloysite nanotubes to form the Halloysite nanocontainers.

4.2.2 Preparation of epoxy coatings doped with Halloysite nanocontainers

Epoxy coatings are one of the most widely used coatings in industry for corrosion protection, and are thus chosen in this work. To home-make the epoxy coating, an epoxy resin (diglycidyl ether of bisphenol A, DGEBA, $C_{21}H_{24}O_4$, with a molecular weight of 340 g mol^{-1}) was ultrasonically stirred with xylenes at room temperature for 30 min, and then mixed with various contents of the prepared Halloysite nanocontainers for another 30 min. Finally, an amine hardener, N-Aminoethylpiperazine (NAEP, $C_6H_{15}N_3$ with a molecular weight of 129 g mol^{-1}, 98% purity), was added in the mixture and stirred for 2 h. The ratio of DGEBA to NAEP was adjusted to optimize the coating property. The prepared coating with and without Halloysite nanocontainers was coated on a X65 steel panel by dip coating application using a withdrawal angle of 30^o and an immersion time of 100 seconds. After coating, the coated steel panels were left at room temperature for 7 days to allow a full curing of the coating.

The chemical composition of X65 steel was given previously [103]. Prior to coating application, the working face of the steel with 1 cm^2 in area was subsequently ground with 120, 240, 600, and 800 grit emery papers, and clean in distilled water, ethanol and acetone.

The dry film thickness was measured using a Fischer digital thickness gauge on five different locations on the coated steel panels, ensuring a uniform coating thickness achieved. The average thickness of the coating is 90 ± 10 μm.

4.2.3 Characterization of the nanocontainers

Fourier transforms infrared (FTIR) measurements were conducted through a Nicolet iS50 spectrometer at room temperature to characterize the structure of the prepared Halloysite nanocontainers. For comparison, the structure of the as-received Halloysite was also measured. Continuous scans were performed from 4000 - 400 cm^{-1} with a resolution of 4 cm^{-1}.

The morphology of the Halloysite nanocontainers was characterized by a Philips XL30 SEM and an optical microscope by dispersing the as-received and fabricated Halloysite on a smooth glass.

Optical morphological observation was conducted on coated steel specimens after corrosion testing.

4.2.4 Electrochemical measurements

EIS measurements were conducted on a three-electrode system through a Solartron 1280C electrochemical workstation. The coated steel specimen was used as the working electrode (WE), a saturated calomel electrode (SCE) as the reference electrode (RE), and a Pt wire as the counter electrode (CE). All tests were performed in a 3.5 wt.% NaCl solution at 60^{o}C.

Prior to testing, the steel WE was immersed in the solution for 60 min to achieve a steady state. A sinusoidal AC perturbation of 10 mV amplitude was applied on the WE which was maintained at the free corrosion potential. The EIS was measured in the frequency range from 10 kHz to 0.01 Hz. The impedance data was analysed using the associated Zview software.

During electrochemical impedance measurements, each test was performed at least three times to ensure reproducibility of the testing data. When the measured EIS obtained from three tests were similar, the curve lied in between was presented herein. If big deviations of the results were found in three tests, the fourth or even fifth test was conducted. The deviated result(s) was disregarded, and the data presentation followed the procedure mentioned above.

It is noted that, as the first part of a series work, this work did not pre-load corrosion inhibitors in the prepared Halloysite nanocontainers. Instead, investigations were focused on the compatibility of the added Halloysite with epoxy coating.

4.3 Results and discussion

4.3.1 Preparation of epoxy coatings

Epoxy coatings are made by epoxy resin which contains epoxy functional groups reacting or cross-linking with either themselves through catalytic polymerisation, or with a wide range of reactants such as polyfunctional amines, acid anhydrides, phenols, alcohols and thiols. These reactants are often referred as hardeners or curatives, and the cross-linking reaction is commonly referred as curing. In order to make high-quality cross-linking epoxy coatings, the influence of the content of amine hardener on the solubility of cured epoxy coatings in acetone solution is studied in this work. Theoretically, 3 mol DGEBA completely reacts with 2 mol NAEP to form a cured coating. In reality, the amount of hardener NAEP is usually slightly greater than the stoichiometric ratio mentioned above. The contents of the two components used in this

work is listed in Table 4.1. The NAEP is over-stoichiometric and DGEBA is sub-stoichiometric for coatings no.2, 3, 4 and 5. For coating no. 1, they are stoichiometric.

Table 4.1 Contents of DGEBA and NAEP (both mass and molar values) as well as xylenes used in this work for preparation of epoxy coatings.

	Coating sample no.				
	1	2	3	4	5
DGEBA/g	1	1	1	1	1
DGEBA/mol	$2.94x10^{-3}$	$2.94x10^{-3}$	$2.94x10^{-3}$	$2.94x10^{-3}$	$2.94x10^{-3}$
NAPA/g	0.26	0.29	0.31	0.34	0.36
NAPA/mol	$2.02x10^{-3}$	$2.24x10^{-3}$	$2.40x10^{-3}$	$2.64x10^{-3}$	$2.79x10^{-3}$
Xylenes/g	1.24	1.26	1.29	1.31	1.35
NAPA extra proportion/%	0	10	20	30	40

Acetone has a strong capacity to dissolve DGEBA and NAEP. The prepared epoxy coatings are evaluated by soaking them in acetone to measure the weight change upon soaking. Depending on the curing level of coatings with varied combinations of bisphenol a diglycidyl ether resin (BADE) and NAEP, un-reacted BADE and NAEP molecular can be released from the coating, causing a change of the coating weight. Fig. 4.2 shows the weight of the coating samples as a function of time in acetone. It is seen that the total weight of the prepared coating increases with time until a maximum value is reached. This is due to the permeation and absorption of acetone into the coating. It takes about 24 hours for the coating to achieve the saturated absorption state. After the maximum absorption is reached, the weight of the coating decreases with time, which is probably attributed to the extraction of sol molecules upon swelling in acetone. Coating

sample 1 has the biggest weight increment upon absorption of acetone, and a relatively small weight loss in acetone. This formulation, which contains the least NAEP in relation to the amine curing compound compared to other formulations, would contain a greater polymer-free volume in which small molecular species such as water and acetone would be mobile. At the same time, the DGEBA is a long-chain molecule, and is not easy to release from the cured coating when soaking in acetone. Thus, coating sample 1 is associated with a big weight increment and relatively small weight loss. On the contrary, coating samples 4 and 5 reach the saturated absorption of acetone quickly, and have a relatively big weight loss after soaking. This is due to the fact that acetone can permeate into the coatings through microchannels formed by extra NAEP. Moreover, the NAEP, which is relatively smaller than DGEBA in terms of the molecular size, is easy to release form coatings in acetone.

By comparison of the weight changes of the five coating samples, coating samples 2 and 3 have the lowest polymer-free volume when compared with samples 1, 4 and 5. On comparing samples 2 with 3, sample 2 has a slightly smaller weight loss in acetone. It is thus assumed that coating 2 possesses a better cross-linking and cured performance. This coating formulation is thus chosen for further research.

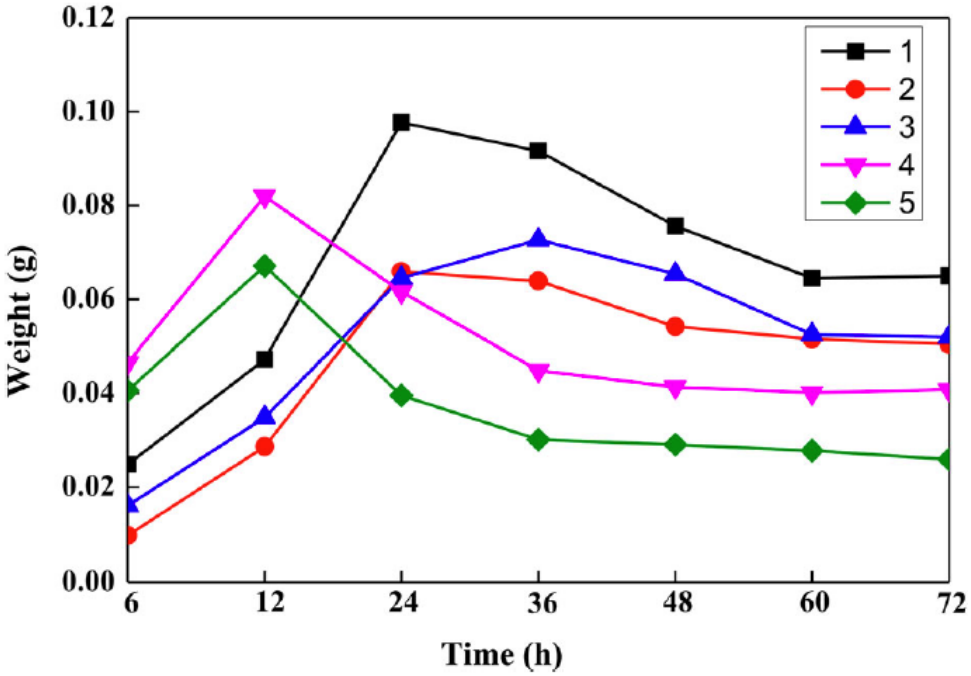

Fig. 4.2 Weight changes of the coating as a function of time in acetone, where curves 1, 2, 3, 4 and 5 refer to 0, 10%, 20%, 30% and 40% of extra amount of NAPA, respectively.

4.3.2 Morphological characterization of prepared Halloysite nanocontainers

Fig. 4.3 shows the optical view of as-received Halloysite and the prepared Halloysite nanocontainers. It is seen in Fig. 4.3a and 4.3b that the as-received Halloysite is a white powder, and particles tend to agglomerate to form big, irregular aggregates with non-uniform sizes. The prepared Halloysite nanocontainers have a more uniform scale and better dispersion, as seen in Fig. 4.3c. This is due to the adsorption of polyelectrolyte on the surface of Halloysite, decreasing the agglomeration of the Halloysite particles.

Fig. 4.4 shows the SEM view of the as-received and prepared Halloysite. It is seen that the as-received Halloysite (Fig. 4.4a) agglomerates much more seriously compared

to the prepared Halloysite in Fig. 4.4b. Despite the adsorption of polyelectrolyte on the surface of Halloysite, the agglomeration still occurs on the prepared Halloysite. It is noted that the particle agglomeration may affect the anti-corrosion performance of the host coating. Thus, further improvements to enhance the dispersion of Halloysite nanocontainers in the coating are being conducted in authors' lab, while this work focuses on investigation of the compatibility of Halloysite nanocontainers with the epoxy coating.

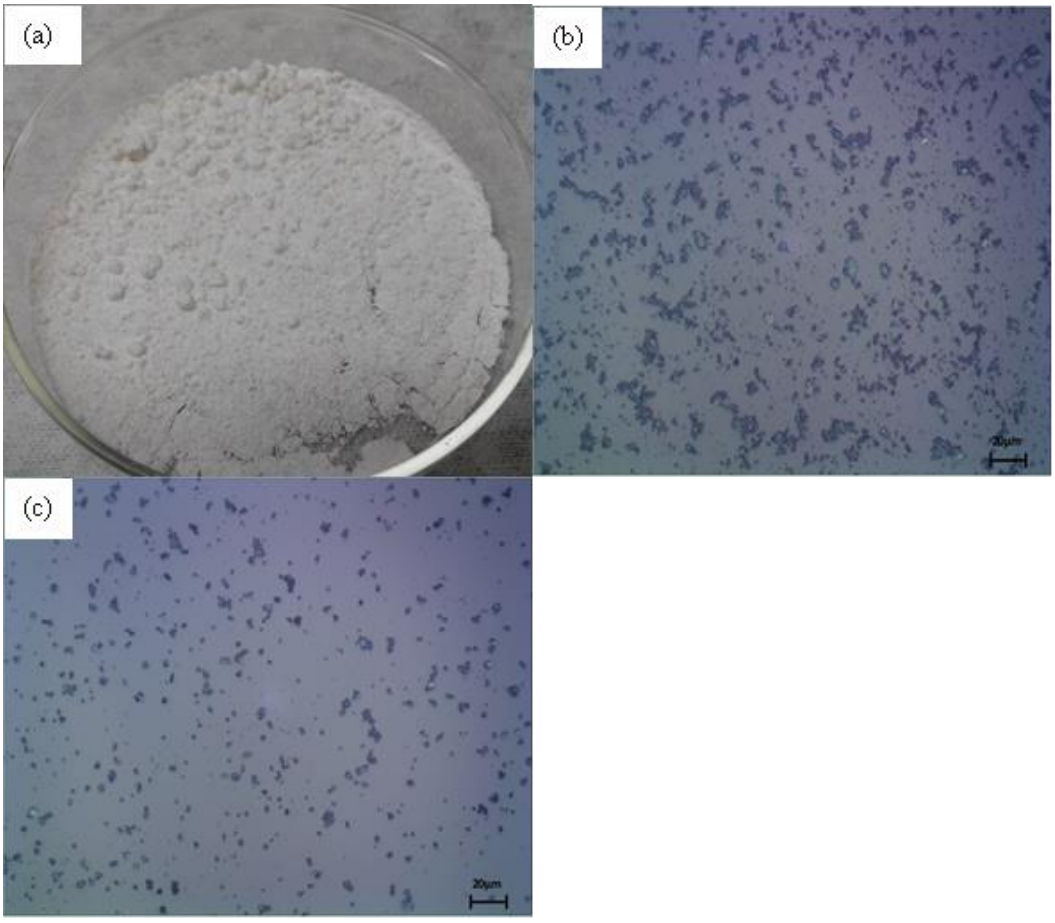

Fig. 4.3 Optical view of (a) and (b) as-received Halloysite and (c) prepared Halloysite nanocontainers.

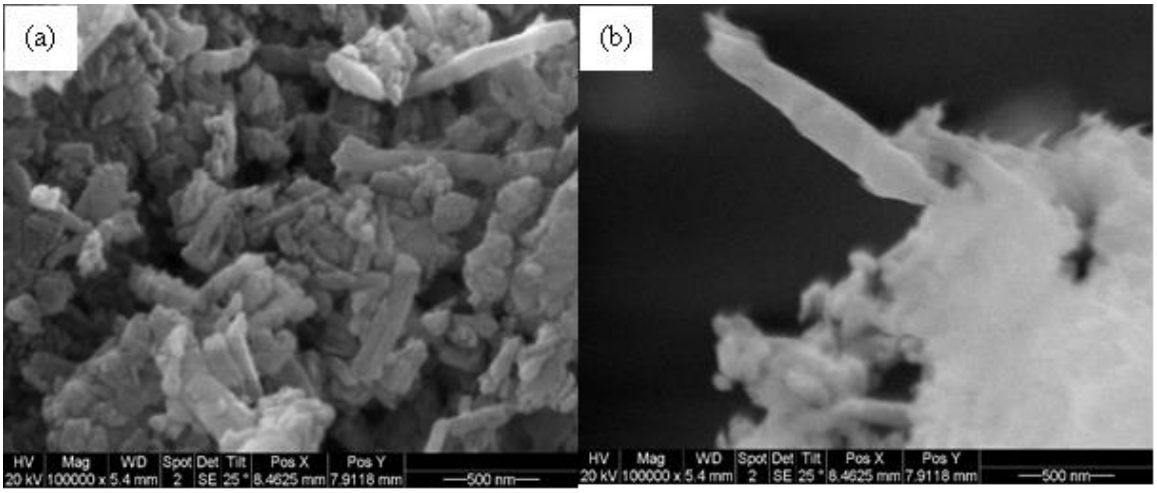

Fig. 4.4 SEM view of (a) as-received and (b) prepared Halloysite materials.

4.3.3 FTIR characterization

Fig. 4.5 shows the FTIR spectra measured on the as-received and prepared Halloysite. Several characteristic peaks are observed in the range of 600 ~ 3700 cm^{-1}. Particularly, inner OH^- stretching vibrations of Halloysite's aluminium groups occur at 3620 and 3690 cm^{-1}, the Si-O-Si deformations at 1100 ~ 1200 cm^{-1}, the Si-O-Al perpendicular stretching at 800 cm^{-1}, symmetric Si-O- Si stretching at 1000 cm^{-1}, respectively [104]. For the prepared Halloysite in this work, in addition to the characteristic peaks identical to those obtained on the as-received Halloysite, two additional peaks are observed and labelled in the figure. The peak at 2930 cm^{-1} is attributed to the presence of C-H flexible vibration due to the absorption of PDDA on the surface of Halloysite, while the peak at 1470 cm^{-1} corresponds to the C=C functional groups from PSS [105]. The results confirm that the PDDA and PSS are present on the surface of the prepared Halloysite. Thus, the processing in this work introduces new functional groups in Halloysite, but does not change its intrinsic structure.

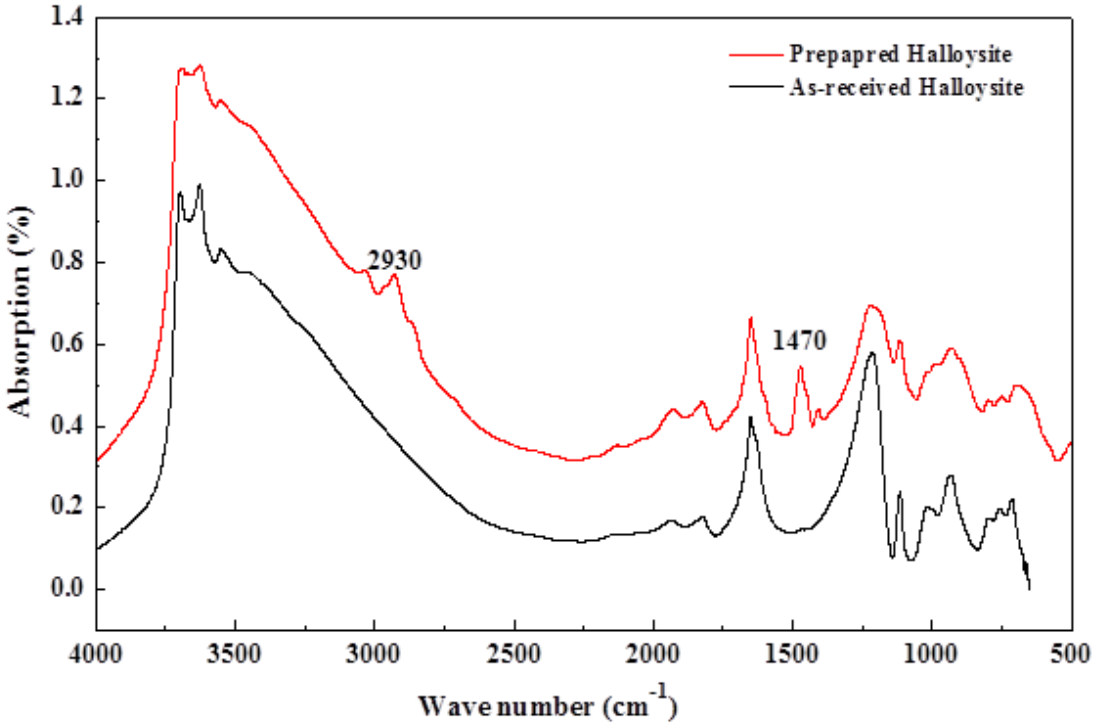

Fig. 4.5 FTIR spectra of as-received and prepared Halloysite.

4.3.4 EIS measurements

Fig. 4.6 shows the Bode plots measured on X65 steel electrode coated with epoxy coating undoped and doped with various contents of the prepared Halloysite nanocontainers in 3.5 wt.% NaCl solution over 84 hours. It is seen that, for both undoped and doped epoxy coatings, the measured low-frequency impedance decreases with time, indicating the water permeation into the coating. Upon addition of the Halloysite nanocontainers, the low-frequency impedance of the coated steel is bigger compared to that measured on the undoped coating at individual times. For example, the low-frequency impedance of the undoped coating is about 10^7 Ω cm^2, while that measured on the coating containing 20 wt.% Halloysite nanocontainers is approximately 10^9 Ω cm^2.

The addition of Halloysite nanocontainers improves the corrosion resistance of the epoxy coating by blocking the permeation of corrosive media through the coating systems.

(a)

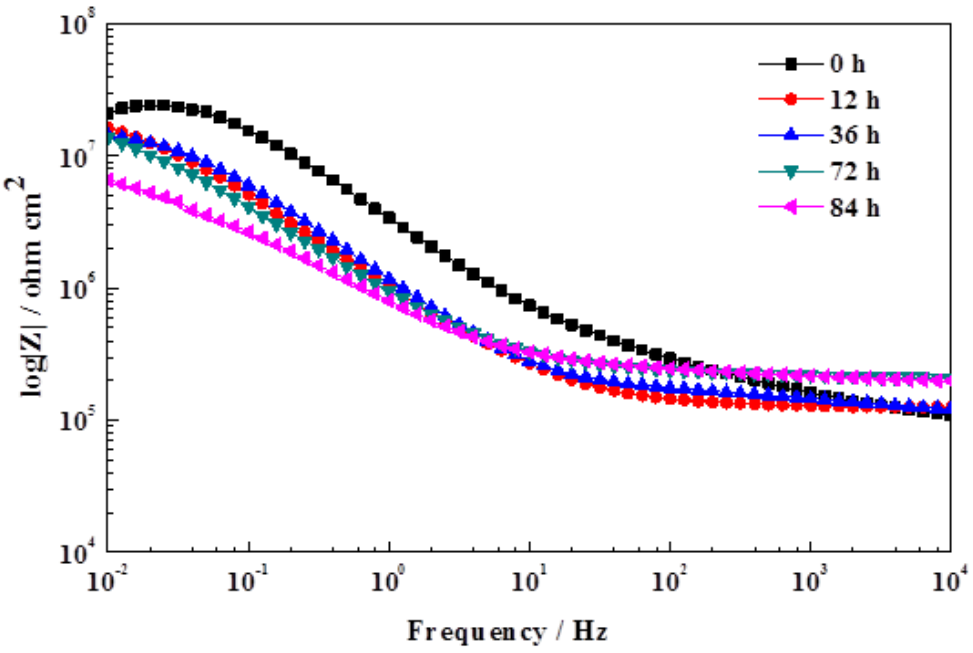

(b)

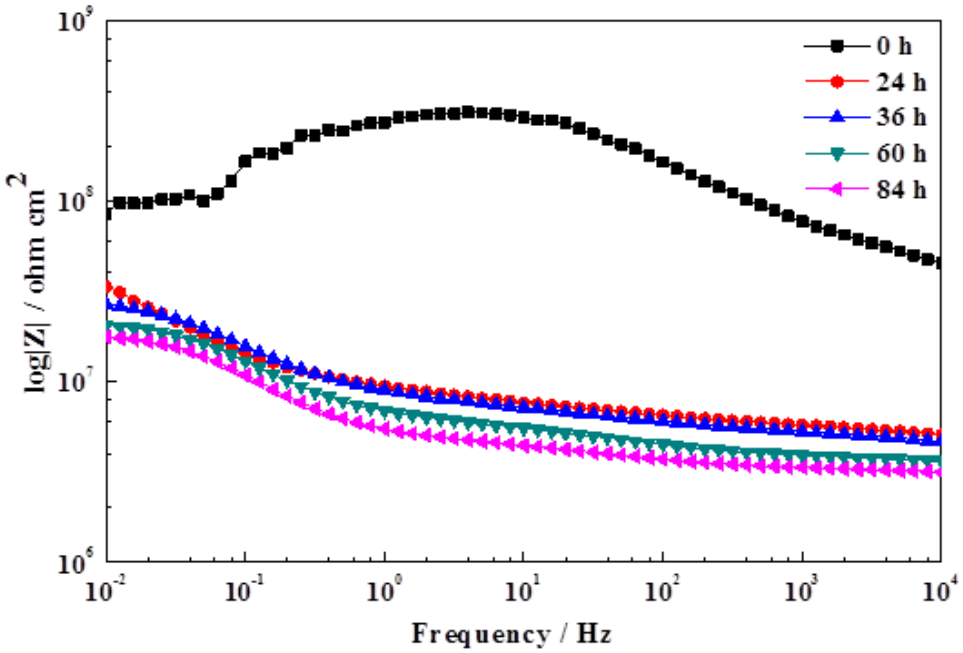

(c)

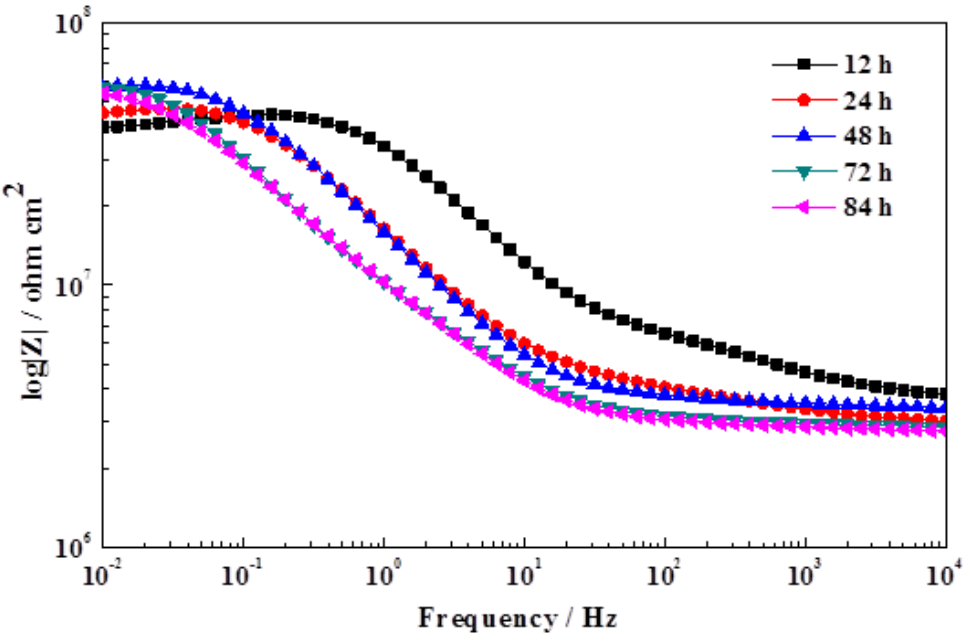
12 h
24 h
48 h
72 h
84 h
log|Z| / ohm cm 2
Frequency / Hz

(d)

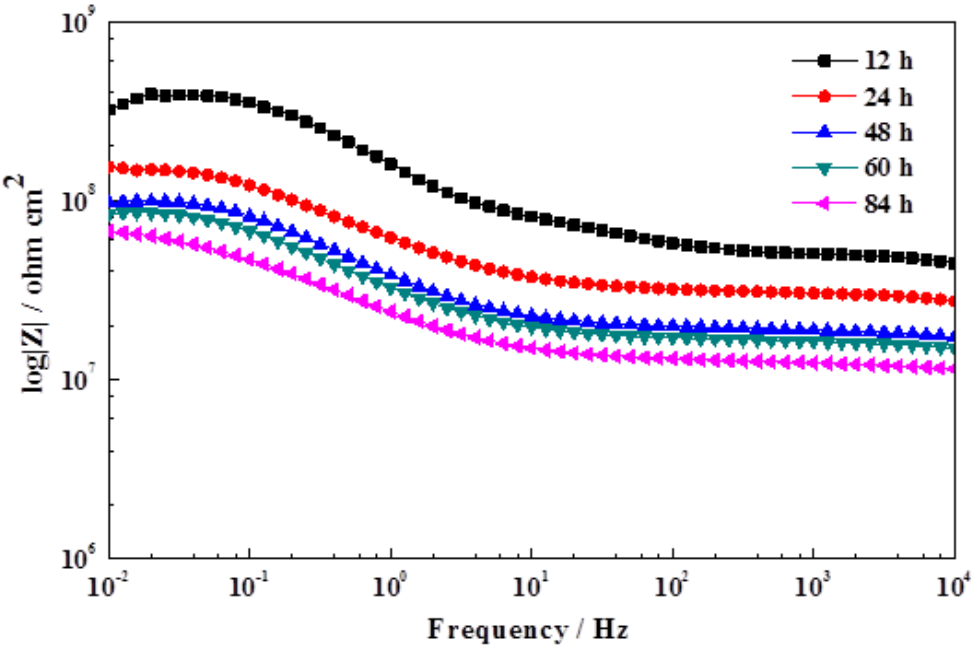
12 h
24 h
48 h
60 h
84 h
log|Z| / ohm cm 2
Frequency / Hz

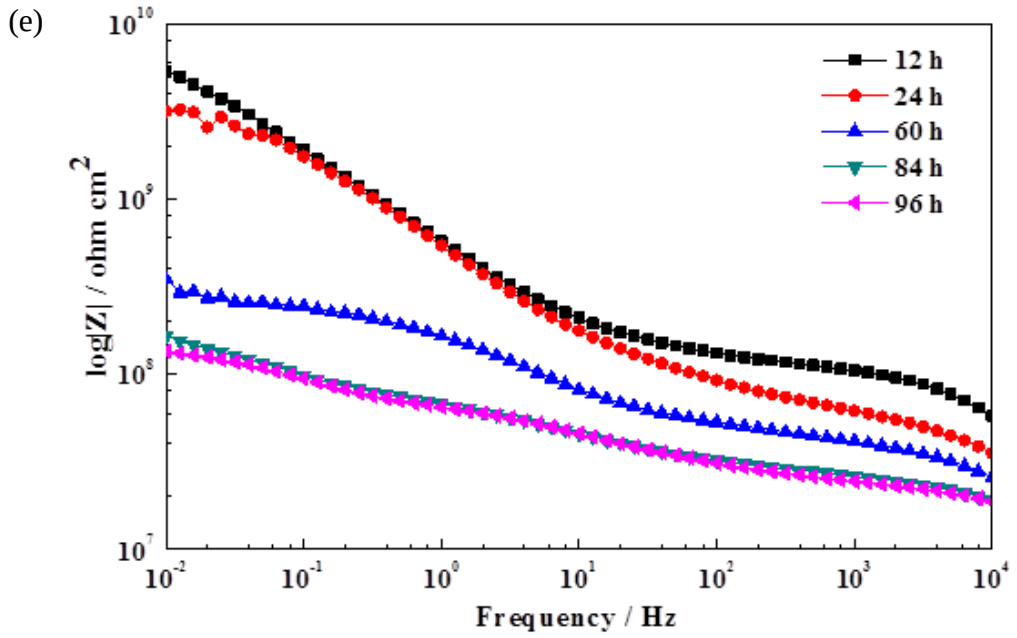

Fig. 4.6 Bode diagrams measured on X65 steel electrode coated with epoxy coating undoped and doped with various contents of the prepared Halloysite nanocontainers in 3.5 wt.% NaCl solution at 60°C. (a) undoped, (b) 3wt.%, (c) 5wt.%, (d) 10wt.%, (e) 20wt.%.

4.3.5 Morphological observation of coated steel electrodes

Fig. 4.7 shows the morphology of the coated steel electrodes with epoxy coatings containing various contents of the prepared Halloysite nanocontainers after 84 h of testing in 3.5 wt.% NaCl solution. It is seen that the steel corrodes over a larger area under the undoped coating compared to those coated with coatings doped with Halloysite nanocontainers. As the Halloysite content increases in the coating, the corrosion area on the steel surface decreases. This result is consistent with the impedance measurements that the added Halloysite is able to improve the anti-corrosion ability of the coating.

Moreover, the morphological observation shows that corrosion occurs under coating, indicating that the coating is disbonded, and the corrosive solution permeates under the coating. Thus, the Halloysite addition would also be able to decrease the disbonding area. Particularly, the epoxy coating containing 20 wt.% Halloysite nanocontainers shows the best resistance to corrosion attack as it results in the smallest disbonding area for corrosion to occur among all the coatings.

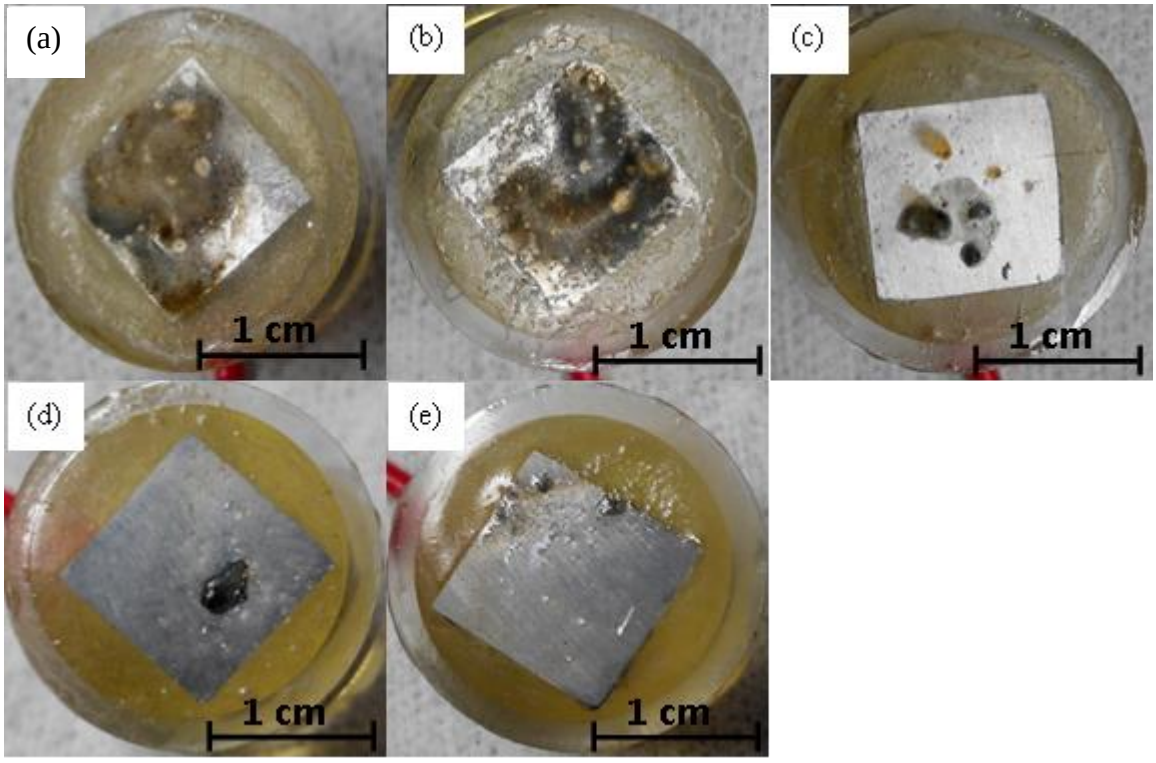

Fig. 4.7 Morphology of the coated steel electrodes with epoxy coating containing various contents of the prepared Halloysite nanocontainers after 84 h of testing in 3.5 wt.% NaCl solution at 60ºC. (a) undoped, (b) 3 wt.%, (c) 5 wt.%, (d) 10 wt.%, (e) 20 wt.%.

It is noted that the coating applied on steel panels is a home-made, pure bisphenol-A epoxy coating, without addition of any other pigments and additives. The main components contained in the coating include epoxy resin BADE, amine hardener NAEP and the prepared Halloysite nanocontainers. Thus, the anti-corrosion performance of the coating is not compared to commercial coating products. This is the key reason that corrosion occurs on the coated steel specimen in a short time period of immersion in NaCl solution at 60^{o}C. Furthermore, this work is attempted to understand the potential effect of the addition of Halloysite nanocontainers in the epoxy coating on its structure and corrosion resistance, i.e., the compatibility of the bisphenol-A epoxy coating with Halloysite. Actually, the doping of the prepared Halloysite in commercial coatings is being discussed with a coating manufacturer.

4.3.6 Analysis of the compatibility of Halloysite nanocontainers with epoxy coating and the anticorrosion performance of the prepared Halloysite-contained coatings

The present work shows that, compared to undoped epoxy coating, the coating containing Halloysite nanocontainers possesses an enhanced corrosion resistance, as indicated by the EIS measurements and morphological characterization. Moreover, with the increasing content of the added Halloysite nanocontainers in the coating, the corrosion resistance is further improved. Therefore, the prepared Halloysite nanocontainers are highly compatible with the epoxy coating in terms of its corrosion protection, and they actually enhance the corrosion resistance of the coating.

Addition of nanoscale particles is able to improve the corrosion resistance of organic coatings [106-108]. Moreover, the effect is more apparent for epoxy coating incorporated

with Halloysite nanoparticles than those added with SiO_2 and Zn nanoparticles [108]. It was proposed that at least two possible mechanisms contribute to the enhanced corrosion protection of epoxy coating upon addition of nanoparticles. First, nanoparticles improve the quality of the cured epoxy coating, reduce the porosity of the coating matrix, and zigzag the diffusion path available by deleterious species, leading to improved barrier performance of the coating. Second, nanoparticles improve the adherence of epoxy coating to the underlying substrate and alter the physiochemical properties of the coating-steel interface.

Furthermore, it is found that the epoxy coating containing 20 wt.% of the prepared Halloysite nanocontainers shows the best anti-corrosion performance under the testing condition in this work. Further corrosion analysis is performed on this coating to understand the mechanistic aspect of corrosion of steel under the coating. Fig. 4.8 shows the Nyquist diagrams and Bode plots measured on steel electrode coated with the epoxy coating containing 20 wt.% Halloysite in 3.5 wt.% NaCl solution at 60^{o}C as a function of time. At the initial stage, i.e., 12 h, the measured impedance plots contain two time constants, as shown in Fig. 4.8a. The high-frequency time constant is ascribed to the capacitive behaviour of the coating, and the low-frequency one is associated with the charge-transfer reaction at the steel-coating interface. The coating can provide sufficient protection over the substrate steel from corrosion at this stage.

With the increase in immersion time to 60 h, the coating is degraded and corrosive species reach the steel/coating interface for corrosion reaction, resulting in the decrease of the low-frequency impedance. The high-frequency capacitive behaviour reduces and is gradually replaced by the resistive behaviour. However, the corrosion mechanism does

not change, and the impedance plots still contain two time constants, as shown in Fig. 4.8b.

(a)

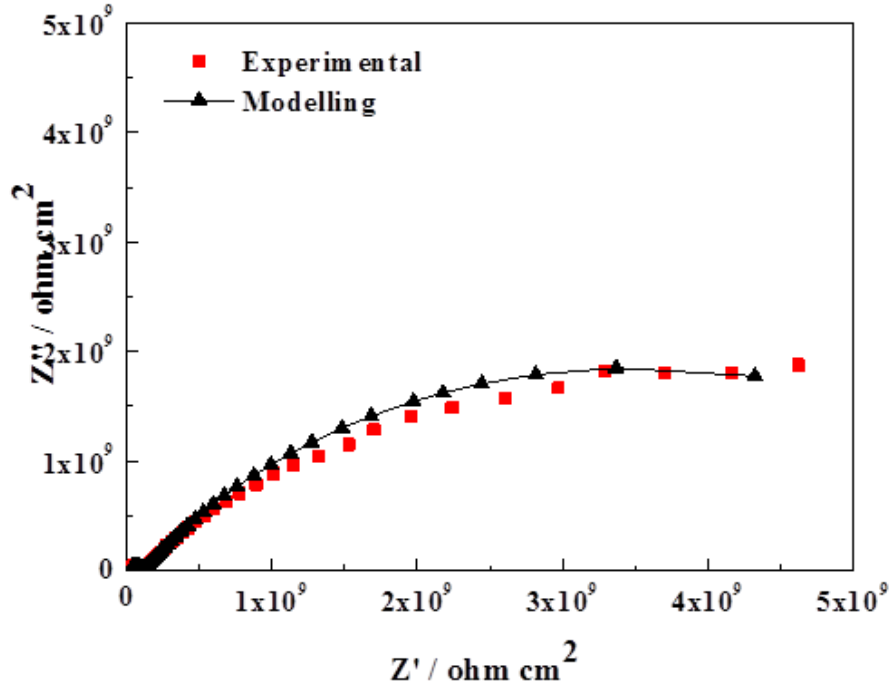

(a)

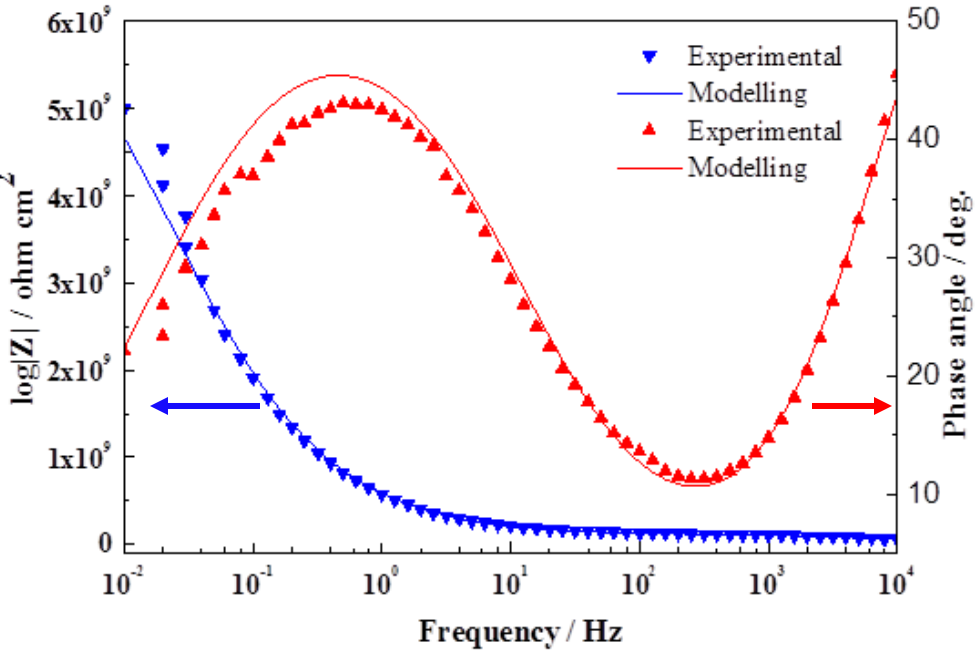

(b)

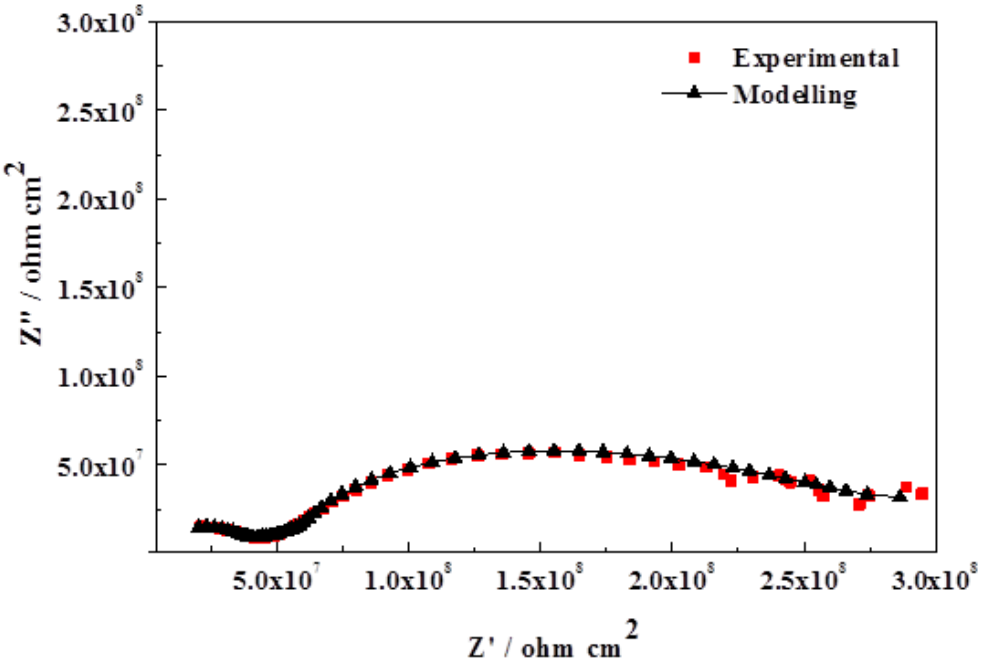
Experimental
Modelling
Z'' / ohm cm2
Z' / ohm cm2
3.0x10^8
2.5x10^8
2.0x10^8
1.5x10^8
1.0x10^8
5.0x10^7
5.0x10^7
1.0x10^8
1.5x10^8
2.0x10^8
2.5x10^8
3.0x10^8

(b)

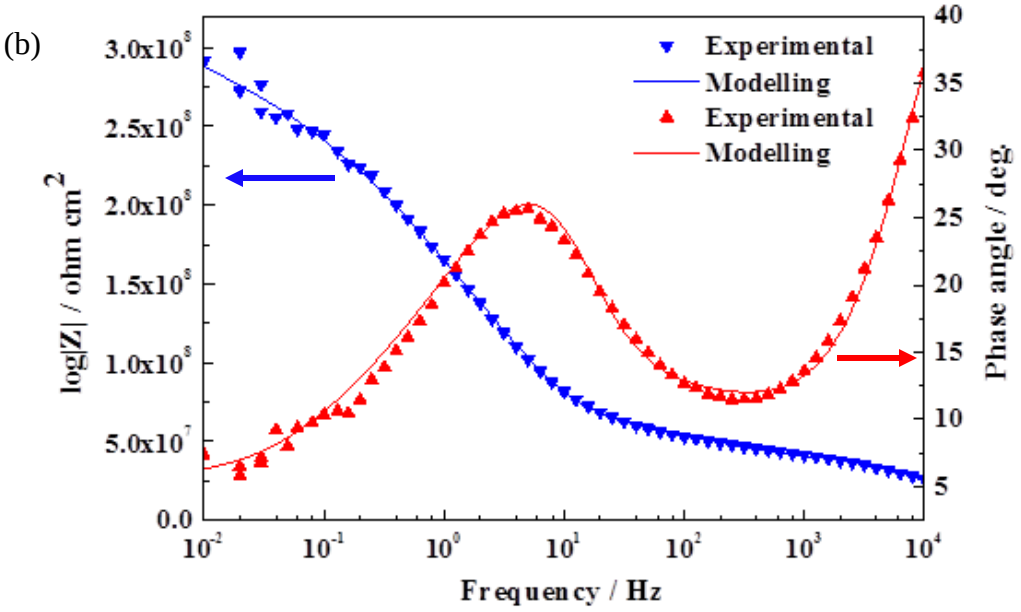
Experimental
Modelling
Experimental
Modelling
log|Z| / ohm cm2
Phase angle / deg
Frequency / Hz
3.0x10^8
2.5x10^8
2.0x10^8
1.5x10^8
1.0x10^8
5.0x10^7
0.0
40
35
30
25
20
15
10
5
10^-2
10^-1
10^0
10^1
10^2
10^3
10^4

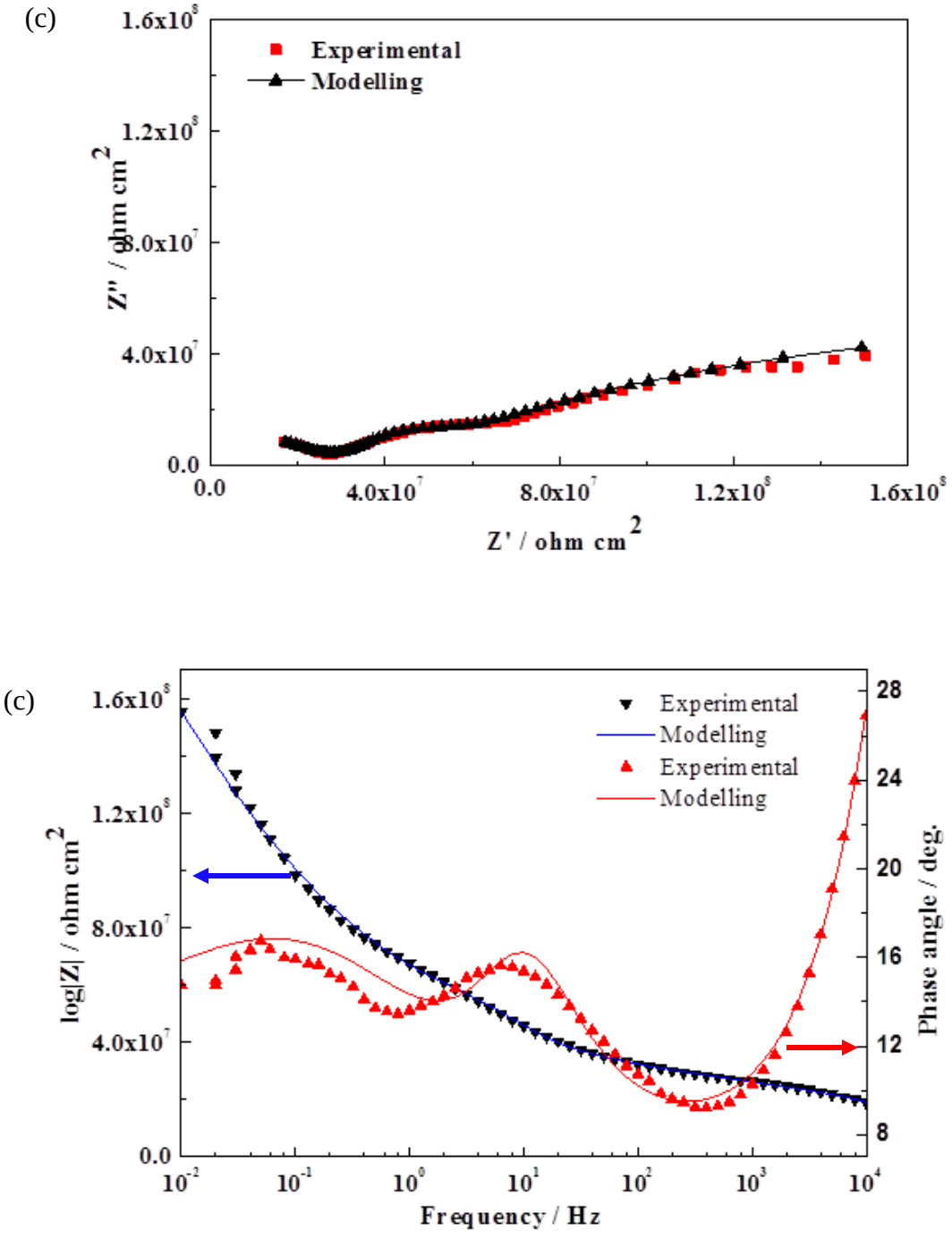

Fig. 4.8 Nyquist diagrams and Bode plots measured on steel electrodes coated with the epoxy coating containing 20 wt.% Halloysite in 3.5 wt.% NaCl solution as a function of time. (a) 12 h, (b) 60 h, (c) 84 h.

After 84 h of immersion in the solution, three time constants are observed in the measured impedance plots, as shown in Fig. 4.8c. The high-frequency time constant is associated with the capacitive behaviour of the coating, and the low-frequency one is attributed to the interfacial charge-transfer reaction. The impedance semicircle in the middle frequency range is probably due to the deposit of corrosion product on the electrode surface, reflecting the resistance of the corrosion product layer. It is expected that the deposit layer would affect the further corrosion. Thus, the corrosion of steel under coating experiences mechanistic change with time in this system.

For quantitative determination of the coating properties and electrochemical corrosion parameters, the measured impedance data are fitted with electrochemical equivalent circuits shown in Fig. 4.9, where a constant phase element (CPE) is used to replace capacitance to consider the heterogeneous surface condition of the coated steel electrode. R_s is solution resistance, R_{ct} is charge-transfer resistance, R_c is coating resistance, R_h is the resistance of the corrosion product layer, CPE_{dl} is CPE of double-charge layer, CPE_c is CPE of the coating and CPE_h is CPE of the corrosion product layer. After 12 hours and 60 hours of testing, the impedance data are fitted by the circuit in Fig. 4.9a to consider the interfacial behaviour with two time-constants. The circuit in Fig. 4.9b is considered for the impedance spectroscopy measured at 84 hours of testing, where a three-time-constant behaviour is observed. The fitting results are shown in Table 4.2.

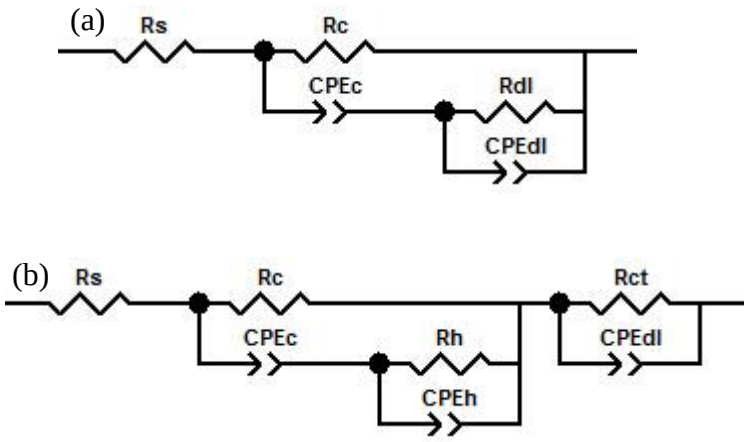

Fig. 4.9 Electrochemical equivalent circuits proposed to model impedance data of coated steel containing 20 wt. % Halloysite in the 3.5 wt.% NaCl at (a) 12, 60 hours and (b) after 84 hours.

Table 4.2 Electrochemical impedance parameters fitting with the equivalent circuits shown in Fig. 4.9.

Sample	R_{ct} (Ω cm2)	CPE_{dl}		C_{dl}	R_c	CPE_{dl}		C_c	R_h(Ω cm2)	CPE_h	
		Y	n			Y	n			Y	n
12h	1.73×10^{8}	2.94×10^{-12}	0.76	2.63×10^{-13}	7.36×10^{10}	4.70×10^{-10}	0.53	1.07×10^{-8}			
60h	4.37×10^{7}	6.90×10^{-10}	0.74	1.75×10^{-11}	2.50×10^{8}	1.73×10^{-9}	0.57	9.28×10^{-8}			
84h	6.90×10^{6}	4.12×10^{-09}	0.50	1.23×10^{-10}	8.91×10^{7}	3.26×10^{-8}	0.80	4.26×10^{-8}	2.53×10^{7}	8.35×10^{-13}	0.73

It is seen that both R_{ct} and R_c decrease, and the CPE_{dl} and CPE_c increase with time, which is attributed to the water uptake and penetration of ions into the coating, causing corrosion of the steel. After 84 hours of immersion in the solution, corrosion products

generated form a layer deposit on the steel surface, which results in the appearance of a new time-constant in the impedance spectroscopy.

4.4 Summary

Multi-layered Halloysite nanocontainers are fabricated, which have a more uniform scale and better dispersion than the as-received Halloysite particles. The PDDA and PSS are present on the surface of the Halloysite nanocontainers, introducing new functional groups in the material, but does not change its intrinsic structure.

An epoxy coating, which contains the mass ratio of DGEBA to NAPA of 1:0.29, i.e., 10% more hardener than the ideal stoichiometric ratio, is prepared. The coating is featured with the relatively slow absorption of acetone and a small weight loss in the acetone solution, and possesses a good cross-linking and cured performance.

The coating containing Halloysite nanocontainers possesses enhanced corrosion resistance. Moreover, with the increase in the content of the Halloysite nanocontainers in the coating, the corrosion resistance is further improved. Therefore, the prepared Halloysite nanocontainers are highly compatible with the epoxy coating in terms of the corrosion protection.

The corrosion of pipeline steel under the epoxy coating with addition of Halloysite nanocontainers experiences mechanistic changes with time. In the beginning, the impedance of the coated steel is dominant by the capacitive behaviour of the coating, which protects effectively the substrate steel from corrosion. With the increase in time, the coating degrades and corrosion is increased. Along with the corrosion occurrence,

corrosion product generates and deposits on the steel surface, affecting the mechanism of further corrosion.

Chapter Five: Fabrication of SiO_2 Nanoparticle-polyelectrolyte Nanocontainers with Preloaded Benzotriazole Inhibitors and Their Self-Releasing Mechanism and Kinetics*

5.1 Introduction

In chapter 3 and chapter 4, the inhibition performance of inhibitor BTA for steel and the compatibility of polyelectrolytes modification Halloysite with epoxy coating were discussed respectively. The method to fabricate the smart capsules by encapsulating BTA in nano SiO_2 particles with polyelectrolytes modification will be stated in this chapter.

Technologies for encapsulation of corrosion inhibitors have been developed, and various nanocontainers serving as inhibitor-carriers with specific triggering mechanisms for inhibitor-releasing have been reported [109-114]. For example, acid and alkaline dual stimuli-responsive hollow mesoporous silica nanoparticles were fabricated as inhibitor-loaded nanocontainers for development of smart coatings, where supermolecular nanovalves were installed on the external surface of the silica nanoparticles to enable pH-responsive controlled release for corrosion inhibitors [115]. Halloysite clay nanotubes were used to prepare nanocontainers by using a layer-by-layer (LBL) assembly of polycations on Halloysite surface to control release of protective agents in its hollow [109, 116].

* This work has been published as: Yuanchao Feng, Shougang Chen, Y. Frank Cheng, Fabrication of SiO_2 Nanoparticle-polyelectrolyte Nanocontainers with Pre-loaded Benzotriazole Inhibitors and Their Self-Releasing Mechanism and Kinetics. *Journal of Materials Science*, 52 (2017) 8576–8590.

While the smart coating technology based on encapsulation of corrosion inhibitors BTA in the fabricated nanocontainers and self-releasing of the inhibitors by appropriate triggering mechanisms has been propsoed and tested in recent years as a promising alternative for corrosion control, there has been limited work to investigate the releasing kinetics of the pre-loaded inhibitors out of the nanoscaled containers. Actually, the majority of the work focused on fabrication and characterization of the inhibitor-loading nanocontainers and the testing for corrosion inhibition. The inhibitor-releasing kinetics has so far not been paid appropriate attentions although the knowkedge is critical to predict the service life of the inhibitor-loaded nanocontainers and thus the smart coatings.

In this work, we fabricated SiO_2 nanoparticle based nanocontainers by established LBL deposition of polyelectrolytes [111, 117, 118] for storage of corrosion inhibitors BTA. The pH selective triggering mechanism for BTA releasing was determined. The structure of the nanocontainers and the amount of the loaded inhibitors was characterized, respectively. The inhibition performance and inhibition efficiency of the released BTA from the nanocontainers for corrosion of an X65 pipeline steel in NaCl solutions with varied pH values was measured. The surface topography of the steel specimen after corrosion testing was characterized. The inhibitor-releasing mechanism from the nanocontainers was discussed. A Langmuir adsorption isotherm, combined with the Korsmeyer-Peppas releasing model, was derived to define the releasing kinetics of the inhibitors.

5.2 Experimental

5.2.1 Materials and chemicals

Specimens used in this work were cut from a X65 steel pipe, with a chemical composition (wt.%): C 0.04%, Si 0.2%, Mn 1.5%, P 0.011%, S 0.003%, Mo 0.02% and Fe balance. The specimens were cut into 1 cm × 1 cm dimension, and sealed in epoxy. The exposed face was subsequently ground by 240, 400, 600, 800 and 1,200 grit SiC emery papers, and then washed with deionized water and degreased with ethanol and acetone, and dried in air.

SiO_2 nanopowders with a purity of 98+% were purchased from U.S. Research Nanomaterials, Inc., with an average diameter of 70 nm in the as-received state. The nanopowders were amorphous in structure, and separated in individual particles.

Corrosion inhibitors BTA (i.e., $C_6H_5N_3$) were used for inhibition of steel corrosion. Various chemicals used in this work, including sodium poly-(styrene sulfonate) (SPSS, molecular weight M_w of about 70,000), poly-(diallyldimethylammonium chloride) (PDDAC, M_w of about 100–200 kDa), HCl, NaCl and NaOH, were analytical grade. All solutions were prepared by deionized water.

5.2.2 Preparation of inhibitor-loaded nanocontainers

A 15 wt.% water suspension was made by adding as-received SiO_2 nanopowders to deionized water under a continuous stirring using an electrical blender in order to avoid aggregation. The dispersion of the SiO_2 nanoparticles was further improved by heating at 60 °C under stirring for 12 h. The resulting SiO_2 nanoparticles were separated by centrifugation, and washed three times with deionized water.

The surface of the SiO_2 nanoparticles was modified by a LBL deposition method to improve the inhibitor adsorption. A layer of positively charged PDDAC was deposited on the surface of the negatively charged SiO_2 nanoparticles in 2 mg/mL polyelectrolyte + 0.5 M NaCl solution for 15 min under stirring. The resulting materials were washed by centrifugation to remove loosely adsorbed polyelectrolytes. A layer of negatively charged polyelectrolyte was then deposited in 2 mg/mL SPSS + 0.5 M NaCl solution for 15 min, with co-adsorption of the inhibitors BTA, as shown in Fig. 5.1. Alternating adsorptions were repeated until the final assembly, i.e., PDDAC/SPSS/$(BTA/SPSS)_2$/PDDAC/SPSS, was prepared on the surface of SiO_2 nanoparticles to form the nanocontainers.

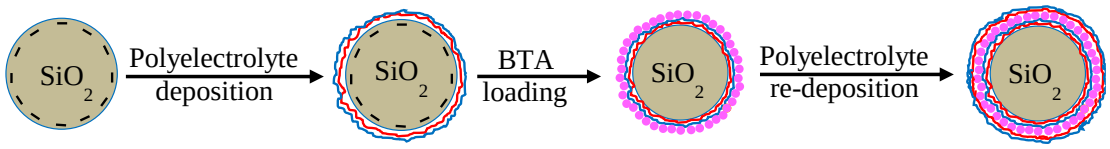

Fig. 5.1 Schematic illustration of the procedure for fabrication of BTA loaded nanocontainers with SiO_2 nanoparticles as carriers.

It is noted that, while BTA is a neutral molecule, it, when dissolved in aqueous solutions, becomes charged. Generally, BTA exists in the form of protonated cations (i.e., $BTAH^+$) at pH < 8, or in deprotonated anionic species (i.e., BTA^-) at pH > 8. In this work, the BTA solution used to encapsulate the inhibitors on nano-SiO_2 surface was adjusted by HCl to pH 3 in order to increase the solubility of BTA. At this pH value, the BTA is in the form of $BTAH^+$, i.e., positively charged.

5.2.3 Characterization of the nanocontainers

A FTIR (Model Nicolet iS50) was used to characterize the functional groups and structure of the prepared nanocontainers. For all spectra recorded, the nanocontainer samples experienced a 64-scan data accumulation in the range of 600 - 4000 cm^{-1} at a spectra resolution of 4.0 cm^{-1}.

The thermal gravity analysis (TGA) was performed at a temperature range of 30 - 600 ^{o}C using a PerkinElmer STA 6000 at a heating rate of 15 ^{o}C/min in helium atmosphere. The amount of the loaded inhibitors in the prepared nanocontainers was measured during thermal decomposition of BTA at high temperatures.

5.2.4 EIS measurements

Electrochemical measurements were conducted using a Solartron 1280C electrochemical system on a three-electrode cell, where the X65 steel specimen was used as the working electrode, and a carbon rod and a saturated calomel electrode (SCE) as counter electrode and reference electrode, respectively. The testing solution was 0.1 M NaCl with the pH values of 2, 5, 7, 9 and 11 adjusted by HCl or NaOH solution. The 1 wt.% prepared nanocontainers was added into the solution at 21 ±1 ^{o}C.

After immersing the steel electrode in the solution until a steady-state open-circuit potential (OCP) was achieved, EIS measurements were performed over a frequency range from 10 kHz to 0.01 Hz, with a disturbance AC voltage of 10 mV. Each test was performed three times to ensure the reproducibility of the results. The electrochemical parameters were obtained by fitting the EIS data by using ZView software.

5.2.5 Topographic characterization of the steel electrodes

The AFM characterization was conducted on the steel electrodes after testing in 0.1 M NaCl solution in the absence and presence of 1 wt.% prepared nanocontainers using a Keysight 5500 AFM system. The AFM tip was made of Si, and mounted on triangular cantilevers (450 μm × 50 μm × 2 μm) with an average spring constant of 0.02-0.77 N/m. The scanning mode was configured as contact, with a scanning rate of 1 Hz, and resolution of 256 × 256 pixel.

5.3 Results and discussion

5.3.1 Characterization of the prepared BTA-loaded nanocontainers

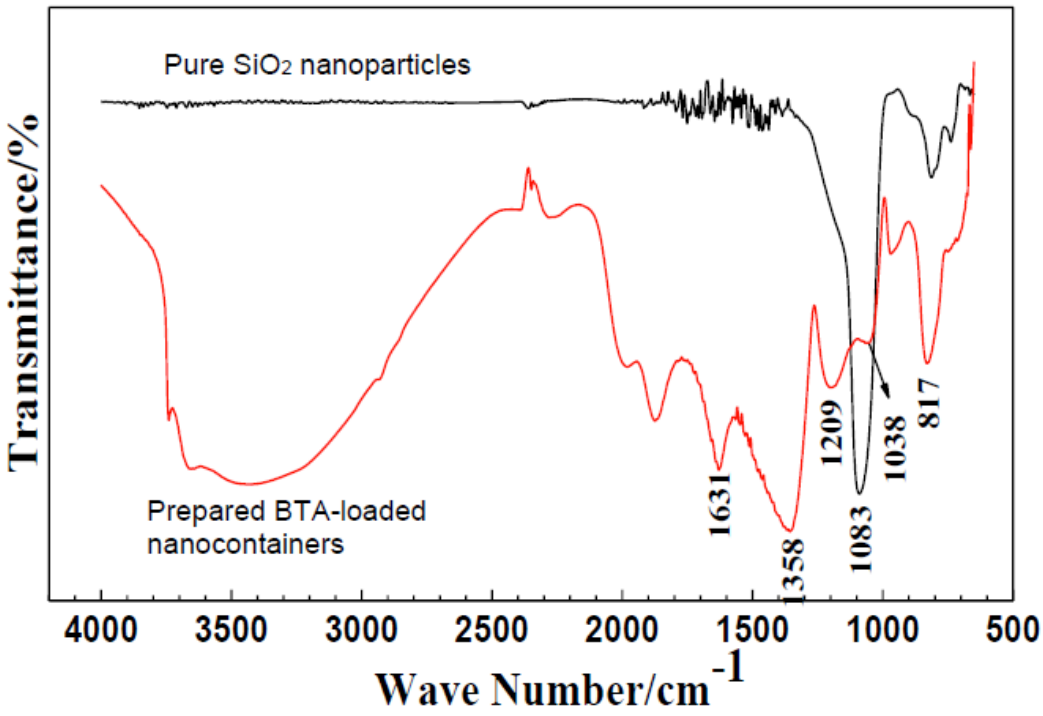

Fig. 5.2 FTIR spectra of pure SiO_2 nanoparticles and the prepared BTA-loaded nanocontainers, respectively.

Table 5.1 Characteristic bonds of pure SiO_2 particles and the prepared BTA-loaded nanocontainers in the measured FTIR spectra.

Wavelength (cm^{-1})	Bonds	Ref.
817	Si-O-Si bending vibration	[119]
1038	N-H stretching vibration	[89]
1083	Si-O-Si stretching vibration	[33]
1209	-N=N-N- breathing vibration	[120]
1358	C-N stretching vibration	[85]
1361	Benzene ring stretching vibration	[121]
3300-3600	Hydrogen bands O–H, N–H, and C–H	[122, 123]

The SiO_2 nanoparticle-based nanocontainers with pre-loaded inhibitors BTA were fabricated by LBL deposition in this work. It was aimed at, by using the well-established technique to prepare inhibitor-loading nanocontainers, determining the self-releasing mechanism and kinetics of the inhibitors from the nanocontainers.

The FTIR spectrometer is used to identify whether inhibitors BTA are loaded in the nanocontainers. Fig. 5.2 shows the FTIR spectra of pure SiO_2 nanoparticles and the prepared BTA-loaded nanocontainers, respectively. The characteristic functional groups identified are listed in Table 5.1, where the reference sources for specific bonding groups are also included. For both spectra, the characteristic peaks for SiO_2 are associated with the stretching and bending vibration of Si-O-Si bonds at 1083 cm^{-1} and 817 cm^{-1}, respectively. In the spectrum obtained from the prepared nanocontainers, the peak at 1209 cm^{-1} is from the vibration of typical triazole rings contained in inhibitors BTA. The low-intensity peak at 1038 cm^{-1} is attributed to N-H stretching vibration. The benzene

rings in BTA exhibit a peak at 1361 cm^{-1}. The peak with a considerable intensity at 1358 cm^{-1} is due to the C-N stretching vibration, which is associated with the C-N functional groups in inhibitors BTA. Moreover, a broad bond at 3300 ~ 3600 cm^{-1} is attributed to hydrogen bonds O-H and N-H, which are from the interactions between SiO_2 nanoparticles and polyelectrolytes as well as the inhibitors BTA. The FTIR results demonstrate that inhibitors BTA are loaded in the prepared nanocontainers.

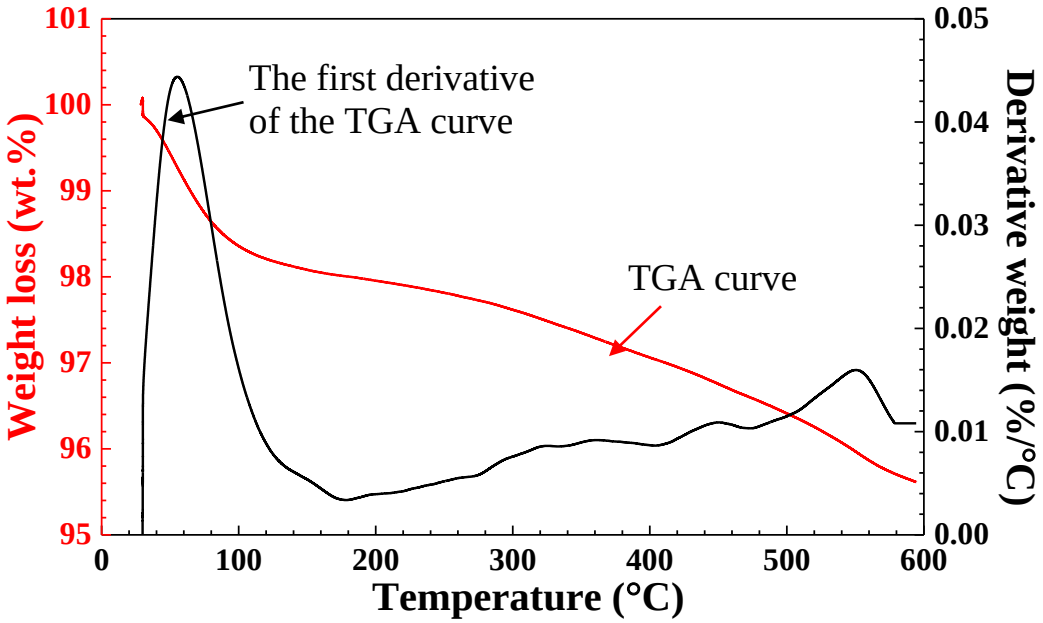

Fig. 5.3 Thermogravimetric profile of the prepared nanocontainers and the first derivative of the TGA curve.

The thermogravimetric profile of the prepared nanocontainers is shown in Fig. 5.3, where the first derivative of the measured TGA curve is also included. Two stages of weight loss are observed. In stage one, nearly 1.8% weight loss occurs at temperatures

between 30 and 120 ^{o}C. It is attributed to the loss of remaining water in the nanocontainers. The weight loss of 2.5% occurs from 120 to 550 ^{o}C in helium atmosphere at stage two, where the weight loss rate increases gradually with time. As the SiO_2 nanoparticles remain stable up to 600 ^{o}C, the weight loss in this stage is primarily due to the thermal decomposition of the loaded inhibitors BTA. The weight percentage of the encapsulated inhibitors BTA are about 2.5 wt.% in the nanocontainers determined by the thermal stability test.

5.3.2 EIS measurements

Fig. 5.4 shows the Nyquist diagrams measured on the steel electrode at its OCP in 0.1 M NaCl solutions with various pH values (pH = 2, 5, 7, 9 and 11) in the absence and presence of 1 wt.% BTA-loaded nanocontainers at different immersion times, respectively. It is seen that all impedance plots feature a depressed semicircle over the whole frequency range, with inductive loops present in some measured impedance plots. The depressed impedance semicircles and low-frequency inductive behaviour are often associated with heterogeneity of the electrode surface resulted from inhibitor adsorption, surface roughness and porous film formation [124]. In the solutions containing nanocontainers, the size of the semicircle is bigger than that recorded in the absence of nanocontainers in the solutions. Moreover, the semicircle becomes bigger with time. Since the size of the semicircle is proportional to the charge-transfer resistance of the corrosion reaction, the increasing semicircle size indicates that the inhibitors BTA release from the nanocontainers to the solution for corrosion inhibition. Moreover, the inhibiting effect becomes more effective with time.

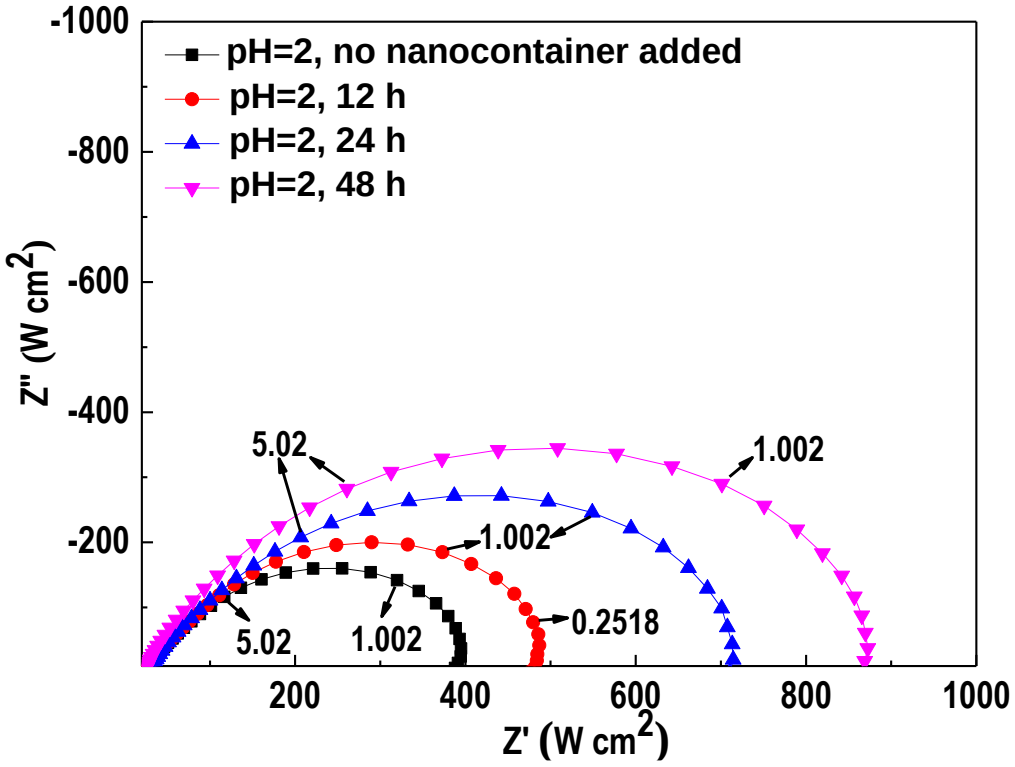
pH=2, no nanocontainer added
pH=2, 12 h
pH=2, 24 h
pH=2, 48 h
-1000
-800
-600
-400
-200
Z'' (W cm2)
200
400
600
800
1000
Z' (W cm2)
5.02
1.002
1.002
0.2518
5.02
1.002

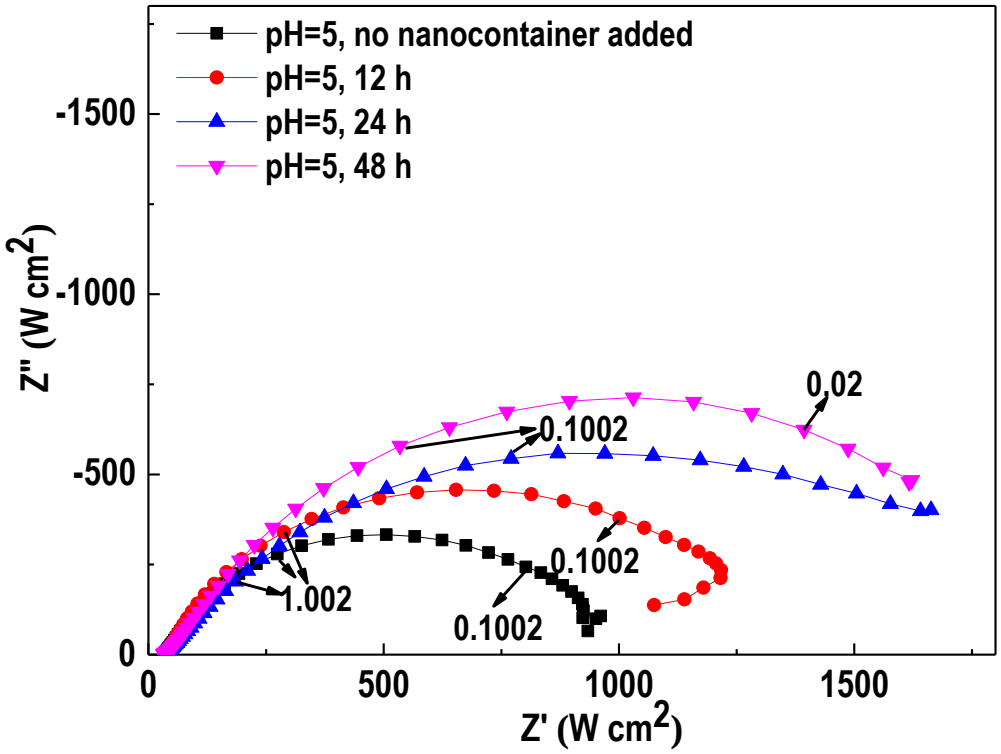
pH=5, no nanocontainer added
pH=5, 12 h
pH=5, 24 h
pH=5, 48 h
-1500
-1000
-500
0
Z'' (W cm2)
0
500
1000
1500
Z' (W cm2)
0,02
0.1002
0.1002
1.002
0.1002

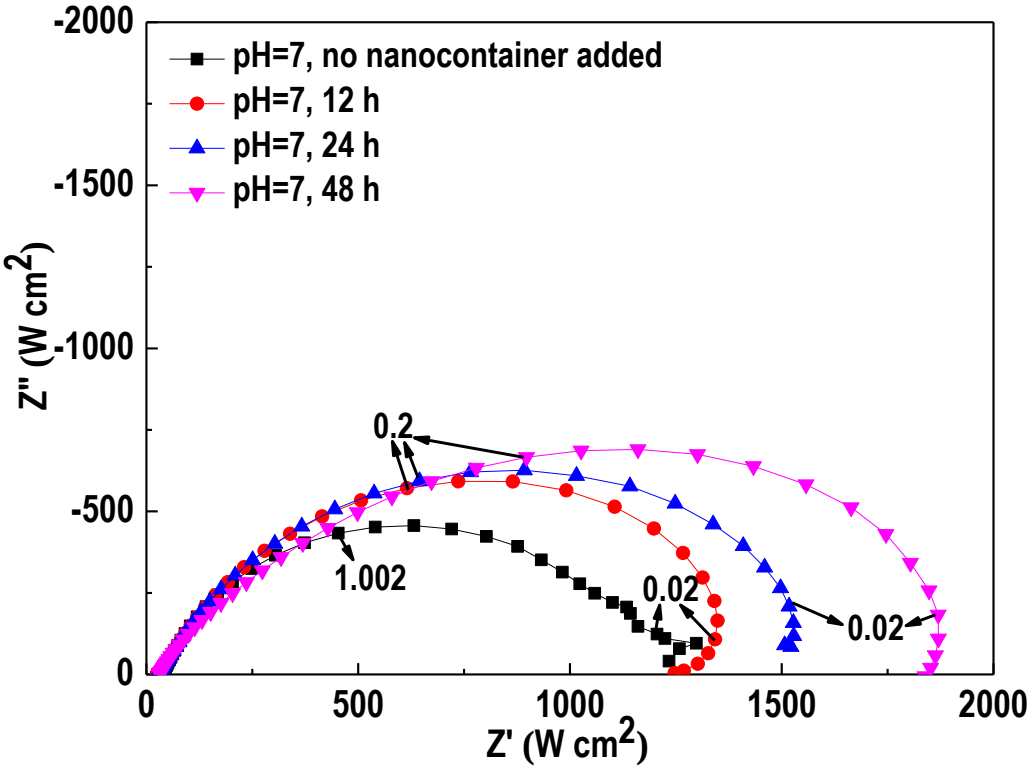
pH=7, no nanocontainer added
pH=7, 12 h
pH=7, 24 h
pH=7, 48 h
-2000
-1500
-1000
-500
0
Z'' (W cm2)
0
500
1000
1500
2000
Z' (W cm2)
0.2
1.002
0.02
0.02

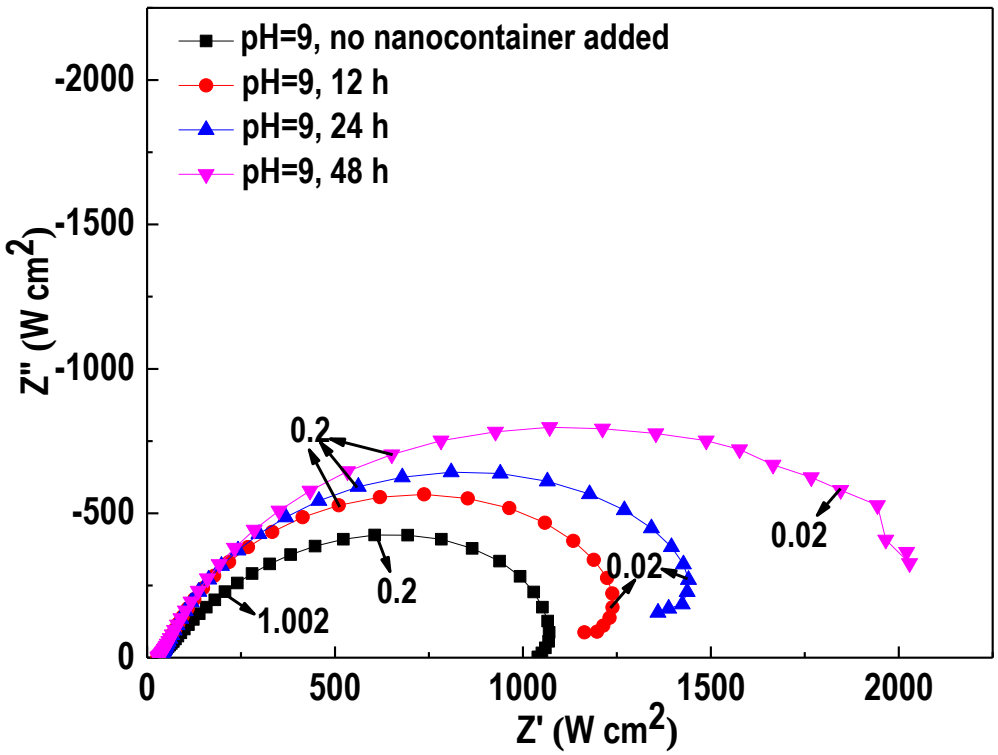
pH=9, no nanocontainer added
pH=9, 12 h
pH=9, 24 h
pH=9, 48 h
-2000
-1500
-1000
-500
0
Z'' (W cm2)
0
500
1000
1500
2000
Z' (W cm2)
0.2
1.002
0.2
0.02
0.02

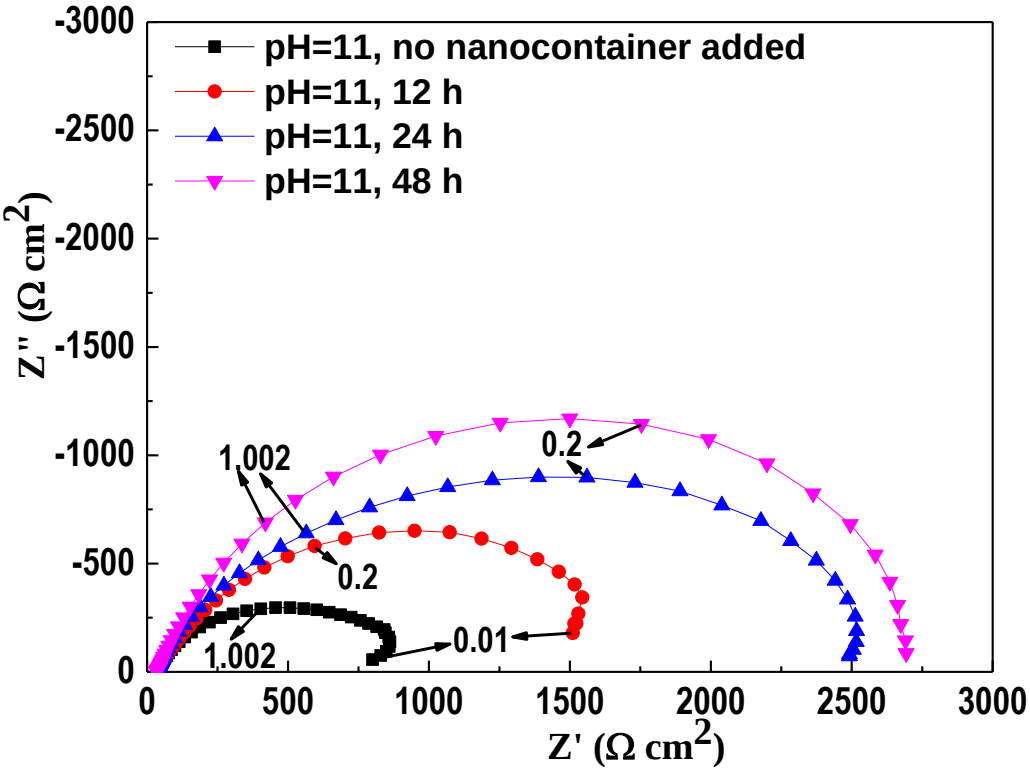

Fig. 5.4 Nyquist diagrams measured on X65 steel electrode at its open-circuit potential after 12 h, 24 h and 48 h of immersion in 0.1 M NaCl solutions with pH = 2, 5, 7, 9, and 11 in the absence and presence of 1wt.% BTA-loaded nanocontainers, respectively.

To obtain the electrochemical impedance parameters from the measured impedance data, an electrochemical equivalent circuit, which consists of a solution resistance (R_s) connected in series with a parallel connection of a charge-transfer resistance (R_{ct}) and a double-layer capacitance (C_{dl}), is used. Consider the data scattering in the low frequency range, the inductive parameters are not fitted. The inhibition performance of the released inhibitors is evaluated by changes of R_{ct} and C_{dl} as a function of time.

Table 5.2 Electrochemical impedance parameters derived from the measured impedance data.

pH	Solution	R_s (Ω cm^2)	R_{ct} (Ω cm^2)	C_{dl} (μF/cm^2)	*IE* (%)
2	No nanocontainer added	26.81	329.7	262.4	/
	12 h	24.1	462.7	224.0	28.74
	24 h	28.25	668.4	181.6	50.67
	48 h	23.17	906.4	133.7	63.63
5	No nanocontainer added	38.18	986.4	286.41	/
	12 h	38.83	1075	240.85	8.24
	24 h	36.43	1191	107.56	17.18
	48 h	34.67	1324	154.53	25.50
7	No nanocontainer added	38.6	1003	483.82	/
	12 h	30.09	1127	408.15	11.00
	24 h	29.68	1167	373.48	14.05
	48 h	30.93	1189	310.66	15.64
9	No nanocontainer added	31.16	1199	974.23	/
	12 h	30.81	1393	906.22	13.93
	24 h	30.82	1638	841.29	26.80
	48 h	30.74	1894	750.17	36.69
11	No nanocontainer added	34.37	847.9	551.3	/
	12 h	36.31	1328	441.9	36.15
	24 h	37.68	1782	301.4	52.42
	48 h	35.9	2876	239.9	70.52

Table 5.2 shows the fitted impedance parameters. It is seen that the R_{ct} increases while the C_{dl} decreases as the immersion time increases. It is proposed that, with the releasing of inhibitors BTA, a protective adsorption film is formed on the steel surface

[125]. As a result, the corrosion of the steel is reduced, accompanying a decrease of the C_{dl}. This phenomenon can be described according to the Helmholtz model, where C_{dl} is proportional to the surface charge by [9]:

$$C_{dl} = \frac{\varepsilon^0 \varepsilon}{d} A \tag{5-1}$$

where ε^0 is the vacuum permittivity, ε is the local dielectric constant, d is the thickness of the film, and A is the electrode area. Generally, the decrease in C_{dl} is attributed to the replacement of adsorbed water molecules on the metal surface with the inhibitor molecules which have a lower dielectric constant [126]. Moreover, the increase in the thickness of the adsorptive film may also cause the decrease of C_{dl} according to Eq. (5-1).

The charge-transfer resistance, R_{ct}, refers to the resistance of the charge-transfer reactions occurring at the steel electrode/solution interface during corrosion. It is directly related to the resistance of corrosion reactions, while the double-layer capacitance is not related to corrosion rate directly. Thus, the change of the charge-transfer resistances is usually used to indicate the change of corrosion rate of the steel in the system. To evaluate the performance of an inhibitor for corrosion inhibition, the inhibition efficiency is frequently calculated by:

$$IE\% = \frac{R_{ct} - R_{ct}^0}{R_{ct}^0} \times 100\% \tag{5-2}$$

where R_{ct} and R_{ct}^{0} are the charge-transfer resistances of the steel in the presence and absence of the prepared BTA-loaded nanocontainers, respectively. It is seen that the inhibition efficiency is quite low in the near-neutral pH solutions (pH from 5 to 9), and increase to 64% and 70% in pH 2 and 11 solutions, respectively. It further increases with the immersion time. The results indicate that the steel corrosion is inhibited due to the continuous releasing of BTA inhibitors from the nanocontainers in low and high pH ranges. While in near-neutral pH ranges, the nanocontainers are kept closed and the inhibitors cannot be not released into the solution.

5.3.3 Topographic characterization of steel electrodes

To demonstrate whether the corrosion inhibition is due to the formation of an adsorptive inhibitor film on the steel surface, the AFM is used to visualize the surface topography of the steel electrode after 2 days of immersion in 0.1 M NaCl solutions with various pH values in the absence and presence of 1 wt.% prepared BTA-loaded nanocontainers, as shown in Fig. 5.5. The derived surface roughness and root-mean-square height from the AFM images are shown in Table 5.3. It is seen that, in the absence of BTA-loaded nanocontainers in the solution, the steel electrode suffers from obvious corrosion, and the electrode surfaces are much rougher than those obtained in the nanocontainer-added solution. This is more obvious in low pH solutions such as pH 2, where severe corrosion happens on the steel to cause the surface roughness of the electrode to be 322 nm in the absence of nanocontainers in the solution, as seen in Fig. 5.5a and Table 5.3. When the BTA-loaded nanocontainers are included in the solution,

the steel surface is quite even and a layer of film is formed on the electrode surface, as seen in Fig. 5.5b. The surface roughness is 76 nm only. The presence of BTA-loaded nanocontainers in the solution decreases the steel corrosion and the surface roughness of the electrode due to formation of a layer of inhibitor adsorptive film on the steel surface. The similar results were reported previously [127]. In near-neutral pH solutions (pH 5 and 9), the steel corrosion is not so severe (as seen in Figs. 5.5c and 5.5g) since the solution environments are mild. However, the electrode surface is still covered with a uniform film in the solutions with the addition of nanocontainers (Figs. 5.5d and 5.5h). The solution at pH 7 shows similar AFM topographies and surface roughness in both the absence and presence of nanocontainers in the solution, indicating that the loaded inhibitors are not released appreciably to the solution. In the high pH solution (i.e., pH 11), the presence of nanocontainers does not decrease the surface roughness of the steel remarkably, as seen in Table 5.3, as the alkaline solution is not corrosive to the steel.

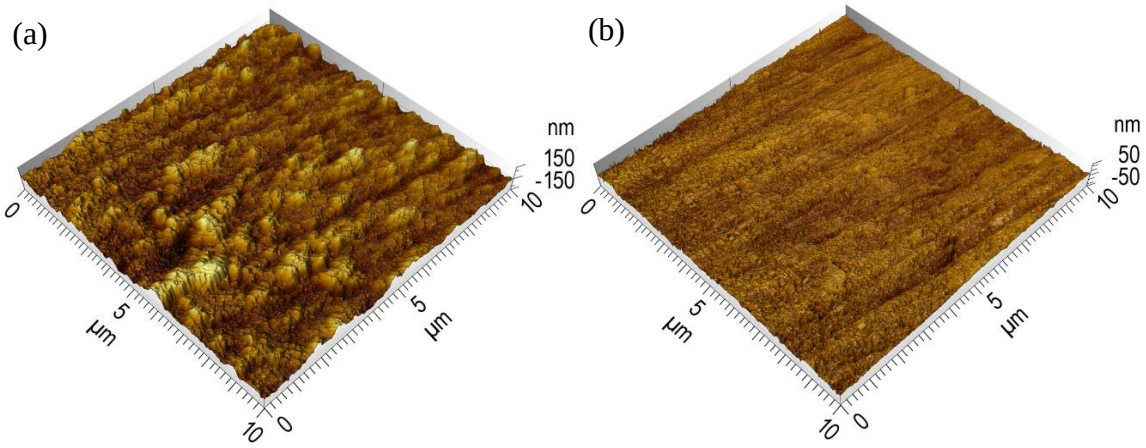

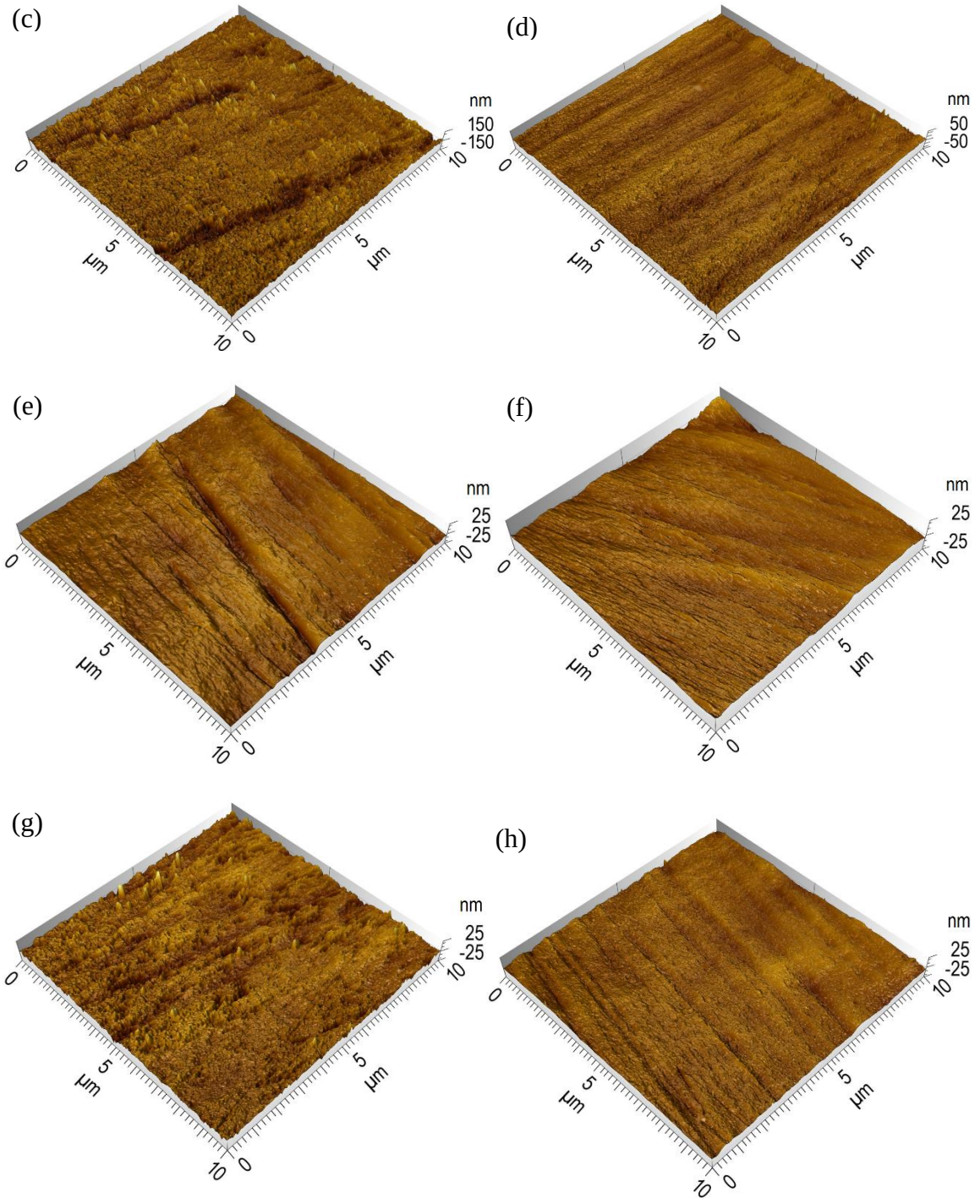
(c)
nm
150
-150
0
5
10
µm
(d)
nm
50
-50
(e)
nm
25
-25
(f)
nm
25
-25
(g)
nm
25
-25
(h)
nm
25
-25

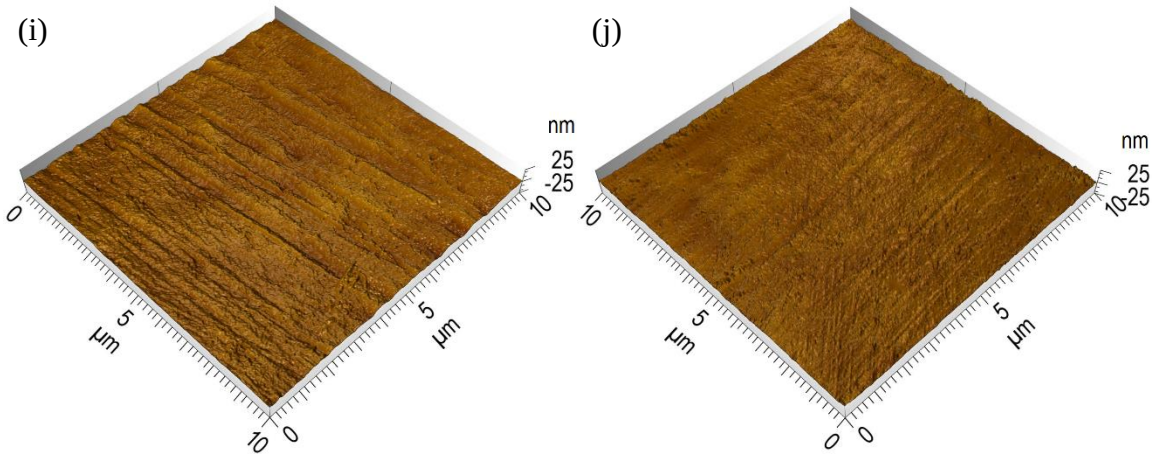

Fig. 5.5 AFM image of the surface topography of the steel electrode after 48 h of immersion in 0.1 M NaCl solutions in the absence (*left row*) and presence (*right row*) of 1 wt.% prepared BTA-loaded nanocontainers, respectively (a)(b) pH = 2, (c)(d) pH = 5, (e)(f) pH = 7, (g)(h) pH = 9, and (i)(j) pH =11.

Table 5.3 Surface roughness and root-mean-square height of the steel electrode derived from the AFM images.

pH	Solution	Surface roughness	Root-mean-square height (nm)
2	No nanocontainer added	322	38
	With nanocontainers	75.9	5.89
5	No nanocontainer added	285	24.7
	With nanocontainers	63.5	5.11
7	No nanocontainer added	31.3	2.54
	With nanocontainers	24.4	2
9	No nanocontainer added	59.5	4.12
	With nanocontainers	26.1	2.15
11	No nanocontainer added	20.3	1.37
	With nanocontainers	16.8	1.27

5.3.4 pH sensitive self-releasing of BTA inhibitors from the nanocontainers

The present work shows that the prepared nanocontainers are pH sensitive. At low and high pH values (such as pH 2 and 11), the pre-loaded inhibitors BTA can self-release out of the nanocontainers for corrosion inhibition; while in near-neutral pH ranges, such as pH 5-9, the nanocontainers are kept closed. In general, polyelectrolytes are sensitive to pH changes, with “open” or “close” state by “swelling” to break the shell layer or “shrinking” to recover to original state, respectively [62]. It was reported that polyelectrolytes, i.e., PDDAC and SPSS, used in this work possess a pH-buffering capability and can stabilize pH values between 5 and 9 on steel surface in corrosive environments [128]. Inhibitors can release from the multilayer polyelectrolytes shell for corrosion inhibition in environments with the solution pH drops to an acidic range which can cause corrosion to steels. When the solution pH is elevated to a near-neutral value, polyelectrolytes are back to “close” state, where the inhibitors become sealed in the nanocontainers.

Fig. 5.6 shows the pH dependences of the inhibition efficiency of BTA released from the nanocontainers for steel corrosion after 48 h of immersion in 0.1 M NaCl solution determined by EIS results. The rapid increase of the inhibition efficiency at low or high pH values (pH 2 or 11) is observed. The smart release of inhibitors BTA in acidic environments shows that the PDDAC-BTA-SPSS multilayer assembly possesses the ability to respond to the corrosive environment generated where the coating is damaged and the electrolyte becomes acidic.

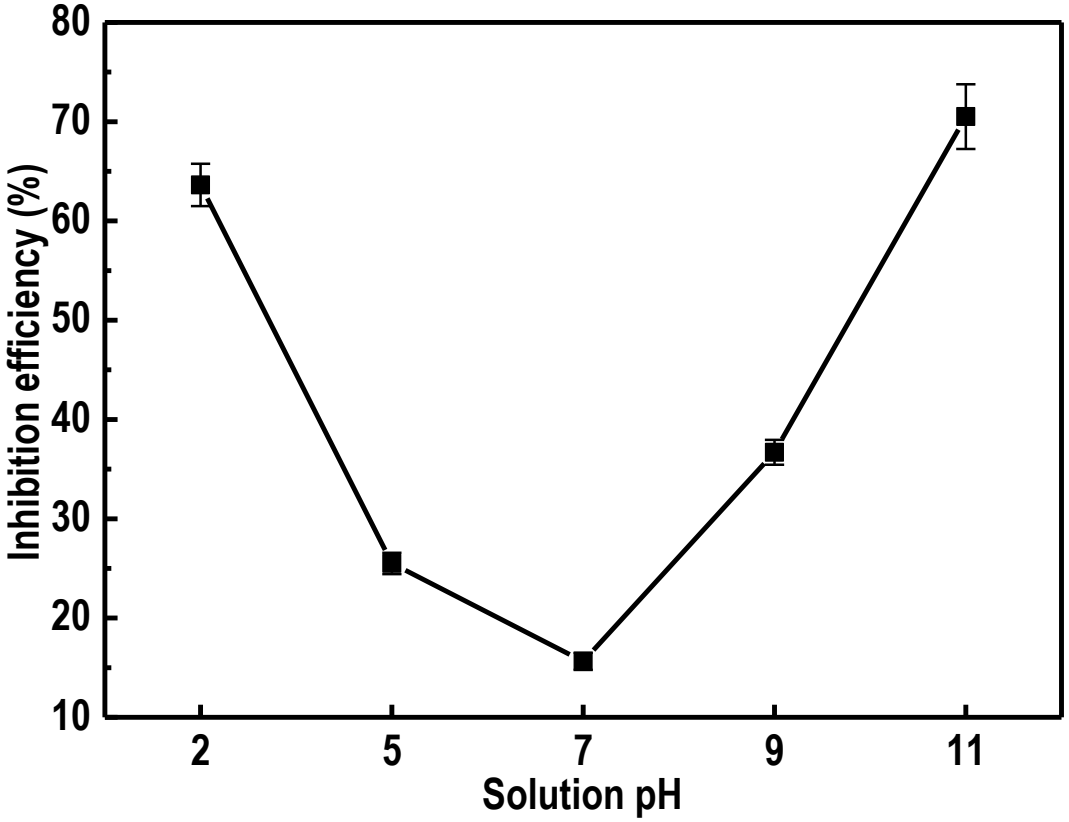

Fig. 5.6 pH dependences of the inhibition efficiency of BTA inhibitors released from the nanocontainers for steel corrosion after 48 h of immersion in 0.1 M NaCl solution determined by EIS results.

5.3.5 Kinetic for inhibitor releasing from the nanocontainers

Upon releasing of BTA inhibitors from the nanocontainers to the solution, the steel corrosion is inhibited by forming an adsorptive inhibitor film. Assume the inhibition efficiency, η, is proportional to the surface coverage, θ, of the inhibitor molecules, and the inhibitor adsorption obeys the Langmuir isothermal equation [129]:

$$\theta_t = \frac{I_{corr}^0 - I_{corr}^t}{I_{corr}^0} = \frac{\eta_t}{100} \quad (5\text{-}3)$$

$$\frac{C_t}{\theta_t} = \frac{1}{K_a} + C_t \quad (5\text{-}4)$$

where t is time (h), η_t is the inhibition efficiency after t h, θ_t is the instant surface coverage, I_{corr}^0 (μA/cm^2) and I_{corr}^t (μA/cm^2) are corrosion current densities in the absence and presence of inhibitor-loaded nanocontainers in the solution, respectively, C_t is the concentration of the released inhibitors in the solution, and K_a is the adsorptive equilibrium constant. Combine Eqs. (5-3) and (5-4) gives:

$$C_t = \frac{\eta_t}{(100 - \eta_t)K_a} \quad (5\text{-}5)$$

The present results show that the inhibition efficiency is low in the pH 7 solution. It is thus assumed that the amount of BTA inhibitors released from the nanocontainers in the pH 7 solution is negligible. The kinetic study of inhibitor-releasing is conducted in solutions with pH values of 2, 5, 9 and 11 only. It was reported that the Korsemeyer-Peppas model is appropriate to simulate the pH-dependent releasing of inhibitors from nanocapsules [130-132]:

$$\frac{C_t}{C_0} = K_r t^n \quad (5\text{-}6)$$

where C_0 is for the initial amount of BTA inhibitors in the prepared nanocontainers, K_r is the releasing rate constant, and n is the diffusion exponent subject to the inhibitor-releasing mechanism and type.

Combine Eqs. (5-5) and (5-6) to have the relationship between the inhibition efficiency and time:

$$\eta_t = \frac{100 C_0 K_a K_r t^n}{1 + C_0 K_a K_r t^n} \tag{5-7}$$

Rearrange and transform Eq. (5-7) to its logarithmic form:

$$\ln \frac{\eta_t}{100 - \eta_t} = \ln C_0 K_a K_r + n \ln t \tag{5-8}$$

The inhibition efficiencies obtained from the EIS measurements in Table 5.2 are normalized with this model. Fig. 5.7 shows the time dependence of the fitting results for BTA inhibitor releasing from the prepared nanocontainers by Eq. (5-8). It is seen that linear relationships are obtained by plotting $\ln \frac{\eta_t}{100 - \eta_t}$ vs. $\ln t$ for all the solutions with varied pH values. The n values are obtained from the slope of the lines and the results are shown in Table 5.4. The TGA results in Fig. 5.2 shows that there is approximately 2.5 wt.% BTA contained in the prepared nanocontainers. In EIS measurements, 1 wt.% of nanocontainers was added in 50 mL of the test solution. Thus, the initial amount of BTA

inhibitors in the prepared nanocontainers, C_0 is calculated as 0.0021 mol/L. The R^2 in Table 5.4 is the coefficient measuring the reliability of data fitting, where a value close to 1 indicates a good fitting. Obviously, all R^2 values are close to 1, and the experimental results agree with the modelling very well.

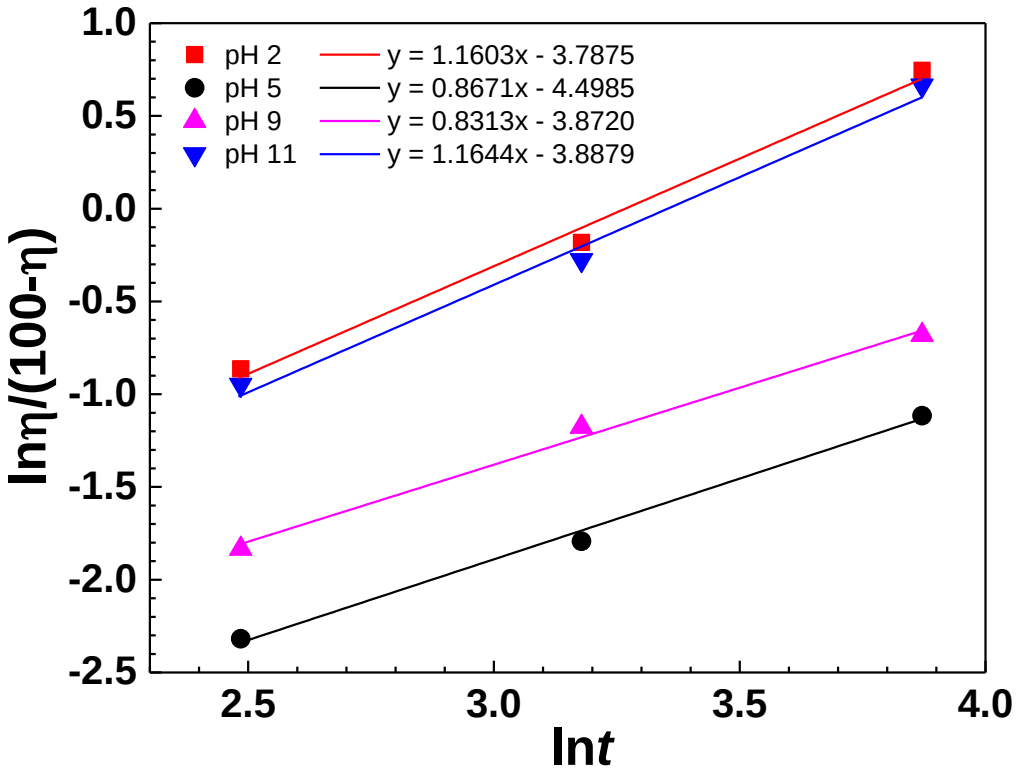

Fig. 5.7 Time dependence of the fitting results for BTA inhibitors releasing from the prepared nanocontainers by Eq. (5-8).

From the data fitting in Fig. 5.7 and Table 5.4, it is seen that the Korsmeyer-Peppas kinetic model gives an accurate fitting with the experimental results. Hence, the Korsemeyer-Peppas model is appropriate to predict the releasing of BTA inhibitors from

the prepared nanocontainers in response to pH changes. The model is able to provide information about the releasing rate and service time of the pre-loaded inhibitors, avoiding the difficulty, and frequently inability, of real-time monitoring of the inhibitor performance in practice.

Table 5.4 Kinetic data for BTA releasing from the prepared nanocontainers to the solution with various pH values.

pH	n	$\ln(C_0K_aK_r)$	K_aK_r	R^2
2	1.16	-3.79	10.75	0.9923
5	0.87	-4.50	5.29	0.9948
9	0.83	-3.87	9.93	0.9934
11	1.16	-3.89	9.74	0.9908

5.3.6 Mechanisms for inhibitors BTA releasing from the nanocontainers

This work demonstrates that the inhibitor molecules BTA encapsulated in the multilayer polyelectrolyte shells on the SiO_2 nanoparticle carrier can self-release to the corrosive electrolyte in response to solution pH changes as the triggering mechanism. Generally, there are four types of mechanism for BTA molecules releasing from nanocontainers based on the value of n in Eq. (5-8). For $n \leq 0.45$, the releasing of inhibitor molecules follows the Fickian diffusion mechanism; for $0.45 < n < 0.89$, a non-Fickian transport applies; For $n = 0.89$, the inhibitor-releasing follows a relaxational transport mode; and for $n > 0.89$, the super-relaxational transport applies [133, 134]. The values of n listed in Table 5.4 show that the n is 0.87 and 0.83 in solutions pH 5 and 9, respectively. This indicates that, in these solutions, the releasing of inhibitor molecules follows a non-Fickian, diffusion-controlled transport mechanism. Actually, the BTA

molecules release slightly from the nanocontainers in neutral pH solutions within the test time period in this work. When the solution pH is at 2 or 11, the kinetic diffusion exponent *n* is up to 1.16. The BTA molecules follow the super-relaxational transport mechanism to release from the nanocontainers by swelling-controlled releasing processes. The polyelectrolytes shells are open sufficiently, and the BTA-releasing is fast through relaxational steps as described in Fig. 5.8.

In near-neutral pH environments, the multilayer polyelectrolytes and BTA inhibitors are in an electrostatic equilibrium state. The electrostatic forces existing among oppositely charged BTA, SPSS and PDDAC are in equilibrium that makes the multi-layers in a shrinking state and the BTA inhibitors are stored in the shell, avoiding their leaking, as shown in Fig. 5.8a. Upon generation of a corrosive environment, the solution pH changes. As the pH deceases (or increases), the concentration of cations or anions increases, which would disturb the charge balance in the solution, and that in the multi-layers deposited on SiO_2 nanoparticles. The additional positive or negative charges preferentially adsorb on negatively or positively charged SPSS or PDDAC molecules, respectively. The electrostatic force between SPSS and PDDAC becomes unbalanced. An electrostatic repulsion on the chain of polyelectrolytes increases their mutual distances, leading to swelling of the shell structure, as shown in Fig. 5.8b. The swelling of the shell deposited on SiO_2 nanoparticles opens the shell to release BTA molecules from the nanocontainers to the solution.

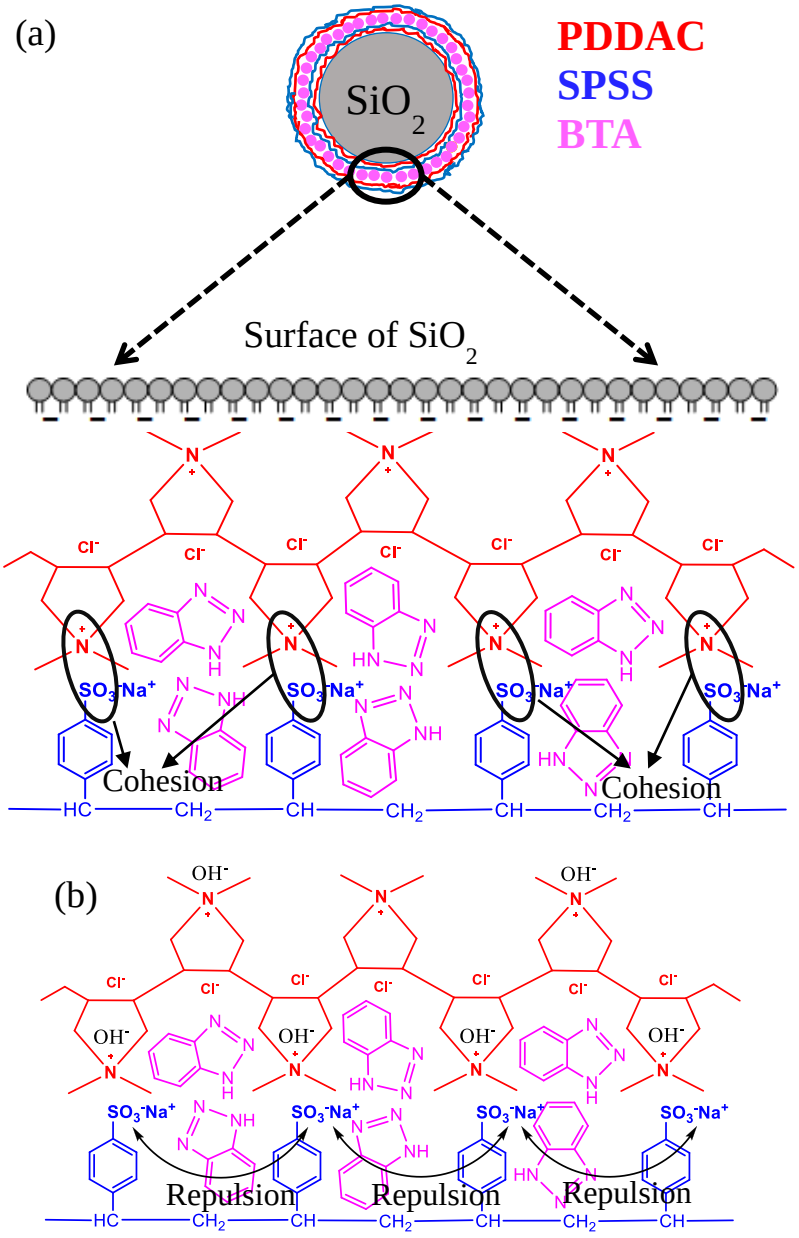

Fig. 5.8 Illustration of swelling of the nanocontainers due to electrostatic repulsions between negative charges of SPSS (a) an electrostatic equilibrium state, (b) electrostatic repulsions between negative charges on SPSS.

5.3.7 Mechanism for corrosion inhibition by BTA

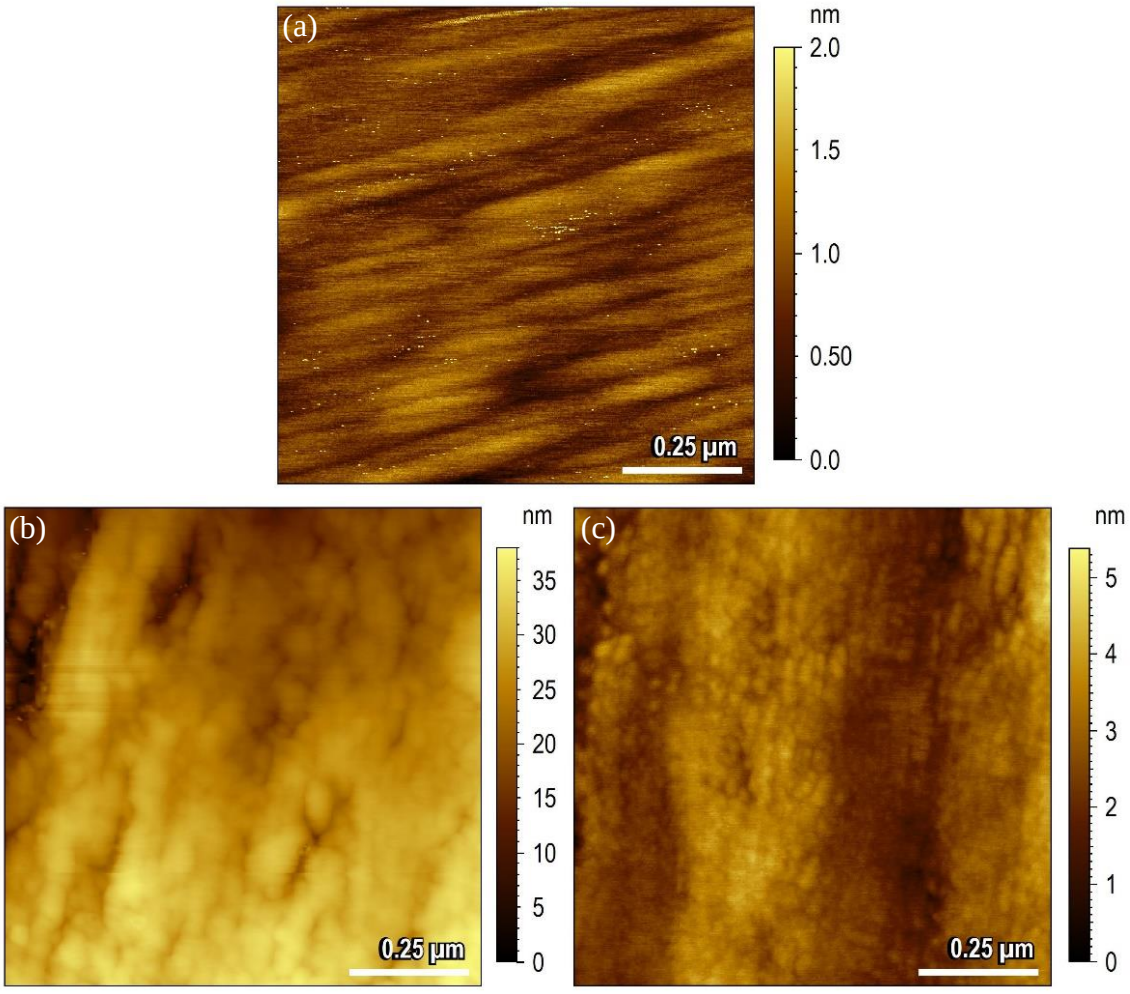

Fig. 5.9 AFM top view of the surface morphology of X65 steel electrode after 48 h of immersion in 0.1 M NaCl solution containing 1wt.% of BTA-loaded nanocontainers at (a) pH 7, (b) pH 2, and (c) pH 11, respectively.

Generally, organic inhibitors inhibit steel corrosion by formation of an adsorptive inhibitor film on the metal surface. In order to prove the formation of an adsorptive film

on X65 steel surface upon releasing of BTA from the nanocontainers to the solution, the AFM surface topographic images of X65 steel electrode after 48 h of immersion in 0.1 M NaCl solution with 1 wt.% of BTA-loaded nanocontainers at pH 2, 7 and 11, respectively are shown in Fig. 5.9. It is seen from Fig. 5.9a that, in pH 7 solution, small granule particles are present along the mechanical scratches on the steel surface. The bright stripes maybe from the deposition of corrosion products, which is similar to the corroded steel as reported previously [85]. In pH 2 solution, an uneven surface with compact spherical or bread-like particles are observed on the steel surface (Fig. 5.9b). When the solution pH is 11, similar bread-like particles, but with finer size, are distributed on the steel surface. The bread-like particles were confirmed as the adsorption of inhibitors on the steel surface [135].

The BTA inhibitors released to the solution can form adsorptive films on the steel surface in both acidic (pH 2) and alkaline (pH 11) solution. However, the scale of the bread-like particles is different. While the features formed in the pH 11 solution have several nm of dimension, the features are over 30 nm in the pH 2 solution. The difference is attributed to the different adsorption mechanisms of BTA inhibitors in the solutions. The polar unit of three heterocyclic nitrogen atoms in BTA molecules is regarded as the core for the chemisorption process. Generally, BTA exists as the form of protonated cations, i.e., $BTAH^+$, at pH lower than 8, and in the deprotonated anionic species, i.e., BTA^-, at pH > 8 by:

$$BTAH^+ \xleftarrow{\text{Acid}} BTA \xrightarrow{\text{Alkali}} BTA^- \qquad (5\text{-}9)$$

In acidic chloride solutions, the corrosion of steels follows the following mechanism [136, 137].

$$Fe + Cl^- \rightarrow (FeCl^-)_{ads} \quad (5\text{-}10)$$

$$(FeCl^-)_{ads} \rightarrow (FeCl)_{ads} + e \quad (5\text{-}11)$$

$$(FeCl)_{ads} \rightarrow FeCl^+ + e \quad (5\text{-}12)$$

$$FeCl^+ \rightarrow Fe^{2+} + e \quad (5\text{-}13)$$

In acidic solutions, the BTA exists in the form of cations, i.e., protonated $BTAH^+$, which produces electrostatic repulsions to the positively charged steel surface. Thus, a physical adsorption takes place due to electrostatic interactions between the positively charged protonated molecules ($BTAH^+$) and negatively charged $(FeCl^-)_{ads}$ species [126]. It is noted that the molecular structure of protonated BTA remains unchanged. When adsorbed on the steel surface, strong covalent bonds can form between two N atoms in the triazole ring and iron atoms by sharing electrons between the inhibitor molecules and iron [135, 138], as shown in Fig. 5.10a. Thus, BTA or protonated BTA can form a protective film on the steel surface in acidic solutions through physical and chemical adsorption, with the morphology of the film shown in Fig. 5.9b. The formation of the protective film is confirmed by the EIS results in Table 5.2, where the decrease in C_{dl} as a function of time in pH 2 solution is attributed to the formation and growth of adsorptive BTA film on the steel surface. This film has a lower dielectric constant and decreases the active corrosion area on the steel. Moreover, due to the interaction between protonated BTA with corrosion products $(FeCl^-)_{ads}$, the anodic reaction in Eq. (5-11) can be retarded,

making the charge-transfer step more difficult and causing an increase in R_{ct}, as shown in Table 5.2. Since the protonated BTA directly adsorbs on corrosion products $(FeCl^-)_{ads}$, the AFM view shows the bread-like particles on the steel surface.

In alkaline chloride solutions, the corrosion of the steel occurs by [139, 140]:

$$Fe + OH^- \rightarrow (FeOH)_{ads} + e \quad (5\text{-}14)$$

$$(FeOH)_{ads} \rightarrow (FeOH^+)_{ads} + e \quad (5\text{-}15)$$

$$(FeOH^+)_{ads} \rightarrow Fe^{2+} + OH^- \quad (5\text{-}16)$$

An iron chloride complex can be formed by:

$$Fe^{2+} + mOH^- + nCl^- \rightarrow [Fe(OH)_mCl_n]^{2-m-n} \quad (5\text{-}17)$$

In alkaline solutions, corrosion intermediates, $(FeOH)_{ads}$, can largely cover the steel surface due to the high concentration of OH^-, reducing the steel corrosion. This can be confirmed by the lower R_{ct} from EIS measurements and the AFM image with a low surface roughness of the steel in pH 11 solution. The result from Yao et al. [141] indicated that each iron atom may coordinate with several deprotonated BTA (BTA^-) species through N-atoms in the triazole rings. Some BTA^- can adsorb on the steel surface. The results from Mennucci et al. [125] also found that the corrosion protection of steels in alkaline NaCl solution by BTA involves the formation of a complex. The BTA present in its deprotonated form in the alkaline chloride solution can form the complex $[Fe(OH)_mCl_n]^{2-m-n}$, which adsorbs on the steel surface by coordination of the pairs of free

electrons from nitrogen atoms with iron. The complex covers the steel surface acting as a barrier to the access of corrosive species to the substrate steel to reduce corrosion, as shown in Fig. 5.10b.

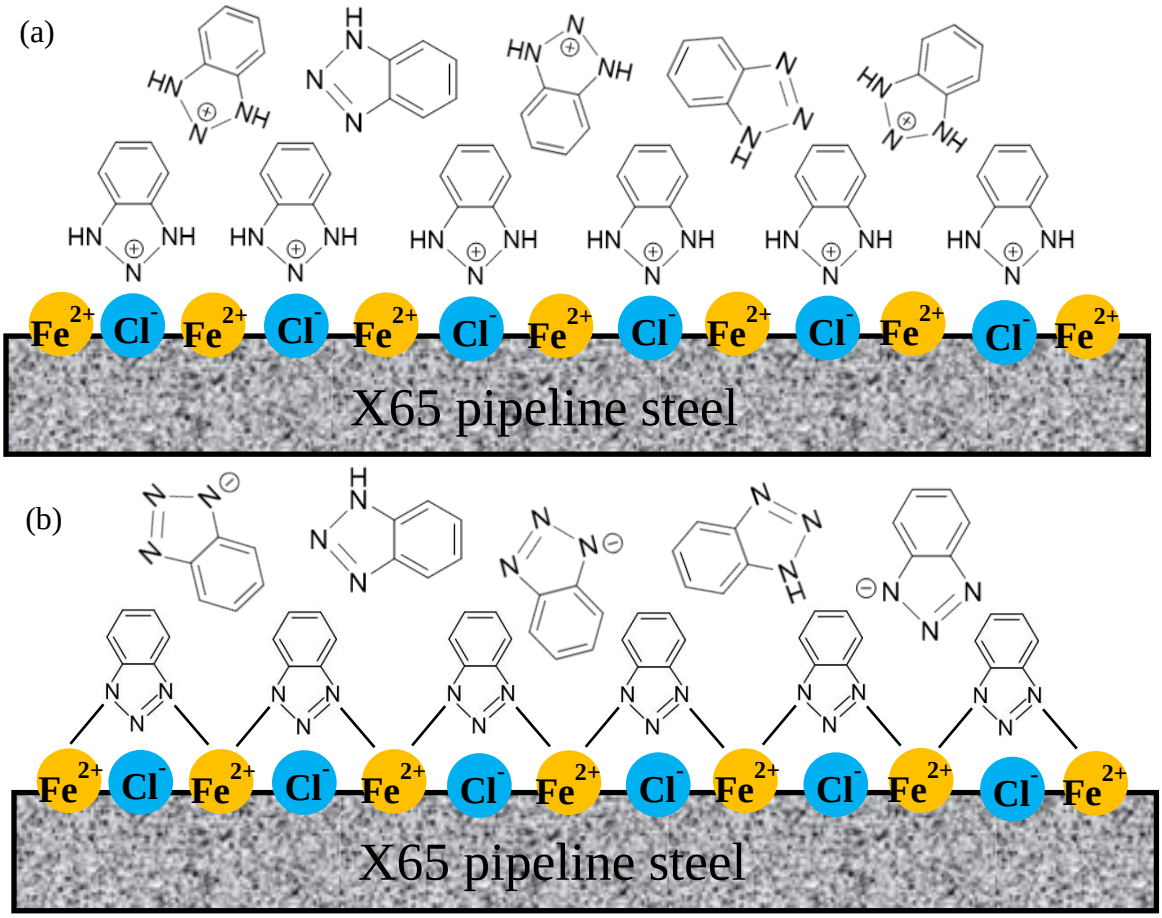

Fig. 5.10 Schematic of adsorption of BTA on X65 surface in (a) acidic solution and (b) alkaline solution.

5.4 Summary

The polyelectrolyte deposition method was used to prepare SiO_2 nanoparticle based nanocontainers to store inhibitors BTA. Both structural characterization by FTIR and thermal gravity analysis by TGA show that there are approximately 2.5 wt.% BTA loaded in each nanocontainers.

The releasing of the pre-loaded BTA from the nanocontainers is pH selective. The inhibitors can self-release into the solution to inhibit steel corrosion at either low or high pH values, such as pH 2 or 11. In the near-neutral pH range from 5 to 9, the nanocontainers remain closed and the inhibitors are not able to release at an appreciable level. In pH 2 and pH 11 solutions, the added BTA-loaded nanocontainers decrease the corrosion rate of the steel, with an inhibition efficiency up to 64% and 71% after 48 h of testing, respectively. Moreover, the inhibition efficiency is increased with time, subject to continuous releasing of the loaded inhibitors. The inhibition to steel corrosion by BTA is through formation of an inhibitor film on the steel surface by physical and chemical adsorption, which is influenced by solution pH.

The Korsemeyer-Peppas model is appropriate to illustrate and predict the releasing of BTA inhibitors from the nanocontainers in response to pH changes, providing information on the releasing rate of the pre-loaded BTA inhibitors.

In solutions with pH 5 and 9, the inhibitor molecules show a non-Fickian, diffusion-controlled transport mechanism with a limited releasing. When the solution pH is at 2 or 11, the BTA molecules follow the super-relaxational transport mechanism to release from the nanocontainers by swelling-controlled releasing processes.

Chapter Six: An Intelligent Coating Doped with Inhibitor-encapsulated Nanocontainers for Corrosion Protection of Pipeline Steel*

6.1 Introduction

Intelligent coatings refer to coating systems with "corrosion-sensing" and "self-healing" properties, providing not only a barrier to the environment, but also a self-release of corrosion inhibitors, which are preloaded into the coating, as demanded by coating damage/degradation and the presence of a corrosive environment on metals [12, 142-145]. In particular, BTA is an excellent choice of corrosion inhibitors encapsulated in intelligent coatings. The protective action of BTA is attributed to formation of an adsorptive protective film on the steel surface [124, 146]. It was found [147-149] that encapsulation of corrosion inhibitors in micro- or nanocontainers which are inert to the host coating provides a meaningful method, where the inhibitors pre-loaded in the nanocontainers can "sense" the generation of corrosive environments and self-release to inhibit the corrosion of metals in response to certain triggering mechanisms. For example, Chen and Fu [61] prepared inhibitor-loaded capsules based on hollow mesoporous silica spheres. The pre-stored inhibitors BTA can release from the silica spheres based on the change of local pH caused by the corrosion of metals.

While the intelligent coatings based on encapsulation of corrosion inhibitors in micro- or nanocontainers and self-releasing of the inhibitors based on appropriate triggering mechanisms were proposed and tested as a promising coating alternative for

* This work has been published as: Yuanchao Feng, Y. Frank Cheng, An intelligent coating doped with inhibitor-encapsulated nanocontainers for corrosion protection of pipeline steel, *Chemical Engineering Journal* 315 (2017) 537-551.

corrosion prevention, none of them has been developed at an industrial scale, especially for pipeline corrosion control. To date, the majority of the relevant research was conducted in lab, where the host matrix coatings were not industrial ones used in the field. Moreover, the technologies to encapsulate inhibitors in the containers, such as the vacuum method, are very complicated and impractical at the industry scale, both technically and economically. With these challenges, in the previous work at chapter three, the authors used a field-used epoxy coating as the host coating and investigated its compatibility with the prepared inhibitor capsules. It was found that doping of the nanocapsules does not affect the coating properties. This work furthers pervious one and attempts to develop an industry-feasible intelligent coating technology by encapsulation of inhibitors in fabricated nanocontainers that are uniformly doped in a field-used pipeline coating and by self-releasing of the encapsulated inhibitors on demand for pipeline corrosion control. The used materials in the work, including inhibitors BTA, epoxy coating and SiO_2 nanoparticles, are economic and available in the market. The method to fabricate nanocontainers and the inhibitor-loading process are simple and well-established. Moreover, the inhibitor-loaded nanocontainers are doped in an industry epoxy coating currently used on pipelines. All of them will contribute to develop a technically feasible and cost-effective smart coating technology for improved pipeline integrity in practice.

In this work, an intelligent coating was developed by fabrication of SiO_2 nanoparticle based polyelectrolyte nanocontainers where corrosion inhibitors BTA were pre-loaded and the doping of the nanocontainers in an industry-used epoxy coating. The morphology and structure of the prepared nanocontainers and the doped amount of the nanocontainers

in the host coating were characterized by SEM, energy-dispersive X-ray spectrum (EDS), FTIR, TGA and differential thermal gravity (DTG). The dispersity of the nanocontainers in the epoxy coating was characterized by SEM and EDS, and the potential influence of the nanocontainers on the coating property, i.e., glass-transitional temperature, was determined by TGA and differential scanning calorimetry (DSC). The self-releasing of the encapsulated BTA in response to changes of the solution pH was measured by UV–vis spectroscopy. The anticorrosion performance of the developed coatings and the corrosion resistance of the coated steel were measured by EIS in a chloride solution. Long-term tests were conducted to investigate the self-releasing of the pre-loaded BTA inhibitors for corrosion inhibition of the steel in the solution. The inhibitor adsorption on the steel surface was confirmed by EDS and FTIR measurements. It is expected that this work develops an intelligent coating technology with the ability to smart sense the corrosion occurrence and self-release the pre-loaded inhibitors on demand for corrosion control in practice.

6.2 Experimental

6.2.1 Materials and chemicals

Steel specimens used in this work were cut from a X65 steel pipe, with a chemical composition (wt.%): C 0.04%, Si 0.2%, Mn 1.5%, P 0.011%, S 0.003%, Mo 0.02% and Fe balance. The specimens were cut into 1 cm × 1 cm area, sealed in epoxy, and subsequently ground up to 800 grit SiC emery papers. They were then washed with deionized water, degreased with ethanol and acetone, and dried in air. The SiO_2 nanoparticles with a purity of 98+% were purchased from U.S. Research Nanomaterials,

Inc., with an average diameter of 70 nm in the as-received state. They were amorphous in structure.

Corrosion inhibitors BTA were analytical grade. The BTA, i.e., $C_6H_5N_3$, is a heterocyclic chemical compound containing three nitrogen atoms, with the molecular structure shown in Fig. 6.1a. Various chemicals used in this work, including sodium poly-(styrene sulfonate) (SPSS, molecular weight M_w ~ 70000) and poly-(diallyldimethylammonium chloride) (PDDAC, M_w ~ 100–200 kDa), were also analytic grade. Their molecular structures are shown in Fig. 6.1a. The water used to prepare solutions was deionized water.

6.2.2 Fabrication of BTA-encapsulated nanocontainers

To fabricate BTA-encapsulated nanocontainers, 10 wt.% of as-received SiO_2 nanoparticles (negatively charged) were added in deionized water containing 1.5 wt.% BTA (pH=3) under a continuous stirring using an electrical blender to make a suspension solution. In order to improve the dispersion of the SiO_2 nanoparticles, they were heated at 60 °C under stirring for 12 h. The resulting SiO_2 nanoparticles were then separated by centrifugation, and washed three times with deionized water.

The surface of SiO_2 nanoparticles was modified by a layer-by-layer deposition method in order to improve the adsorption of inhibitors BTA. A layer of positively charged PDDAC was deposited on the surface of the negatively charged SiO_2 nanoparticles in 2 mg/mL polyelectrolyte + 0.5 M NaCl solution for 15 min under stirring. The resulting materials were washed by centrifugation to remove loosely adsorbed polyelectrolytes. A layer of negatively charged polyelectrolyte was then

deposited in 2 mg/mL SPSS + 0.5 M NaCl solution for 15 min. The modified silica nanoparticles were added to BTA solution between steps of polyelectrolyte deposition. Alternating adsorptions were repeated until the final assembly, i.e., PDDAC/SPSS/(BTA/SPSS)$_2$ /PDDAC/SPSS, as shown in Fig. 6.1b, was prepared on the surface of SiO_2 nanoparticles to form the nanocontainers.

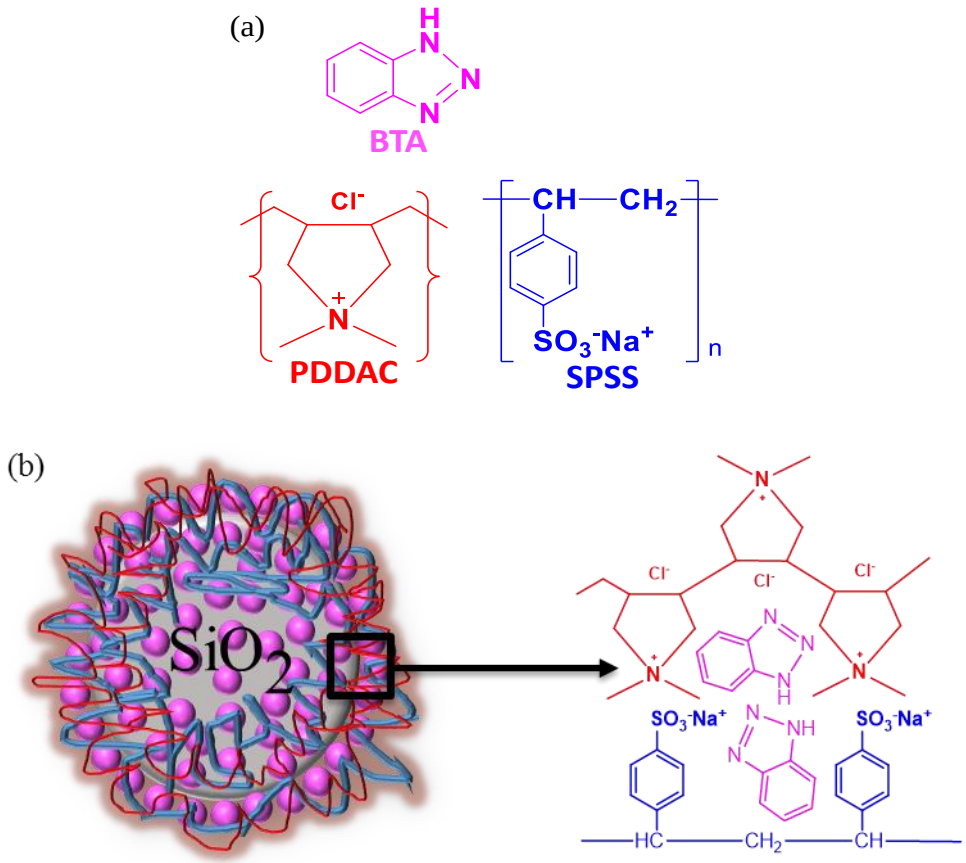

Fig. 6.1 Schematic diagram of (a) the molecular structure of inhibitor BTA and polyelectrolytes PDDAC and SPSS, and (b) the prepared SiO_2 nanoparticle based BTA-encapsulated polyelectrolyte nanocontainers.

It is noted that, while BTA is a neutral molecule, it, when dissolved in aqueous solutions, becomes charged. Generally, BTA exists in the form of protonated cations (i.e., $BTAH^+$) at pH < 8, or in deprotonated anionic species (i.e., BTA^-) at pH > 8. In this work, the BTA solution used to encapsulate the inhibitors on nano-SiO_2 surface was adjusted by HCl to pH 3 in order to increase the solubility of BTA. At this pH value, the BTA is in the form of $BTAH^+$, i.e., positively charged.

6.2.3 Characterization of the nanocontainers

A FTIR (Model Nicolet iS50) was used to characterize the functional groups and structure of the prepared nanocontainers. For all spectra recorded, the nanocontainer samples experienced a 64 scan data accumulation in the range of 600 cm^{-1} - 4000 cm^{-1} at a spectra resolution of 4.0 cm^{-1}.

In order to obtain the amount percentage of loaded BTA in nanocontainers, a TGA/DTG synchronization analyser was utilized to investigate the thermal stability of the nanocontainers under nitrogen atmosphere. The TGA/DTG was performed within the temperature range of 30 ^oC – 600 ^oC using a PerkinElmer STA 6000 at a heating rate of 20 ^oC/min in nitrogen atmosphere. The amount of the loaded BTA inhibitors in the nanocontainers was measured during thermal decomposition of BTA at high temperatures.

The morphology and elemental composition of the nanocontainers, as well as the as-received SiO_2 nanoparticles were characterized by SEM and EDS.

6.2.4 Preparation of nanocontainer-doped intelligent coatings

A liquid epoxy coating, which has been a commonly used pipeline coating in practice, was supplied by Canusa-CPS, Canada. The coating is a type of non-solvent epoxy composite coating, and can be cured at room temperature. The coating contains 30~60% pigments and other hydrocarbon resins, with varied contents of the prepared nanocontainers doped in this work. The nanocontainers were mixed in the resin, while kept stirring for 10 min. The hardener was then added to the mixture under stirring for 2 min. The processed coating was applied on the ground X65 steel surface, as shown in Fig. 6.2. The coated steel specimen was kept at room temperature for 5 days to allow a full curing, with a dry-film thickness of about 110 μm.

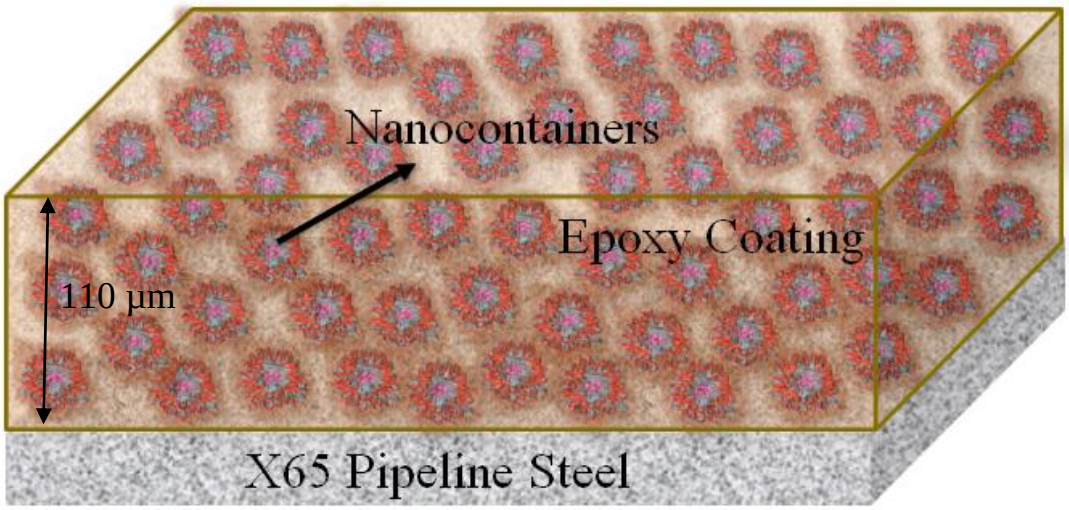

Fig. 6.2 Schematic diagram of the nanocontainer doped intelligent epoxy coating processed in this work.

6.2.5 Characterization of the prepared coatings and coated steel specimens

The dispersion of the nanocontainers doped in the epoxy coating matrix was characterized by SEM and EDS. The molecular structure of the processed intelligent coating, which was applied on X65 steel (1 cm x 1 cm in area, the most commonly used size of coated steel specimens for lab study), was characterized by FTIR before and after 30 days of immersion in 0.1 M NaCl solution. The glass-transition temperatures (T_g) of the coating, with various contents of nanocontainers, was measured by DSC (PerkinElmer STA 6000) at a heating rate of 20 °C/min under the nitrogen atmosphere. The T_g of the coating was determined as the inflection temperature from the endothermic peak in the DSC curve.

The UV-vis spectroscopy (Shimadzu UV-1800 spectrometer) was used to characterize the self-releasing of encapsulated BTA from the nanocontainers, and determine the specific solution pH conditions to trigger the inhibitor-releasing. For the purpose, 0.5 g prepared nanocontainers with BTA encapsulation was added in 10 mL NaCl solution (0.1 M) to make a suspension. The solution pH was adjusted to 2, 5, 7, 9 and 11 by dropping HCl and NaOH solutions, respectively. The amount of released BTA from the nanocontainers to the solution as a function of time was measured by the UV-vis spectroscopy.

6.2.6 EIS measurements

In this work, the EIS technique was used for measurements and evaluation of corrosion resistance of the coated steel specimens. The main reasons include that EIS is a non-destructive method, and does not disturb the measured specimen. It is thus very

suitable for continuous measurements over a long-term period. Moreover, the EIS is a good technique for measurements of a high-impedance system, such as the coated steel specimen. In addition to corrosion resistance of the specimen, the EIS can provide more information on the coating film.

The corrosion resistance of the intelligent coating with addition of varied contents of BTA-encapsulated nanocontainers was studied by EIS measurements in 0.1 M NaCl solution on a three-electrode cell, where the coated X65 steel specimen was used as working electrode, a platinum wire as counter electrode and a saturated calomel electrode (SCE) as reference electrode. The EIS measurement was conducted over a frequency range from 10 kHz to 0.01 Hz, with a disturbance AC voltage of 50 mV. Each test was performed at least three times to ensure the reproducibility of the results. The electrochemical impedance parameters were fitted with appropriate equivalent circuits using the ZSimpWin software.

To ensure the reproducibility of testing results, all tests were conducted on at least three parallel specimens.

6.3 Results and discussion

6.3.1 Morphology and composition of as-received SiO_2 nanoparticles and the prepared BTA-loaded nanocontainers

Fig. 6.3 shows the SEM images (at two magnifications) of as-received SiO_2 nanoparticles and the prepared SiO_2 based polyelectrolyte nanocontainers, respectively. It is seen that, while the as-received SiO_2 nanoparticles feature with an amorphous, spherical shape with a rough texture (Fig. 6.3a and c), the prepared SiO_2 based

polyelectrolyte nanocontainers are globularly shaped, with a smooth surface, as shown in Fig. 6.3b and d. The SiO_2 nanoparticles serve as carrier, and the inhibitors BTA are wrapped in the polyelectrolytes, with a homogenous surface morphology. As the as-received silica nanoparticles possess an amorphous and rough surface texture, the nanoparticles aggregate easily to form big particles, as shown in Fig. 6.1c. While attempts have been made to separate the SiO_2 nanoparticles by heating at 60 ^oC under stirring for 12 h, it is still possible that each silica nanoparticle cannot be deposited individually.

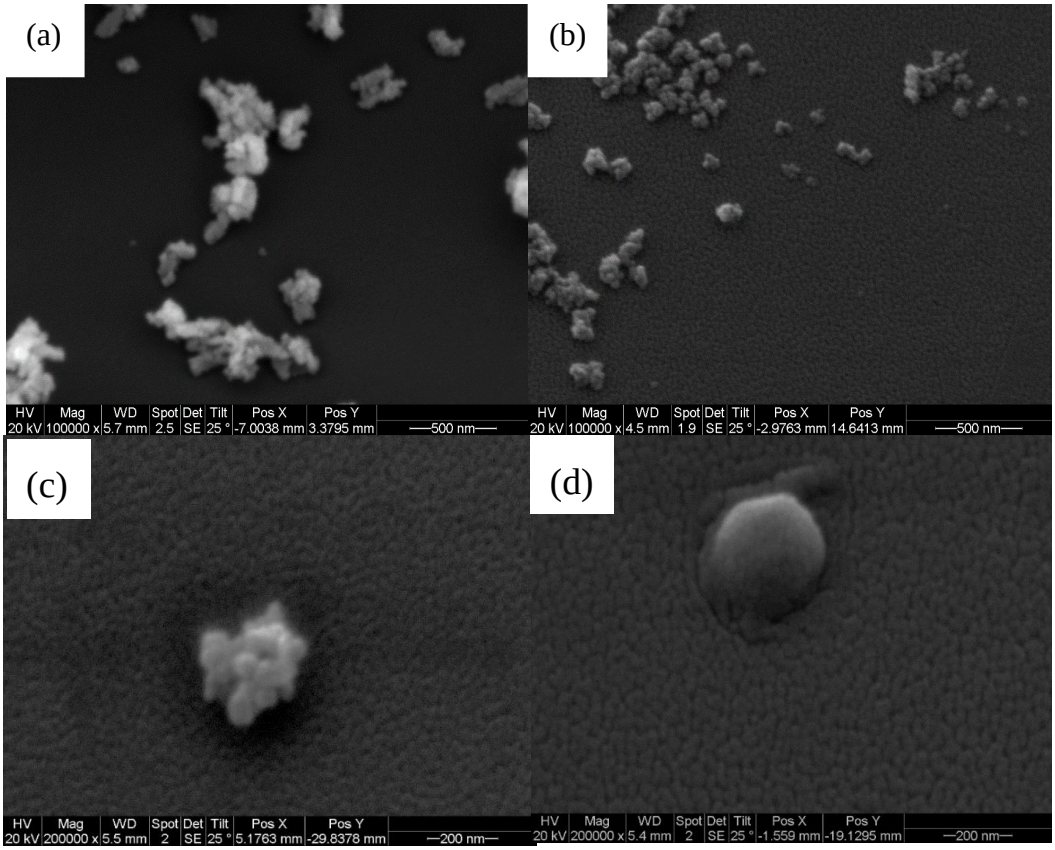

Fig. 6.3 SEM images of (a, c) as-received SiO_2 nanoparticles and (b, d) the prepared SiO_2 based polyelectrolyte nanocontainers, respectively.

The EDS results obtained on as-received SiO_2 particles and the prepared BTA-encapsulated nanocontainers are shown in Table 6.1. It is seen that elements Si, O, C and N are identified, where the elements Si and O are from SiO_2 nanoparticles. Compared to the elemental composition of the as-received SiO_2 nanoparticles, there is an obvious increase of the atomic weight of elements C and N in the nanocontainers. While element C is from the polyelectrolytes, the N elements are from the inhibitors BTA. The EDS results indicate that inhibitors BTA are encapsulated in the prepared nanocontainers.

Table 6.1 EDS results (weight percentage, %) obtained on as-received SiO_2 particles and the prepared BTA-encapsulated nanocontainers.

	C	N	O	Si
As-received SiO_2	9.29	1.84	32.39	56.48
Prepared BTA-encapsulated nanocontainers	21.06	5.76	57.33	15.85

6.3.2 FTIR analysis of BTA-encapsulated nanocontainers

Fig. 6.4 shows the FTIR spectra of the as-received SiO_2 nanoparticles and the prepared BTA-encapsulated nanocontainers, respectively. The characteristic functional groups identified are listed in Table 6.2, where the reference sources for all the bonds are also included. It is seen that, for both spectra, the characteristic peaks for SiO_2 are associated with stretching and bending vibrations of Si-O-Si bonds at 1090 cm^{-1} and 817 cm^{-1}, respectively. In the spectrum obtained from the BTA-encapsulated nanocontainers, the peak at 1209 cm^{-1} is from the vibration of typical triazole rings contained in inhibitors

BTA. The low-intensity peak at 1038 cm^{-1} and a considerable intensity peak at 1626 cm^{-1} are attributed to N-H stretching vibration.

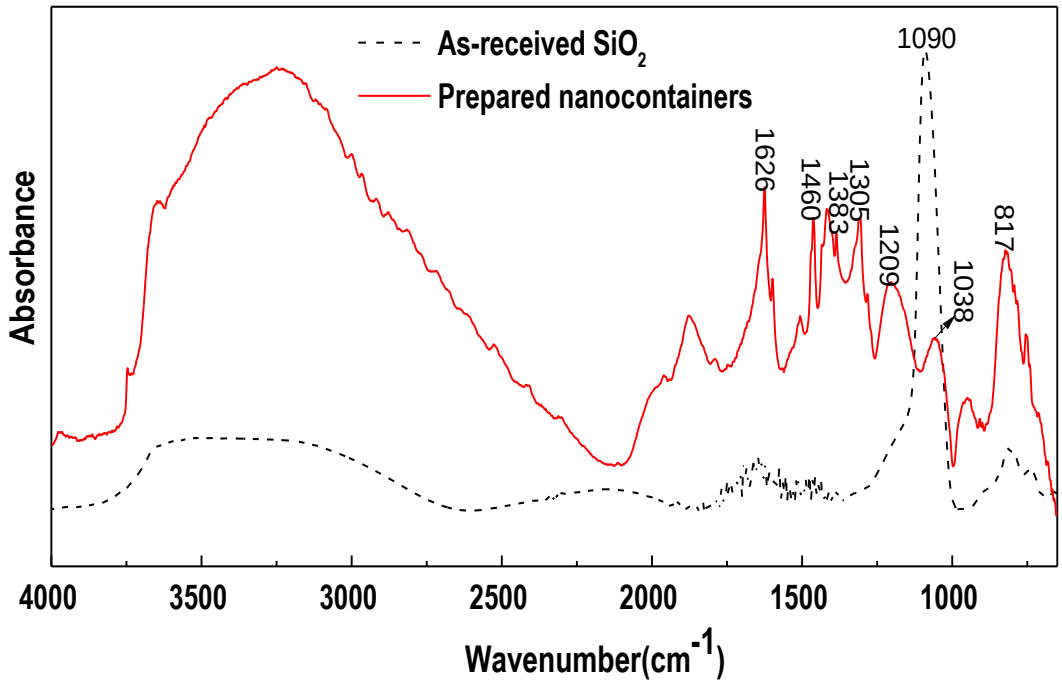

Fig. 6.4 FTIR spectra of the as-received SiO_2 nanoparticles and the prepared BTA-encapsulated nanocontainers, respectively.

By comparison with the spectrum for SiO_2 nanoparticles, the spectrum for the nanocontainers contains peaks with a considerable intensity at 1305 cm^{-1} and 1460 cm^{-1}, which are due to C-N stretching vibration from the C-N functional groups contained in inhibitors BTA and positively charged polyelectrolyte PDDAC. The peak at 1383 cm^{-1} can be clearly seen in nanocontainers' spectrum, and is attributed to the C-H deformation absorption of the polyelectrolytes deposited on the surface of SiO_2 nanoparticles. The

broad bond at 3300 cm^{-1} ~ 3600 cm^{-1} is due to hydrogen bonds of O-H and N-H, which are from the interactions between SiO_2 nanoparticles and the polyelectrolytes and inhibitors BTA. Obviously, the FTIR measurements demonstrate that inhibitors BTA are encapsulated in the prepared nanocontainers.

Table 6.2 Characteristic peaks identified in FTIR spectra in Fig. 6.4.

Peaks (cm^{-1})	Characteristic bonds	Ref.
817	Si-O-Si bending vibration	[119]
1038	N-H stretching vibration	[89]
1090	Si-O-Si stretching vibration	[33]
1209	-N=N-N- breathing vibration	[120]
1305, 1460	C-N stretching vibration	[115, 150]
1383	C-H deformation absorption	[60]
1626	N-H stretching vibration	[121]
3300-3600	Hydrogen bands O–H, N–H, and C–H	[122, 123]

6.3.3 Thermal stability of the BTA-encapsulated nanocontainers

The thermal stability of the prepared nanocontainers and the loaded amount of BTA inhibitors in the nanocontainers are characterized by TGA and DTG, and the results are shown in Fig. 6.5**.** It is seen that the weight lost rate of SiO_2 nanoparticles keeps approximately consistent when temperature is elevated to 600 ^oC. Obviously, the SiO_2 particles have an excellent thermal stability up to 600°C, and the weight loss is 0.18% only. Different from the spectrum obtained on SiO_2 nanoparticles, there are three stages of weight loss for the BTA-encapsulated nanocontainers, as shown in Figs. 6.5a and 6.5b. In stage one from ambient temperature (about 30 ^oC) to 120 ^oC, nearly 0.99% weight loss

occurs, which is attributed to the loss of remaining water in the nanocontainers. Thus, nanocontainers tend to absorb water during polyelectrolyte deposition and inhibitor-loading, which is consistent with the presence of the broad FTIR peak from 3000 cm^{-1}-3600 cm^{-1} in Fig. 6.4. Stage two is from 120 ^{o}C to 250 ^{o}C, where a weight loss of 6.70% occurs due to the thermal decomposition of the loaded inhibitors BTA. The melting and boiling points of BTA are 98.5 ^{o}C and 204 ^{o}C, respectively. When the temperature reaches 250 ^{o}C, the encapsulated BTA is decomposed completely. The maximum decomposition rate is at about 200 ~ 210 ^{o}C (Fig. 6.5b). In stage three from 250 ^{o}C to 550 ^{o}C, the 2.07% weight loss is due to degradation of the polyelectrolyte backbone. Thus, the weight percentage of the encapsulated inhibitors BTA are about 6.70% in the nanocontainers determined by the thermal stability test.

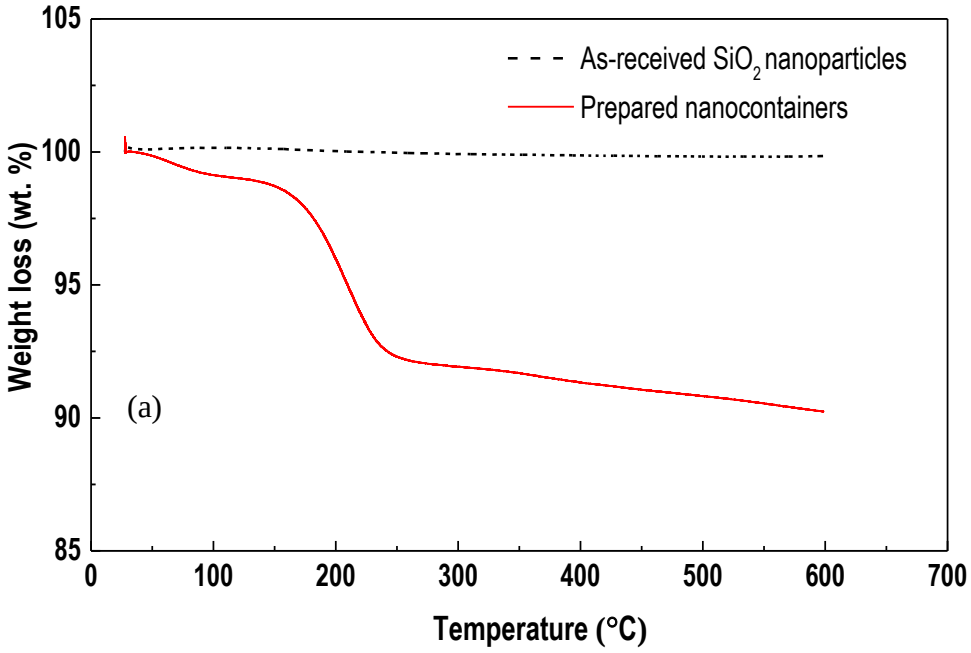

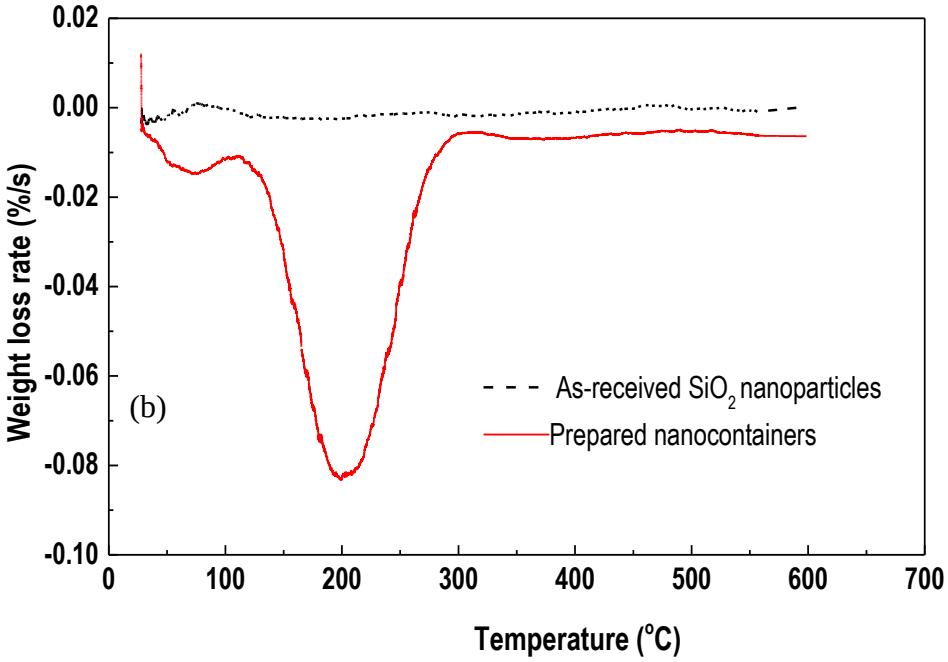

Fig. 6.5 (a) TGA curves of as-received SiO_2 nanoparticles and the prepared BTA-encapsulated nanocontainers, and (b) their DTG spectra.

6.3.4 Dispersity of the doped nanocontainers in the epoxy coating matrix

The SEM views of the epoxy coating without and with doping of various contents of nanocontainers are shown in Fig. 6.6, where the compositional mapping of element Si is also given to sever as the indicator for the doping of the prepared SiO_2 nanoparticle based nanocontainers in the host coating. It is seen in Fig. 6.6a that the as-received epoxy coating is smooth in surface, but contains micro-cracks. The detected Si elements are mainly from the quartz contained in the coating. It was reported [96] that deposition of polyelectrolyte layers not only encapsulates the corrosion inhibitors, but also improves the dispersity of nanocontainers in the coating. Upon doping of the prepared nanocontainers, the surface morphology of the coating is changed obviously. There is no

micro-crack observed in the doped coatings. This is because the polyelectrolyte layer of the nanocontainers has a good cohesion with epoxy coatings. As the doped content of the nanocontainers increases, the Si content detected increases, as shown in Figs. 6.6d, 6.6f and 6.6h. More important, the Si element mapping shows that the nanocontainers distribute uniformly in the epoxy matrix, especially at the high doping content such as 8wt.% of the nanocontainers. The results demonstrate that this work enables a relatively uniform distribution of the BTA-encapsulated nanocontainers in the coating matrix to process the intelligent coating.

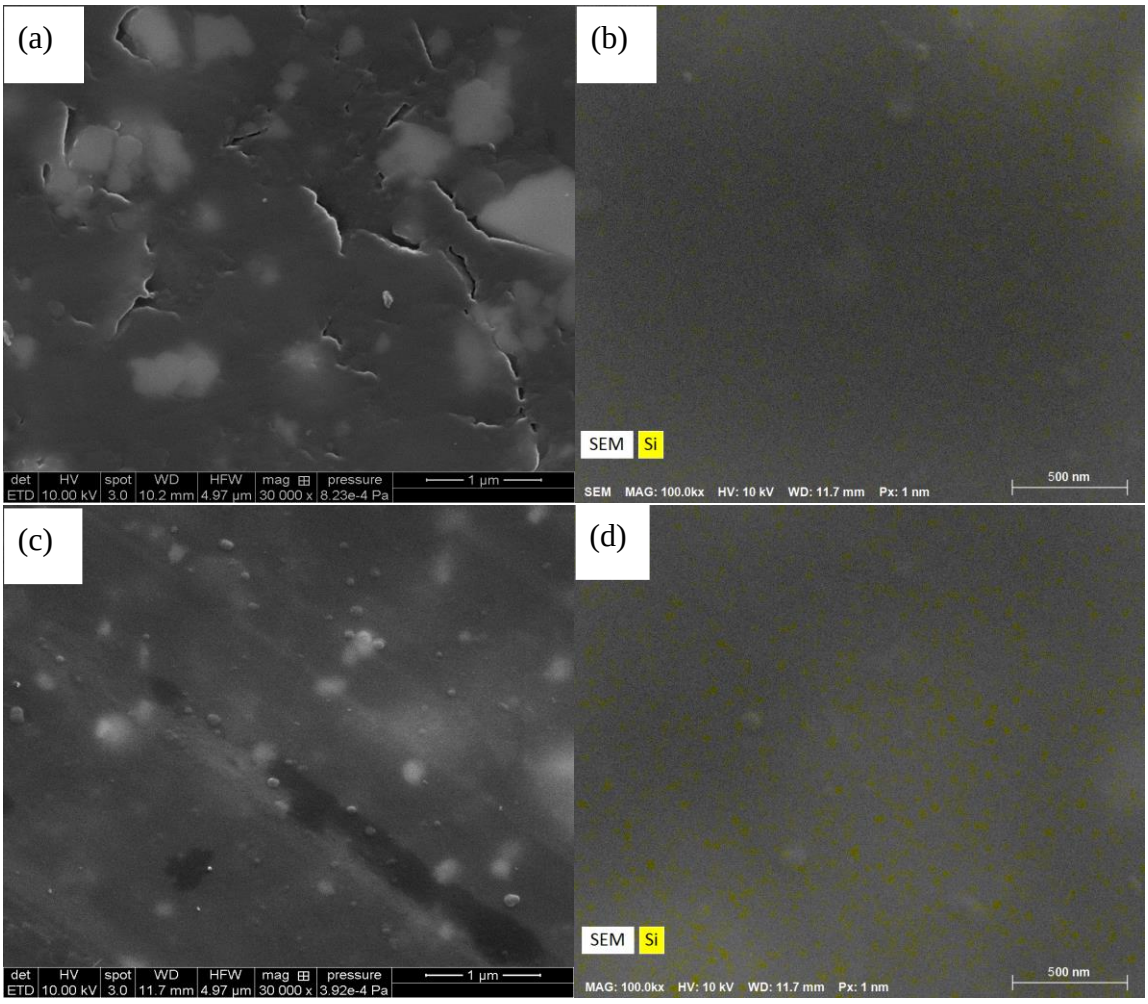

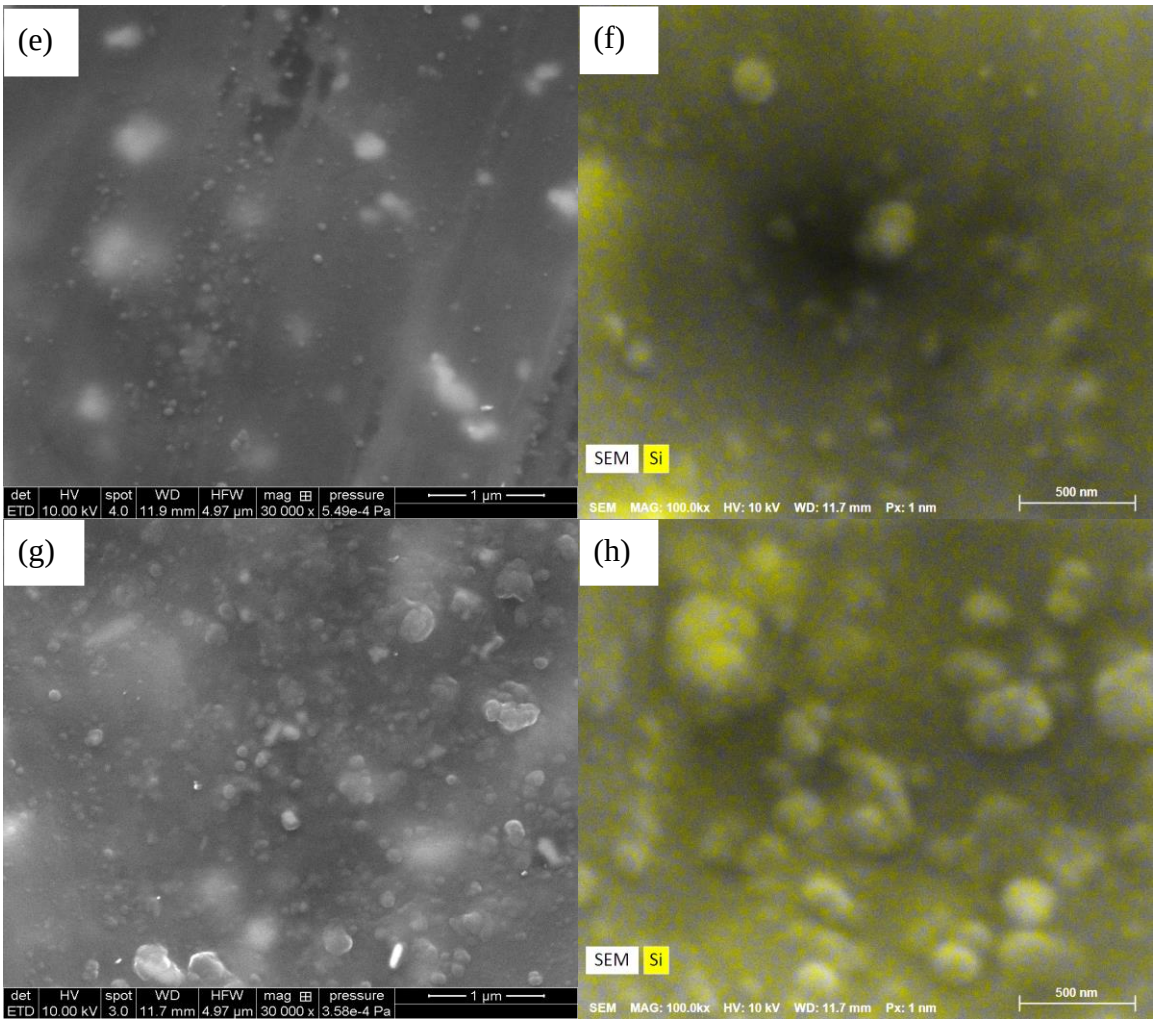

Fig. 6.6 SEM views of the epoxy coating without and with doping of various contents of nanocontainers, and the compositional mapping of element Si in the coatings (a, b) no nanocontainers added, (c, d) 2 wt.%, (e, f) 5 wt.%, (g, h) 8 wt.%.

6.3.5 Thermal stability of the nanocontainer doped epoxy coatings

Fig. 6.7 shows the thermal weight loss curves of the processed epoxy coatings doped with varied contents of the prepared nanocontainers. It is seen that all measured curves almost copy each other due to the small weight percentages of the doped nanocontainers

in the epoxy coating. However, it is still visible that there is a slightly larger weight loss for nanocontainer-doped coatings than the undoped one. The small weight loss observed for doped coatings up to 300 ^{o}C is mainly due to decomposition of the encapsulated BTA inhibitors in the nanocontainers, as confirm in Fig. 6.5. As the weight of the loaded inhibitors is much smaller than that of the coating itself, the weight-change difference among the coatings is so small that it is not distinguishable. The big weight loss for all coatings from 300 ^{o}C to about 500 ^{o}C is due to cleavage of epoxy resin chains in the coating skeleton. The maximum thermal decomposition temperature is 360 ^{o}C - 370 ^{o}C as seen in Fig. 6.7b. The deposited polyelectrolytes decompose in this temperature range, but the weight of the polyelectrolytes is much smaller than that of the epoxy coating. After 500 ^{o}C, the remaining weight is mainly from pigments and other additives in the coating matrix [151].

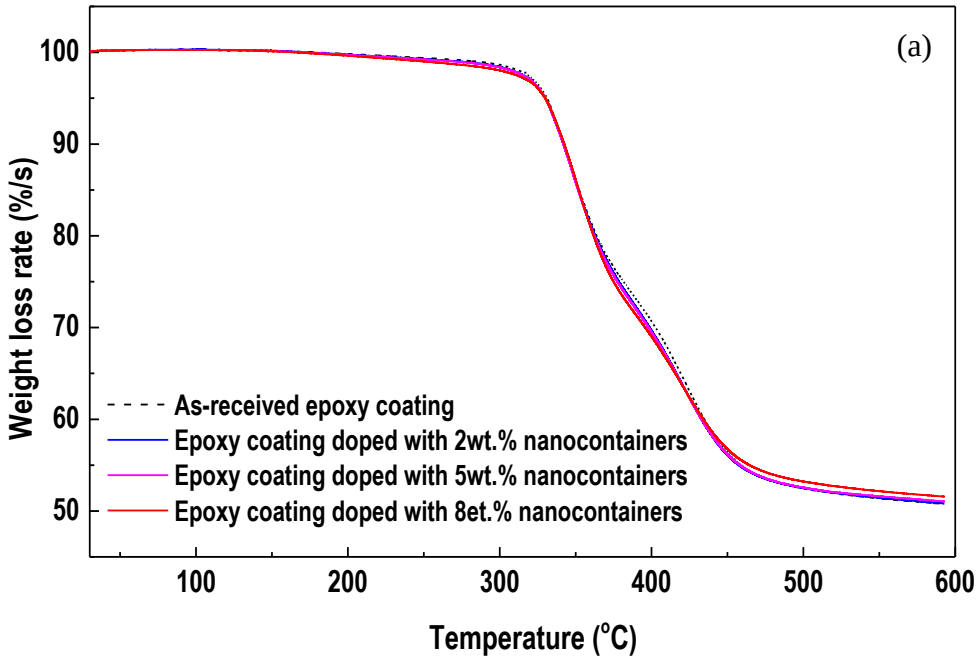

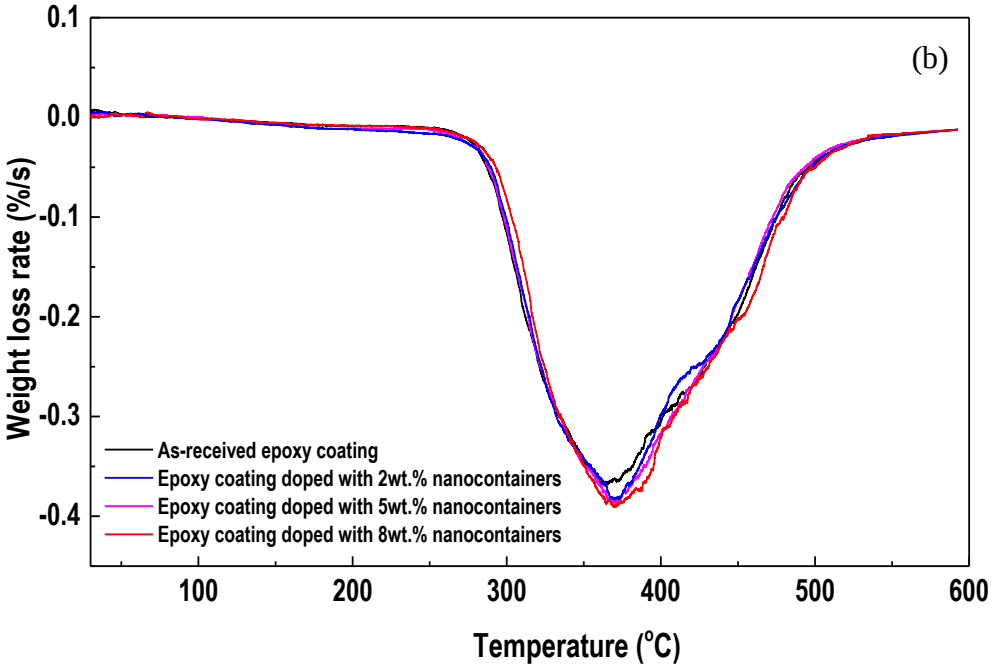

Fig. 6.7 (a) The TGA curves of the processed epoxy coatings doped with varied contents of the prepared nanocontainers, (b) the derived DTG curves.

Furthermore, DSC was used to examine the cross-linking property of the nanocontainer-doped epoxy coatings, and the results are shown in Fig. 6.8. It is seen that both undoped and doped coatings have an identical glass-transitional temperature, T_g, which is about 200 °C. Thus, the addition of the nanocontainers would not change the chemical cross-linking structure of the epoxy coating.

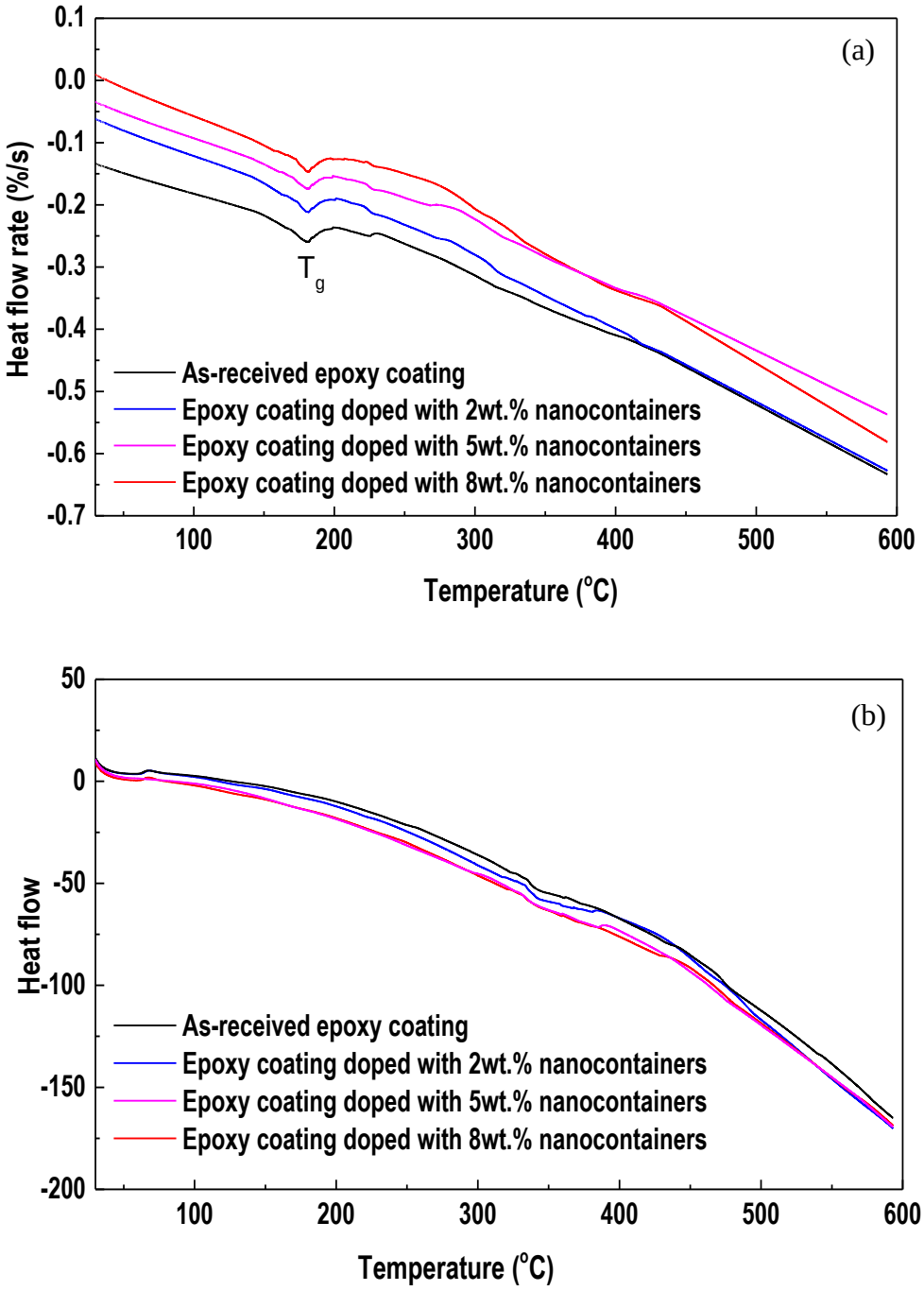

Fig. 6.8 (a) DSC curves of the epoxy coatings doped with varied contents of nanocontainers, and (b) the derivative spectra.

6.3.6 Measurements of self-releasing of the encapsulated BTA in response to solution pH

Figs. 6.9 show the UV-vis spectra of the BTA-encapsulated nanocontainers after 1 h and 1 day of immersion in 0.1 M NaCl solutions with various pH values, respectively. It is seen that the inhibitor-releasing is time dependent. After 1 h of immersion, the spectra measured in all solutions almost copy each other. The peaks at 260 nm and 273 nm wavelengths, which are attributed to the presence of BTA in the solution, have approximately identical intensity, as seen in Fig. 6.9(a). After one day of immersion of the nanocontainers in the solution, the absorbance peak intensities measured in different solutions change remarkably. Generally, the intensity of the bond at BTA peak position is primarily influenced by the amount of BTA in the solution. A higher peak indicates the higher concentration of BTA contained in the solution [152, 153]. It is seen from Fig. 6.9(b) that there is a slight increase in the absorbance peak when the solution pH is 7. However, for solution pH of 2 and 11, the absorbance intensities increase obviously, indicating that the BTA selectively release from the nanocontainers at these pH environments. When the solution pH is 5 or 9, the BTA absorbance intensity is in between.

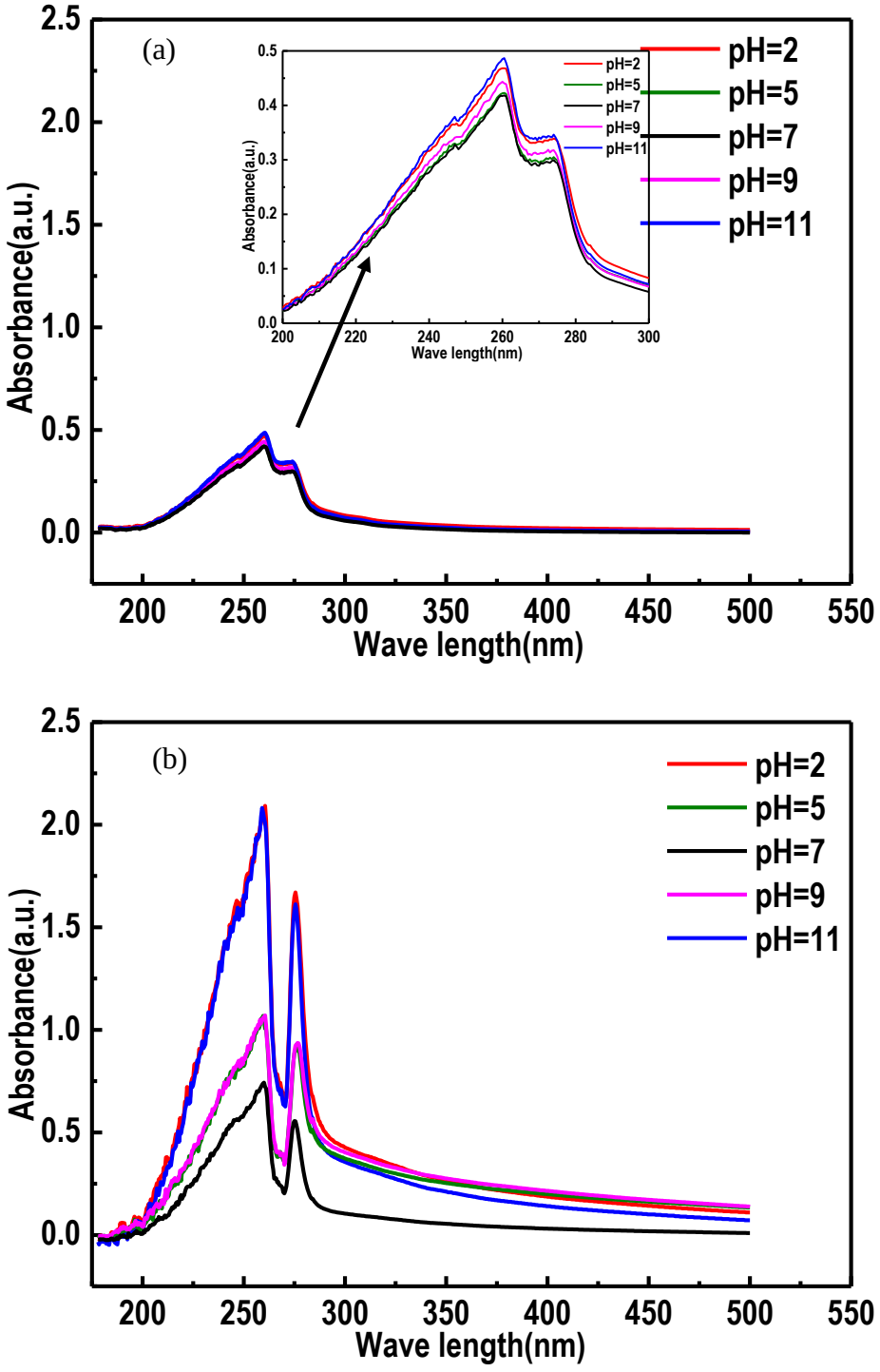

Fig. 6.9 UV-vis spectra of the BTA-encapsulated nanocontainers after (a) 1 h and (b) 1 day of immersion in 0.1 M NaCl solutions with various pH values.

6.3.7 Corrosion resistance of the epoxy coatings doped with BTA-loaded nanocontainers

Fig. 6.10 shows the time dependence of OCP of the steel electrode coated with epoxy coatings without and with various contents of BTA-encapsulated nanocontainers in 0.1 M NaCl solution. It is seen that, initially, the OCP of all specimen is relatively positive, and is between 0.1 V (SCE) and 0.15 V (SCE). As time increases, the OCP decrease gradually. After 14 days of testing, the OCP drops rapidly to about -0.1 V (SCE). For the specimen coated with the undoped epoxy coating, the OCP continues to decrease and reaches a relatively steady value of -0.2 V (SCE) after 26 days of immersion in the solution. For the epoxy coating containing 2 wt.% BTA encapsulated nanocontainers, the OCP of the coated steel also deceases after 14 days of immersion in the solution, but the relatively stable value of about -0.16 V (SCE) is less negative than that for the undoped coating. When the amount of the doped nanocontainers in the coating increases to 5 wt.% and 8 wt.%, the OCP shifts positively after the 14 days of immersion. The stable values after 26 days of testing in the solution are about -0.09 V (SCE) and 0.11 V (SCE), respectively. Obviously, the steady-state OCP of the coated steel becomes more positive as the amount of the nanocontainers doped in the coating increases. Similar results for coated metal specimens' coatings doped with inhibitor-loaded nanocontainers were also reported by other researchers [154]. This phenomenon is attributed to the ability of the coating to sense the generation of corrosive environments on the steel due to water permeation through the coating during exposure to the solution, and self-release the pre-loaded BTA from the nanocontainers after 30 days of immersion. The inhibitor-releasing can be triggered by the change of the electrolyte pH on the steel surface [42, 102, 110,

155], as determined above. The released inhibitors are able to form a protective adsorptive film on the steel surface, enhancing the corrosion resistance of the steel, as indicated by the positive shift of OCP of the steel with the increasing amount of the nanocontainers doping the coating [146, 156].

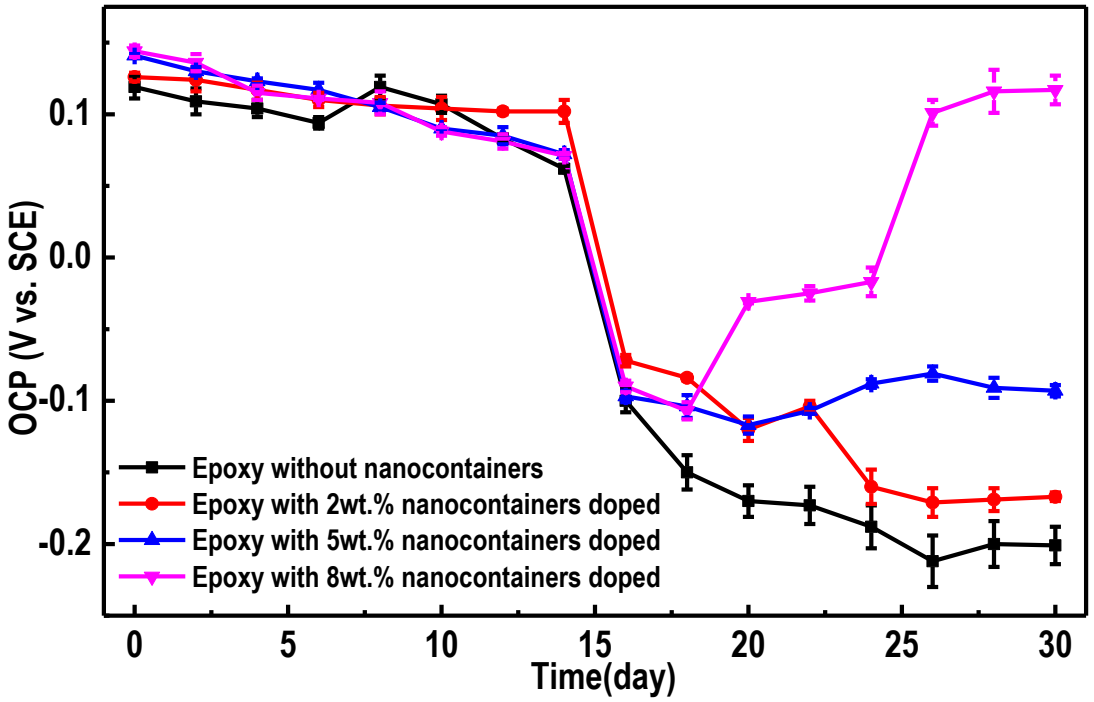

Fig. 6.10 Time dependence of OCP of the steel electrode coated with epoxy coatings without and with various contents of BTA-encapsulated nanocontainers in 0.1 M NaCl solution.

Fig. 6.11 shows the Bode plots (both impedance modulus and phase angle) measured on the steel electrode coated with epoxy coatings doped with various contents of BTA-encapsulated nanocontainers after 6, 12, 18, 24 and 30 days of immersion in 0.1 M NaCl

solution at 60 ^{o}C. It is seen that, for the undoped coating, a high low-frequency impedance of over 10^9 Ω cm^2 is observed after 6 days of immersion in the solution, with one maximum phase angle. This is typical of the capacitive behavior for a coated steel electrode, where the coating serves as an effective barrier to protect the steel from corrosion at this time. With the increase of the immersion time, the low-frequency impedance decreases due to water uptake by the coating. At the 18th day, the low-frequency impedance is about 3×10^7 Ω cm^2, and another maximum phase angle is observed between 0.1 Hz and 1 Hz. This indicates that, in addition to the impedance response from the coating, corrosion occurs on the steel surface. With the time increasing to 24 and 30 days, the low-frequency impedance further decreases due to the coating degradation with time. The low-frequency phase angle maximum becomes more apparent compared to that at the 18th day.

When the epoxy coating contains BTA-encapsulated nanocontainers, the measured Bode plots show the similar feature to that in the absence of nanocontainers in the coating. In the first 12 days, a capacitive impedance behavior is observed, and the coating is able to protect the steel from corrosion. At day 18, the doped coatings start to lose their protective ability, as shown by the reduced low-frequency impedance with time. For the coating doped with 2 wt.% nanocontainers, the low-frequency impedance further decreases as the immersion time increases to 24 days. However, the low-frequency impedance measured at the 30th day becomes higher than that measured at the 24th day, as seen in Fig. 6.11c, which is different from that obtained in the undoped coating in Fig. 6.11a. The same phenomenon is also observed for the coating doped with 5wt.% nanocontainers in Fig. 6.11e. The difference is that the low-frequency impedance

measured at the 30th day for 5 wt.% nanocontainer doped coating is higher than that for 2 wt.% nanocontainer doped coating. When the doped nanocontainers are increased to 8 wt.% in the epoxy coating, the low-frequency impedance measured at the 24th day is higher than that measured at the 18th day. With the immersion time increasing to 30 days, the low-frequency impedance further increases, as seen in Fig. 6.11g.

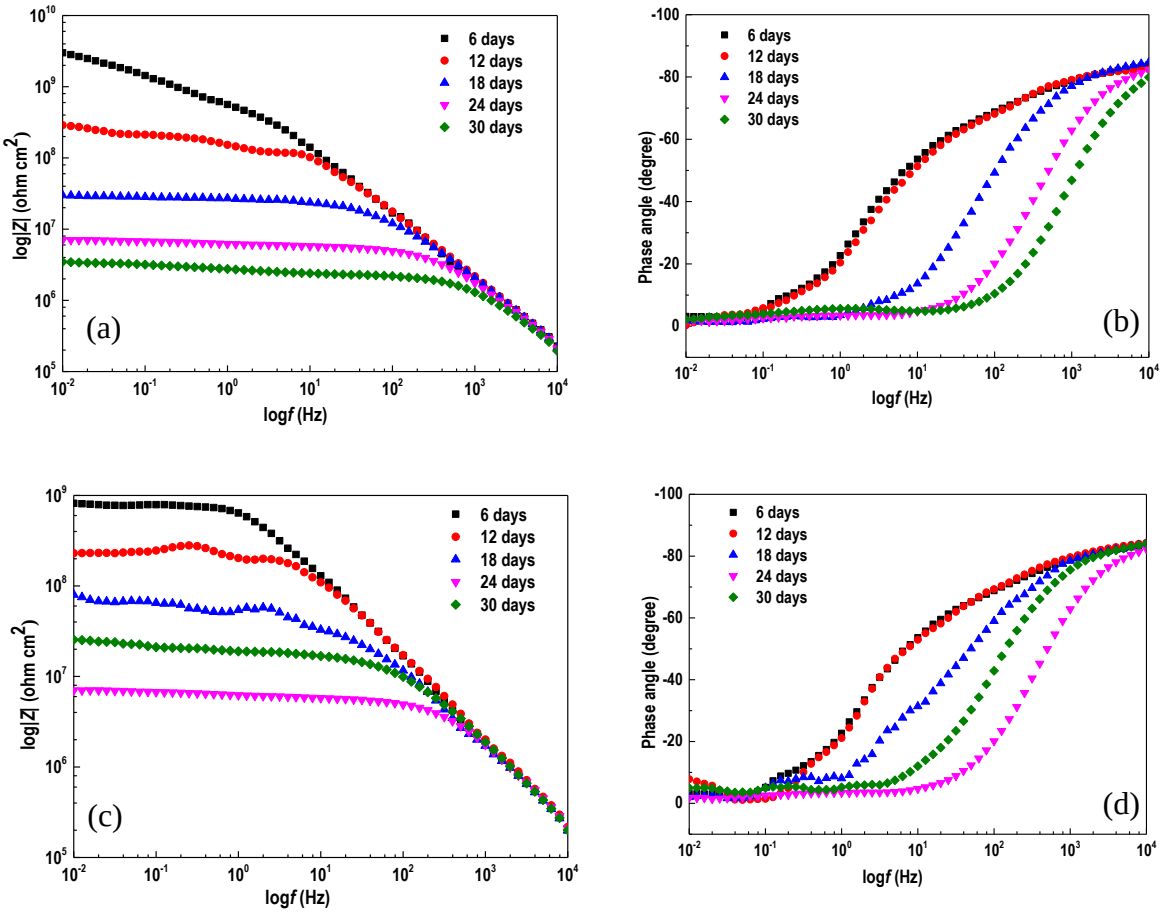

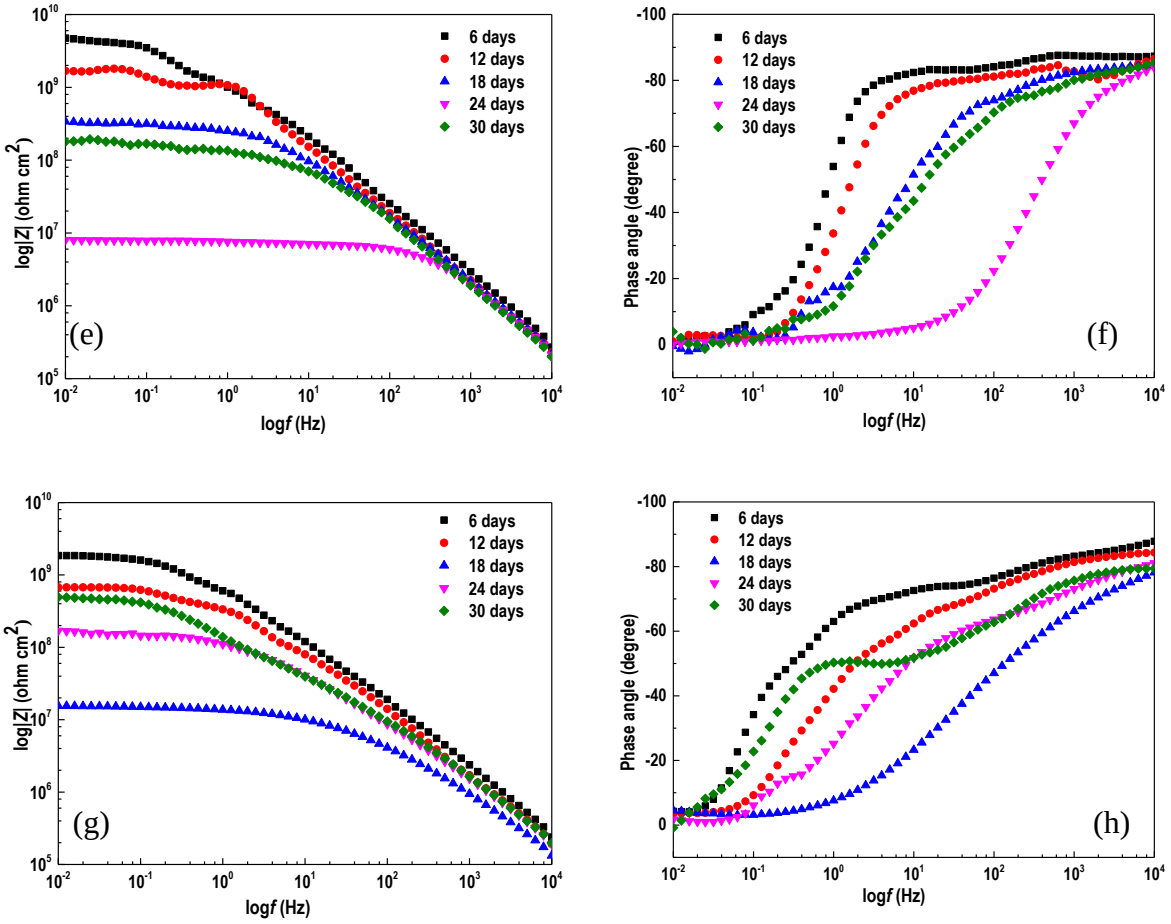

Fig. 6.11 Bode plots, i.e., both impedance modulus (a, c, e, g) and phase angle (b, d, f, h) measured on the steel electrode coated with the epoxy coating doped with various contents of BTA loaded nanocontainers after 6, 12, 18, 24 and 30 days of immersion in 0.1M NaCl solution at 60 ºC (a, b) no doped nanocontainer, (c, d) 2wt.%, (e, f) 5wt.%, (g, h) 8wt.% nanocontainers.

To derive electrochemical impedance parameters for various coated steel electrodes, the measured impedance data are fitted with appropriate equivalent circuits, as shown in Fig. 6.12, where R_{sol}, R_{ct}, $R_{c,}$ Q_{dl} and Q_c are solution resistance, charge-transfer resistance,

coating resistance, constant-phase element of double-charge layer and constant-phase element of the coating, respectively. The equivalent circuits in Figs. 6.12a and 6.12b are chosen to fit the impedance plots with one and two time constants, respectively. To determine appropriate circuits for fitting the measured impedance data, in addition to EIS, the time dependence of OCP of the coated steel specimen is also used for corrosion analysis. It is seen in Fig. 6.10 that, in the first 14 days, the OCP of all specimen maintains at relatively positive values.

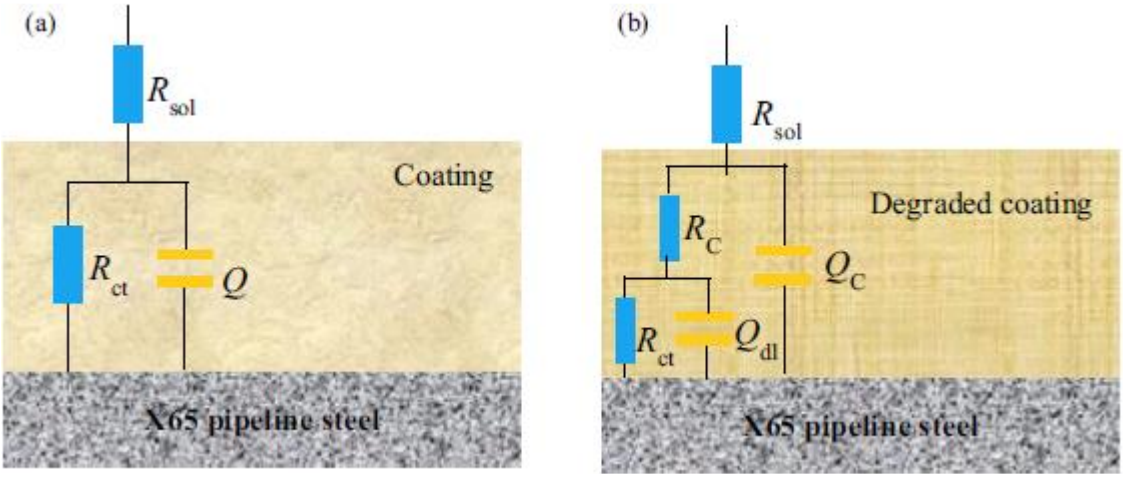

Fig. 6.12 Electrochemical equivalent circuits used to fit the measured impedance data, where R_{sol}, R_{ct}, R_c, Q_{dl} and Q_c are solution resistance, charge-transfer resistance, coating resistance, constant-phase element of double-charge layer and constant-phase element of the coating, respectively (a) for one time constant impedance plots, and (b) for two time constant impedance plots.

In the first 12 days, there is only one time constant, as indicated by one maximum phase angle in Fig. 6.11, for the measured impedance spectra. After 16 days of

immersion, the measured impedance plots are associated with two time constants due to the low frequency charge-transfer reaction and the high frequency response from the coating. The results show that, prior to 14 days of immersion, corrosion of the coated steel is marginal, and the coating is considered protective. Although the slope of the impedance modulus changes around 0.1-1 Hz after 6 and 12 days (Fig. 6.11), the phase angle curves do not show obvious changes. It is thus assumed that, while the coating is permeable to water at these times, corrosion is yet to occur and the circuit with one time constant is used for the impedance fitting. Thus, in the first 12 days, the circuit with one time constant is used to fit the measured impedance spectra. After 16 days of immersion, the measured impedance plots are associated with two time constants due to the low frequency charge-transfer reaction and the high frequency response from the coating.

In this work, the constant-phase elements, *Q*, is used to model the capacitances of the coating and the double-charge layer in the equivalent circuits. This element usually describes the interfacial heterogeneity due to either localized corrosion or adsorption of reaction products and intermediates. The constant-phase element is related to an equivalent capacitance such as coating capacitance (C_c) and the capacitance of double-charge layer (C_{dl}), by [150, 157]:

$$C_x = (Q_x \times R_x^{1-n})^{1/n} \quad (6\text{-}1)$$

where C_x, Q_x, R_x and n are capacitance, constant-phase element, resistance (either R_{ct} or R_c) and the empirical exponent, respectively. The electrode closes to an ideal capacitor when the exponent n approaches to 1.

Table 6.3 The electrochemical impedance parameters fitted from the measured impedance data in Fig. 6.11.

Coatings	Time (day)	R_c (Ω cm^2)	Qc Y (Ω^{-1}cm^{-2}s^n)	n	C_c (F/cm^2)	R_{ct} (Ω cm^2)	Q_{dl} Y (Ω^{-1}cm^{-2}s^n)	n	C_{dl} (F/cm^2)
As-received epoxy coating	6	$4.48\pm0.66\times10^{9}$	$1.22\pm0.08\times10^{-10}$	0.80 ± 0.02	$1.05\pm0.12\times10^{-10}$				
	12	$2.37\pm0.21\times10^{9}$	$2.72\pm0.22\times10^{-10}$	0.85 ± 0.02	$2.51\pm0.32\times10^{-10}$				
	18	$1.52\pm0.15\times10^{8}$	$1.14\pm0.01\times10^{-8}$	0.80 ± 0.07	$1.29\pm0.01\times10^{-8}$	$2.94\pm0.16\times10^{6}$	$1.66\pm0.18\times10^{-9}$	0.87 ± 0.04	$1.07\pm0.03\times10^{-9}$
	24	$4.72\pm0.23\times10^{6}$	$1.52\pm0.12\times10^{-7}$	0.83 ± 0.01	$1.42\pm0.17\times10^{-7}$	$3.08\pm0.12\times10^{6}$	$2.02\pm0.06\times10^{-7}$	0.85 ± 0.04	$1.85\pm0.12\times10^{-7}$
	30	$2.23\pm0.16\times10^{6}$	$3.30\pm0.19\times10^{-7}$	0.88 ± 0.03	$3.15\pm0.27\times10^{-7}$	$3.12\pm0.04\times10^{6}$	$1.37\pm0.03\times10^{-5}$	0.97 ± 0.02	$1.55\pm0.01\times10^{-5}$
Coating doped with 2 wt.% nanocontainers	6	$5.16\pm0.47\times10^{9}$	$1.21\pm0.11\times10^{-10}$	0.80 ± 0.02	$1.07\pm0.16\times10^{-10}$				
	12	$9.43\pm0.85\times10^{8}$	$1.75\pm0.15\times10^{-10}$	0.80 ± 0.02	$1.12\pm0.21\times10^{-10}$				
	18	$4.99\pm0.19\times10^{7}$	$2.57\pm0.05\times10^{-8}$	0.80 ± 0.02	$2.73\pm0.07\times10^{-8}$	$2.26\pm0.07\times10^{7}$	$1.42\pm0.07\times10^{-7}$	0.81 ± 0.01	$1.86\pm0.10\times10^{-7}$
	24	$4.72\pm0.18\times10^{6}$	$1.58\pm0.14\times10^{-7}$	0.92 ± 0.01	$1.47\pm0.16\times10^{-7}$	$1.20\pm0.05\times10^{7}$	$2.33\pm0.06\times10^{-7}$	0.86 ± 0.04	$2.36\pm0.01\times10^{-7}$
	30	$5.04\pm0.15\times10^{6}$	$2.58\pm0.08\times10^{-7}$	0.87 ± 0.02	$8.25\pm0.01\times10^{-8}$	$8.17\pm0.36\times10^{7}$	$1.09\pm0.07\times10^{-7}$	0.87 ± 0.04	$1.50\pm0.01\times10^{-7}$
Coating doped with 5wt.% nanocontainers	6	$2.49\pm0.04\times10^{9}$	$7.19\pm0.11\times10^{-11}$	0.80 ± 0.02	$4.70\pm0.28\times10^{-11}$				
	12	$1.52\pm0.06\times10^{9}$	$7.28\pm0.43\times10^{-10}$	0.80 ± 0.02	$7.46\pm0.60\times10^{-10}$				
	18	$8.08\pm0.18\times10^{6}$	$9.90\pm0.64\times10^{-7}$	0.88 ± 0.06	$3.93\pm0.10\times10^{-8}$	$8.43\pm0.16\times10^{7}$	$1.20\pm0.03\times10^{-7}$	0.83 ± 0.01	$1.93\pm0.01\times10^{-7}$
	24	$2.32\pm0.05\times10^{7}$	$1.05\pm0.03\times10^{-8}$	0.88 ± 0.02	$8.67\pm0.63\times10^{-9}$	$2.94\pm0.08\times10^{8}$	$2.02\pm0.03\times10^{-8}$	0.95 ± 0.04	$2.27\pm0.16\times10^{-8}$
	30	$1.60\pm0.07\times10^{8}$	$2.71\pm0.25\times10^{-9}$	0.95 ± 0.01	$2.59\pm0.13\times10^{-9}$	$8.06\pm0.09\times10^{8}$	$4.36\pm0.24\times10^{-9}$	0.87 ± 0.03	$5.24\pm0.11\times10^{-9}$
Coating doped with 8wt.% nanocontainers	6	$2.36\pm0.08\times10^{9}$	$2.76\pm0.24\times10^{-11}$	0.80 ± 0.01	$1.41\pm0.14\times10^{-11}$				
	12	$1.86\pm0.05\times10^{9}$	$3.97\pm0.09\times10^{-10}$	0.80 ± 0.02	$3.67\pm0.16\times10^{-10}$				
	18	$1.39\pm0.07\times10^{7}$	$1.12\pm0.01\times10^{-8}$	0.80 ± 0.03	$7.01\pm0.73\times10^{-9}$	$1.56\pm0.04\times10^{7}$	$3.11\pm0.14\times10^{-8}$	0.85 ± 0.06	$2.73\pm0.13\times10^{-8}$
	24	$4.94\pm0.29\times10^{8}$	$1.29\pm0.07\times10^{-9}$	0.86 ± 0.02	$1.19\pm0.11\times10^{-9}$	$7.64\pm0.41\times10^{8}$	$1.09\pm0.01\times10^{-8}$	0.81 ± 0.06	$1.82\pm0.02\times10^{-8}$
	30	$9.19\pm0.30\times10^{8}$	$8.75\pm0.37\times10^{-10}$	0.81 ± 0.02	$8.31\pm0.55\times10^{-10}$	$4.11\pm0.10\times10^{9}$	$2.57\pm0.20\times10^{-9}$	0.87 ± 0.08	$3.72\pm0.05\times10^{-9}$

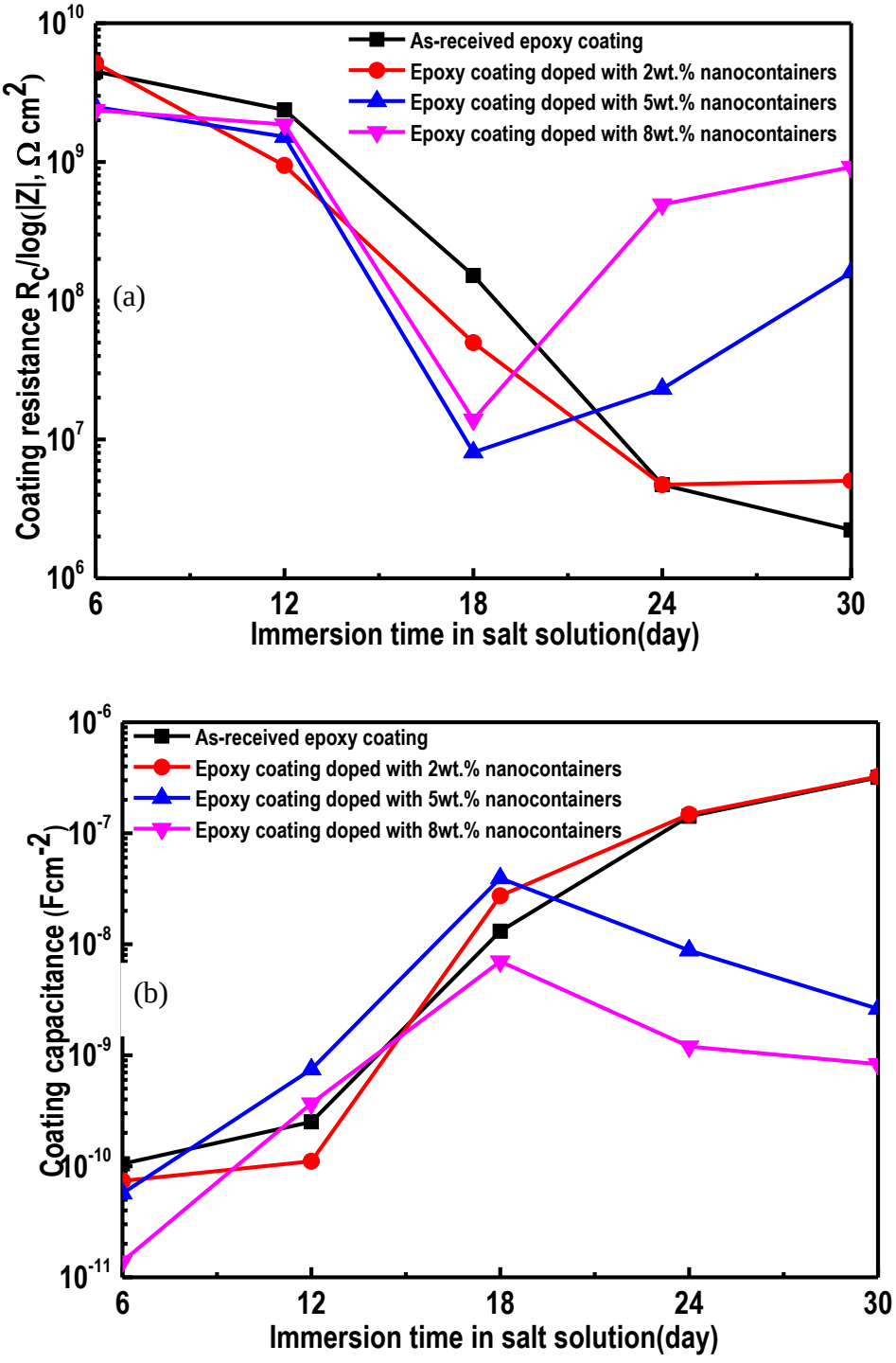

Fig. 6. 13 The fitting results of collected EIS data of different coating: (a) coating resistance, (b)coating capacitance.

Table 6.3 lists the fitted electrochemical impedance parameters from the measured impedance data in Fig. 6.11. The tendencies of coating resistance and coating capacitance as the immersion time increasing to 30 days are shown in Fig. 6.13. It is seen from Fig. 6.13 that, for undoped epoxy coating, the coating resistance R_c decreases and C_c increases with time, indicating the continuous degradation of the coating in the solution. The fitted charge-transfer resistance R_{ct}, which is inversely to corrosion rate of the steel, fluctuates around 3.00×10^6 Ω cm^2 when the coating starts to degrade at the 18th day. The value is much lower than the original coating resistance. When the coating is doped with BTA-encapsulated nanocontainers, the R_c decreases and the C_c increases with time initially, but they increase and decrease, respectively, after a certain time period of immersion in the solution. For example, after 24 days of immersion, the R_c is 4.72×10^6 Ω cm^2 and 2.32×10^7 Ω cm^2 for 2 wt.% and 5 wt.% nanocontainer doped epoxy coatings, respectively. At the 30th day, the R_c is increased to 5.04×10^6 Ω cm^2 and 1.60×10^8 Ω cm^2, respectively. Correspondingly, the R_{ct} increases from the 24th day to the 30th day of immersion. When the doped nanocontainers are up to 8 wt.%, the R_c increases and C_c decreases at the 24th day, and the values are 1.39×10^7 Ω cm^2, 4.94×10^8 Ω cm^2 and 9.19×10^8 Ω cm^2 after 18 days, 24 days and 30 days of immersion, respectively. At the same time, the R_{ct} increases from 1.56×10^7 Ω cm^2 at the 18th day to 7.64×10^8 Ω cm^2 and 4.11×10^9 Ω cm^2 after 24 days and 30 days of immersion, respectively.

Generally, the evolution of R_c measures the resistance of a coating in a corrosive environment, and C_c is associated with water uptake of the coating. Coatings with a high R_c values and a low C_c are considered to offer a good anticorrosion performance. The R_{ct} is inversely to the corrosion rate of a steel and describes the corrosion resistance of the

steel in the corrosive environment. During the immersion period, the decreased R_c and the increased C_c of the undoped epoxy coating indicate that the barrier property of the coating is gradually deteriorated with time. In comparison, the R_c and C_c of the coating doped with 2 wt.% nanocontainers have similar values to the undoped coating until 24 days of immersion. After that, a small increase of R_c and drop in C_c are observed. This slight change is believed to be from the releasing of pre-encapsulated BTA inhibitors in the nanocontainers. This is confirmed by the slight increase of R_{ct} of the steel. It is noted that the 2 wt.% nanocontainer doped coating improves the corrosion resistance of the steel after 24 days of immersion in the solution, but slightly only.

The doping content of the inhibitor-encapsulated nanocontainers in the coating is a critical parameter to affect the anticorrosion performance of the developed intelligent coating. Upon the increase of the BTA-encapsulated nanocontainers to 5 wt.% and 8 wt.% in the epoxy coating, there are further increases of R_c and drops in C_c, as shown in Fig. 6.13. Particularly, the increase of R_{ct} of the steel is apparent, indicating the enhanced corrosion resistance of the steel. Therefore, the prepared BTA-encapsulated nanocontainers is critical in improving the anticorrosion performance of the developed coatings and the corrosion resistance of the steel in the solution. This effect is mainly attributed to two aspects. First, the prepared nanocontainers have a good compatibility with the host epoxy coating, and would not affect the coating properties. Second, once a corrosive environment associated with a low or high solution pH is generated to cause steel corrosion, the preloaded inhibitors would release on demand for corrosion inhibition.

6.3.8 Morphological, compositional and structure characterizations of coated steels after 30 days of immersion in the solution

(a)

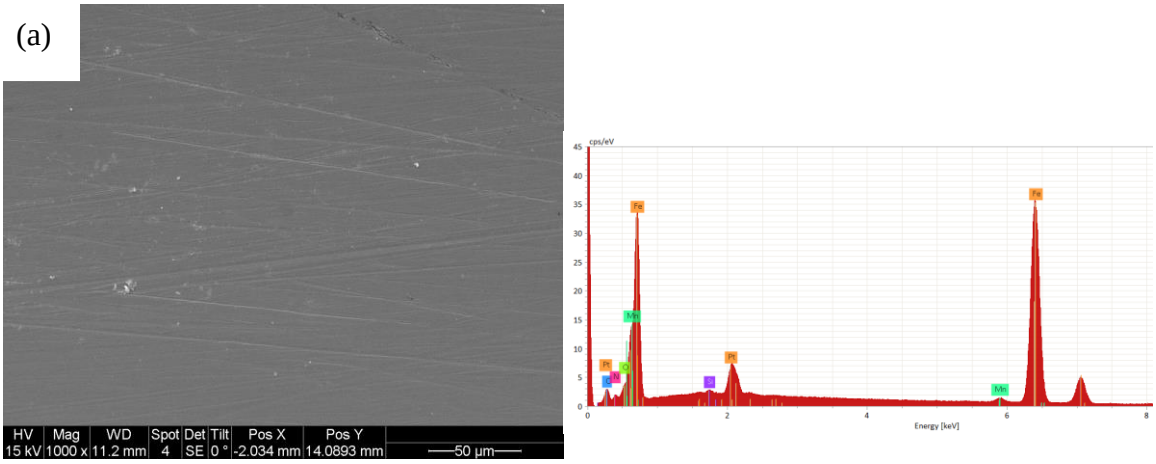

(b)

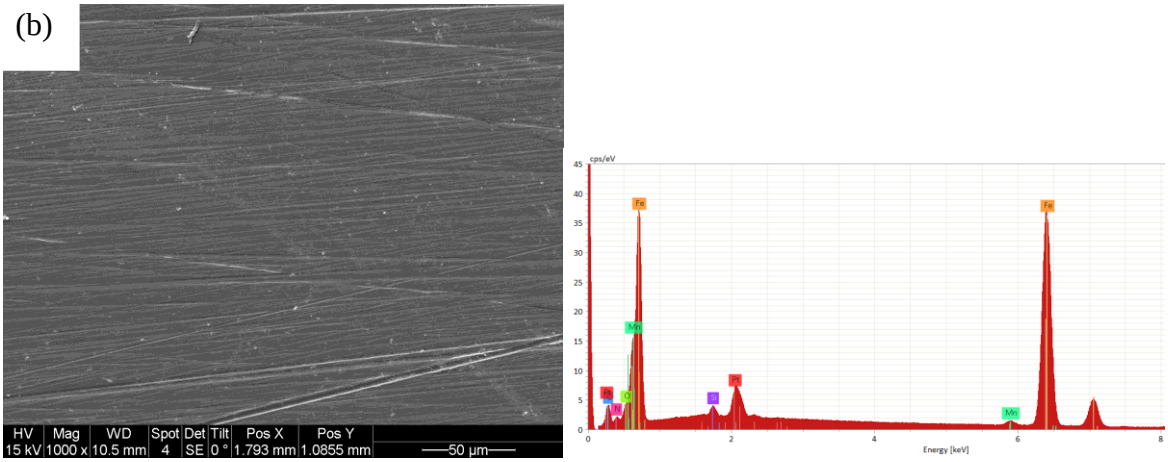

(c)

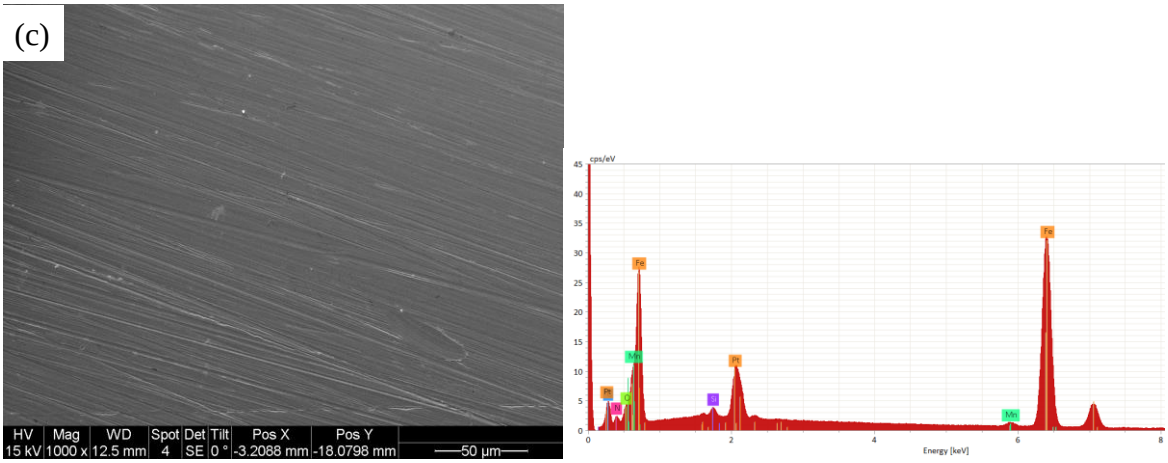

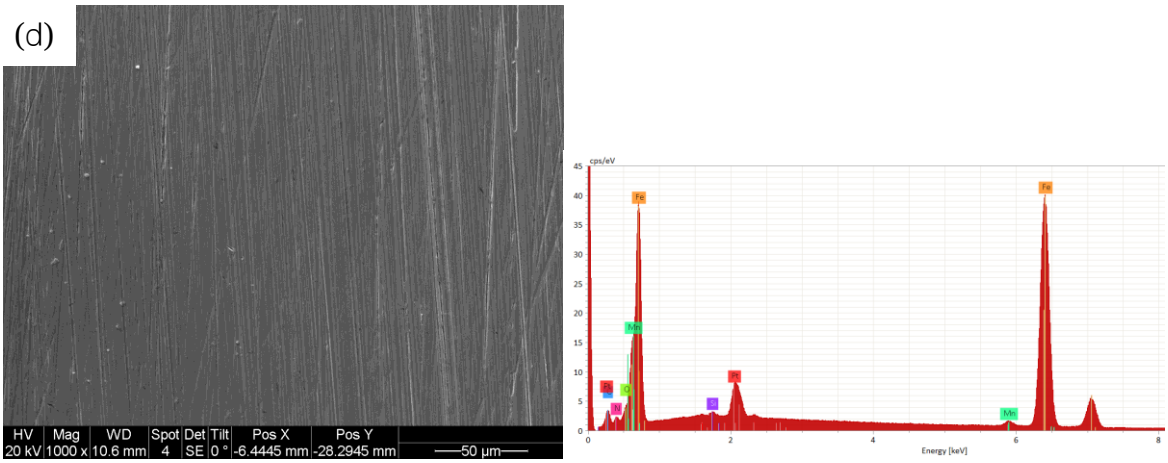

Fig. 6.14 SEM morphology and EDS spectra of the steel electrode, where the coating is peeled off, after 30 days of immersion in 0.1 M NaCl solution (a) no nanocontainer doped, (b) 2 wt.%, (c) 5 wt.%, (d) 8 wt.% nanocontainers.

Table 6.4 EDS elemental compositions of results of the steel surface, after the coatings are peeled off, after 30 days of immersion in 0.1 M NaCl solution.

Element (wt.%)	C	N	O	Si	Mn	Fe
Steel coated with as-received epoxy coating	20.73	1.47	2.12	1.00	1.03	72.66
Steel coated with 2 wt.% nanocontainer doped epoxy coating	18.38	2.76	2.09	0.39	1.23	76.74
Steel coated with 5 wt.% nanocontainer doped epoxy coating	16.14	3.74	1.38	0.37	1.11	77.26
Steel coated with 8 wt.% nanocontainer doped epoxy coating	15.42	4.60	1.25	0.37	1.15	77.22

The morphological and structural characterizations and EIS measurements demonstrate that the prepared BTA-encapsulated nanocontainers have a good

compatibility with the epoxy coating. The nanocontainers distribute uniformly in the host epoxy coating. It has been established [124, 146] that BTA inhibitors, after released from the nanocontainers, would adsorb on the steel surface to form a protective adsorptive film. The polar unit of three heterocyclic nitrogen atoms in BTA molecule serve as the reaction center for chemisorption with the steel. Strongly covalent bonds can form between N-atoms in the triazole ring and iron atoms by displacement of water molecules from the steel surface, and sharing electrons between the BTA molecules and iron through partial transference of electrons from the polar N-atoms to the steel. The formed adsorptive film can be confirmed by the EIS results in Table 6.3, as indicated by the decreasing C_{dl} when the coating is doped with 5 wt.% and 8 wt.% nanocontainers. The decrease of C_{dl} is attributed to the BTA adsorptive film on the steel surface, which has a lower dielectric constant and reduces the area for corrosion to occur. Moreover, due to the adsorption interaction between protonated BTA with corrosion products, the anodic reaction of the steel can be hindered, causing an increase in R_{ct}, as shown in Table 6.3.

Fig. 6.14 shows the SEM morphology and EDS spectra of the steel electrode, where the coating is peeled off, after 30 days of immersion in 0.1 M NaCl solution. The EDS elemental composition results are shown in Table 6.4. It is noted that the SEM, rather than an optical microscope, was used for characterization of corrosion morphology of the specimen due to the fact that the base coating used in this work contains carbon back as the pigment, which makes the microscopical view very dark. Thus, the SEM is the better method for morphological characterization. It is seen that, with the increase of the doped nanocontainers in the epoxy coating, the scratches introduced during the electrode grounding become more apparent. Actually, for the steel electrode coated with undoped

epoxy coating, there is no mechanical scratch observed. The morphology of the steel electrode is typical of that suffering from corrosion. It is thus seen that the steel experiences reduced corrosion when the coating contains a higher content of BTA-encapsulated nanocontainers. The elemental composition results show an increasing N content and decreasing O content with the increasing content of nanocontainers in the coating. As stated, the element N is from the adsorptive inhibitors BTA on the steel surface upon releasing from the nanocontainers. With effective inhibition of the steel corrosion, the content of element O present in corrosion products decreases.

Furthermore, the adsorptive inhibitors BTA on the steel surface can be confirmed by FTIR results obtained before and after 30 days of immersion in the solution, as shown in Fig. 6.15. Prior to corrosion testing, the FTIR spectra for all coatings include a peak at 851 cm^{-1}, which is attributed to the C-O-C stretching vibration due to the cross-linking reaction of the epoxy with added hardeners [158]. After 30 days of immersion, the peak at 851 cm^{-1} disappears. This may be due to the coating failure and the hydrolysis of C-O-C functional groups. At the same time, a weak peak at 3600 cm^{-1} is observed, which is associated with the -OH functional group coming from the coating [159]. More important, a new peak is observed at 1209 cm^{-1} in the spectra obtained for the coated steel with high nanocontainer contents such as 5 wt.% and 8 wt.%. This peak is attributed to the -N=N-N- breathing vibration, and comes from the BTA inhibitors only [120]. It is seen that this peak is not observed on the undoped coating and the coating doped with a low content of nanocontainers such as 2 wt.%.

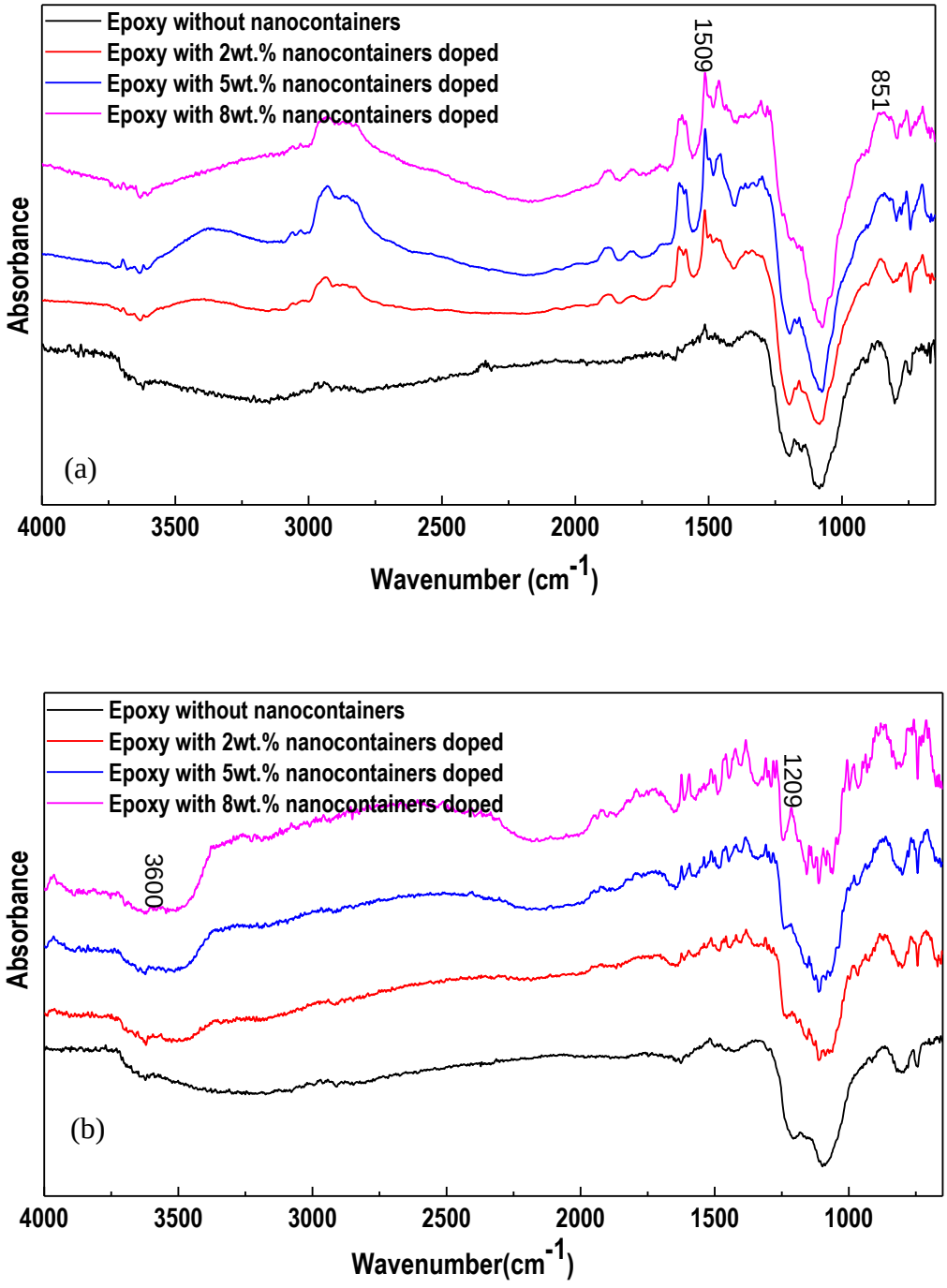

Fig. 6.15 FTIR spectra obtained on the coated steel electrode (a) before and (b) after 30 days of immersion in 0.1 M NaCl solution.

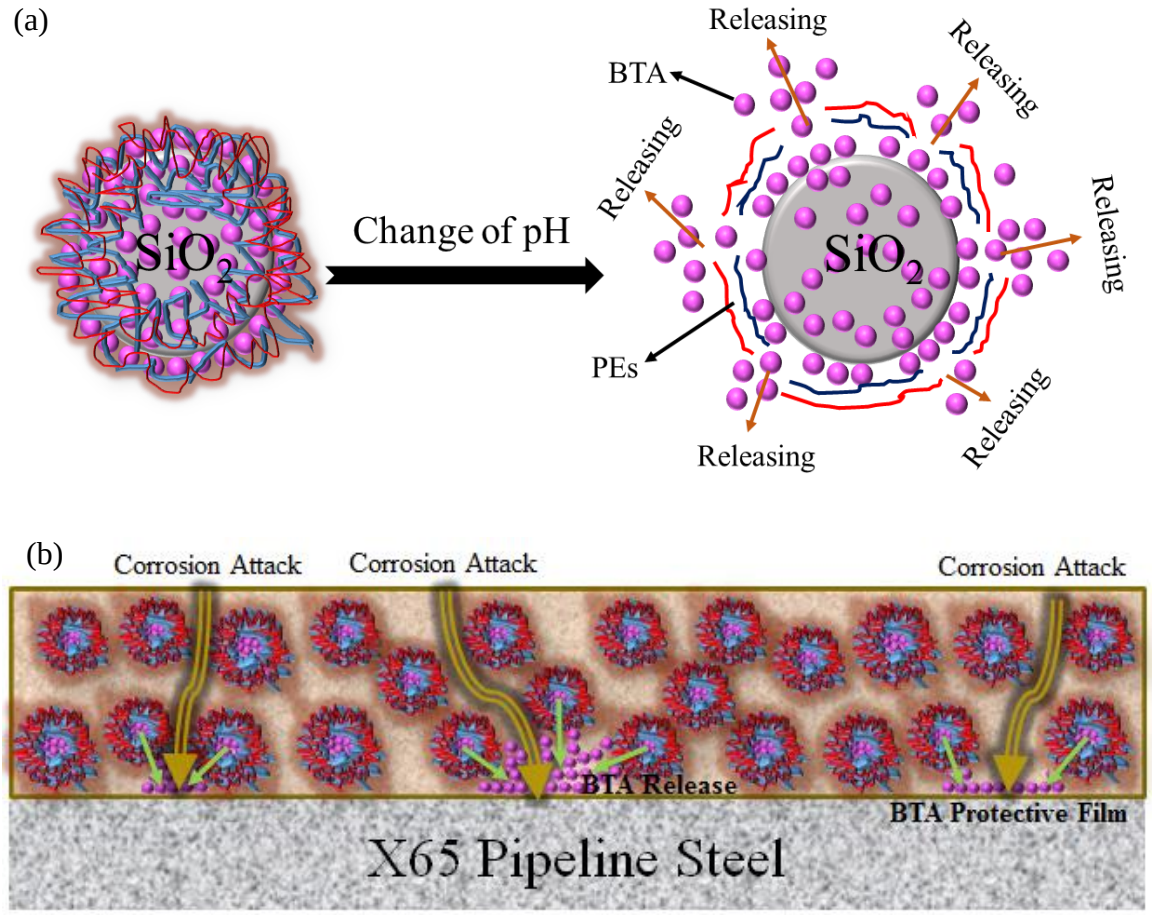

Fig. 6.16 Schematic diagram illustrating (a) the swelling of the polyelectrolytes in response to pH changes to release encapsulated inhibitors BTA and (b) the principle of corrosion protection for substrate steel by an intelligent coating doped with inhibitor-encapsulated nanocontainers.

As confirmed by the UV–vis spectroscopy, the self-releasing of the preloaded inhibitors BTA is specific to changes of the solution pH. Generally, polyelectrolytes are sensitive to pH changes, with either ‘open’ or ‘close’ state by ‘swelling’ to thinner the layer or ‘shrinking’ back to the original state [62], as schematically described in Fig.

6.16a. It was reported [128, 160] that the PDDAC and SPSS that are used to prepare the nanocontainers in this work have a pH-buffering activity, and can buffer the solution pH in near neutral pH ranges, such as pH 5-9. Inhibitors BTA are able to release from the multilayer polyelectrolytes shell to reduce steel corrosion when the solution pH becomes acidic. When the solution pH is at near neutral values or is back from acidic to near neutral, the polyelectrolytes remain closed, and the inhibitors are sealed in the nanocontainers. The principle of corrosion inhibition for an intelligent coating is schematically described in Fig. 6.16b.

6.4 Summary

An intelligent coating is developed based on encapsulation of BTA inhibitors in the prepared SiO_2 nanoparticle based polyelectrolyte nanocontainers, and self-releasing of the inhibitors for corrosion inhibition to pipeline steel in chloride solutions. The nanocontainers have a smooth surface with a globular geometry. Both EDS and FTIR measurements demonstrate that the inhibitors are effectively encapsulated in the nanocontainers. There are about 6.7 wt.% of inhibitors loaded in the nanocontainer, as determined by the thermal stability test.

The prepared BTA-encapsulated nanocontainers are dispersed uniformly in an industry-used epoxy coating under the testing condition. The doping of the nanocontainers would not change the chemical cross-linking structure of the coating, as shown by the identical glass-transitional temperature of the coatings doped with various contents of nanocontainers. Moreover, the encapsulated inhibitors can self-release from the nanocontainers in response to changes of solution pH, specifically low and high pH

values (pH 2 and 11), for corrosion inhibition. At near-neutral solution pH, the nanocontainers remain “closed” and the inhibitors would not release.

For the steel coated with the processed coatings doped with inhibitor-encapsulated nanocontainers, the corrosion inhibition is time dependent upon the self-release of the inhibitors from the nanocontainers. The doping content of the nanocontainers in the coating is a critical parameter to affect the anticorrosion performance of the developed coating, and the corrosion resistance of the substrate steel. Moreover, with the increasing content of the BTA-encapsulated nanocontainers in the coating, both the coating resistance and the corrosion resistance of the steel increase, resulting in a reduced corrosion. The released inhibitors decrease the steel corrosion by forming a layer of inhibitor adsorptive film, which is detected on the steel surface after 30 days of immersion in the solution.

Chapter Seven: Stearic Acid Modified Superhydrophobic Zinc Nano-films for Enhanced Antifouling, Self-cleaning and Corrosion Resistance*

7.1 Introduction

An intelligent coating that was fabricated by doping BTA encapsulated nanocontainers in epoxy coating was investigated in the former chapters. Generally, the superhydrophobic coating with self-cleaning and antifouling performance is also attributed as one kind of intelligent coating because of the initiative action when corrosive environment generates on its surface.

It has been acknowledged [161] that a micro/nanoscale surface structure and its low surface energy contribute to the superhydrophobicity. When a superhydrophobic material is exposed to aqueous environments, an "air-cushion" is formed on its surface due to the non-wettability of the material. This effectively blocks the diffusion of corrosive species in the environment towards the substrate material. At the same time, a superhydrophobic surface serves like a vertically cylindrical tube placed in liquid. Due to the Laplace pressure, the corrosive electrolyte can be pushed out of the pores contained in the superhydrophobic surface film [162-164]. For example, Sethi et al. [163] prepared a superhydrophobic coating on steels to create a carbon nanotube mesh structure. The coating is able to withstand environmental attack to the substrate steel. Li et al. [78] used a hydrothermal treatment method to fabricate superhydrophobic ZnO films on a pipeline

* This work has been submitted as: Yuanchao Feng, Shougang Chen, Y. Frank Cheng, Stearic acid modified superhydrophobic zinc nano-films for enhanced antifouling, self-cleaning and corrosion resistance, *Corrosion Science*, March 2017

steel to achieve a water contact angle of 157.59°, which is effective for protection of the steel from corrosion.

Electrochemical techniques possess the advantages of low cost, convenient controlling of operating conditions, and high effectiveness to engineering materials to achieve desirable structures and properties [165, 166]. In particular, the electrodeposition technique is able to fabricate micro-/nano-patterned structures conveniently, achieving the hydrophobic or superhydrophobic property [167]. To date, most of the reported work have been conducted on metals such as Al, Cu, Zn and their alloys [168-172]. There has been rare work conducted on carbon steels, the most commonly used engineering materials. This work attempts to develop superhydrophobic Zn nano-films on carbon steel, with antifouling, self-cleaning and anticorrosion properties, by a simple and feasible process.

In the present work, superhydrophobic Zn nano-films were prepared on a X65 carbon steel by electrodepostion and the stearic acid modification. The morphology, composition and structure of the prepared films were characterized by SEM, EDS, X-ray diffraction (XRD), and FTIR, respectively. The water and oil contact angles of the filmed steels were measured, and the antifouling and self-cleaning performance were determined. The corrosion resistance of the film was studied by EIS in a chloride solution. The optimal electrodepositing condition to achieve the superhydrophobity and desired properties was determined.

7.2 Experimental

7.2.1 Material and specimens

Steel specimens used in this work were cut from a X65 carbon steel pipe, with a chemical composition (wt.%): C 0.04%, Si 0.2%, Mn 1.5%, P 0.011%, S 0.003%, Mo 0.02% and Fe balance. The specimens were machined into 1 cm × 1 cm × 1 cm square shape, and sealed in epoxy, leaving an exposed area of 1 cm^2. The working face of the specimen was subsequently ground up to 1,200 grit SiC emery papers, washed with deionized water, degreased with ethanol and acetone, and dried in air.

7.2.2 Electrodeposition of Zn nano-films on steel specimens

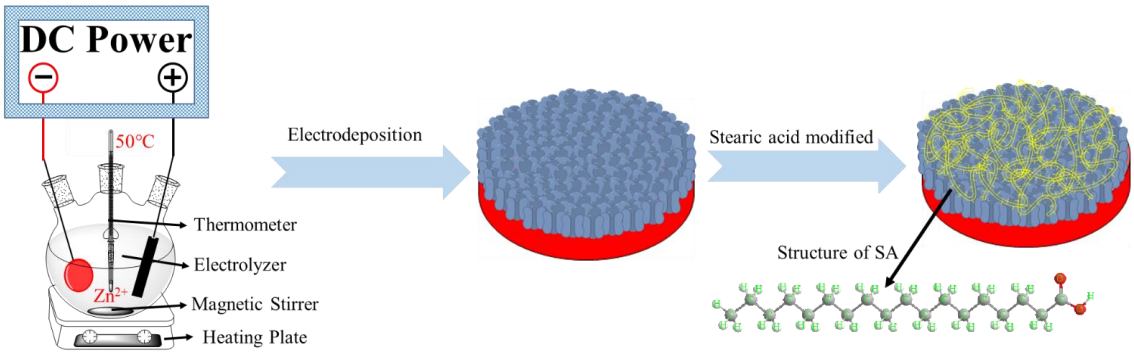

Fig. 7.1 Schematic diagram of the experimental setup for electrodeposition and the stearic acid modification to prepare the superhydrophobic Zn nano-films on the steel specimen, where SA refers to stearic acid.

Prior to electrodeposition, the steel specimens were ultrasonically degreased in an alkaline solution containing 20 g/L NaOH, 10 g/L $NaCO_3$ and 10 g/L Na_3PO_4 at 50 ˚C for

10 mins. The specimens were then immersed in 50 g/L H_2SO_4 for 1 min at room temperature to remove oxides from the surface, and then rinsed thoroughly with deionized water and dried in high-purity nitrogen (99.999%). Fig. 7.1 shows the schematic diagram of the experimental setup for electrodeposition and the post-modification by stearic acid to prepare superhydrophobic Zn nano-films on the steel substrate. The steel specimen was installed in a cell containing 250 g/L $ZnSO_4$ solution with a pH of 2.0 adjusted by 50 g/L H_2SO_4. The specimen, which served as the cathode, was connected to the negative pole of a direct current (DC) power supply. A carbon rod, used as the anode, was connected to the positive pole of the DC power source. The distance between the anode and the cathode was 2 cm. The bath solution, which was under magnetic stirring, was maintained at 50 ˚C with a heating plate.

After electrodeposition, the specimen was removed from the solution, rinsed with deionized water and dried in air. The Zn filmed specimen was then immersed in 0.05 mol/L stearic acid ethanol solution for 5 h at room temperature, which would generate a stearic acid layer with a low surface energy. The specimen was then removed, washed with ethanol and dried with cold air to obtain the superhydrophobic Zn nano-film on the steel substrate.

To control the reproducibility of the prepared Zn nano-films, three parallel steel specimens were prepared for electrodeposition under the identical condition.

7.2.3 Characterization of the prepared zinc nano-films

The water contact angle of the filmed steel specimen was measured with a 3 μL water droplet using an environmental goniometer (100-26-TH, Ramé-hart Instrument

Co.) at room temperature. Each data point present in this work was the average of five measurements conducted at different locations on the specimen. The oil contact angles were measured following the same procedure, but using a mineral oil droplet as the testing material.

The morphology and chemical composition of the prepared Zn nano-films were characterized using a SEM equipped with an EDS. A FTIR (Model Nicolet iS50) was used to characterize the functional groups and structure of the films. For all spectra recorded, the specimens were experienced a 64-scan data accumulation in the range of 600 - 4000 cm^{-1} at a spectral resolution of 4.0 cm^{-1}. The XRD (Rigaku Multiflex θ-θ diffractometer) was used to measure the crystalline structure of the prepared Zn nano-films with a Cu Kα radiation (40 kV, 40 mA, λ=1.5418 Å). A scan range of 2θ = 20°~90° and a scan speed of 0.2°/min was used.

The antifouling and self-cleaning properties of the prepared films were investigated by immersing the filmed specimen in a mud liquid and spreading soil on the film surface, respectively. For the former, the specimen was removed after various time periods of immersion to observe visually its surface color and condition. For self-cleaning testing, the soil spreading on the filmed steel specimen was washed off by spraying water, while the specimen was inclined at an angle of 10 - 15°.

7.2.4 Corrosion resistance of the prepared zinc nano-films

The corrosion resistance of the prepared zinc nano-films was measured by EIS measurements in 3.5 wt.% NaCl solution on a three-electrode cell using a Solartron 1280C electrochemical workstation. The filmed steel specimen was used as working

electrode, a carbon rod as counter electrode and a SCE as reference electrode. The EIS measurement was conducted at the corrosion potential (E_{corr}) of the specimen over a frequency range from 10 kHz to 0.01 Hz, with a disturbance AC voltage of 10 mV. The electrochemical impedance data were fitted with appropriate equivalent circuits using the ZSimpWin software.

7.3 Results and discussion

7.3.1 Characterization of morphology and composition of the prepared Zn nano-films

Figs. 7.2-7.4 show the SEM morphological views of the prepared Zn nano-films after 5, 10, 20 and 30 mins of electrodeposition at current densities of 50, 100 and 200 mA/cm^2, respectively, followed by stearic acid modification. It is seen that compact, nanoscale Zn films are formed under all conditions. The morphological features of the films depend on the electrodepositing current density and time. Generally, at individual current densities, the size of the particles present on the films increases, and the film becomes rougher with the increasing time. Under the electrodepositing current density of 50 mA/cm^2, the films are featured from a tiny wrinkled texture to formation of large particles, and then to layered particles as the depositing time increases. After 5 and 10 mins of electrodeposition, the films are compact and the adjacent particles are linked coherently (Figs. 7.2a and 7.2b). When the depositing time increases to 20 mins, the particles grow, with layered waves observed. As the depositing time is up to 30 mins, the film is further rougher, and more layered waves are observed on the particles. The valley-peak fluctuations of the particles reduce compared to the structure of the film formed after 20 mins.

Under the electrodepositing current density of 100 mA/cm^2, the nano-films have the similar feature to those formed under the current density of 50 mA/cm^2, but with an increased surface roughness at the identical electrodepositing time. The film formed after 5 mins of electrodeposition possesses a homogeneous, wrinkled texture, as seen in Fig. 3a. When the depositing time increases to 10 mins, the particles becomes larger and the films are rougher (Fig. 7.3b). After 20 mins of electrodeposition, the film changes to a regular layered structure. Cavities and crevices generate between particles, as shown in the enlarged photo in Fig. 7.3c. After 30 mins of electrodeposition, the film is rougher, with cracks produced between enlarged particles. The valley-peak fluctuations decrease, i.e., the film formed after 30 mins tends to be flatter compared to that formed after 20 mins.

Under the 200 mA/cm^2 of electrodepositing current density, the surface structure is quite different from those formed at 50 and 100 mA/cm^2 after 5 mins of electrodeposition. A compact nano-film is formed, containing numerous particles with the diameter of about 5 μm. The wrinkled texture is not observed. As the depositing time increases to 10 mins, large particles grow on the film, which is much rougher than before. After 20 mins of electrodeposition, many cavities and spaces with increased size present between particles. The film starts to show non-uniform growth, with locally preferential deposition of the film. After 30 mins, the film is more heterogeneous, with further local growth of the film. The particles become a layered structure, with the scale of several to 10 microns.

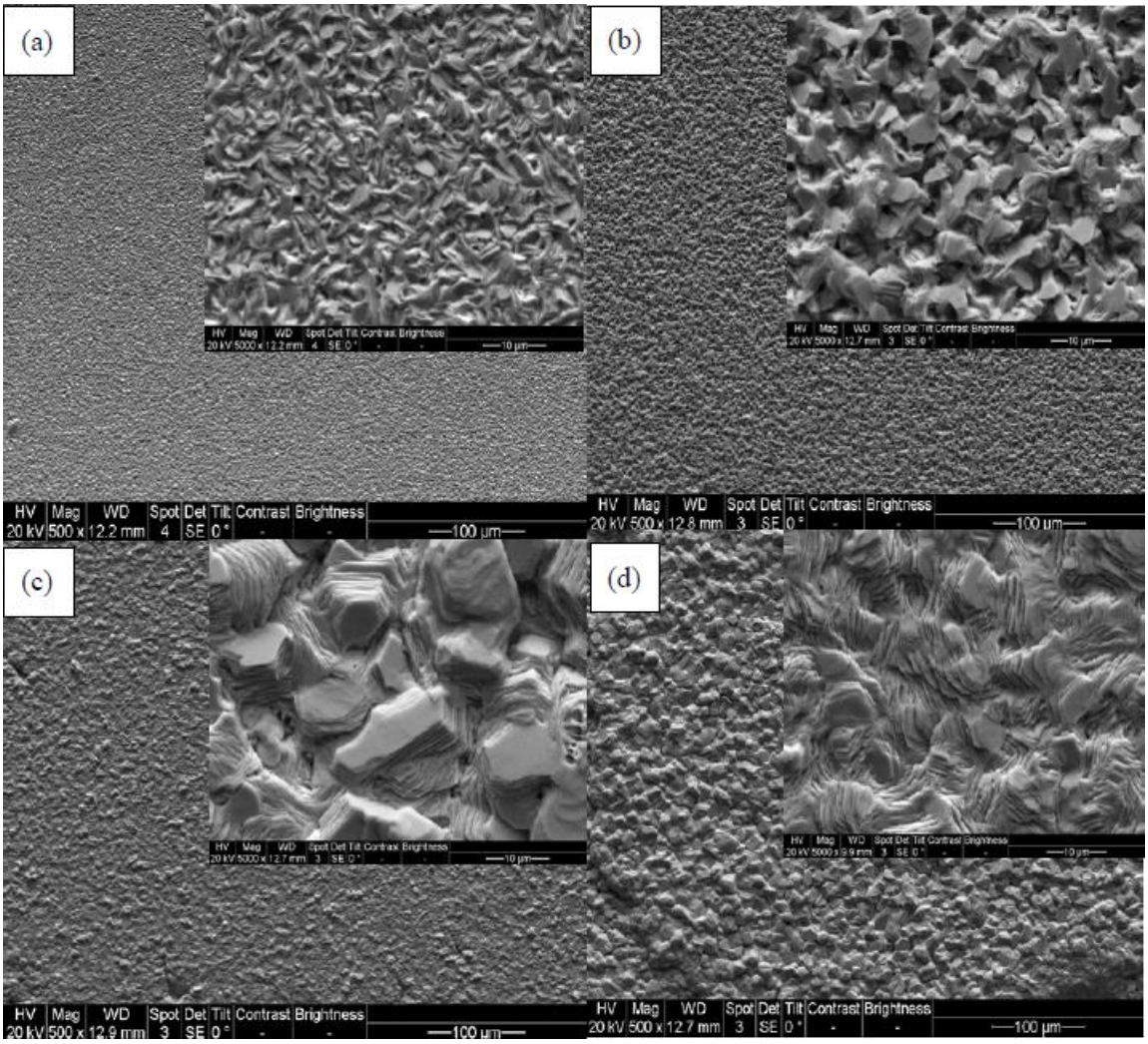

Fig. 7.2 SEM morphological views of the prepared Zn nano-films after (a) 5, (b) 10, (c) 20 and (d) 30 mins of electrodeposition at the current density of 50 mA/cm^2, followed by stearic acid modification, where images with a large magnification are also included.

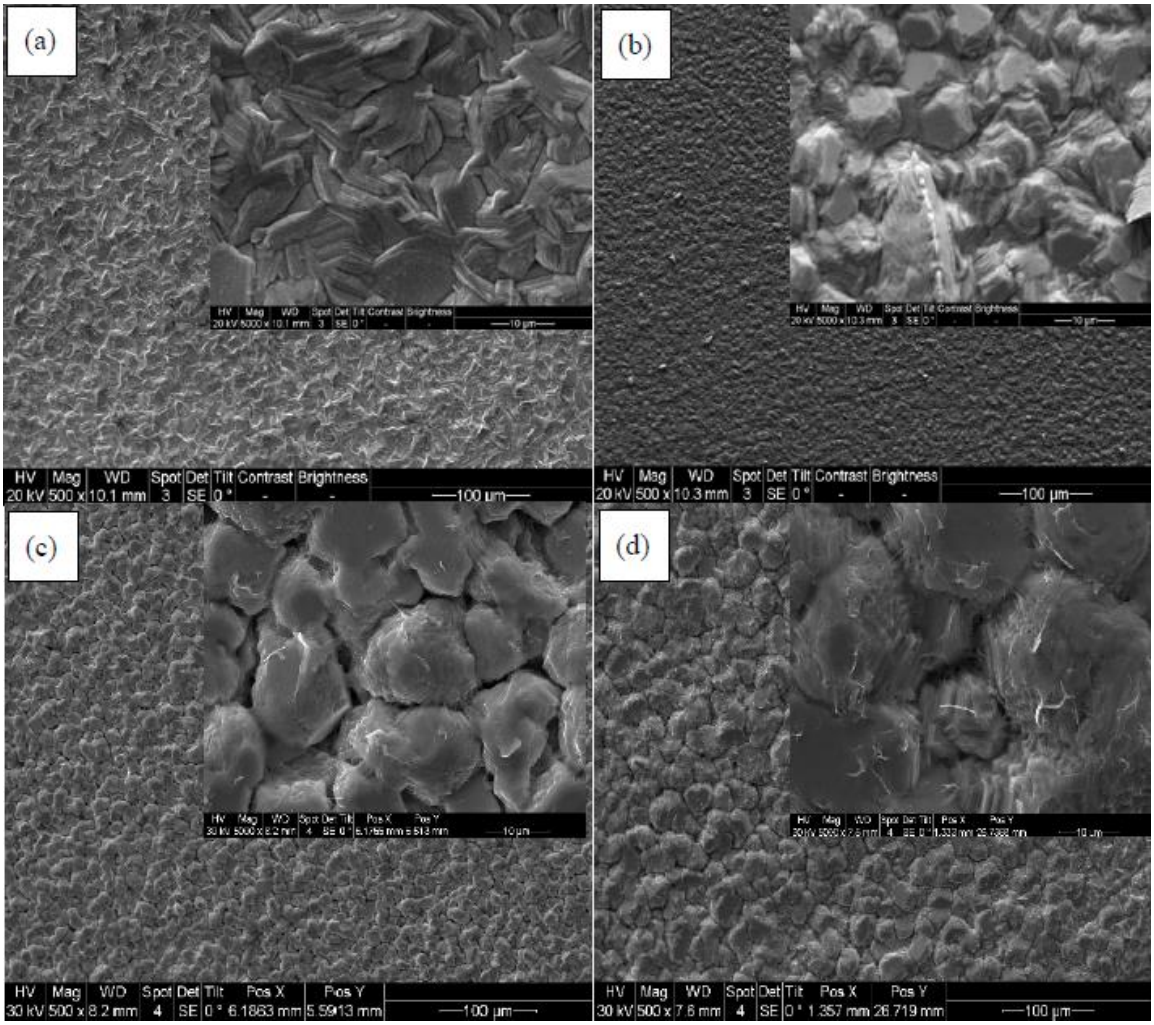

Fig. 7.3 SEM morphological views of the prepared Zn nano-films after (a) 5, (b) 10, (c) 20 and (d) 30 mins of electrodeposition at the current density of 100 mA/cm^2, followed by stearic acid modification, where images with a large magnification are also included.

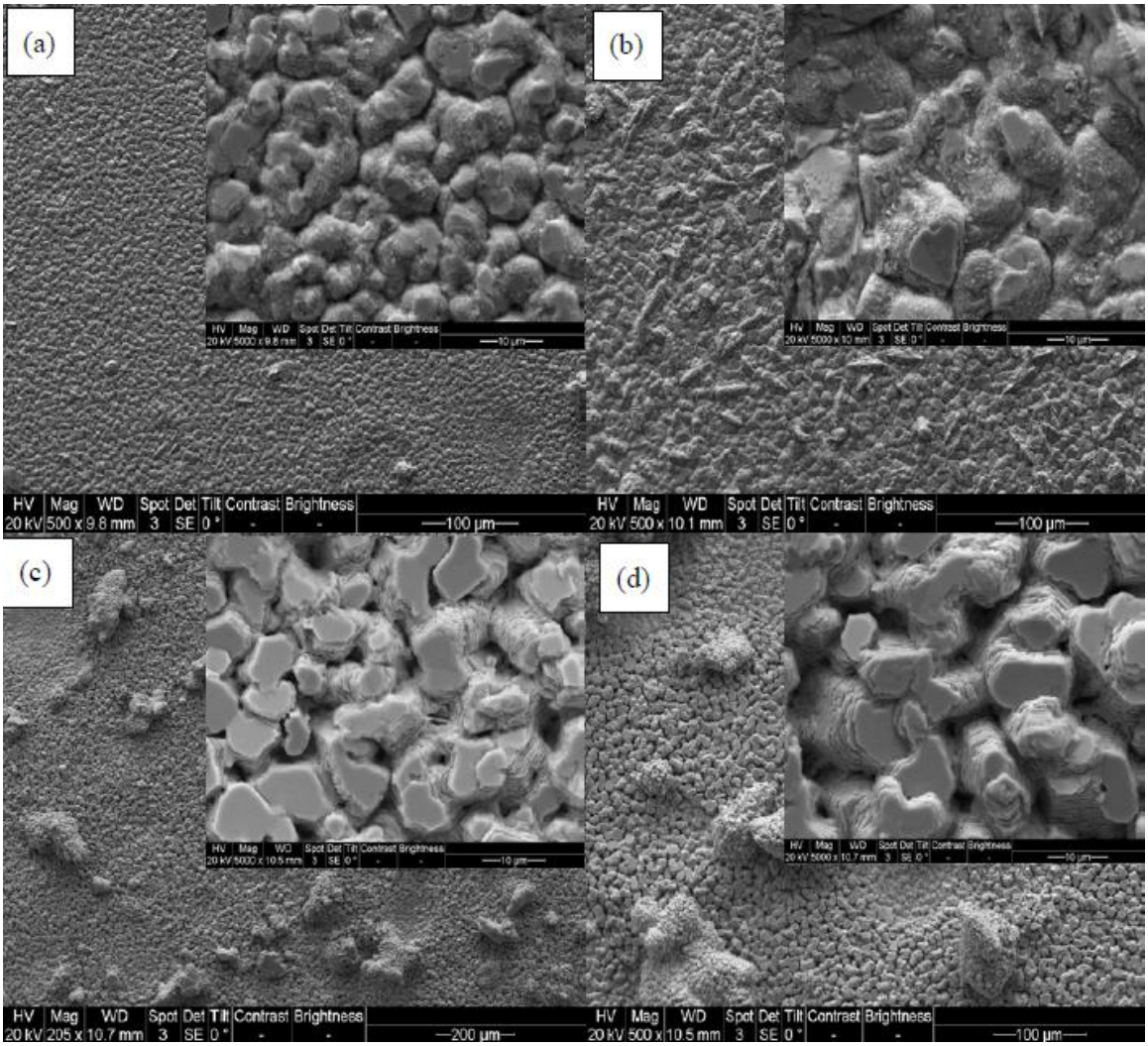

Fig. 7.4 SEM morphological views of the prepared Zn nano-films after (a) 5, (b) 10, (c) 20 and (d) 30 mins of electrodeposition at the current density of 200 mA/cm^2, followed by stearic acid modification, where images with a large magnification are also included.

From the morphological characterization of the prepared Zn nano-films, it is seen that typical micro-/nanoscale structure can be formed on the films. This is the typical feature of the leaf-like morphology similar to that of the lotus leaf surface [173]. This

type of surface structure contains numerous grooves and cavities to entrap air. The resulting “air-cushion” can effectively prevent water from wetting the substrate material. Under the depositing current density of 50 mA/cm^2 tends to produce compact Zn nano-films, which do not enable remarkable hydrophobic property by generation of the so-called “air-cushion’ structure. However, the current density of 200 mA/cm^2 is too high to generate a homogeneous film, especially at extended depositing times. The current density of 100 mA/cm^2 is appropriate by adjusting the electrodepositing time to produce uniform, “air-cushion” typed nano-films, which is expected to result in the surface superhydrophobity.

Fig. 7.5a shows the SEM cross-sectional view of the Zn nano-film formed under 100 mA/cm^2 current density for 20 mins followed by stearic acid modification, and Fig. 7.5b shows the high magnificational top-view of the cavity present on the film. It is seen that the Zn nano-film is formed uniformly on the steel surface, with an average thickness of 56.54 μm. The film close to the steel substrate is more compact than that nearby the surface, where the micro-/nanoscale structure is present. It is noted that some dark artifacts in the cross-sectional view are not associated with the film, but generated during preparation of the specimen for metallographic observation. Particularly, the enlarged view of the cavity proposed to form the “air-cushion” structure possesses nanoscale layered structure internally. Fig. 7.5c shows the EDS elemental analysis along the yellow line in Fig. 7.5a. The results confirm the formation of Zn film on the steel.

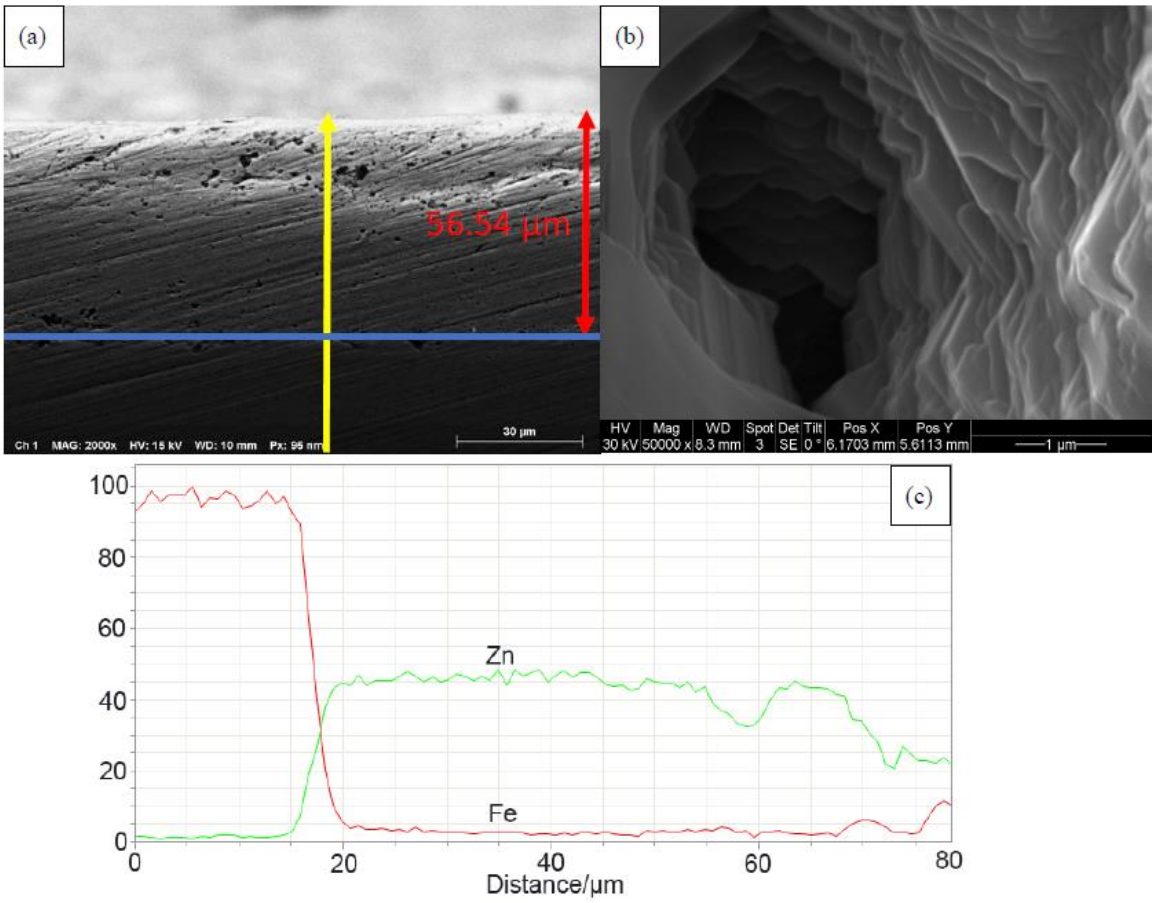

Fig. 7.5 (a) SEM cross-sectional view of the Zn nano-film formed under 100 mA/cm^2 current density for 20 mins followed by stearic acid modification. (b) The high magnificational top-view of the cavity contained in the film. (c) EDS elemental analysis along the yellow line in Fig. 7.5a.

7.3.2 Structural and Compositional Characterization of the Zn Nano-films

Fig. 7.6 shows the FTIR spectra of the Zn nano-films formed after 20 mins of electrodeposition at the current density of 100 mA/cm^2 without and with the stearic acid modification. Specifically, the peaks at 1398 and 1461 cm^{-1} are from the chelating coordination of zinc with stearic acid[162], and the peak at 1649 cm^{-1} is ascribed to the

vibration adsorption of –COO [174]. There are two adsorption peaks at 2887 and 2972 cm^{-1} are associated with the CH_2 asymmetric and symmetric stretching vibrations [175, 176], respectively. All the five peaks are absent in the prepared Zn film without modification by stearic acid. The results confirm the interaction of stearic acid with the zinc film.

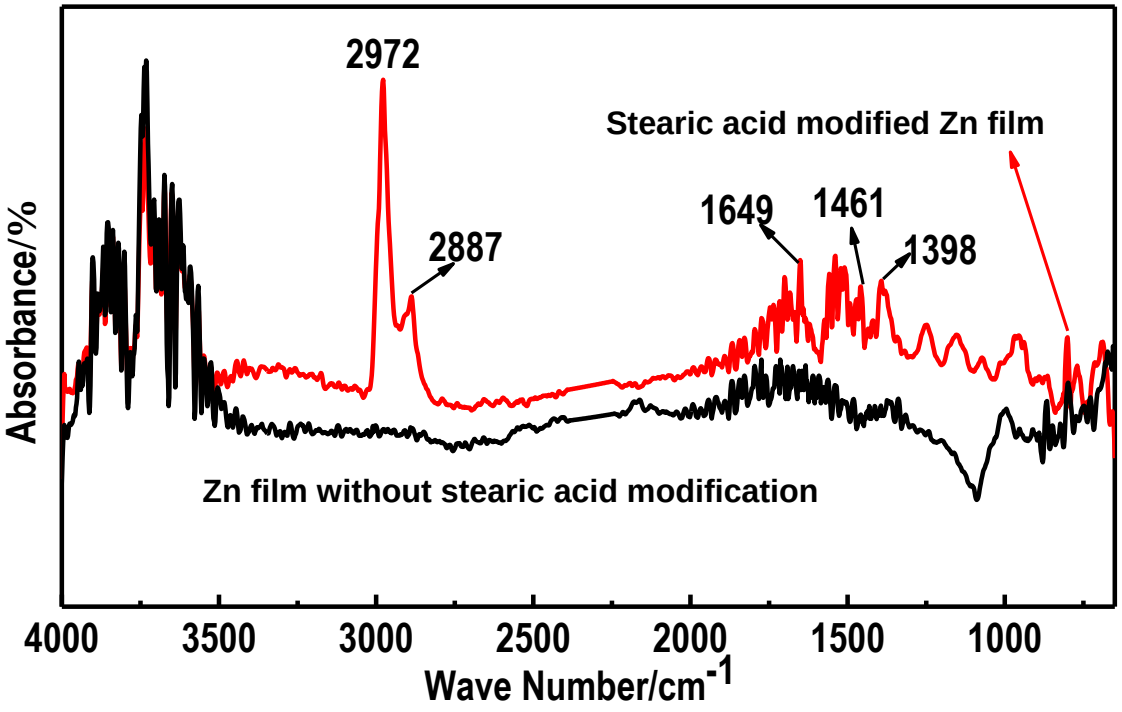

Fig. 7.6 FTIR spectra of the Zn nano-films after 20 mins of electrodeposition at the current density of 100 mA/cm^2 without and with the stearic acid modification.

Fig. 7.7 shows XRD spectra of the Zn nano-films formed after 10 and 20 mins of electrodeposition under the current density of 100 mA/cm^2 and the stearic acid modification. The peaks at $2\theta = 42.9°$, 54.0° and 69.7° are indexed as Zn (101), (102) and

(103), respectively. The approximately similar intensity of these peaks for the film formed after 10 mins of electrodeposition indicates that these crystalline faces grow at a nearly equal rate. After 20 mins, the peak at 2θ = 69.7 becomes much more distinct and sharper than the other ones, showing the preferential growth of the film on the (103) plane, which is orientated parallel to the film surface to form a layered particle structure. As reported [177], the growth of electrodeposited Zn film is initiated by formation of a subcrystalline layer, on which the crystalline layer of Zn film builds up rapidly. Thus, the structural change of the Zn films as visualized in Figs. 7.2 – 7.4 is due to the growth of Zn from the initial subcrystalline structure to the preferential growth on specific planes with a certain orientation.

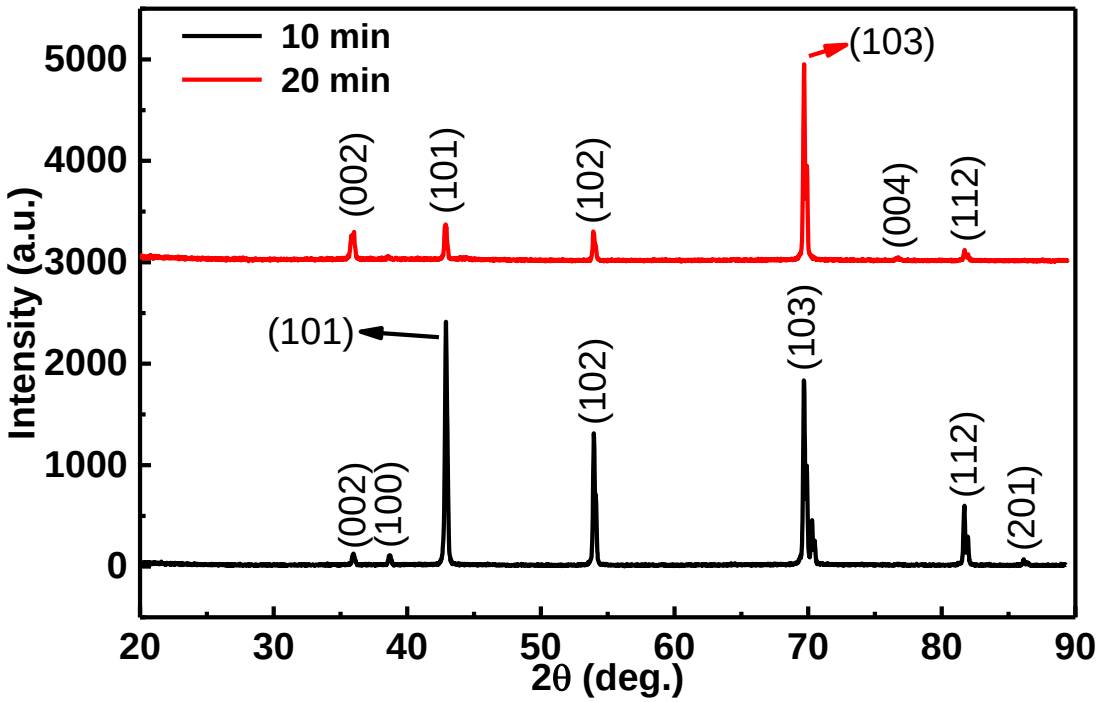

Fig. 7.7 XRD spectra of the Zn nano-films formed after 10 and 20 mins of electrodeposition at the current density of 100 mA/cm^2.

7.3.3 Measurements of Water and Oil Contact Angles

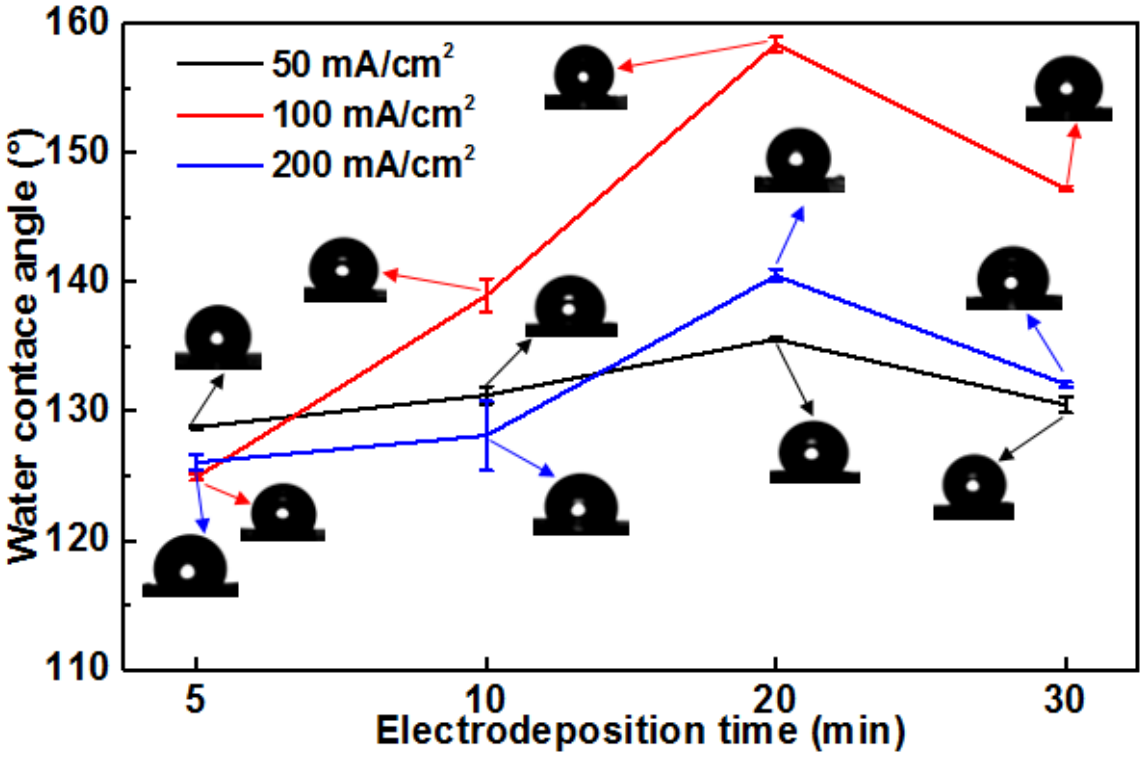

Fig. 7.8 Water contact angles measured on the steel specimen with Zn nano-films formed by electrodeposition at various times and current densities followed by stearic acid modification.

To understand the influence of electrodepositing parameters on the hydrophobic property of the prepared Zn nano-films, the water contact angles are measured on the filmed steel specimen, as shown in Fig. 7.8. The water contact angle on the bare steel is 74.8°. After filming, the contact angle increases remarkably, indicating that the Zn nano-films possess the hydrophobic property. Under individual depositing current densities, the contact angle increases with time from 5 to 20 mins. After reaching a maximum value,

the contact angle decreases as the time increases to 30 mins. The optimal depositing time in the present system to achieve the best hydrophobic performance is 20 mins for all the electrodepositing current densities. The Zn nano-films formed under 100 mA/cm^2 have larger contact angles than those formed under 50 and 200 mA/cm^2. Particularly, after 20 mins of electrodeposition under 100 mA/cm^2, the water contact angle is up to 158.4 ± 1.5°, where the nano-film shows a superhydrophobic property. As a comparison, prior to the stearic acid modification, the water contact angle of the Zn nano-film formed under 100 mA/cm^2 for 20 mins is 103.7±1.2°. Thus, the stearic acid modification for the Zn nano-film results in a further increase of the water contact angle. This is attributed to the formation of a stearic acid layer which possesses a low surface energy.

The hydrophobic and superhydrophobic properties of the Zn nano-films formed under various electrodepositing current densities and times depend on their surface morphology and structure, as the composition of the films is identical under the present condition. As shown in Figs. 7.2-7.4, with the increased depositing time, the films tend to change from the initial compact structure to the one with the increased surface roughness, with the presence of numerous nano- and micro-scale particles or features. This structure results in the increasing surface hydrophobic property. After 20 mins of electrodeposition under various current densities, the “air-cushion” type of structure is formed, enabling the best hydrophobic performance for the film. Under a low electrodepositing current density such as 50 mA/cm^2, the particle growth is slow and the formed micro-/nanoscale structure is not sufficiently effective to produce a good hydrophobic performance. However, at the high current density of 200 mA/cm^2, the growth of the particles is too fast to generate a satisfactory surface structure. Both depositing current densities are not

able to produce a surface structure to achieve the superhydrophobic level. When the depositing current density is 100 mA/cm^2, the growth of surface micro-/nanoscale structure is appropriate. After 20 mins of electrodeposition, a superhydrophobic surface is produced, representing the optimal film-forming condition in this work.

According to Cassie-Baxter's model about the wettability of a rough surface[73], liquid drops cannot enter cavities, if they are sufficiently small, present on the surface. Instead, they would rest on tops of the asperities, leading to a composite interface including trapped air in these cavities. Therefore, a rough surface possessing a micro-/nanoscale structure is required in order to achieve a superhydrophobic performance. To obtain the superhydrophobic state, the surface roughness of the material must reach the Cassie-Baxter state, which is regarded as a composite film consisting of a rough material surface, and air is trapped in the micro-/nanoscale cavities. The water contact angle is calculated by [178]:

$$\cos(\theta)=f_1 \cos(\theta_0) - f_2 \quad (7\text{-}1)$$

$$f_1 + f_2 = 1 \quad (7\text{-}2)$$

where θ and θ_0 represent the water contact angles of the rough and smooth surfaces with the same chemical composition, respectively, and f_1 and f_2 are the fractional areas estimated for the solid and air contact with the surface, respectively. In this work, the water contact angles of the prepared Zn nano-films with and without stearic acid modification are θ=158.4° and θ_0 =103.7°, respectively. The calculated f_1 and f_2 are thus 0.092 and 0.908, respectively. The results mean that the air- occupied part of the total

contact area between the water droplet and the micro-/nanoscale structured Zn film is up to 90.8%. Only 9.2% of the surface area contact with water. Thus, the superior superhydrophobicity of the prepared Zn nano-film is resulted from the formation of a unique, layered micro-/nanoscale architecture, where a large fraction of air is trapped.

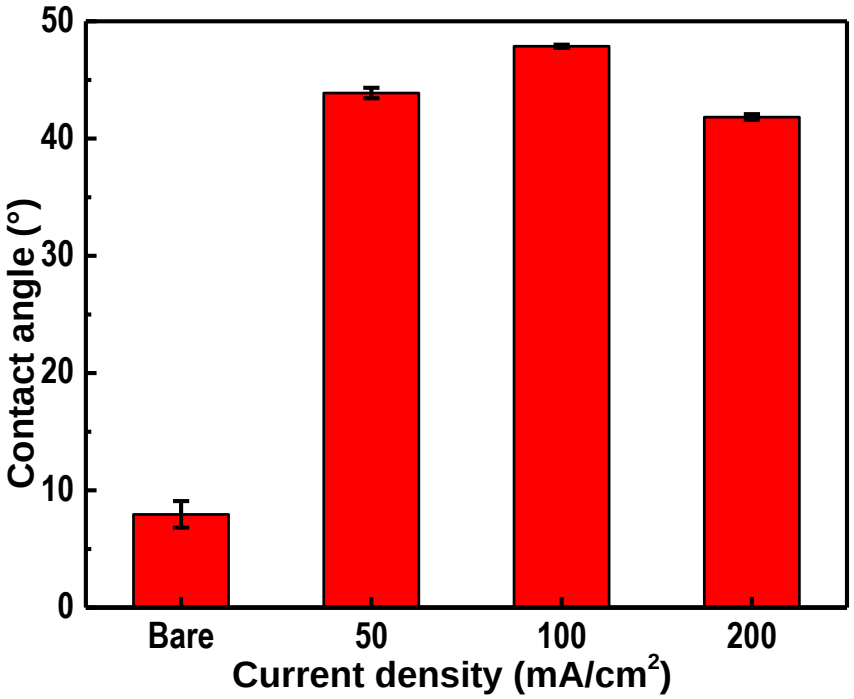

Fig. 7.9 Oil contact angles measured on the Zn nano-films formed after 20 mins of electrodeposition under 50, 100 and 200 mA/cm^2 current densities and the stearic acid modification.

At the same time, the oleophobic properties of the prepared Zn nano-films are also investigated by measuring the oil contact angles on the films formed after 20 mins of electrodeposition under various conditions and stearic acid modification, as shown in Fig.

7.9. The oil contact angle of bare steel is 8.6° only, showing that the steel is highly oleophilic. After filming, the oil contact angle increases nearly 5 times to 44.2°, 48.1° and 42.9° under the current densities of 50, 100 and 200 mA/cm^2, respectively. The results show that the prepared Zn nano-films are also able to improve the oleophobic property. In particular, the condition to achieve the superhydrophobicity, i.e., the electrodepositing current density of 100 mA/cm^2 and the time of 20 mins with the stearic acid modification, results in the best oleophobic performance.

7.3.4 Anti-fouling and Self-cleaning Performance of the Prepared Zn Nano-films

One of the main functions possessed by a superhydrophobic surface is its antifouling and self-cleaning properties. Fig. 7.10 shows the optical top-views of a droplet of water, tea, milk, and a soil solution, respectively, on the Zn nano-film prepared under the electrodepositing current density of 100 mA/cm^2 for 20 mins and followed by stearic acid modification. It is seen that the water droplet has a perfectly spherical shape with a contact angle of 158.4° (Fig. 7.10a), demonstrating the superhydrophobicity of the prepared Zn nano-film. To measure the hydrophobic properties of the Zn nano-film to withstand other aqueous environments, Figs. 10b-10d show the droplet of tea, milk and a soil solution on the prepared Zn nano-film, respectively. It is seen that the tea, milk and soil solution droplets exhibit typical spherical shapes on the film as well, with the measured contact angles of 156.3°, 154.7° and 154.3°, respectively. The results confirm that there is an excellent superhydrophobicity of the prepared Zn nano-film to these liquids.

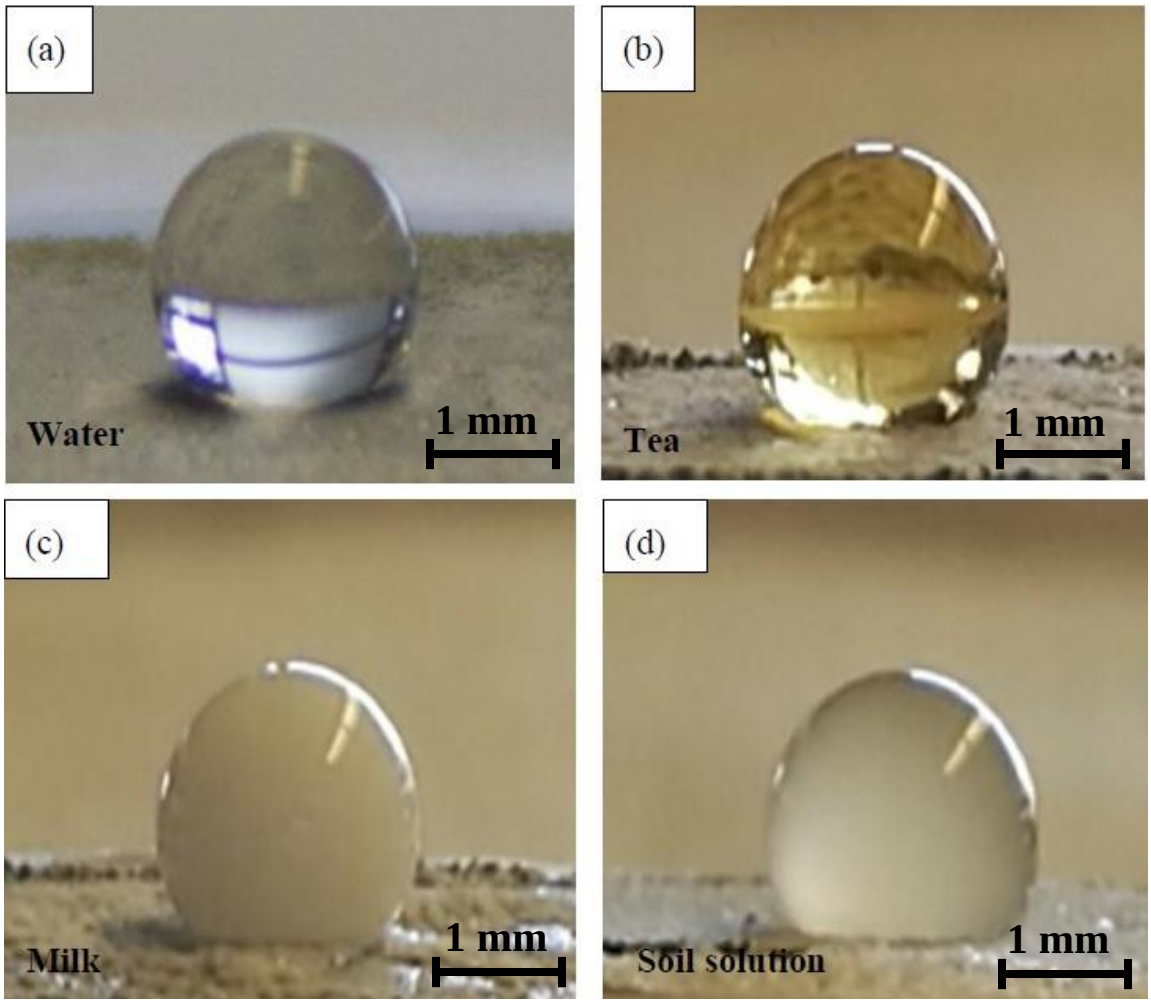

Fig. 7.10 Optical top-views of a droplet of (a) water, (b) tea, (c) milk, (d) a soil solution on the surface of the Zn nano-film prepared under the electrodepositing current density of 100 mA/cm^2 for 20 mins and followed by stearic acid modification.

Fig. 7.11 shows the antifouling performance of the superhydrophobic Zn nano-film, the steel treated by stearic acid, and the bare steel, respectively, after 1 min and 1 h of immersion in a mud water with the mud content of 100 kg/m^3. It is seen that the superhydrophobic Zn nano-film is very clean without mud water remnant after 1 min of

immersion. As a comparison, there are some mud water signs on both the stearic acid modified steel and bare steel, as shown in Fig. 7.11a. After 1 h of immersion in the mud water, there are extensive brown liquid and iron rusts on the bare steel, and some brown mud and rusts on the stearic acid modified steel surface. However, the superhydrophobic Zn nano-film surface remains its original clean state, without any contaminant observed.

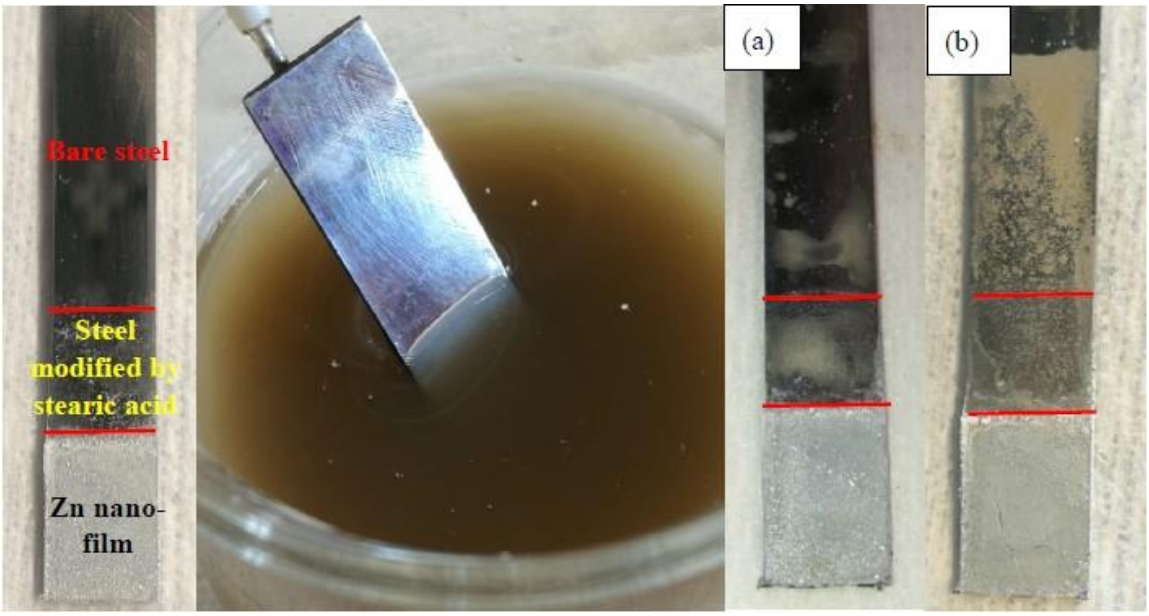

Fig. 7.11 Antifouling performance of the superhydrophobic Zn nano-film, the steel treated by stearic acid, and the bare steel, respectively, after (a) 1 min and (b) 1 h of immersion in a mud liquid with the mud content of 100 kg/m^3.

The self-cleaning property of the prepared Zn nano-film is also investigated by spreading soil as contaminant on its surface. The self-cleaning performance of the Zn nano-film forming at the current density of 100 mA/cm^2 for 20 mins followed by stearic acid modification is shown in Fig. 7.12. Soil is spread on the surface of the Zn nano-film.

The surface is then washed by distilled water, while the specimen is maintained at an inclination angle of 10 - 15°. The soil present on the Zn nano-film is immediately dissolved with water and is washed away. The film surface becomes very clean, indicating an excellent antifouling ability of the prepared Zn nano-film.

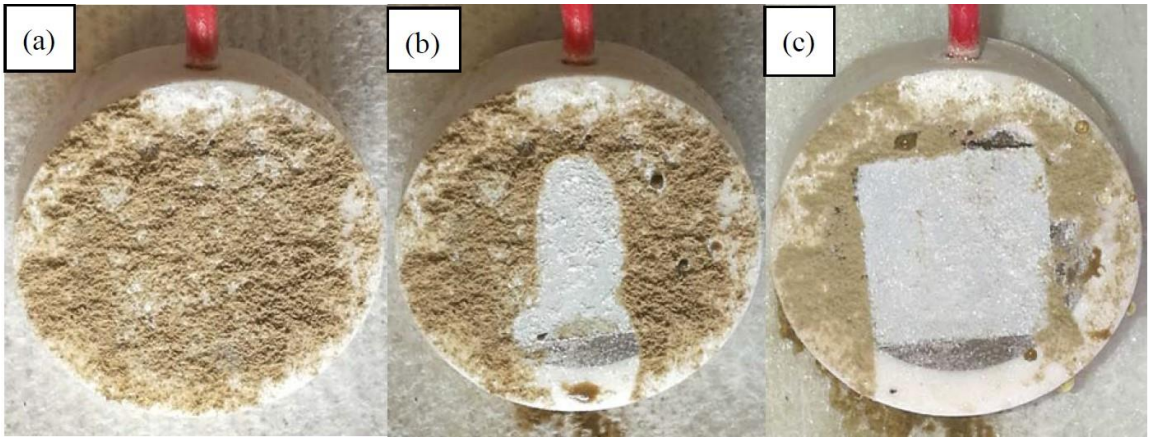

Fig. 7.12 Self-cleaning property of the superhydrophobic Zn nano-film prepared at the current density of 100 mA/cm^2 for 20 mins followed by stearic acid modification was investigated by spreading soil as contaminant on its surface. (a) Spread soil on the Zn nano-film, (b) Clean with distilled water, (c) Soil completely removed from the film, while the soil remains on the epoxy holder.

The antifouling and self-cleaning properties of the prepared Zn nano-film is due to the joint action of the micro-/nanoscale structure of the film and the generation of a low energy surface by stearic acid modification. As mentioned, the micro-/nanoscale surface structure of the Zn film can trap air and restrain the contact of dirt with the substrate. At

the same time, the treatment of the Zn film by stearic acid decreases the surface energy, further preventing direct contact of liquid and solid dirt with the Zn film.

7.3.5 Corrosion Resistance of the Prepared Zn Nano-films

Fig. 7.13 shows the EIS Bode diagrams measured on the steel specimen after 20 mins of electrodeposition under the current density of 100 mA/cm^2 followed by stearic acid modification in 3.5% NaCl solution. As a comparison, the measurements on bare steel and the electrodeposited Zn nano-film without stearic acid treatment are also included. It is seen that, for bare steel, the maximum phase angle appears in the middle frequency range, and the low-frequency impedance is 10^3 Ω cm^2 only, indicating that the steel experiences active corrosion in the solution. The EIS data measured on the bare steel is thus fitted with the equivalent circuit shown in Fig. 7.14a, where R_s is solution resistance, and Q_{dl} and R_{ct} are the constant phase element modelling the double-charge layer capacitance and charge-transfer resistance, respectively. The constant-phase element is related to the capacitance of the double-charge layer (C_{dl}) by [179]:

$$C_{dl} = (Q_{dl} \times R_{ct}^{1-n})^{1/n} \quad (7\text{-}3)$$

where n is the empirical exponent. The value of 1 for the exponent n indicates that the electrode closes to an ideal capacitor.

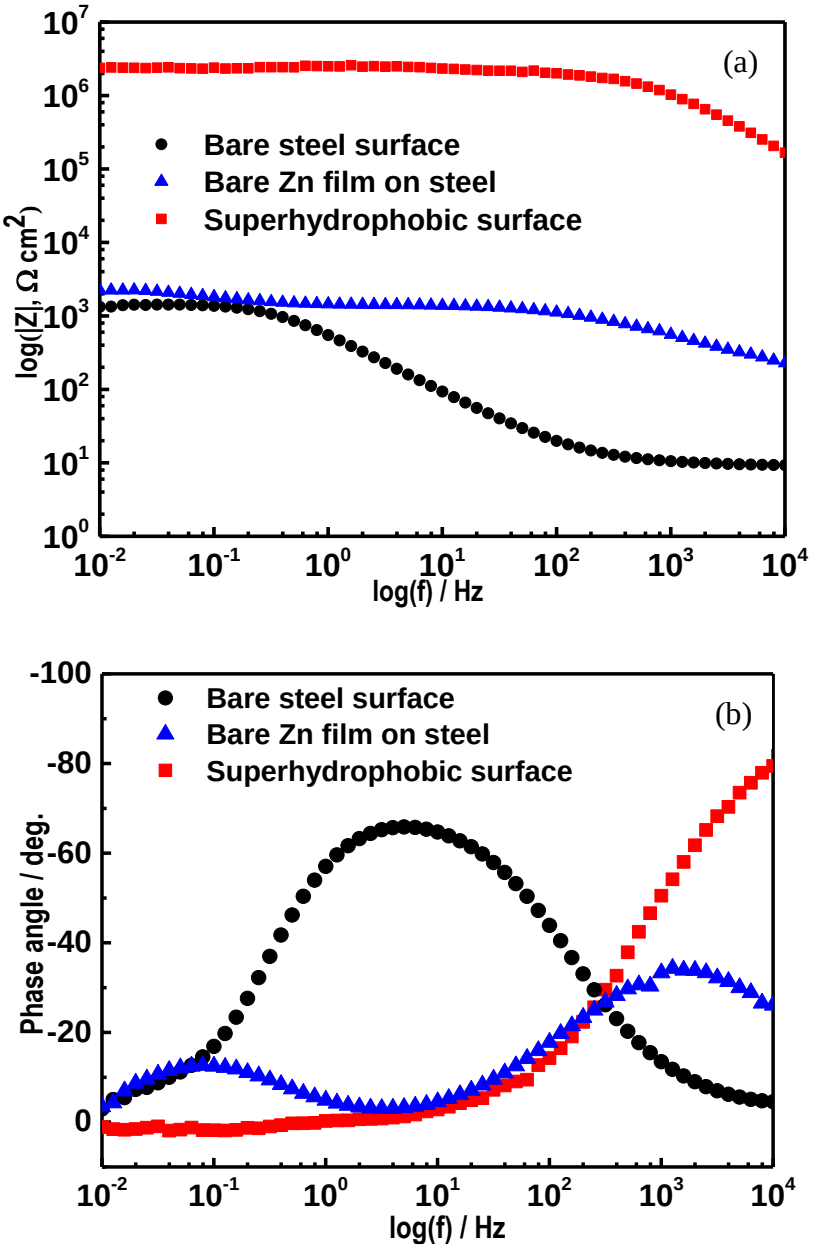

Fig. 7.13 EIS Bode diagrams measured on the steel specimen after 20 mins of electrodeposition under the current density of 100 mA/cm^2 followed by stearic acid modification in 3.5% NaCl solution. (a) Impedance modulus plots, (b) Phase angle plots. As a comparison, the measurements on bare steel and the electrodeposited Zn nano-film without stearic acid modification are also included.

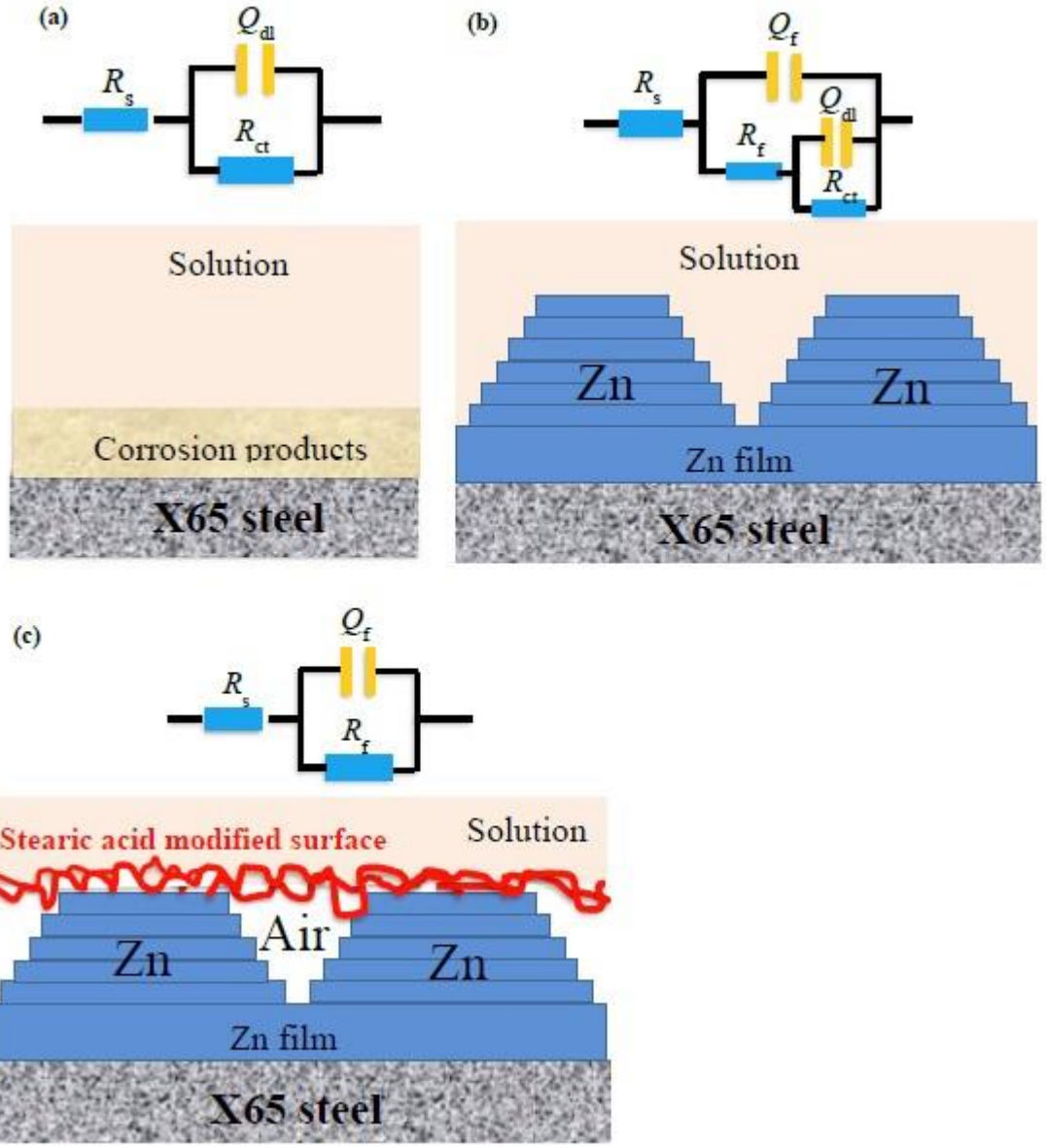

Fig. 7.14 Electrochemical equivalent circuits used to fit the measured impedance data. (a) Bare steel, (b) Steel with Zn nano-film without the stearic acid modification, (c) Superhydrophobic Zn nano-film modified by stearic acid.

For the electrodeposited Zn nano-film without stearic acid modification, two maximum values of phase angle are observed in the high and low frequency ranges,

respectively, which are associated with the electrochemical responses from the Zn film and the charge-transfer reaction, respectively. The equivalent circuit shown in Fig. 7.14b is used to fit the impedance results, where R_f is the film resistance and Q_f is the constant phase element modelling the film capacitance. Without modified by stearic acid, the solution can enter the space between Zn particles to cause corrosion of the zinc film.

When the electrodeposited Zn nano-film is modified by stearic acid to form a layer with a low surface energy, there is only one maximum phase angle in the high frequency end and the phase angle of zero over the majority of the measuring frequency range, as seen in Fig. 7.13b. This is associated with a resistive impedance feature. The low-frequency impedance is approximately over three orders of magnitude higher than those of bare steel and the Zn nano-film without the stearic acid modification. Thus, the superhydrophobic Zn nano-film upon stearic acid modification provides an excellent corrosion protection to the substrate steel in chloride solution. The equivalent circuit in Fig. 7.14c is used to fit the impedance data measured on the superhydrophobic film in the solution, where the capacitive superhydrophobic film dominates the impedance behavior.

Table 7.1 lists the fitted electrochemical impedance parameters of bare steel, Zn nano-film without stearic acid modification, and the superhydrophobic Zn nano-film with stearic acid modification, respectively. It is seen that the electrodeposited Zn nano-film has similar R_{ct} to the bare steel. The Zn film generally acts as a sacrificial anode for corrosion protection to the substrate steel. The electrolyte contacts the film and causes corrosion of Zn. This work thus demonstrates that the micro-/nanoscale structure of the electrodeposited Zn films does not possess the ability for corrosion protection. Instead, it serves as the foundation to generate a superhydrophobic film upon the stearic acid

modification. The charge transfer cannot occur in the film where air is trapped. As a result, a closed current circuit enabling electrochemical corrosion reaction is not established between the steel/Zn and the solution because of the insulating effect of the superhydrophobic film.

Table 7.1 The electrochemical impedance parameters fitted from the measured impedance data in Fig. 7.13.

Specimen	R_f (Ω cm^2)	Q_f		C_f (F/cm^2)	R_{ct} (Ω cm^2)	Q_{dl}		C_{dl} (F/cm^2)
		Y (Ω^{-1}cm^{-2}s^n)	n			Y (Ω^{-1}cm^{-2}s^n)	n	
Bare steel	-	-	-	-	1027.00 ±16.40	(5.27±0.12) ×10^{-4}	0.80 ±0.05	(4.52±0.18) ×10^{-6}
Zn nano-film, without stearic acid modification	1319.13 ±10.62	(5.83±0.30) ×10^{-5}	0.71 ±0.06	(1.94±0.02) ×10^{-5}	1249.48 ±15.45	(2.30±0.01) ×10^{-4}	0.84 ±0.03	(5.86±0.23) ×10^{-5}
Superhydrophobic Zn nano-film with stearic acid modification	(2.29±0.05) ×10^6	(3.54±0.85) ×10^{-9}	0.80 ±0.02	(1.06±0.01) ×10^{-9}	-	-	-	

7.4 Summary

Hydrophobic and superhydrophobic zinc nano-films are fabricated on steel by electrodeposition and stearic acid modification. The superhydrophobicity of the films is resulted from formation of a layered micro-/nanoscale surface microstructure and the presence of the stearic acid layer which has a low surface energy.

The morphological and structural features of the Zn nano-films depend on the electrodepositing current density and time. The optimal condition for electrodeposition is

under the current density of 100 mA/cm^2 for 20 mins, under which an “air-cushion” typed micro-/nanoscale structure is produced, which, combined with the stearic acid modification, results in the surface superhydrophobity. The water contact angle is up to 158.4 ± 1.5°. It is estimated that the air-occupied part of the total contact area between the water droplet and the micro-/nanoscale structured Zn film is up to 90.8%. Only 9.2% of the surface area contacts water. The Zn nano-film prepared under the optimal electrodepositing condition and stearic acid modification is also oleophobic, with the oil contact angle increasing from 8.6° on bare steel to 48.1° on the film. In addition to the superhydrophobity in water droplet, the prepared Zn nano-film is also superhydrophobic to the droplet of tea, milk and a soil solution.

The prepared superhydrophobic Zn nano-film possesses an excellent antifouling and self-cleaning property in a mud liquid and under soil spreading on the film surface. This is also attributed to the joint action of the micro-/nanoscale surface structure of the electrodeposited Zn film and the stearic acid layer with a low surface energy.

The prepared superhydrophobic Zn nano-film provides an excellent corrosion protection to the substrate steel in chloride solution. The measured low-frequency impedance is approximately over three orders of magnitude higher than those of bare steel and the Zn nano-film without the stearic acid modification. The micro-/nanoscale structure of the electrodeposited Zn films does not possess the ability for corrosion protection. Instead, it serves as the foundation to generate a superhydrophobic film upon the stearic acid modification.

Chapter Eight: Conclusions and recommendations

8.1 Conclusions

Nanocontainers for encapsulation of corrosion inhibitors were successful fabricated to develop intelligent coatings for steel corrosion protection. The mechanism for triggering the self-releasing of pre-loaded inhibitors from the nanocontainers was determined. The releasing kinetics of the inhibitor molecules was derived based on numerical calculation and experimental verification. Moreover, a superhydrophobic nano Zn film was developed on steel surface for enhanced self-cleaning and anticorrosion performance. Primary conclusions are drawn as follows.

Inhibitors BTA are able to effectively inhibit corrosion of pipeline steels in bicarbonate solutions. The inhibiting efficiency is increased by the increasing inhibitor concentration. A layer of smooth, adsorptive inhibitor film with a surface roughness of nanometer scale is formed on the steel surface for corrosion prevention.

An epoxy coating contains the mass ratio of DGEBA to NAEP of 1:0.29, i.e., 10% more hardener than the ideal stoichiometric ratio, is prepared with a good cross-linking and cured performance. The fabricated multi-layered Halloysite nanocontainers have a more uniform scale and better dispersion than the as-received Halloysite particles. The coating containing Halloysite nanocontainers possesses enhanced corrosion resistance. With the increase of the content of the Halloysite nanocontainers in the coating, the corrosion resistance is further improved. The prepared Halloysite nanocontainers are highly compatible with the epoxy coating in terms of the corrosion protection. For inhibitors BTA pre-loaded in the fabricated SiO_2 nanoparticle based polyelectrolyte

nanocontainers, the inhibitor releasing is pH selective. The inhibitors can self-release into the solution to inhibit the steel corrosion at either low or high pH values. In pH 2 and pH 11 solutions, the added BTA-loaded nanocontainers decrease the corrosion rate of the steel, with an inhibition efficiency up to 64% and 71% after 48 h of testing, respectively. The corrosion inhibition by BTA is through the formation of an inhibitor film on the steel surface by physical and chemical adsorption, which is influenced by solution pH. The Korsmeyer–Peppas model is appropriate to illustrate and predict the releasing of BTA inhibitors from the nanocontainers in response to pH changes, providing information on the releasing rate of the preloaded BTA inhibitors. In solutions with pH 5 and 9, the inhibitor molecules show a non-Fickian, diffusion-controlled transport mechanism with a limited releasing. When the solution pH is at 2 or 11, the BTA molecules follow the super-relaxational transport mechanism to release from the nanocontainers by swelling-controlled releasing processes.

Encapsulation of BTA inhibitors in the prepared SiO_2 nanoparticle based polyelectrolyte nanocontainers is an effective method to fabricate intelligent coatings. The nanocontainers have a smooth surface with a globular geometry. There are about 6.7 wt.% of inhibitors loaded in the nanocontainer. The prepared BTA-encapsulated nanocontainers are dispersed uniformly in an industry-used epoxy coating. The doping of the nanocontainers would not change the chemical cross-linking structure of the coating, which means that it has a good compatibility with the industrial in-use epoxy coating. The content of the doped nanocontainers in the coating is a critical parameter to affect the anticorrosion performance of the coating and the corrosion resistance of the substrate steel. With the increasing content of the BTA-encapsulated nanocontainers in the coating,

both the coating resistance and the corrosion resistance of the steel increase, resulting in a reduced corrosion.

A layered micro-/nanoscale surface microstructure and the presence of the stearic acid layer which has a low surface energy is used to fabricate superhydrophobic zinc nano-films on steel surface by electrodeposition method. The optimal condition for electrodeposition is under the current density of 100 mA/cm^2 for 20 mins, under which an "air-cushion" typed micro-/nanoscale structure is produced, which results in the surface superhydrophobity with the water contact angle up to 158.4 ± 1.5°. Up to 90.8% of the total contact area between the water droplet and the micro-/nanoscale structured Zn film is the air-occupied part. Only 9.2% of the surface area contacts water. The surface is also oleophobic, with the oil contact angle increasing from 8.6° on bare steel to 48.1° on the film. In addition to the superhydrophobity in water droplet, the prepared Zn nano-film is also superhydrophobic to the droplet of tea, milk and a soil solution. The prepared superhydrophobic Zn nano-film possesses an excellent antifouling and self-cleaning property in a mud liquid and under soil spreading on the film surface. The prepared superhydrophobic Zn nano-film provides an excellent corrosion protection to the substrate steel in chloride solution. The measured low-frequency impedance is approximately over three orders of magnitude higher than those of bare steel and the Zn nano-film without the stearic acid modification.

8.2 Recommendations

This research advances development of functional coating technology for corrosion protection. Further work is recommended to improve the applicability of the research

outcomes in practice, and if possible, combine those two technologies to further improve the anticorrosion performance.

1) The fabricating method of intelligent coating technologies should be refined to produce the intelligent coating in large scale to meet the industrial use. The fabrication method is very reproducible at a lab scale. Industrial using focuses on a large scale of production of the intelligent coating to meet the actual needs.
2) It is meaningful to extend the concept of intelligent capsules to other coatings that have been used in industry. The home-made SiO_2 capsules with pre-loaded inhibitors have already been demonstrated with a very good compatibility with the commercial epoxy coating. The concept can be used for other coatings such as polyethylene based coatings, composite coatings, etc.
3) The method to increase the durability of superhydrophobic coatings on steels is a direction for further research. The further research can focus on development of high performance superhydrophobic coatings with a higher water contact angle and oil contact angle with a durable service life.

References

[1] R.W. Revie, H.H. Uhlig, Corrosion and corrosion control: an introduction to corrosion science and engineering, 4th ed, John Wiley & Sons, (2008).

[2] P.R. Roberge, Corrosion engineering principles practice, McGraw-Hill (2008).

[3] L.T. Popoola, A.S. Grema, G.K. Latinwo, B. Gutti, A.S. Balogun, Corrosion problems during oil and gas production and its mitigation, International Journal of Industrial Chemistry, 4 (2013) 1-15.

[4] Protecting and Maintaining Transmission Pipelines, eBook published by Journal of Protective Coatings & Linings (JPCL) (2012).

[5] E. Brooman, Modifying organic coatings to provide corrosion resistance—Part I: Background and general principles, Metal finishing, 100 (2002) 48-53.

[6] S. Roux, P. Audebert, J. Pagetti, M. Roche, Design of a new bilayer polypyrrole–xerogel hybrid coating for corrosion protection, Journal of Materials Chemistry, 11 (2001) 3360-3366.

[7] S. Papavinasam, R.W. Revie, Coatings for pipelines, Coatings for corrosion protection: offshore oil and gas operation facilities, marine pipelines, and ship structures, Ed. C. , 1035 (2004) 178.

[8] D. Snihirova, S. Lamaka, M. Taryba, A. Salak, S. Kallip, M. Zheludkevich, M. Ferreira, M. Montemor, Hydroxyapatite microparticles as feedback-active reservoirs of corrosion inhibitors, ACS applied materials & interfaces, 2 (2010) 3011-3022.

[9] S.K. Ghosh, Self-healing materials: fundamentals, design strategies, and applications, John Wiley & Sons, 2009.

[10] M.D. Hager, P. Greil, C. Leyens, S. van der Zwaag, U.S. Schubert, Self‐healing materials, Advanced Materials, 22 (2010) 5424-5430.

[11] J.S. Park, K. Takahashi, Z. Guo, Y. Wang, E. Bolanos, C. Hamann-Schaffner, E. Murphy, F. Wudl, H.T. Hahn, Towards development of a self-healing composite using a mendable polymer and resistive heating, Journal of Composite Materials, 42 (2008) 2869-2881.

[12] D. Grigoriev, D. Akcakayiran, M. Schenderlein, D. Shchukin, Protective organic coatings with anticorrosive and other feedback-active features: micro-and nanocontainers-based approach, Corrosion, 70 (2013) 446-463.

[13] C. Challener, The intelligence behind smart coatinqs, JCT coatingstech, 3 (2006) 50-55.

[14] M.F. Montemor, Functional and smart coatings for corrosion protection: A review of recent advances, Surface & Coatings Technology, 258 (2014) 17-37.

[15] G. Koch, J. Varney, N. Thompson, O. Moghissi, M. Gould, J. Payer, International measures of prevention, application, and economics of corrosion technologies study, in, NACE International, 2016.

[16] E. McCafferty, Introduction to corrosion science, Springer, (2010).

[17] R.W. Revie, Uhlig's corrosion handbook, (2011).

[18] K. Nalli, Corrosion and its mitigation in the Oil & Gas industry–An overview, Pmpipeliner, Jan-Mar 2010 report, (2010).

[19] F. CHENG, Controversy contained, World pipelines, 13 (2013) 50-54.

[20] J. Leeds, S. Leeds, Control of external corrosion on underground or submerged metallic piping systems, Journal of Pipeline & Gas, 231 (2013) 32-35.

[21] S. Papavinasam, Corrosion control in the oil and gas industry, Elsevier, (2014).

[22] L. Niu, Y.F. Cheng, Development of innovative coating technology for pipeline operation crossing the permafrost terrain, Construction and Building Materials, 22 (2008) 417-422.

[23] J.A. Kehr, FBE pipeline and rebar corrosion coatings, in, Ottawa: NACE National Corrosion Co/-zfP3" e13, 2000.

[24] J. Perdomo, I. Song, Chemical and electrochemical conditions on steel under disbonded coatings: the effect of applied potential, solution resistivity, crevice thickness and holiday size, Corrosion Science, 42 (2000) 1389-1415.

[25] X. Shi, T.A. Nguyen, Z. Suo, Y. Liu, R. Avci, Effect of nanoparticles on the anticorrosion and mechanical properties of epoxy coating, Surface & Coatings Technology, 204 (2009) 237-245.

[26] D. Kuang, Y.F. Cheng, Study of cathodic protection shielding under coating disbondment on pipelines, Corrosion Science, 99 (2015) 249-257.

[27] S.A. Shipilov, I. Le May, Structural integrity of aging buried pipelines having cathodic protection, Engineering Failure Analysis, 13 (2006) 1159-1176.

[28] Y.F. Cheng, Stress corrosion cracking of pipelines, John Wiley & Sons, 2013.

[29] M. Baker, Department of transportation, office of pipeline safety, TTO Number 10, Integrity management program–dent study, Delivery Order DTRS56-02-D-70036, final report, (2004).

[30] A. Eslami, B. Fang, R. Kania, B. Worthingham, J. Been, R. Eadie, W. Chen, Stress corrosion cracking initiation under the disbonded coating of pipeline steel in near-neutral pH environment, Corrosion Science, 52 (2010) 3750-3756.

[31] R.V. Dennis, L.T. Viyannalage, J.P. Aldinger, T.K. Rout, S. Banerjee, Nanostructured magnesium composite coatings for corrosion protection of low-alloy steels, Industrial & Engineering Chemistry Research, 53 (2014) 18873-18883.

[32] E.V. Skorb, A.G. Skirtach, D.V. Sviridov, D.G. Shchukin, H. Möhwald, Laser-Controllable Coatings for Corrosion Protection, ACS Nano, 3 (2009) 1753-1760.

[33] A.S. Kumar, H. Bhandari, C. Sharma, F. Khatoon, S.K. Dhawan, A new smart coating of polyaniline-SiO2 composite for protection of mild steel against corrosion in strong acidic medium, Polymer International, 62 (2013) 1192-1201.

[34] Y. Shao, H. Huang, T. Zhang, G. Meng, F. Wang, Corrosion protection of Mg-5Li alloy with epoxy coatings containing polyaniline, Corrosion Science, 51 (2009) 2906-2915.

[35] A.S.H. Makhlouf, Handbook of smart coatings for materials protection, (2014).

[36] E. Brooman, Modifying organic coatings to provide corrosion resistance: Part II—Inorganic additives and inhibitors, Metal Finishing, 100 (2002) 42-53.

[37] A.S.H. Makhlouf, Handbook of smart coatings for materials protection, Elsevier, 2014.

[38] A. Hartwig, M. Sebald, D. Pütz, L. Aberle, Preparation, characterisation and properties of nanocomposites based on epoxy resins–An overview, Macromolecular symposia, 221 (2005) 127-136.

[39] F. Dietsche, Y. Thomann, R. Thomann, R. Mülhaupt, Translucent acrylic nanocomposites containing anisotropic laminated nanoparticles derived from intercalated layered silicates, Journal of applied polymer science, 75 (2000) 396-405.

[40] O. Becker, R. Varley, G. Simon, Morphology, thermal relaxations and mechanical properties of layered silicate nanocomposites based upon high-functionality epoxy resins, Polymer, 43 (2002) 4365-4373.

[41] S.V. Lamaka, M.L. Zheludkevich, K.A. Yasakau, R. Serra, S. Poznyak, M. Ferreira, Nanoporous titania interlayer as reservoir of corrosion inhibitors for coatings with self-healing ability, Progress in organic coatings, 58 (2007) 127-135.

[42] D.V. Andreeva, D.G. Shchukin, Smart self-repairing protective coatings, Materials Today, 11 (2008) 24-30.

[43] R. Dubey, Microencapsulation technology and applications, Defence Science Journal, 59 (2009) 82.

[44] X. He, X. Shi, Self-repairing coating for corrosion protection of aluminum alloys, Progress in Organic Coatings, 65 (2009) 37-43.

[45] G.L. Li, M. Schenderlein, Y. Men, H. Möhwald, D.G. Shchukin, Monodisperse polymeric core-shell nanocontainers for organic self‐healing anticorrosion coatings, Advanced Materials Interfaces, 1 (2014).

[46] C.Y. Zhang, X.B. Jiang, M.Z. Rong, M.Q. Zhang, Free radical polymerization aided self-healing, Journal of Intelligent Material Systems and Structures, 25 (2014) 31-39.

[47] A. Latnikova, D.O. Grigoriev, H. Möhwald, D.G. Shchukin, Capsules made of cross-linked polymers and liquid core: possible morphologies and their estimation on the basis of hansen solubilityparameters, The Journal of Physical Chemistry C, 116 (2009) 8181-8187.

[48] D.G. Shchukin, S.V. Lamaka, K.A. Yasakau, M.L. Zheludkevich, M.G.S. Ferreira, H. Mohwald, Active anticorrosion coatings with halloysite nanocontainers, J Phys Chem C, 112 (2008) 958-964.

[49] E. Abdullayev, Y. Lvov, Halloysite clay nanotubes for controlled release of protective agents, J Nanosci Nanotechnol, 11 (2011) 10007-10026.

[50] E. Abdullayev, R. Price, D. Shchukin, Y. Lvov, Halloysite tubes as nanocontainers for anticorrosion coating with benzotriazole, ACS Appl Mater Interfaces, 1 (2009) 1437-1443.

[51] D. Borisova, H. Mohwald, D.G. Shchukin, Influence of embedded nanocontainers on the efficiency of active anticorrosive coatings for aluminum alloys part I: influence of nanocontainer concentration, ACS Appl Mater Interfaces, 4 (2012) 2931-2939.

[52] D. Borisova, H. Möhwald, D.G. Shchukin, Influence of embedded nanocontainers on the efficiency of active anticorrosive coatings for aluminum alloys part II: influence of nanocontainer position, ACS Applied Materials & Interfaces, 5 (2013) 80-87.

[53] D.O. Grigoriev, K. Koehler, E. Skorb, D.G. Shchukin, H. Moehwald, Polyelectrolyte complexes as a "smart" depot for self-healing anticorrosion coatings, Soft Matter, 5 (2009) 1426-1432.

[54] D.G. Shchukin, H. Möhwald, Surface-engineered nanocontainers for entrapment of corrosion inhibitors, Advanced Functional Materials, 17 (2007) 1451-1458.

[55] D.V. Andreeva, E.V. Skorb, D.G. Shchukin, Layer-by-layer polyelectrolyte/inhibitor nanostructures for metal corrosion protection, ACS Applied Materials & Interfaces, 2 (2010) 1954-1962.

[56] G. Williams, S. Geary, M. Loveridge, H.N. McMurray, Smart-release inhibition of corrosion-driven organic coating delamination on galvanized steel surfaces, in: M. Rohwerder, V.J. Gelling (Eds.) Coatings for Corrosion Protection, 2012, pp. 93-103.

[57] M. Zheludkevich, R. Serra, M. Montemor, K. Yasakau, I.M. Salvado, M. Ferreira, Nanostructured sol–gel coatings doped with cerium nitrate as pre-treatments for AA2024-T3: corrosion protection performance, Electrochimica Acta, 51 (2005) 208-217.

[58] M.D. Wang, M.Y. Liu, J.J. Fu, An intelligent anticorrosion coating based on pH-responsive smart nanocontainers fabricated via a facile method for protection of carbon steel, Journal of Materials Chemistry A, 3 (2015) 6423-6431.

[59] J. Fu, T. Chen, M. Wang, N. Yang, S. Li, Y. Wang, X. Liu, Acid and alkaline dual stimuli-responsive mechanized hollow mesoporous silica nanoparticles as smart nanocontainers for intelligent anticorrosion coatings, ACS Nano, 7 (2013) 11397-11408.

[60] Y. He, W. Xu, R. Tang, C. Zhang, Q. Yang, pH-responsive nanovalves based on encapsulated halloysite for the controlled release of a corrosion inhibitor in epoxy coating, RSC Advances, 5 (2015) 90609-90620.

[61] T. Chen, J. Fu, pH-responsive nanovalves based on hollow mesoporous silica spheres for controlled release of corrosion inhibitor, Nanotechnology, 23 (2012) 235605.

[62] H. Shi, F. Liu, E.-H. Han, Surface-engineered microcapsules by layer-by-layer assembling for entrapment of corrosion inhibitor, Journal of Materials Science & Technology, 31 (2015) 512-516.

[63] G. Williams, H.N. McMurray, M.J. Loveridge, Inhibition of corrosion-driven organic coating disbondment on galvanised steel by smart release group II and Zn(II)-exchanged bentonite pigments, Electrochimica Acta, 55 (2010) 1740-1748.

[64] G. Williams, S. Geary, H.N. McMurray, Smart release corrosion inhibitor pigments based on organic ion-exchange resins, Corrosion Science, 57 (2012) 139-147.

[65] A. Kumar, L. Stephenson, J.N. Murray, Self-healing coatings for steel, Progress in Organic Coatings, 55 (2006) 244-253.

[66] M. Ma, R.M. Hill, Superhydrophobic surfaces, Current Opinion in Colloid & Interface Science, 11 (2006) 193-202.

[67] K.C. Chang, H.I. Lu, C.W. Peng, M.C. Lai, S.C. Hsu, M.H. Hsu, Y.K. Tsai, C.H. Chang, W.I. Hung, Y. Wei, J.M. Yeh, Nanocasting technique to prepare lotus-leaf-like superhydrophobic electroactive polyimide as advanced anticorrosive coatings, ACS Appl Mater Interfaces, 5 (2013) 1460-1467.

[68] C.T. Hsieh, S.Y. Yang, J.Y. Lin, Electrochemical deposition and superhydrophobic behavior of ZnO nanorod arrays, Thin Solid Films, 518 (2010) 4884-4889.

[69] Y.Q. Qing, C.N. Yang, Z.Y. Yu, Z.F. Zhang, Q.L. Hu, C.S. Liu, Large-area fabrication of superhydrophobic zinc surface with reversible wettability switching and anticorrosion, Journal of the Electrochemical Society, 163 (2016) D385-D391.

[70] S.H. He, M.J. Zheng, L.J. Yao, X.L. Yuan, M. Li, L. Ma, W.Z. Shen, Preparation and properties of ZnO nanostructures by electrochemical anodization method, Applied Surface Science, 256 (2010) 2557-2562.

[71] L. Oberli, D. Caruso, C. Hall, M. Fabretto, P.J. Murphy, D. Evans, Condensation and freezing of droplets on superhydrophobic surfaces, Advances in colloid and interface science, 210 (2014) 47-57.

[72] Y.Y. Yan, N. Gao, W. Barthlott, Mimicking natural superhydrophobic surfaces and grasping the wetting process: a review on recent progress in preparing superhydrophobic surfaces, Adv Colloid Interface Sci, 169 (2011) 80-105.

[73] A. Cassie, S. Baxter, Wettability of porous surfaces, Transactions of the Faraday society, 40 (1944) 546-551.

[74] R.N. Wenzel, Resistance of solid surfaces to wetting by water, Industrial & Engineering Chemistry, 28 (1936) 988-994.

[75] H.Y. Wang, Y.X. Zhu, Z.Y. Hu, X.G. Zhang, S.Q. Wu, R. Wang, Y.J. Zhu, A novel electrodeposition route for fabrication of the superhydrophobic surface with unique self-cleaning, mechanical abrasion and corrosion resistance properties, Chemical Engineering Journal, 303 (2016) 37-47.

[76] R. Blossey, Self-cleaning surfaces-virtual realities, Nature materials, 2 (2003) 301-306.

[77] M. Laurenti, A. Verna, M. Fontana, S. Stassi, G. Canavese, S.L. Marasso, V. Cauda, How micropatterning and surface functionalization affect the wetting behavior of ZnO nanostructured surfaces, Advanced Materials Interfaces, 3 (2016).

[78] H. Li, S.R. Yu, X.X. Han, Preparation of a biomimetic superhydrophobic ZnO coating on an X90 pipeline steel surface, New Journal of Chemistry, 39 (2015) 4860-4868.

[79] Y.-q. Qing, C.-n. Yang, Y.-z. Sun, Y.-s. Zheng, Y. Shang, C.-s. Liu, Simple method for preparing ZnO superhydrophobic surfaces with micro/nano roughness, Journal of Adhesion Science and Technology, 29 (2015) 2153-2159.

[80] G. Wang, Z.X. Zeng, J.J. Chen, M.Y. Xu, J.F. Zhu, S. Liu, T.H. Ren, Q.J. Xue, Ultra low water adhesive metal surface for enhanced corrosion protection, Rsc Advances, 6 (2016) 40641-40649.

[81] X.-F. Zhang, R.-J. Chen, J.-M. Hu, Superhydrophobic surface constructed on electrodeposited silica films by two-step method for corrosion protection of mild steel, Corrosion Science, 104 (2016) 336-343.

[82] H. Li, S. Yu, X. Han, Fabrication of CuO hierarchical flower-like structures with biomimetic superamphiphobic, self-cleaning and corrosion resistance properties, Chemical Engineering Journal, 283 (2016) 1443-1454.

[83] V. Pandarinathan, K. Lepkova, S.I. Bailey, T. Becker, R. Gubner, Adsorption of corrosion inhibitor 1-dodecylpyridinium chloride on carbon steel studied by in situ AFM and electrochemical methods, Industrial & Engineering Chemistry Research, 53 (2014) 5858-5865.

[84] T. Kosec, I. Milosev, B. Pihlar, Benzotriazole as an inhibitor of brass corrosion in chloride solution, Applied Surface Science, 253 (2007) 8863-8873.

[85] Q. Qu, S. Jiang, W. Bai, L. Li, Effect of ethylenediarnine tetraacetic acid disodium on the corrosion of cold rolled steel in the presence of benzotriazole in hydrochloric acid, Electrochimica Acta, 52 (2007) 6811-6820.

[86] S. John, A. Joseph, Electroanalytical studies of the corrosion-protection properties of 4-amino-4H-1,2,4-triazole-3,5-dimethanol (ATD) on mild steel in 0.5 N sulfuric acid, Research on Chemical Intermediates, 38 (2012) 1359-1373.

[87] Y. Miao, S. Wang, C. Wang, Y. Liu, M. Sun, Y. Chen, Effect of chelating agent on benzotriazole removal during post copper chemical mechanical polishing cleaning, Microelectronic Engineering, 130 (2014) 18-23.

[88] A.K. Singh, M. Quraishi, Inhibiting effects of 5-substituted isatin-based Mannich bases on the corrosion of mild steel in hydrochloric acid solution, Journal of Applied Electrochemistry, 40 (2010) 1293-1306.

[89] X. Li, S. Deng, H. Fu, T. Li, Adsorption and inhibition effect of 6-benzylaminopurine on cold rolled steel in 1.0 M HCl, Electrochimica Acta, 54 (2009) 4089-4098.

[90] M.T. Tobiszewski, A. Zieliński, K. Darowicki, Dynamic nanoimpedance characterization of the atomic force microscope tip-surface contact, Microscopy and Microanalysis, 20 (2014) 72-77.

[91] D. Kuang, Y. Cheng, Effect of alternating current interference on coating disbondment and cathodic protection shielding on pipelines, Corrosion Engineering, Science and Technology, 50 (2015) 211-217.

[92] A. Fu, Y. Cheng, Characterization of the permeability of a high performance composite coating to cathodic protection and its implications on pipeline integrity, Progress in Organic Coatings, 72 (2011) 423-428.

[93] E.V. Skorb, A.G. Skirtach, D.V. Sviridov, D.G. Shchukin, H. Möhwald, Laser-controllable coatings for corrosion protection, ACS nano, 3 (2009) 1753-1760.

[94] H. Li, D. Wei, J. Duan, J. Zhou, X. Min, Effect of sealing treatment on corrosion behaviours of arc sprayed zinc coatings, Corrosion Engineering, Science and Technology, 48 (2013) 65-70.

[95] Y. Wu, T. Liu, S. Luo, Corrosion characteristics of electroless Ni–P coating in dichloropropanol (DCP) solution, Corrosion Engineering, Science and Technology, 46 (2011) 245-248.

[96] S. Kumar, H. Bhandari, C. Sharma, F. Khatoon, S.K. Dhawan, A new smart coating of polyaniline–SiO2 composite for protection of mild steel against corrosion in strong acidic medium, Polymer International, 62 (2013) 1192-1201.

[97] M. Fedel, F. Deflorian, S. Rossi, P. Kamarchik, Study of the effect of mechanically treated CeO2 and SiO2 pigments on the corrosion protection of painted galvanized steel, Progress in Organic Coatings, 74 (2012) 36-42.

[98] M. Rostami, S. Rasouli, B. Ramezanzadeh, A. Askari, Electrochemical investigation of the properties of Co doped ZnO nanoparticle as a corrosion inhibitive pigment for modifying corrosion resistance of the epoxy coating, Corrosion Science, 88 (2014) 387-399.

[99] M.L. Zheludkevich, D.G. Shchukin, K.A. Yasakau, H. Möhwald, M.G. Ferreira, Anticorrosion coatings with self-healing effect based on nanocontainers impregnated with corrosion inhibitor, Chemistry of Materials, 19 (2007) 402-411.

[100] Y. Lvov, R. Price, B. Gaber, I. Ichinose, Thin film nanofabrication via layer-by-layer adsorption of tubule halloysite, spherical silica, proteins and polycations, Colloids and Surfaces A: Physicochemical and Engineering Aspects, 198 (2002) 375-382.

[101] D.G. Shchukin, S. Lamaka, K. Yasakau, M. Zheludkevich, M. Ferreira, H. Möhwald, Active anticorrosion coatings with halloysite nanocontainers, The Journal of Physical Chemistry C, 112 (2008) 958-964.

[102] D.G. Shchukin, H. Möhwald, Surface‐engineered nanocontainers for entrapment of corrosion inhibitors, Advanced Functional Materials, 17 (2007) 1451-1458.

[103] A. Fu, Y. Cheng, Effects of alternating current on corrosion of a coated pipeline steel in a chloride-containing carbonate/bicarbonate solution, Corrosion Science, 52 (2010) 612-619.

[104] E. Abdullayev, A. Joshi, W. Wei, Y. Zhao, Y. Lvov, Enlargement of halloysite clay nanotube lumen by selective etching of aluminum oxide, ACS nano, 6 (2012) 7216-7226.

[105] D.-Q. Yang, J.-F. Rochette, E. Sacher, Spectroscopic evidence for π− π interaction between poly (diallyl dimethylammonium) chloride and multiwalled carbon nanotubes, The Journal of Physical Chemistry B, 109 (2005) 4481-4484.

[106] S. Radhakrishnan, C. Siju, D. Mahanta, S. Patil, G. Madras, Conducting polyaniline–nano-TiO2 composites for smart corrosion resistant coatings, Electrochimica Acta, 54 (2009) 1249-1254.

[107] M. Alexandre, P. Dubois, Polymer-layered silicate nanocomposites: preparation, properties and uses of a new class of materials, Materials Science and Engineering: R: Reports, 28 (2000) 1-63.

[108] X. Shi, T.A. Nguyen, Z. Suo, Y. Liu, R. Avci, Effect of nanoparticles on the anticorrosion and mechanical properties of epoxy coating, Surface and Coatings Technology, 204 (2009) 237-245.

[109] Y. Feng, Y.F. Cheng, Fabrication of Halloysite nanocontainers and their compatibility with epoxy coating for anti-corrosion performance, Corrosion Engineering, Science and Technology, 51 (2016) 489-497.

[110] A. Khajouei, E. Jamalizadeh, A. Jafari, S. Hosseini, Layer-by-layer surfactants on silica nanoparticles for active corrosion protection, Corrosion Engineering, Science and Technology, 49 (2014) 743-748.

[111] M. Saremi, M. Yeganeh, Application of mesoporous silica nanocontainers as smart host of corrosion inhibitor in polypyrrole coatings, Corrosion Science, 86 (2014) 159-170.

[112] M. Haghayegh, S. Mirabedini, H. Yeganeh, Microcapsules containing multi-functional reactive isocyanate-terminated polyurethane prepolymer as a healing agent. Part 1: synthesis and optimization of reaction conditions, Journal of materials science, 51 (2016) 3056-3068.

[113] A. Latnikova, D.O. Grigoriev, H. Möhwald, D.G. Shchukin, Capsules made of cross-linked polymers and liquid core: possible morphologies and their estimation on the basis of hansen solubility parameters, The Journal of Physical Chemistry C, 116 (2012) 8181-8187.

[114] D. Borisova, D. Akcakayiran, M. Schenderlein, H. Mohwald, D.G. Shchukin, Nanocontainer-based anticorrosive coatings: effect of the container size on the self-healing performance, Advanced Functional Materials, 23 (2013) 3799-3812.

[115] W. Sun, L. Wang, T. Wu, M. Wang, Z. Yang, Y. Pan, G. Liu, Inhibiting the corrosion-promotion activity of graphene, Chemistry of Materials, 27 (2015) 2367-2373.

[116] E. Abdullayev, Y. Lvov, Halloysite clay nanotubes for controlled release of protective agents, Journal of nanoscience and nanotechnology, 11 (2011) 10007-10026.

[117] Y. Feng, Y. Cheng, Fabrication of Halloysite nanocontainers and their compatibility with epoxy coating for anti-corrosion performance, Corrosion Engineering, Science and Technology, 51 (2016) 489-497.

[118] P. Li, N.H. Kim, Siddaramaiah, J.H. Lee, Swelling behavior of polyacrylamide/laponite clay nanocomposite hydrogels: pH-sensitive property, Composites Part B: Engineering, 40 (2009) 275-283.

[119] G. Ruhi, H. Bhandari, S.K. Dhawan, Designing of corrosion resistant epoxy coatings embedded with polypyrrole/SiO2 composite, Progress in Organic Coatings, 77 (2014) 1484-1498.

[120] Y.H. Lei, N. Sheng, A. Hyono, M. Ueda, T. Ohtsuka, Effect of benzotriazole (BTA) addition on Polypyrrole film formation on copper and its corrosion protection, Progress in Organic Coatings, 77 (2014) 339-346.

[121] K. Zhang, L. Wang, W. Sun, G. Liu, Corrosion inhibitor embedded spherical micro-pits fabricated using cetyltrimethyl ammonium bromide as etching template for self-healing corrosion protection, Corrosion Science, 88 (2014) 444-451.

[122] Z. Chen, L. Huang, G. Zhang, Y. Qiu, X. Guo, Benzotriazole as a volatile corrosion inhibitor during the early stage of copper corrosion under adsorbed thin electrolyte layers, Corrosion Science, 65 (2012) 214-222.

[123] M.A. Bratescu, D.B. Allred, N. Saito, M. Sarikaya, O. Takai, Attenuated total reflectance spectroscopy of simultaneous processes: Corrosion inhibition of cuprous oxide by benzotriazole, Applied Surface Science, 254 (2008) 2960-2966.

[124] K. Ramya, R. Mohan, A. Joseph, Interaction of benzimidazoles and benzotriazole: its corrosion protection properties on mild steel in hydrochloric acid, Journal of materials engineering and performance, 23 (2014) 4089-4101.

[125] M. Mennucci, E. Banczek, P. Rodrigues, I. Costa, Evaluation of benzotriazole as corrosion inhibitor for carbon steel in simulated pore solution, Cement and Concrete Composites, 31 (2009) 418-424.

[126] A.K. Singh, M. Quraishi, Effect of Cefazolin on the corrosion of mild steel in HCl solution, Corrosion Science, 52 (2010) 152-160.

[127] A.K. Singh, M. Quraishi, The effect of some bis-thiadiazole derivatives on the corrosion of mild steel in hydrochloric acid, Corrosion Science, 52 (2010) 1373-1385.

[128] C. Jiang, S. Markutsya, Y. Pikus, V.V. Tsukruk, Freely suspended nanocomposite membranes as highly sensitive sensors, Nature materials, 3 (2004) 721-728.

[129] S. Zhao, F. Zhou, L. Li, M. Cao, D. Zuo, H. Liu, Removal of anionic dyes from aqueous solutions by adsorption of chitosan-based semi-IPN hydrogel composites, Composites Part B: Engineering, 43 (2012) 1570-1578.

[130] S. Dash, P.N. Murthy, L. Nath, P. Chowdhury, Kinetic modeling on drug release from controlled drug delivery systems, Acta Pol Pharm, 67 (2010) 217-223.

[131] R.W. Korsmeyer, R. Gurny, E. Doelker, P. Buri, N.A. Peppas, Mechanisms of solute release from porous hydrophilic polymers, International journal of pharmaceutics, 15 (1983) 25-35.

[132] D. Quintanar-Guerrero, B.N. Zorraquín-Cornejo, A. Ganem-Rondero, E. Piñón-Segundo, M.G. Nava-Arzaluz, J.M. Cornejo-Bravo, Controlled release of model substances from pH-sensitive hydrogels, Journal of the Mexican Chemical Society, 52 (2008) 272-278.

[133] P.L. Ritger, N.A. Peppas, A simple equation for description of solute release I. Fickian and non-Fickian release from non-swellable devices in the form of slabs, spheres, cylinders or discs, Journal of controlled release, 5 (1987) 23-36.

[134] P.L. Ritger, N.A. Peppas, A simple equation for description of solute release II. Fickian and anomalous release from swellable devices, Journal of controlled release, 5 (1987) 37-42.

[135] A. El-Warraky, H. El-Dahan, Corrosion inhibition of Al–bronze in acidified 4% NaCl solution, Journal of materials science, 32 (1997) 3693-3700.

[136] A. Yurt, A. Balaban, S.U. Kandemir, G. Bereket, B. Erk, Investigation on some Schiff bases as HCl corrosion inhibitors for carbon steel, Materials Chemistry and Physics, 85 (2004) 420-426.

[137] R.J. Chin, K. Nobe, Electrodissolution kinetics of iron in chloride solutions III. Acidic solutions, Journal of the Electrochemical Society, 119 (1972) 1457-1461.

[138] P. Cao, R. Gu, Z. Tian, Electrochemical and surface-enhanced Raman spectroscopy studies on inhibition of iron corrosion by benzotriazole, Langmuir, 18 (2002) 7609-7615.

[139] S. Asakura, K. Nobe, Electrodissolution kinetics of iron in chloride solutions Part II. Alkaline solutions, Journal of The Electrochemical Society, 118 (1971) 19-22.

[140] J.M. Bockris, D. Drazic, A. Despic, The electrode kinetics of the deposition and dissolution of iron, Electrochimica Acta, 4 (1961) 325-361.

[141] J. Yao, B. Ren, Z. Huang, P. Cao, R. Gu, Z.-Q. Tian, Extending surface Raman spectroscopy to transition metals for practical applications IV. A study on corrosion inhibition of benzotriazole on bare Fe electrodes, Electrochimica acta, 48 (2003) 1263-1271.

[142] X.-Z. Gao, H.-J. Liu, F. Cheng, Y. Chen, Thermoresponsive polyaniline nanoparticles: Preparation, characterization, and their potential application in waterborne anticorrosion coatings, Chemical Engineering Journal, 283 (2016) 682-691.

[143] X. Li, I. Nikiforow, K. Pohl, J. Adams, D. Johannsmann, Polyurethane coatings reinforced by halloysite nanotubes, Coatings, 3 (2013) 16-25.

[144] M. Quinet, B. Neveu, V. Moutarlier, P. Audebert, L. Ricq, Corrosion protection of sol–gel coatings doped with an organic corrosion inhibitor: chloranil, Progress in organic coatings, 58 (2007) 46-53.

[145] M. Montemor, Functional and smart coatings for corrosion protection: a review of recent advances, Surface and Coatings Technology, 258 (2014) 17-37.

[146] Y. Feng, Y.F. Cheng, Inhibitive performance of benzotriazole for steel corrosion studied by electrochemical and AFM characterization, Journal of Materials Engineering and Performance, 24 (2015) 4997-5001.

[147] D.G. Shchukin, H. Möhwald, Smart nanocontainers as depot media for feedback active coatings, Chemical Communications, 47 (2011) 8730-8739.

[148] H. Singh, K. Yeole, S. Mhaske, Synthesis and characterization of layer-by-layer assembled magnesium zinc molybdate nanocontainer for anticorrosive application, Chemical Engineering Journal, 295 (2016) 414-426.

[149] M. Zheludkevich, J. Tedim, M. Ferreira, “Smart” coatings for active corrosion protection based on multi-functional micro and nanocontainers, Electrochimica Acta, 82 (2012) 314-323.

[150] A. Mostafaei, F. Nasirpouri, Epoxy/polyaniline–ZnO nanorods hybrid nanocomposite coatings: Synthesis, characterization and corrosion protection performance of conducting paints, Progress in Organic coatings, 77 (2014) 146-159.

[151] Y. Lei, N. Sheng, A. Hyono, M. Ueda, T. Ohtsuka, Effect of benzotriazole (BTA) addition on Polypyrrole film formation on copper and its corrosion protection, Progress in Organic Coatings, 77 (2014) 339-346.

[152] Z. Ding, Smart release of corrosion inhibitors by a novel encapsulation method, (2016).

[153] S.A. Vasudevan, Y. Xu, S. Karwal, H.G. van Ostaay, G.M. Meesters, M. Talebi, E.J. Sudhölter, J.R. van Ommen, Controlled release from protein particles encapsulated by molecular layer deposition, Chemical Communications, 51 (2015) 12540-12543.

[154] D.G. Shchukin, M. Zheludkevich, K. Yasakau, S. Lamaka, M.G. Ferreira, H. Möhwald, Layer‐by‐layer assembled nanocontainers for self‐healing corrosion protection, Advanced Materials, 18 (2006) 1672-1678.

[155] J. Fu, T. Chen, M. Wang, N. Yang, S. Li, Y. Wang, X. Liu, Acid and alkaline dual stimuli-responsive mechanized hollow mesoporous silica nanoparticles as smart nanocontainers for intelligent anticorrosion coatings, ACS nano, 7 (2013) 11397-11408.

[156] B. Bhanvase, Y. Kutbuddin, R. Borse, N. Selokar, D. Pinjari, P. Gogate, S. Sonawane, A. Pandit, Ultrasound assisted synthesis of calcium zinc phosphate pigment and its application in nanocontainer for active anticorrosion coatings, Chemical engineering journal, 231 (2013) 345-354.

[157] Y. Qiang, L. Guo, S. Zhang, W. Li, S. Yu, J. Tan, Synergistic effect of tartaric acid with 2, 6-diaminopyridine on the corrosion inhibition of mild steel in 0.5 M HCl, Scientific Reports, 6 (2016).

[158] S. Meure, D.-Y. Wu, S.A. Furman, FTIR study of bonding between a thermoplastic healing agent and a mendable epoxy resin, Vibrational Spectroscopy, 52 (2010) 10-15.

[159] D. Kuang, F. Cheng, Coating degradation in the presence of alternating current interference, in: CORROSION 2016, NACE International, 2016.

[160] N. Kotov, Membrane sensors: Nanocomposites are stretched thin, Nature materials, 3 (2004) 669-671.

[161] X. Feng, L. Feng, M. Jin, J. Zhai, L. Jiang, D. Zhu, Reversible super-hydrophobicity to super-hydrophilicity transition of aligned ZnO nanorod films, Journal of the American Chemical Society, 126 (2004) 62-63.

[162] P. Wang, D. Zhang, R. Qiu, B. Hou, Super-hydrophobic film prepared on zinc as corrosion barrier, Corrosion Science, 53 (2011) 2080-2086.

[163] S. Sethi, A. Dhinojwala, Superhydrophobic conductive carbon nanotube coatings for steel, Langmuir, 25 (2009) 4311-4313.

[164] F. Guo, X. Su, G. Hou, P. Li, Bioinspired fabrication of stable and robust superhydrophobic steel surface with hierarchical flowerlike structure, Colloids and Surfaces A: Physicochemical and Engineering Aspects, 401 (2012) 61-67.

[165] T. Darmanin, E. Taffin de Givenchy, S. Amigoni, F. Guittard, Superhydrophobic surfaces by electrochemical processes, Adv Mater, 25 (2013) 1378-1394.

[166] P. Wang, D. Zhang, R. Qiu, J. Wu, Super-hydrophobic metal-complex film fabricated electrochemically on copper as a barrier to corrosive medium, Corrosion Science, 83 (2014) 317-326.

[167] Y. Li, X. Pang, R. Epand, I. Zhitomirsky, Electrodeposition of chitosan–hemoglobin films, Materials Letters, 65 (2011) 1463-1465.

[168] N. Xu, D.K. Sarkar, X.G. Chen, W.P. Tong, Corrosion performance of superhydrophobic nickel stearate/nickel hydroxide thin films on aluminum alloy by a

simple one-step electrodeposition process, Surface and Coatings Technology, 302 (2016) 173-184.

[169] S. Ji, P.A. Ramadhianti, T.-B. Nguyen, W.-d. Kim, H. Lim, Simple fabrication approach for superhydrophobic and superoleophobic Al surface, Microelectronic Engineering, 111 (2013) 404-408.

[170] P. Wang, D. Zhang, R. Qiu, Y. Wan, J. Wu, Green approach to fabrication of a super-hydrophobic film on copper and the consequent corrosion resistance, Corrosion Science, 80 (2014) 366-373.

[171] T. Rezayi, M.H. Entezari, Toward a durable superhydrophobic aluminum surface by etching and ZnO nanoparticle deposition, J Colloid Interface Sci, 463 (2016) 37-45.

[172] Y. Zhang, S. Tang, J. Hu, T. Lin, Formation mechanism and corrosion resistance of the hydrophobic coating on anodized magnesium, Corrosion Science, 111 (2016) 334-343.

[173] Y. Tian, B. Su, L. Jiang, Interfacial material system exhibiting superwettability, Adv Mater, 26 (2014) 6872-6897.

[174] Y. Fan, C. Li, Z. Chen, H. Chen, Study on fabrication of the superhydrophobic sol–gel films based on copper wafer and its anti-corrosive properties, Applied Surface Science, 258 (2012) 6531-6536.

[175] G. Fonder, F. Laffineur, J. Delhalle, Z. Mekhalif, Alkanethiol-oxidized copper interface: The critical influence of concentration, Journal of colloid and interface science, 326 (2008) 333-338.

[176] M.-W. Tsao, J.F. Rabolt, H. Schönherr, D.G. Castner, Semifluorinated/hydrogenated alkylthiol thin films: a comparison between disulfides and thiol binary mixtures, Langmuir, 16 (2000) 1734-1743.

[177] K. Sriraman, P. Manimunda, R. Chromik, S. Yue, Effect of crystallographic orientation on the tribological behavior of electrodeposited Zn coatings, RSC Advances, 6 (2016) 17360-17372.

[178] Y. Liu, S. Li, J. Zhang, J. Liu, Z. Han, L. Ren, Corrosion inhibition of biomimetic super-hydrophobic electrodeposition coatings on copper substrate, Corrosion Science, 94 (2015) 190-196.

[179] Y. Feng, Y.F. Cheng, An intelligent coating doped with inhibitor-encapsulated nanocontainers for corrosion protection of pipeline steel, Chemical Engineering Journal, 315 (2017) 537-551.